UNIVERSITY OF PAVIA

FACULTY OF ENGINEERING

DEPARTMENT OF ELECTRICAL, COMPUTER AND BIOMEDICAL ENGINEERING

DOCTORAL DISSERTATION

Modelling, Estimation, and Cell-to-Cell Heterogeneities analysis in Lithium-Ion Battery Systems

Candidate: **Simone Fasolato**

Supervisor: **Prof. Davide Martino Raimondo**

CYCLE XXXVII

Abstract

The development of reliable, long-lasting, and safe energy storage systems is crucial for effectively supporting the transition from fossil fuels to renewable energy resources, thereby driving a sustainable global electrification process. However, ethical concerns regarding the materials used in the battery supply chain, as well as the safety and reliability of large battery modules/packs must be properly addressed. One effective commercially mature solution to mitigate the former challenge is the use of lithium iron phosphate (LFP) batteries. Unlike traditional batteries that rely on cobalt, manganese, and nickel, LFP batteries overcome the scarcity and ethical controversies associated with traditional battery materials, offering a more ethical and sustainable alternative. Despite their advantages, LFP batteries present certain technical challenges. The plateaus in open circuit voltage, hysteresis, and path-dependent dynamics exhibited by LFP batteries make them challenging to model, estimate, and control. In this work, the development of control-oriented reduced-order models based on physics-based electrochemical model for LFP batteries is presented, providing a foundation for the development of advanced LFP-based Battery Management System (BMS) strategies. Additionally, a properly designed BMS can ensure the safe and optimal operation of battery modules and packs regardless the cell chemistry, addressing the second challenge. In particular, it is crucial to recognize and accurately quantify cell-to-cell (CtC) variations, as these can significantly impact the overall performance, heterogeneity, and degradation of the battery system. The ultimate goal is to enhance BMS algorithms to account for CtC variations, increasing, in turn, their reliability and robustness. To address this, in this study the effects of CtC variations on parallel-connected battery modules are extensively analyzed using comprehensive statistical methods. Based on full factorial design of experiments, the impact of different sources of CtC variation, such as uneven interconnection resistance, operating temperature, cell chemistry, and aging conditions, are evaluated on the module performance. The collected experimental data form the foundation for developing data-driven models, including interpretable multilinear regression and black-box machine learning models, which are then used to explain and quantify the contribution of each CtC source to the corresponding module-level responses. Further, the analysis is enhanced using a high-fidelity, experimentally validated electrochemical model that incorporates detailed module-level features, considering both short- and long-term implications on module responses. Additionally, leveraging the battery system digital twin, a straightforward cell arrangement strategy to mitigate thermal gradients in parallel-connected battery modules is proposed. This strategy aims to reduce aging disparities between cells, thereby extending the overall lifespan of the battery module. Finally, a state estimation algorithm for individual cells within parallel-connected battery configurations is formulated and validated against experimental data. Utilizing a Moving Horizon Estimation approach, this algorithm provides accurate state estimates, representing a key step toward enhancing battery pack cell balancing and the development of novel fault detection and isolation strategies.

Contents

1 Introduction 21

2 Lithium-ion batteries 28
- 2.1 Li-ion Cells 30
  - 2.1.1 Working Principle 30
  - 2.1.2 Battery terminology 32
  - 2.1.3 Degradation mechanisms 32
- 2.2 Battery Management system (BMS) 35

3 Battery modelling 38
- 3.1 Cell-level models 42
  - 3.1.1 Equivalent Circuit model (ECM) 42
  - 3.1.2 Electrochemical model (EM) 42
    - 3.1.2.1 Doyle-Fuller-Newman (DFN) model 43
    - 3.1.2.2 ESPM 46
    - 3.1.2.3 CS-ESPM 47
    - 3.1.2.4 SPM 49
  - 3.1.3 Model order reduction 49
    - 3.1.3.1 Spatial discretization techniques 51
    - 3.1.3.2 Function approximation 57
    - 3.1.3.3 Frequency Domain Approximation 60
    - 3.1.3.4 MOR for high-dimensional ODE systems 62
  - 3.1.4 Thermal models 65
    - 3.1.4.1 Thermal-dependent parameters 68
  - 3.1.5 Aging models 68
    - 3.1.5.1 SEI layer growth 69
    - 3.1.5.2 Lithium plating 70
    - 3.1.5.3 Particle cracking 71
    - 3.1.5.4 Loss of active material 71
- 3.2 Module-level models 72
  - 3.2.1 Electrical submodel 72
  - 3.2.2 Thermal submodel 74
- 3.3 Conclusion 75

4 Battery testing **78**
- 4.1 Battery cell batches . . . 80
- 4.2 Experimental activities . . . 81
  - 4.2.1 ELISA campaign . . . 81
    - 4.2.1.1 Testing procedure . . . 83
    - 4.2.1.2 Laboratory facilities . . . 86
  - 4.2.2 SECL campaign . . . 86
    - 4.2.2.1 Cell-level testing . . . 87
    - 4.2.2.2 Module-level testing . . . 88
    - 4.2.2.3 Laboratory facilities . . . 90
- 4.3 Conclusion . . . 92

5 EM parametrization **94**
- 5.1 EMs parameters identification . . . 97
  - 5.1.1 Cell teardown method . . . 97
  - 5.1.2 Parameter sensitivity analysis . . . 99
- 5.2 ESPM identification and validation for LG M50T . . . 103
  - 5.2.1 Single cell ESPM identifiction and validation . . . 103
  - 5.2.2 ESPM-based module-level model validation . . . 108
- 5.3 Conclusion . . . 115

6 CS-ESPM model order reduction **117**
- 6.1 CSa-ESPM numerical solution . . . 120
  - 6.1.1 FDM-based CSa-ESPM: 2P-Region Approximation . . . 120
  - 6.1.2 CSa-ESPM: State-space formulation . . . 123
- 6.2 CSa-ESPM moder order reduction . . . 125
  - 6.2.1 POD-Galerkin ROM . . . 126
    - 6.2.1.1 Simulation results . . . 126
    - 6.2.1.2 POD-Galerkin ROM limitations . . . 129
  - 6.2.2 FVM-based CSa-ESPM . . . 132
    - 6.2.2.1 Parameters identification and results . . . 133
- 6.3 Conclusion . . . 136

7 Data-driven analysis of CtC variation impact on parallel-connected module **138**
- 7.1 Methodology . . . 142
  - 7.1.1 Design of Experiments . . . 142
  - 7.1.2 Data-driven model . . . 144
    - 7.1.2.1 Multilinear-regression (MLR) models . . . 144
    - 7.1.2.2 Machine learning (ML) models . . . 145
    - 7.1.2.3 Performance matrices . . . 146
  - 7.1.3 Feature importance analysis . . . 147
- 7.2 Results and discussion . . . 149
  - 7.2.1 MLR models analysis . . . 149

7.2.2 ML models analysis 152
7.2.3 Models comparison 155
7.2.4 Limitations 157
7.3 Conclusion 158

8 Model-based analysis of CtC variation impact on parallel-connected module 160
8.1 Model and method 163
8.1.1 High-fidelity model 163
8.1.2 CtC variation effect: MLR analysis 163
8.2 Results and discussion 165
8.2.1 MLR analysis: short term CtC heterogeneity effects 165
8.2.2 MLR analysis: long term CtC heterogeneity effects 169
8.2.3 Cell arrangement strategy for thermal gradient reduction 172
8.3 Conclusion 174

9 States estimation for parallel-connected battery module 176
9.1 ECM-based Cell model 180
9.1.1 Single cell first order ECM identification 180
9.1.2 Module-level model formulation 180
9.2 Non-linear observability analysis 184
9.2.1 Nonlinear observability analysis: results from the module-level model 188
9.3 Moving horizon estimation 190
9.3.1 MHE for parallel-connected module 191
9.3.1.1 Validation using simulated data 193
9.3.1.2 Validation with experimental data 195
9.3.1.3 Joint SOC and interconncetion resistance estimation . . . 197
9.4 Conclusion 198

Conclusions 200

Acknowledgments 203

List of Publications 205

Bibliography 207

List of Figures

2.1 Schematic diagram of a LIB working principle. 31
2.2 Degradation mechanisms in Li-ion cells. *Figures from [1]* 33

3.1 Overview of Battery Models, inspired by [2, 3, 4, 5]. 40
3.2 n-order RC ECM scheme 42
3.3 C/4 discharge. The moving boundary (r_p) is plotted to illustate the positive electrode one-phase ($r_p/R_{s,p} = 0$) and two-phase ($r_p/R_{s,p} > 0$) regions. . . . 48
3.4 Schematic overview of the key concentration values needed for the voltage calculation in the ESPM. 49
3.5 Schematic overview of the most commonly used MOR techniques in the context of battery modeling. Figure inspired by [6]. 51
3.6 Derivative approximation using first-order Forward, Backward and Central FDM scheme 52
3.7 (a) FDM and (b) FVM scheme used to discretized the particle radius of the electrode solid phase. 54
3.8 Schematic representation of the module-level ECM-based model for (a) series-connected and (b) parallel-connected scenarios. 73
3.9 Schematic representation of the module-level ECM-based model for (a) series-connected and (b) parallel-connected scenarios. 76

4.1 A visual flowchart illustrating the data usage in the following chapters . . . 80
4.2 (a) Pseudo OCV curves of the fresh 11 cells under C/20 discharge test procedure (Steps 4 in Table 4.2). (b) Boxplot of cell capacities under different temperatures. 84
4.3 (a) HPPC test procedure showing the voltage and current profiles during the test. (b) Detailed view of a discharge pulse highlighting the voltage drop (ΔV_{pulse}) and current drop (ΔI_{pulse}) used to calculate the ohmic resistance ($R_{0,dis}$). (c) Boxplot illustrating the distribution of $R_{0,dis}$, calculated using (4.2), at various SOC and temperatures. 85
4.4 Voltage and current profiles for the (a) WLTP, (b) UDDS, and (c) US06 driving cycles at 25 $°C$. 86
4.5 Equipment available at the Energy Laboratory for Interdisciplinary Storage Applications (ELISA) 86

4.6 A visual flowchart of the implemented experimental procedures, selected steps, and design of experiments. Single-cell characterization (top) is performed before module-level testing (bottom). 87
4.7 (a) Pseudo OCV curves of the fresh 37 cells under C/20 discharge test procedure. (b) Boxplot of cells internal resistances at 10% SOC intervals. . 88
4.8 Equipment available at the Stanford Energy Control Lab [7] 91

5.1 GPSA results: (a-b) show the module voltage responses resulting from the GPSA for a CC+rest and DV scenarios, respectively. (c-d) and (e-f) reports the mean value (μ_{EE_j}) and standard deviation (σ_{EE_j}) of the Elementary Effect (EE) at each time instant for each parameter in both scenarios. (g) shows the average mean value ($\mu_{EE_j}^{avg}$) calculated over the entire operating cycles (CC+rest and DV cycles) for each parameter. 102
5.2 Schematic overview of the identification and validation procedure described in this section. (a) 19 different ESPMs are identified and validated using single-cell characterization data from a batch of LG M50T cells. (b) The single-cell model dynamics are scaled up to the module level, and the resulting current and thermal distributions are validated against experimental data. 104
5.3 Comparison between the modeled cell OCV (i.e., $U_p - U_n$) for the LG M50, obtained using equations (5.8) and (5.9), and the measured OCV obtained through a pseudo-OCV test for the LG M50T (Section 4.2.2.1). 106
5.4 Single-cell parameter identification results at C/20 for the 19 LG M50T cells. (a) Voltage profile comparison between experimental CC discharge and model simulations for cells P12 and P13. (b) RMES between experimental data and model predictions during CC C/20 discharge for all cells. (c) SOC comparison between model predictions and experimental measurements for cell P12. (d) identified parameters (i.e. $\epsilon_{s,n}$ and $\epsilon_{s,p}$) for the 19 tested cells against cell capacity. 108
5.5 Single-cell parameter validation for the 19 LG M50T cells under HPPC+MS testing protocol. (a) and (c) Voltage profile and SOC comparison between experiments and model simulations for cell P12, respectively. (b) RMES between experimental voltage and model predictions for all cells. (d) RMES between reference SOC and electrode SOC for all the cells. 109
5.6 Schematic representation of the physics-based electrochemical-aging-thermal model for the battery module, where the module thermal model and the ESPM coupled with the SEI-based aging model are highlighted. 109
5.7 Module-Level thermal model results for four parallel-connected cells under $R_{int} = 0, 1, \text{and } 3$ mΩ and $T_{amb} = 10, 25, \text{and } 40°C$. (a-d) Comparison of cell temperatures between experimental data and model simulations for the battery module subjected to a 1 mΩ of R_{int} at 25°C. (e-g) Comparisons between $\sigma_{T_{cell}}$ calculated using the simulated and measured cell theraml distribution. (h-l) Comparisons between $\mu_{T_{cell}}$ calculated using the simulated and measured cell theraml distribution. 112

5.8 Module-Level model validation for four parallel-connected cells under $R_{int} = 0, 1, \text{and } 3$ mΩ and $T_{amb} = 10, 25, \text{and } 40°C$. (a) Comparison of voltage profiles between experimental data and model simulations for $R_{int} = 0, 1, \text{and } 3$ mΩ at $25°C$. (b) Voltage RMSE across all module experiment scenarios considered. (c-f) Comparison of cell currents between experimental data and model simulations for the battery module subjected to a 3 mΩ of R_{int} at 25°C. (g-i) Comparisons between $\sigma_{I_{cell}}$ calculated using the simulated and measured cell currents. 113

6.1 Overview of discretization grids used to numerically solve the diffusion PDE in the CSa-ESPM: (a) FDM grid for the solid particles, (b) FVM grid for the solid particles, and (c) FVM mesh for the liquid phase of the CSa-SPM. 121
6.2 Model reduction flowchart applied to the CSa-ESPM 127
6.3 Constant current discharge cycles at C/3, C/6, C/10 and C/12: Cell voltage(a), SOC (b) and moving boundary (c). 129
6.4 Real driving cyle results comparison: Cell current profile (a), voltage (b) and SOC (c). 130
6.5 Constant current discharge results comparison using the combined trucated basis function: Cell voltage(a-b), SOC (c-f) and moving boundary (g-h). . 131
6.6 Comparison results at C/4, C/2, and 1C for (a) voltage, (b) moving boundary, (c) volume-average concentraion, (d) moving boundary during cycling. 135

7.1 Visual overview of the DOE-based CtC variations analysis described in this chapter. 141
7.2 Graphical representation resulting from the four factors and respective levels of the full-factorial DoE. 142
7.3 Visual representation of the eight response variables considered in this study for one of the 54 experiments. The variables are illustrated based on (a) current distribution, (b) thermal distribution, (c) SOC distribution, and (d) TTSB. 144
7.4 Contour plots derived from the multivariate linear models simulated space for (a) σI_{Start}, (b) σT_{Mean}, (c) $TTSB$. The horizontal and vertical axes of individual contour plots are the interconnection resitance and the test temperature, respectively. The columns of each group of six contour plots have new and aged cells configurations, respectively, while the rows differ upon chemistry (NMC, NCA, Mix). 150
7.5 Contour plots derived from the MLR model for TTSB. 153
7.6 Contour plots derived from the NN model for TTSB. 153
7.7 Contour plots derived from the RF model for TTSB. 153
7.8 Random Forest model simulated Shap values for the eight considered response variables (a-h). On the left side of individual graphs the resulting feature importance ranking is reported, while the circles' colour shades indicate their absolute value. 154

7.9 Random Forest (red) and Neural Network (blue) models PDP and ICE plots for five out of the eight response variables (a-e). Each column reports the PDP and ICE plots resulting from one individual feature. 156

8.1 Visual overview of the model-based CtC variations analysis described in this chapter. 162
8.2 Schematic representation of the physics-based electrochemical-aging-thermal model for the battery module, where the module thermal model and the ESPM coupled with the SEI-based aging model are highlighted. 163
8.3 Figure (a) and (b) report the correlation and VIF analyses for the model predictors, respectively. Figures (c.1-g.1) depict the impact of each term in the multilinear regression (MLR) model on the model's R^2. Figures (c.2-g.2) rank the terms of the MLR model according to their influence on increasing R^2. Finally, Figures (c.3-g.3) visually demonstrate the contributions of the two most influential predictors to the corresponding response variable. 167
8.4 Figures (a.1-e.1) illustrate the impact of each term in two MLR models. The blue line represents the predictors set Γ_1, while the orange solid line represents the enhanced model. Figures (a.2-e.2) rank and compare the terms of both MLR models based on their influence on increasing R^2. Figures (a.3-e.3) visually demonstrate the contributions of the two most influential predictors to the corresponding response variable. 170
8.5 MLR analysis long-term simulation results. Figures (a.1-d.1) rank and compare the terms of both MLR models based on their influence on increasing R^2. Figures (a.2-d.2) visually demonstrate the contributions of the two most influential predictors to the corresponding response variable. 171
8.6 Cell arrangement strategy for parallel-connected module graphical overview. (a) shows the battery module with randomly arranged cells (M1) and the optimized cell arranged(M2). (b) compare the modules' response variables. (c), (d), and (e) report the module voltage, the cell current distribution, and the thermal distribution comparison between M1 and M2, respectively. 173

9.1 Visual overview of the MHE-based state estimation procedure presented in this chapter. 179
9.2 ECM identification results for the *LG Chem M50T*: (a) Comparison between the C/20 Pseudo-OCP test and V_{OCP}. (b) Comparison between the HPPC+MS test and the ECM. Both tests refer to cell *P10* in [8]. 181
9.3 Schematic representation of the module-level ECM-based model 183
9.4 Observability analysis results. Panels (a-c) show the voltage across each cell ($V_{cell}^{[i]}$ with $i = 1, \cdots, N_p$) and at the module terminals during a $0.75C$-rate constant current cycle with $R_{int} = 3\ m\Omega$ for $N_p = 2, 3$, and 4, respectively. Panels (d-f) display the rank of $\hat{\Theta}$ (from (9.25)) for $R_{int} = 0, 1$ and $3m\Omega$ and panels (g-i) present the condition number of $\hat{\Theta}$ for the same R_{int} values and $N_p = 2, 3$ and 4. 190

9.5 Comparison of MHE schemes on simulated data: ODE vs. DAE models. (a) shows ΣSOC^{RMS}, (b) presents ΣV_1^{RMS} and (c) displays $MTPI$ under different horizon lengths. 193
9.6 Validation of the MHE-based SOC estimation algorithm in constant current (CC) (a-c) and driving cycle (d-f) scenarios. (a)(d) Comparison of measured and estimated module voltage (V_{mod}). (b)(e) SOC distribution across cells. (c)(f) SOC estimation error for each cell, along with voltage measurement noise. 195
9.7 Validation of the MHE-based SOC estimation algorithm using experimental data under two different R_{int} values: $1m\Omega$ (a-c) and $3m\Omega$ (d-f) scenarios. (a)(d) Comparison of measured and estimated V_{mod}. (b)(e) SOC error for each cell. (c)(f) Comparison of measured and estimated current distribution over the Depth of Discharge (DOD). 196
9.8 Joint SOC and R_{int} estimation results using the same data as Fig. 9.7(d-f). (a) Maximum SOC error (b) Comparison of estimated and reference R_{int} values. 197

List of Tables

3.1 Electrochemical models nomenclature 43
3.2 Electrochemical models overview 44
3.3 Summary of Finite Difference Method (FDM) Schemes for First and Second Derivative Approximations 53
3.4 Examples of lumped thermal models for cylindrial and prismatic/pouch cells. 66

4.1 Technical specifications of the tested cell 82
4.2 ELISA campaign: cell-level characterization procedure 83
4.3 SECL campaign: cell-level characterization procedure 88
4.4 SECL campaign: module-level testing steps 89

5.1 ESPM parameters for the LG 21700 M50T 98
5.2 Cell-level electrochemical-thermal-aging dynamics for the LG M50T. 105
5.3 Parallel-module state-space model matrices and coefficients of state-space model (5.25) 114

6.1 Core-shell ESPM discretized electrochemical governing dynamics [9][10] 124
6.2 POD-Galerkin average core-shell ESPM: Snapshot matrices and ROM state-space formulation 127
6.3 %RMSEs between the ROM and the CSa-ESPM 128
6.4 CSa-ESPM discretized electrochemical governing dynamics 134
6.5 Identified parameters at different C-rates. 134

7.1 Overview of the control and response variables included in the study. N_p refers to the number of cells connected in parallel (in this study, $N_p = 4$). I_{Cellk} denotes the current delivered by the k-th cell, I_{Mod} is the module input current. T_{Amb} is the ambient temperature, SoC_{Cellk} and T_{Cellk}^{Surf} are the SoC and surface temperature of the k-th cell, respectively. t_1, t_2, and t_{end} are the time instants used to split the cell current distribution, as depicted in Figure 7.3. 143
7.2 Multivariate linear regression model equations with 3 most influencing β coefficients underlined ($\uline{1^{st}}$, $\dashuline{2^{nd}}$, $\dotuline{3^{rd}}$) and resulting R^2 values. 149
7.3 Evaluated 5-fold cross-validation models performance mean values and standard deviations. 157

8.1 Multi linear regression model predictor aand response variable 166

9.1 Cell-level and module-level models formulation 181
9.2 Summary of the MHE-based algorithm performance indicators 193

Acronyms

LIB	Lithium-Ion Battery
SOC	State of Charge
SOH	State of Health
DOD	Depth of discharge
BMS	Battery Management System
ECM	Equivalent Circuit Model
EM	Electrochemical Model
DFN	Doyle-Fuller-Newman
ESPM	Enhanced electrolyte Single Particle Model
SPM	Single Particle Model
CS-ESPM	Core-Shell ESPM
CSa-ESPM	Average CS-ESPM
LFP	Lithium Iron Phosphate
NMC	Nickel Manganese Cobalt
NCA	Nickel Cobalt Aluminum
CtC	Cell-to-Cell
ROM	Reduced Order Model
MOR	Model Order Reduction
MHE	Moving Horizon Estimation
MLR	Multi Linear Regression
ML	Machine Learning
POD	Proper Orthogonal Decomposition
P2D	Pseudo-2-Dimensional
PDE	Partial Differential Equation
ODE	Ordinary Differential Equation
AE	Algebraic Equation
SEI	Solid Electrolyte Interface
LLI	Loss os Lithium Inventory
LAM	Loss of Active Material
FDM	Finite Difference Method
FVM	Finte Volume Method
FEM	FInite Element Method
BC	Boundary Condition
CV	Control Volume

PA	Padé Approximation
RG	Residue Grouping
SECL	Stanford Energy Control Lab
ELISA	Energy Laboratory fo Interdisciplinary Storage Applications
LGES	LG Energy Solution
HPPC	Hybrid Pulse Power Characterization
CC	Constant Current
CCCV	Constant Current Constant Voltage
WLTP	Worldwide harmonized Light vehicles Test Procedure
UDDS	Urban Dynamometer Driving Schedule
DAQ	Data Acquisition System
MS	Multi-Sine
DOE	Design Of Experiments
OCV	Open Circuit Voltage
OCP	Open Circuit Potential
PSA	Parameter Sensitivity Analysis
GPSA	Global PSA
LPSA	Local PSA

Chapter 1

Introduction

The urgent need to reduce the environmental impact of energy and transportation sectors has accelerated the shift toward electrification, driving the widespread adoption of smart mobility solutions and electric vehicles. However, a key challenge in fully supporting the shift from fossil fuels to renewable energy sources is the development of reliable, long-lasting, and safe energy storage systems to ensure a smooth and sustainable transition. Currently, Lithium-Ion Batteries (LIBs) dominate the market for applications in portable electronics, automotive industry [11], and renewable energy [12], and their adoption is expected to continue increasing alongside emerging alternative chemistries, primarily sodium-ion and solid-state batteries [13]. The preference for LIBs is primarily due to their high energy density, efficiency, longevity, and cost-effectiveness [14]. Additionlly, to meet precise power and energy demands lithium-ion battery modules or packs, comprising interconnected individual cells arranged in series and/or parallel configurations, are created. However, despite their advantageous properties, LIBs face several critical challenges that hinder their sustainable and widespread adoption. One of the foremost issues is the reliance on scarce and ethically contentious materials such as cobalt, nickel, and manganese. These materials are key components in many LIB cathodes and are not only expensive but also associated with significant ethical concerns, including human rights violations and environmentally destructive mining practices [15]. The geopolitical concentration of cobalt sources exacerbates supply chain vulnerabilities, making the industry susceptible to market fluctuations and ethical scrutiny [16]. In light of these challenges, Lithium Iron Phosphate (LFP) batteries have emerged as a promising alternative. LFP batteries eliminate the need for cobalt and reduce dependence on nickel, offering a pathway to a more resilient battery supply chain [17]. LFP batteries offer several advantages, including superior thermal and chemical stability, enhanced safety by mitigating the risk of thermal runaway, and a significantly longer cycle life exceeding 2,000 cycles, which lowers the total cost of ownership [18]. Major manufacturers, such as Ford, Stellantis and Tesla, have invested in and adopted LFP technology, highlighting its growing importance in the global electric vehicle market [19]. However, LFP batteries are not without their drawbacks. Their lower energy density compared to high-nickel LIBs can limit their applicability in sectors where weight and space are critical, such as in long-range electric vehicles and portable electronics [20]. Additionally, LFP batteries experience plateaus in open circuit voltage, hysteresis, and path-dependent dynamics due to phase transitions during intercalation and de-intercalation [21]. These phenomena are challenging to model and even more difficult to estimate and control. Furthermore, a key challenge in the battery industry is ensuring the safe operation of energy storage systems to prevent harm to both people and property [22]. To address this, battery modules or packs are equipped with Battery Management Systems (BMS) [23]. The BMS plays a crucial role in estimating unmeasurable cell states such as State of Charge (SOC) and State of Health (SOH), ensuring optimal cell performance through cell balancing and fault detection strategies. In addition, the BMS manages thermal regulation, keeping the battery pack within safe temperature limits to prevent overheating and potential failures. A critical aspect of improving BMS control and estimation algorithms lies in recognizing the presence of cell-to-cell (CtC) heterogeneity and understanding its impact on pack/module performance, degradation, and safety [24]. Variations in capacity, internal resistance, and voltage, often induced during manufacturing, combined with suboptimal pack architecture and cooling designs, can cause imbalances in the performance of parallel strings. These heterogeneities lead to uneven current distribution, temperature fluctuations, and SOC discrepancies among the parallel branches. It is important to note that CtC variations in a real parallel-connected battery module are highly interdependent and practically unavoidable. Due to the absence of individual current, temperature, and voltage sensors for each cell, parallel-connected modules are typically treated as a single lumped cell in a BMS, neglecting internal heterogeneity. As a result, undetected current imbalances may cause cell overcharging or overdischarging, leading to large thermal gradients and hotspots within the module, which pose significant safety risks to the entire battery pack. Moreover, varying current rates and temperatures can trigger different degradation mechanisms, causing parallel cells to age at different rates [25, 26].

Thesis overview

This dissertation presents two primary contributions to the advancement of BMS for LFP-based and parallel-connected battery systems. Specifically, building upon the high-fidelity core-shell enhanced electrolyte single particle model (CS-ESPM) developed in [9, 10], two different reduced-order models are proposed. The CS-ESPM is formulated to accurately capture the phase transition behavior of LFP molecules during operation. Therefore, the ROMs represent a crucial first step toward developing control-oriented, model-based strategies aimed at improving BMS algorithms for LFP-based battery systems. Furthermore, the impact of CtC variation in parallel-connected modules is analyzed through statistical methods. A full factorial design of experiments is employed to evaluate how different sources of CtC variation, such as uneven interconnection resistance, operating temperature, cell chemistry, and aging conditions, affect module heterogeneity. Specifically, the study examines their influence on current distribution, thermal behavior, SOC, and the time required for self-balancing within the module. Both traditional linear regression techniques and modern explainable machine learning methods are utilized to rank the importance of these features and predict module-level heterogeneities. The analysis is further enhanced using a high-fidelity, experimentally validated model that incorporates detailed module-level features. Particularly, the effects of varying cell spacing, cell location and manufacturing-inducted CtC variations within the module are added in the analysis and their impact are investigated under both short-term and long-term operations. Further, a straightforward cell arrangement strategy is proposed to mitigate thermal gradients in parallel-connected battery modules. This strategy aims to reduce aging gradients between cells, thereby extending the overall lifespan of the battery module. Finally, a state estimation algorithm for individual cells within parallel-connected battery configurations, is formulated and validated agianst experimental data. Utilizing a Moving Horizon Estimation (MHE) approach, this algorithm provides accurate state estimates representting, in turn, a key step towards enhancing battery pack cell balancing, and the development of novel fault detection and isolation strategies.

Thesis structure

Chapter 2: Lithium-ion batteries

This chapter provides readers with a high-level overview of LIB components, their working principles, and the degradation mechanisms that cells undergo during operations. Furthermore, it presents an overview of the battery terminology that will be used throughout the remainder of the text and summarizes the primary tasks of the BMS.

Chapter 3: Battery modelling

This chapter aims to equip readers with the necessary tools to better comprehend the battery model utilized in the following chapters. It does not, however, intend to offer a comprehensive and complete review of all existing battery modeling methods. Rather, it focuses on detailing and illustrating commonly used techniques in battery modeling. Although not all of these methods will be applied in the research presented, they are crucial for a thorough understanding of the rest of the manuscript.

Chapter 4: Battery testing

This chapter provides an overview of the laboratory experimental campaigns conducted to collect essential battery data, which form the foundation of the research presented in this thesis. It includes detailed specifications of the cell batches used, a comprehensive review of the laboratory equipment, and a clear outline of the data collection procedures. Additionally, it explains how the experimental data are utilized in the subsequent chapters, enhancing the reader's understanding of their integration into the overall research activities.

Chapter 4 contains results published in:

1. [8] Piombo, G., **Fasolato, S.**, Heymer, R., Hidalgo, M. F., Niri, M. F., Raimondo, D. M., Marco, J., and Onori, S. (2024). *Full factorial design of experiments dataset for parallel-connected lithium-ion cells imbalanced performance investigation.* Data in Brief, 53, 110227.

Chapter 5: Model identification and validation

This chapter aims to provide a high-level overview of the methodologies for parameterizing electrochemical models. Further, an example of model identification is presented. Specifically, an enhanced electrolyte single particle model (ESPM) is identified for the LG Chem M50T cells, and validated at both cell- and module-level.

Chapter 5 contains results submitted in:

- [27] **Fasolato, S.**, Allam, A., Onori, S., and Raimondo, D. M. (2024). *Cell-to-Cell Heterogeneities and Module Configurations analysis in Parallel-Connected Battery Modules via physics-based modeling*, Journal of Energy Storage, **Submitted**.

Chapter 6: CS-ESPM model order reduction

This chapter presents the mathematical formulation of two distinct reduced-order models (ROMs) for the CS-ESPM proposed in [10, 9, 28]. Specifically, the Proper Orthogonal Decomposition (POD)-Galerkin projection and the finite volume method are employed to approximate the solid-phase electrochemical dynamics of the CS-ESPM. The resulting control-oriented ROMs provide a foundation for the development of advanced BMS strategies, particularly in the context of LFP applications.

Chapter 6 contains results published in:

- [29] **Fasolato, S.**, Allam, A., Li, X., Lee, D., Ko, J., and Onori, S. (2022). *Reduced-order model of lithium-iron phosphate battery dynamics: A POD-Galerkin approach.* IEEE Control Systems Letters, 7, 1117-1122.

- [30] Xu, L., **Fasolato, S.**, and Onori, S. (2024). *Finite-volume method and observability analysis for core-shell enhanced single particle model for lithium iron phosphate batteries.* IEEE 2024 Conference on Decision and Control (CDC), **Accepted**.

Chapter 7: Data-driven analysis of CtC variation impact on parallel-connected module

Based on a full factorial design of experiments and module-level tests conducted on parallel-connected battery modules, a comprehensive statistical analysis is carried out to evaluate and predict the impact of CtC variants on module performance. In particular, both linear regression and machine learning models are utilized to analyze the effects of uneven interconnection resistance, operating temperature, cell chemistry, and aging conditions on module performance and heterogeneities propagation.

Chapter 7 contains results published in:

- [31] Piombo, G., **Fasolato, S.**, Heymer, R., Hidalgo, M., Niri, M. N., Onori, S., Marco, J. (2024). *Unveiling the performance impact of module level features on parallel-connected lithium-ion cells via explainable machine learning techniques on a full factorial design of experiments*, Journal of Energy Storage, 84, 110783.

Chapter 8: Model-based analysis of CtC variation impact on parallel-connected module

In this chapter, a high-fidelity electrochemical-thermal-aging module-level model is employed to perform high-fidelity offline simulations across various system configurations. The resulting simulated dataset is subsequently utilized to examine the influence of CtC parameter uncertainties and module configurations on cell current and temperature distributions, as well as on the module energy and capacity in both fresh and aged conditions, through a multi linear regression(MLR)-based statistical analysis. Finally, a simple cell arrangement strategy is proposed to mitigate thermal gradients in parallel-connected battery modules, thereby reducing the aging gradient between cells by the end of the simulations.

Chapter 8 contains results submitted in:

- [27] **Fasolato, S.**, Allam, A., Onori, S., and Raimondo, D. M. (2024). *Cell-to-Cell Heterogeneities and Module Configurations analysis in Parallel-Connected Battery Modules via physics-based modeling*, Journal of Energy Storage, **Submitted**.

Chapter 9: States estimation for parallel-connected modules

This chapter explores the estimation of unmeasurable states for individual cells within parallel-connected battery configurations using a MHE approach. The chapter makes three primary contributions. First, a nonlinear observability analysis is conducted to evaluate the feasibility of reconstructing individual cell states from module voltage and current measurements, taking into account interconnection resistance, SOC-dependent parameters, and varying numbers of cells. Finally, the MHE-based estimation algorithms are validated through simulations and experimental data from a four-cell battery. The proposed method serves as a foundation for the development of novel fault detection strategies.

Chapter 9 contains results submitted and published in:

- [32] **Fasolato, S.**, Acquarone, M. and Raimondo, D. M. (2024). *States estimation for parallel-connected battery module: a moving horizon approach*, IEEE Transaction on Control System Technology, **Submitted**

- [33] **Fasolato, S.**, and Raimondo, D. M. (2022). *Observability analysis of a li-ion cell equivalent circuit model based on interval arithmetic*, 2022 IEEE Vehicle Power and Propulsion Conference (VPPC), 1-7.

Chapter 2

Lithium-ion batteries

Contents

2.1 Li-ion Cells 30

2.1.1 Working Principle 30

2.1.2 Battery terminology 32

2.1.3 Degradation mechanisms 32

2.2 Battery Management system (BMS) 35

Introduction

Lithium-ion batteries have become a cornerstone of the global energy infrastructure, dominating the consumer electronics market thanks to their superior specific energy and power density. In response to the escalating threat of climate change, efforts to reduce greenhouse gas emissions and address environmental challenges through electrification have extended lithium-ion technology into the transportation sector. Furthermore, as societies strive to decrease dependence on fossil fuels, lithium-ion batteries are emerging as a promising solution for grid energy storage, facilitating the widespread adoption of renewable energy sources such as solar, tidal, and wind.

Despite their promising potential, lithium-ion batteries face significant challenges related to safety, reliability, and performance. Incidents of battery fires caused by internal short circuits, stemming from aging or manufacturing defects, highlight critical safety concerns. Additionally, issues like reduced cycle life and premature degradation undermine the reliability and longevity of these batteries. Addressing these challenges is essential for ensuring a sustainable future with safer and more durable lithium-ion technologies. To achieve this, the materials science community is focused on developing innovative electrodes and additives to enhance energy density and extend cycle life, while the battery control sector is dedicated to advancing Battery Management Systems (BMSs). These systems aim to optimize safety, performance, and lifespan in real-time across the diverse range of lithium-ion applications.

Chapter contribute

This chapter provides readers with a high-level overview of lithium-ion battery cell components, their working principles, and the degradation mechanisms that cells undergo during operations. Furthermore, it presents an overview of the battery terminology that will be used throughout the remainder of the text and summarizes the primary tasks of the Battery Management System.

Chapter Structure

1. **Section 2.1** introduce the lithium ion batteries. Specifically, the working principle, cell terminology and degradation mechanisms are presented in Sections 2.1.1, 2.1.2 and 2.1.3, respectively.

2. **Section 2.2** revised the main BMS tasks.

2.1 Li-ion Cells

A lithium-ion (Li-ion) cell consists of five primary components, as schematically depicted in Figure 2.1:

- **Negative electrode (Anode)**: Typically composed of graphitic carbon, the anode serves as the storage site for lithium-ions during the charging process. When the cell discharges, the lithium-ions are released from the anode, contributing to the generation of electrical energy.
- **Positive electrode (Cathode)**: The cathode is made from various compounds such as lithium cobalt oxide ($LiCoO_2$), lithium nickel oxide ($LiNiO_2$), lithium manganese oxide ($LiMn_2O_4$), or lithium nickel manganese cobalt oxide ($LiNiMnCoO_2$, commonly referred to as NMC). The specific material combination of the anode and cathode defines the battery's chemistry, influencing its capacity, discharge characteristics, cutoff voltages, and specific energy. The cathode serves as the source of lithium-ions during the charging phase.
- **Separator**: Positioned between the anode and cathode, the separator is a porous membrane made from polymeric material. It permits the passage of lithium-ions between electrodes while preventing the direct flow of electrons, which would cause a short circuit. This function is essential for ensuring the cell's safety during operation.
- **Electrolyte**: The electrolyte is a solution, typically non-aqueous, in which lithium salts are dissolved in organic or inorganic solvents. It fills the space within the cell, facilitating the movement of lithium-ions between the anode and cathode during charging and discharging.
- **Current collectors**: Located at the outer edges of the cell, current collectors are responsible for transferring the electrons between the cell and the external circuit, enabling the flow of electricity to or from the cell during charging or discharging.

2.1.1 Working Principle

The operation of a rechargeable lithium-ion cell is based on the conversion of chemical energy into electrical energy during discharge, and the reverse during charging. This process is driven by the intercalation (insertion) and deintercalation (extraction) of lithium-ions into and out of the electrode materials. Both processes occur within the porous structures of the electrodes and are fully reversible, allowing for multiple charge-discharge cycles.

These processes are governed by electrochemical reactions at the interface between the electrode and the electrolyte. Specifically, oxidation reactions at one electrode release electrons into the external circuit, while reduction reactions at the other electrode accept electrons from the circuit. The movement of lithium-ions through the electrolyte, paired with electron flow through the external circuit, enables the transfer of energy.

During charging, electrical energy from an external source is converted into chemical energy stored in the cell. For a cell with a $LiNiMnCoO_2$ cathode (NMC), the charging

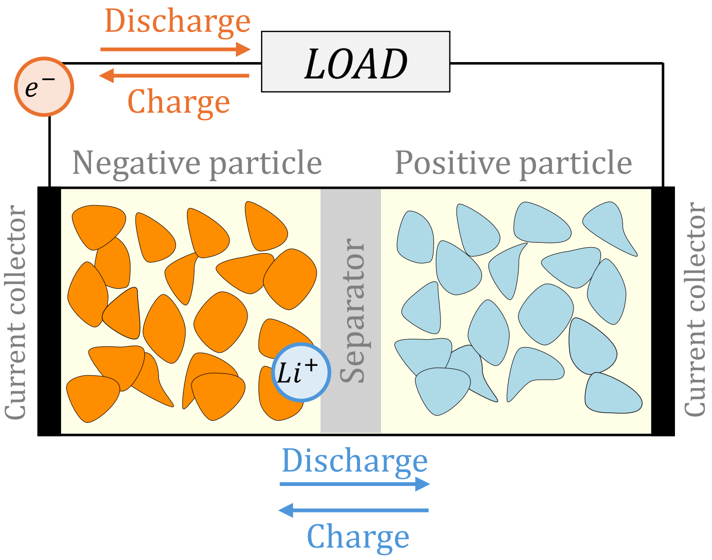

Figure 2.1: Schematic diagram of a LIB working principle.

process involves the deintercalation of lithium-ions from the cathode, facilitated by the oxidation reaction as shown in Equation (2.1). The lithium-ions then migrate through the electrolyte and separator to reach the anode, while the corresponding electrons travel through the external circuit to the anode. Upon reaching the anode, the lithium-ions are intercalated into the carbon structure of the anode through a reduction reaction, as depicted in Equation (2.2).

$$LiNiMnCoO_2 \longrightarrow NiMnCoO_2 + Li^+ + e^- \tag{2.1}$$

$$C_6 + Li^+ + e^- \longrightarrow LiC_6 \tag{2.2}$$

Once the intercalation process is complete, the cell is fully charged and ready for use as a power source.

When the cell is connected to an external load, it discharges, and the stored chemical energy is converted back into electrical energy. During this phase, oxidation occurs at the anode, as described by Equation (2.3), while the reduction reaction at the cathode is represented by Equation (2.4).

$$LiC_6 \longrightarrow C_6 + Li^+ + e^- \tag{2.3}$$

$$NiMnCoO_2 + Li^+ + e^- \longrightarrow LiNiMnCoO_2 \tag{2.4}$$

The lithium-ions flow back to the cathode through the electrolyte, and the electrons move through the external circuit to provide power. Once the process is complete, the cell is fully discharged.

2.1.2 Battery terminology

This section provides a glossary of commonly used terms in this thesis, based on the definitions provided in [34].

- **Battery Cell:** A battery cell is a single unit of an electrochemical system, composed of an anode, cathode, electrolyte, separator, and current collectors. Its function is to store energy and release it in the form of electrical current.

- **Battery Module/Pack:** A battery module consists of several cells connected in series or parallel to achieve desired voltage or capacity. A battery pack is then formed by assembling multiple modules, again connected in series or parallel, to further increase capacity or voltage, as needed for specific applications.

- **C-rate:** The C-rate is a measure of the rate at which a battery is charged or discharged relative to its maximum capacity. For instance, a 1C rate indicates that the battery will be fully charged or discharged in one hour. A 2C rate, conversely, means the process will take half an hour.

- **State of Charge (SOC):** SOC is a dimensionless metric that represents the remaining usable charge in the battery as a percentage of its total capacity. An SOC of 100% indicates a fully charged battery, while 0% indicates a fully discharged battery.

- **State of Health (SOH):** SOH is a critical parameter that indicates the overall condition of a battery in terms of aging and performance degradation. Since there is no single universally accepted definition of SOH, it can be quantified in terms of capacity loss, internal resistance increase, energy fade, or a combination of these factors. SOH is essential for estimating the remaining useful life of the battery.

- **Depth of Discharge (DOD):** DOD is the percentage of the battery's total capacity that has been used or discharged. For example, a DOD of 40% means that 40% of the battery's total capacity has been utilized.

- **Cut-off Voltage:** The cut-off voltage is the minimum allowable voltage for a battery cell. Once this voltage is reached, the cell is considered fully discharged, typically corresponding to an SOC of 0%.

- **Nominal Capacity:** The nominal capacity refers to the total amount of charge that can be extracted from a fully charged battery under specified conditions. It is generally expressed in ampere-hours (Ah).

2.1.3 Degradation mechanisms

The degradation of lithium-ion battery (LIB) cells is a complex, multifaceted process driven by the interaction of chemical side reactions and physical changes within the cell's

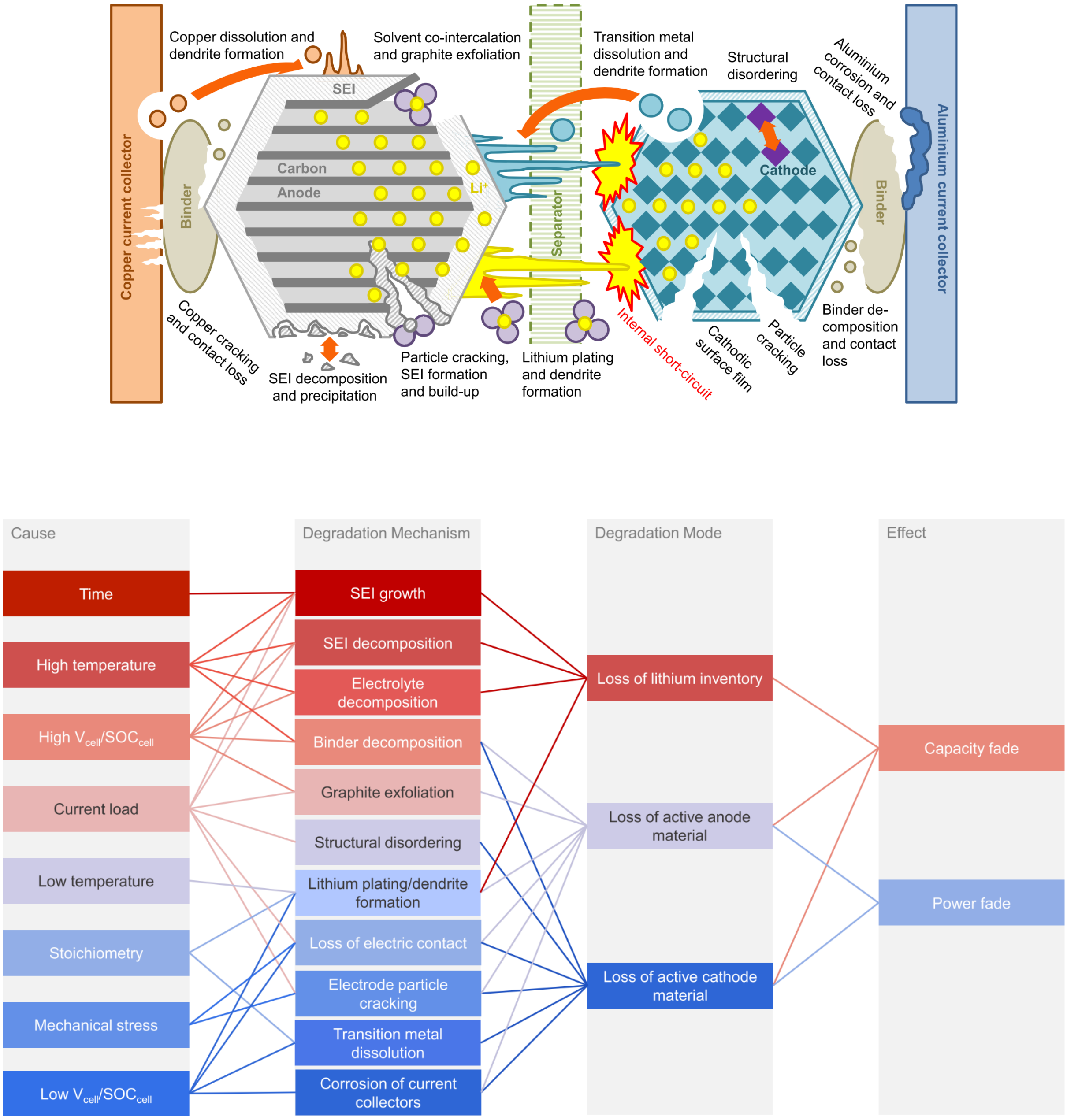
Copper current collector
Binder
Copper dissolution and dendrite formation
Solvent co-intercalation and graphite exfoliation
SEI
Carbon
Anode
Li^+
Separator
Transition metal dissolution and dendrite formation
Structural disordering
Aluminium corrosion and contact loss
Cathode
Binder
Aluminium current collector
Copper cracking and contact loss
SEI decomposition and precipitation
Particle cracking, SEI formation and build-up
Lithium plating and dendrite formation
Internal short-circuit
Cathodic surface film
Particle cracking
Binder de-composition and contact loss
Cause
Degradation Mechanism
Degradation Mode
Effect
Time
High temperature
High V_{cell}/SOC_{cell}
Current load
Low temperature
Stoichiometry
Mechanical stress
Low V_{cell}/SOC_{cell}
SEI growth
SEI decomposition
Electrolyte decomposition
Binder decomposition
Graphite exfoliation
Structural disordering
Lithium plating/dendrite formation
Loss of electric contact
Electrode particle cracking
Transition metal dissolution
Corrosion of current collectors
Loss of lithium inventory
Loss of active anode material
Loss of active cathode material
Capacity fade
Power fade

Figure 2.2: Degradation mechanisms in Li-ion cells. *Figures from [1]*

active materials. This aging process is largely irreversible and eventually leads to the cell's failure, making it critical to understand these mechanisms for the purpose of improving the longevity and performance of LIBs across various applications.

LIB aging is typically quantified using two key metrics: **capacity fade** and **power fade**. Capacity fade refers to the gradual reduction in the battery's ability to hold charge over time, while power fade indicates a decline in the battery's capacity to deliver power, often due to increasing internal resistance or impedance. Both metrics are crucial for assessing the health and remaining lifespan of the battery.

A wide array of degradation mechanisms contribute to LIB aging, as illustrated in Figure 2.2. These mechanisms can be exacerbated by operating conditions such as C-rate (charge/discharge rate), current direction (charging or discharging), temperature, state of charge (SOC), and state of health (SOH). The key degradation mechanisms include:

- **Solid Electrolyte Interphase (SEI) Growth**: The SEI forms on the anode surface during early charging cycles due to electrolyte decomposition. A stable SEI layer is essential for protecting the anode, but its continuous growth consumes lithium ions, leading to a gradual loss of capacity.

- **Lithium Plating**: This occurs when lithium ions deposit as metallic lithium on the anode rather than intercalating into it. Lithium plating is more likely to happen at high charging rates or low temperatures, and it results in reduced capacity and increased internal resistance, which can ultimately lead to safety risks such as dendrite formation.

- **Particle Cracking**: The repeated expansion and contraction of electrode particles during lithiation and delithiation cycles generate mechanical stress. Over time, this can cause the particles to crack, which leads to a loss of electrical contact and reduces the amount of active material available for electrochemical reactions, further contributing to capacity fade.

According to [35], degradation mechanisms are commonly grouped into four primary degradation modes. Firstly, **Loss of Lithium Inventory (LLI)** occurs when lithium ions are irreversibly consumed in parasitic reactions. Key contributors to LLI include Solid Electrolyte Interphase (SEI) growth and lithium plating. Secondly, **Loss of Active Material (LAM)** affects both the positive and negative electrodes. In the anode, LAM is often caused by particle cracking and the subsequent loss of electrical contact. Thirdly, **Stoichiometric Drift** is typically associated with LLI and occurs when the balance between the electrodes becomes disrupted. This imbalance alters the stoichiometry of the electrodes relative to one another, degrading the battery's ability to function optimally. Finally, **Impedance Change** groups together the mechanisms that affect the kinetic behavior of the cell. These include the formation of resistive layers, increased electrolyte degradation, and other factors that hinder ion transport and reaction kinetics, leading to a noticeable decline in the battery's power performance.

2.2 Battery Management system (BMS)

Lithium-ion batteries must operate within the safe and reliable operating area, which is restricted by temperature and voltage windows. Exceeding the voltage and temperature bounds could lead to rapid decrease of battery performance and even result in safety problems. Therefore, the BMS is needed in order to protect the cells and battery packs from being damaged, fulfilling the load requirements. The BMS is composed by any kind of electronic systems, mechanical systems or any other possible technologies that manages the battery, as widely discussed in [36]. The BMS's tasks include:

1. *Battery parameters detection*: Cell monitoring is one of the most important functions of a BMS. It is important to notice that the only accessible measurements related to a lithium-ion cell are the current, the surface temperature, and the terminal voltage, while all the other variables need to be estimated.
2. *Estimation of battery states*: This includes the estimation of cells' State of Charge (SOC), Depth of Discharge (DOD), and State of Health (SOH). These estimations are usually carried out using a battery cell model that interprets the measured parameters.
3. *On-board diagnosis*: This function involves using various sensors to detect any possible faults that could occur within the battery module, such as short circuits, overvoltage, or thermal anomalies.
4. *Battery safety control and alarm*: The BMS includes thermal system control and high voltage safety control. It informs the control unit when a fault is detected to prevent damage to the batteries or injuries to individuals due to high/low temperatures, overcharging, overdischarging, or excessive currents.
5. *Charge control*: The BMS can control the charging process by regulating the charger to ensure that batteries are charged optimally, extending their lifespan and maintaining performance.
6. *Battery equalization*: Based on the information provided by each cell, the BMS adopts equalization methods to ensure that the SOC across all cells remains as consistent as possible, preventing imbalances that can degrade battery performance.
7. *Thermal management*: Depending on the temperature distribution within the battery pack, the BMS decides when to activate the cooling or heating systems to maintain optimal operating temperatures, ensuring safety and efficiency.
8. *Communication interface*: The BMS provides communication interfaces (e.g., CAN bus, LIN) to interact with other vehicle systems or external devices. This allows for data exchange and integration with the vehicle's overall management system.
9. *Energy management*: It manages the energy flow between the battery and the load or charger, optimizing performance and efficiency. This includes directing power where it's needed most and ensuring balanced energy distribution.

10. *Balancing of cells*: Ensures that all cells in the battery pack are balanced in terms of charge. Balancing prolongs battery life, maintains performance, and prevents situations where some cells are overcharged or overdischarged.

Chapter 3

Battery modelling

Contents

3.1 Cell-level models **42**
  3.1.1 Equivalent Circuit model (ECM) 42
  3.1.2 Electrochemical model (EM) 42
  3.1.3 Model order reduction 49
  3.1.4 Thermal models 65
  3.1.5 Aging models 68
3.2 Module-level models **72**
  3.2.1 Electrical submodel 72
  3.2.2 Thermal submodel 74
3.3 Conclusion **75**

Introduction

Dynamic models provide an abstract mathematical representation of concrete systems. In the context of batteries, they play a crucial role in predicting and analyzing cell behavior, refining cell design, and developing Battery Management System (BMS) algorithms for diagnostics, estimation, and control. Figure 3.1 provides a visual summary of different battery models found in the literature [2, 3, 4], ranging from detailed microscopic to broader macroscopic approaches. These models fall into three categories: atomistic, electrochemical, and empirical. Typically, as the scale of the model increases, its accuracy and computational complexity tend to decrease. **Empirical models** rely on historical experimental data to forecast the behavior of lithium-ion batteries, without incorporating electrochemical principles [23]. While their computational simplicity allows for rapid calculations, their predictions are often unreliable under conditions different from those used for model fitting. Notably, the most well-known empirical battery models is the equivalent circuit model (ECM) [23]. Next, the **electrochemical models** (EMs) describe the transport of lithium in the electrode and electrolyte phase via averaged mass and charge transport equations. Unlike empirical models, it offers insight into the inner workings of the battery while alleviating the computational burden compared to the atomistic models. The family of electrochemical models consists of the high-fidelity Doyle-Fuller-Newman (DFN) model [37], the Enhanced Single Particle Model (ESPM) [38], the Single Particle Model (SPM), and core-shell ESPM (CS-ESPM) [39]. It is important to highlight that in recent years, hybrid approaches combining EMs with machine learning (ML) techniques have gained significance [4, 28]. The data-driven methods enhance the accuracy of EMs across a broad range of applications while preserving their interpretability and physical meaning. Finally, in **atomic scale models** fundamental interactions among atoms and electrons are analyzed to understand a material physical and chemical properties [40]. Computational techniques such as Molecular Dynamics [41], Kinetic Monte Carlo [42], and Density Functional Theory [43] are employed to calculate charge distribution and transfer, determine electronic ground states, track atomic movements, and gather crucial information from both kinetic and thermodynamic perspectives. Due to their high computational demands, these models are typically used in off-line simulations to enhance our understanding, characterization, and improvement of cell design.

In this dissertation, the main focus is over ECMs and EMs. Due to their mathematical simplicity, ease of implementation, and low-cost computation requirements, ECMs are the most commonly used tools in the development of BMS algorithms [23]. They are a great platform for developing estimation and control strategies with may be implemented online on a real system. Similarly, based on EMs, various reduced-order models (ROMs) have been developed to decrease computational burden while preserving insights into the cell internal electrochemical states [6], with the goal of facilitating their implementation on hardware-constrained onboard microcontrollers. Additionally, EMs can be used for high-fidelity offline simulations to improve cell and module design, performance, and safety [44, 45]. It is important to note that both modeling frameworks can be enhanced with thermal and/or aging models [46]. Thermal models enable the updating of temperature-dependent parameters, increasing models robustness across a wider range of applications. They also allow the design of algorithms for battery thermal management systems to prevent thermal runaway [47], improving the safety of the overall system. On the other hand, aging models are crucial for predicting capacity and power degradation, optimizing battery usage and extending battery life [48, 49].

Chapter contribute

This chapter aims to equip readers with the necessary tools to better comprehend the content of the following chapters. It does not, however, intend to offer a comprehensive and complete review of all existing battery modeling methods. Rather, it focuses on detailing and illustrating commonly used techniques in battery modeling. Although not all of these methods will be applied in the research presented, they are crucial for a thorough

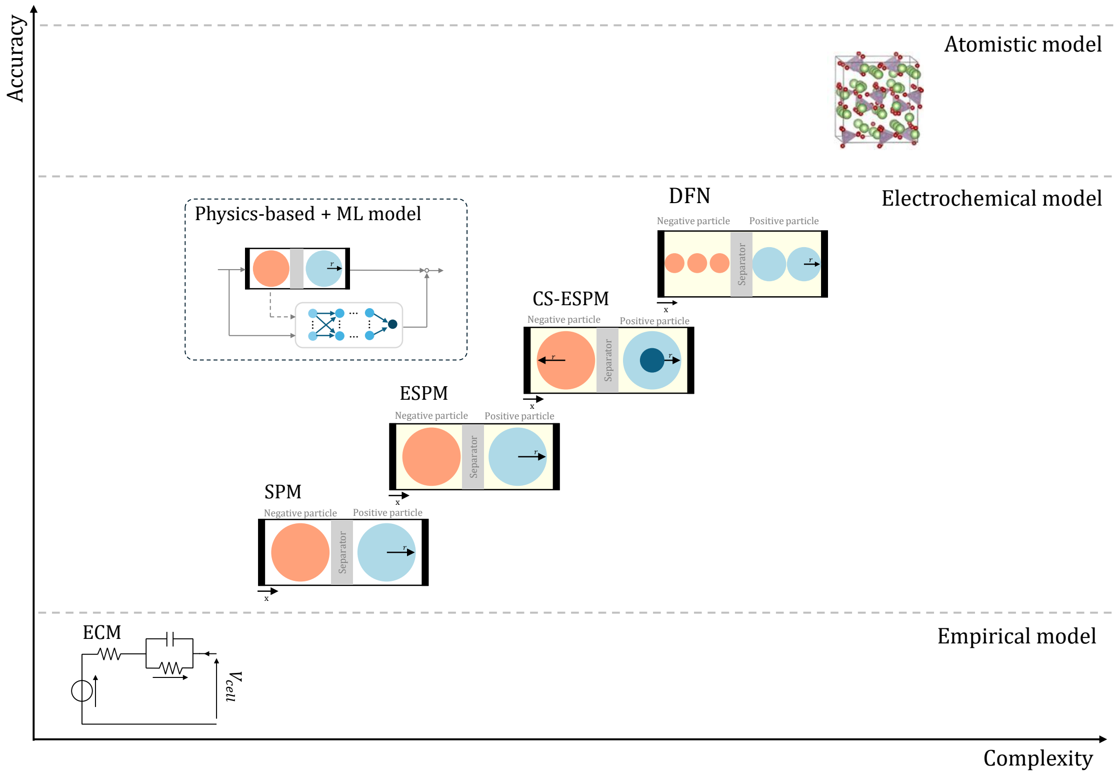
Accuracy
Atomistic model
Electrochemical model
DFN
Negative particle
Positive particle
Separator
Physics-based + ML model
CS-ESPM
ESPM
SPM
Empirical model
ECM
V_{cell}
Complexity
r
x

Figure 3.1: Overview of Battery Models, inspired by [2, 3, 4, 5].

understanding of the rest of the manuscript.
In particular, the ECM model forms the foundation for the model-based algorithms for state estimation, which are developed in Chapter 9. Additionally, the review of EMs governing equations and the corresponding Model Order Reduction (MOR) methods provide the necessary background for understanding the ROMs developed in Chapter 6 for the CS-ESPM. Finally, the combination of a cell-level ESPM with a physics-based aging model, based on solid electrolyte interface (SEI) growth, along with the subsequent development of a model for parallel-connected modules that considers thermal interconnections among cells, forms the basis for the high-fidelity offline simulations presented in Chapter 8. These simulations aim to investigate the effects of cell-to-cell variation on module performance.

Chapter structure

- **Section 3.1** provides an overview of electrochemical, thermal, and aging models for a single battery cell. Specifically, the governing equations for ECMs and EMs are presented in Sections 3.1.1 and 3.1.2, respectively. Section 3.1.3 reviews the most popular MOR techniques for EMs. Finally, Sections 3.1.4 and 3.1.5 offer an overview of thermal and aging models.

- **Section 3.2** shows how to extend the cell-level models, described in the previous section, to the module level. Specifically, module-level electrical and thermal models are introduced in Sections 3.2.1 and 3.2.2, respectively.

- **Section 3.3** summarizes the conclusions drawn and outlines the battery models used in the subsequent chapters.

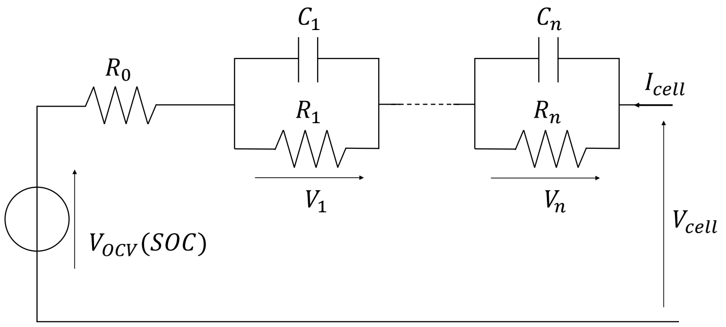

Figure 3.2: n-order RC ECM scheme

3.1 Cell-level models

3.1.1 Equivalent Circuit model (ECM)

An equivalent-circuit model relies on electrical components in order to describe electrochemical dynamics of the cell. Figure 3.2 provides a schematic representation of a general ECM. The model consists of the Open Circuit Voltage (V_{OCV}), an internal resistance (R_0) and a variable number (n) of capacitor-resistor parallel-blocks (R_iC_i with $i = 1, \cdots .n$). These latter represent the battery relaxation phenomena and, in the case in which only two RC pairs are considered, they usually model the ion diffusion and the double-layer charging/discharging effects. The voltages (V_i with $i = 1, \cdots, n$) across the two parallels and the cell state of charge (SOC) are the states of the system, i.e. $x = [V_1 \ \cdots \ V_n \ SOC]'$. The cell current ($I_{cell}$) and voltage ($V_{cell}$) represent respectively the system input u and output y. The state-space model of the cell, with nominal capacity equal to C_{bat}, is written as:

$$\begin{cases} \dot{x}(t) = Ax(t) + Bu(t) \\ y(t) = h(x(t), u(t)) \end{cases} = \begin{cases} \begin{bmatrix} \dot{V}_1(t) \\ \vdots \\ \dot{V}_n(t) \\ \dot{SOC}(t) \end{bmatrix} = \begin{bmatrix} \frac{-1}{R_1C_1} & \cdots & 0 & 0 \\ \vdots & \ddots & \vdots & \vdots \\ 0 & \cdots & \frac{-1}{R_nC_n} & 0 \\ 0 & 0 & 0 & 0 \end{bmatrix} \begin{bmatrix} V_1(t) \\ \vdots \\ V_n(t) \\ SOC(t) \end{bmatrix} + \begin{bmatrix} \frac{1}{C_1} \\ \vdots \\ \frac{1}{C_n} \\ \frac{1}{C_{\text{bat}}} \end{bmatrix} I_{cell}(t) \\ V_{cell}(t) = V_{OCV}(SOC(t)) + \sum_{i=1}^{n} V_i(t) + R_0 I_{cell}(t) \end{cases} \tag{3.1}$$

Note that, the model is linear in the states but non-linear in the output due to the V_{OCV}. In practice, this latter is modeled by fitting the experimental SOC-OCV curve with a non-linear function of the SOC, $V_{OCV}(\text{SOC})$ [50].

3.1.2 Electrochemical model (EM)

This section offers a concise overview of the governing equations employed in battery electrochemical models, focusing specifically on the DFN model (Section 3.1.2.1), ESPM (Section 3.1.2.2), CS-ESPM (Section 3.1.2.3), and SPM (Section 3.1.2.4). For detailed

Table 3.1: Electrochemical models nomenclature

$c_{s,j}$	Conc. in solid phase [mol/m^3], $j \in [n, p]$	$c_{e,j}$	Conc. in electrolyte phase [mol/m^3], $j \in [n, s, p]$
$\Phi_{s,j}$	solid phase potential [V], $j \in [n, p]$	$\Phi_{e,j}$	Liquid phase potential [V], $j \in [n, s, p]$
$D_{s,j}$	Solid phase diffusion [m^2/s], $j \in [n, p]$	$D_{,j}$	Electrolyte phase diffusion [m^2/s]
$a_{s,j}$	Specific interfacial surface area [m^{-1}], $j \in [n, p]$	$R_{s,j}$	Particle radius [m], $j \in [n, p]$
$i_{int,j}$	Pore wall flux [mol/m^2s], $j \in [n, p]$	$i_{o,j}$	Exchange current density [A/m^2], $j \in [n, p]$
$\epsilon_{s,j}$	Active volume fraction of solid phase, $j \in [n, p]$	$\epsilon_{e,j}$	Electrolyte Porosity, $j \in [n, p]$
L_j	Domain thickness [m], $j \in [n, s, p]$	σ_j	Solid phase conductivity [S/m], $j \in [n, p]$
k_j	Intercalation rate constant [m$^{2.5}$/s$\sqrt{mol}$]	$\epsilon_{f,j}$	Active volume fraction of filler/binder
A	Cell cross sectional area [m^2]	$\kappa_{e,j}$	Electrolyte conductivity [S/m]
V_{cell}	Cell voltage [V]	I_{cell}	Cell current [A]
U_j	Electrode open circuit potential [V]	η_j	Electrode overpotential [V]
R	Universal gas constant [J/mol-K]	F	Faraday's constant [C/mol]
t_0^+	Transference number [-]	$brugg$	Bruggeman coefficient [-]
$c_{s,j}^{bulk}$	Electrode bulk conc. [mol/m^3], $j \in [n, p]$	$c_{s,j}^{surf}$	Electrode surface conc. [mol/m^3], $j \in [n, p]$
$c_{s,j}^{max}$	Maximum electrode conc. [mol/m^3], $j \in [n, p]$	$c_{e,j}^{avg}$	Average electrolyte conc. [mol/m^3], $j \in [n, s, p]$
θ_j^{bulk}	Electrode bulk stoichiometry [-], $j \in [n, p]$	θ_j^{surf}	Electrode surface stoichiometry [-], $j \in [n, p]$
$c_{s,p}^{\alpha,\beta}$	Cathode solid phase conc. for α and β phases [mol/m^3]	$\theta_{s,p}^{\alpha,\beta}$	Positive electrode stoichiometry in α and β phases
$\bar{t}$	Time instant of the transition from one-phase to two-phase [s]	$\bar{t}_f$	Time instant of the transition from two-phase to one-phase [s]
r_p	Moving boundary [-]	T_{cell}	Cell temperature [$°C$]

schematics and a comprehensive list of nomenclature used in these models, please refer to Table 3.2 and Table 3.1, respectively.

3.1.2.1 Doyle-Fuller-Newman (DFN) model

The DFN model, also known as the Pseudo-2-Dimensional (P2D) model, was first introduced in 1993 [37]. Based on the porous electrode and concentrated solution theories [51], it models the diffusion and migration of lithium ions, as well as charge transfer within the two porous electrodes, a separator, two current collectors, and the electrolyte. The active material in the porous electrodes is modeled as spherical particles oriented along the battery thickness direction. The DFN model is characterized by the radial coordinate (r) for the solid spherical particles and the linear Cartesian coordinate (x) for the liquid electrolyte phase along the battery thickness. It is described by a set of Partial Differential Equations (PDEs) and Algebraic Equations (AEs), forming a comprehensive PDAE framework. The four primary PDEs that describe the battery dynamics are:

1. **Mass conservation in the solid phase:** The Fick's law of diffusion in spherical coordinates is used to describe the conservation of lithium ions in the solid phase:

   $$\frac{\partial c_{s,j}}{\partial t} = \frac{D_{s,j}}{r^2}\frac{\partial}{\partial r}\left[r^2 \frac{\partial c_{s,j}}{\partial r}\right] \tag{3.2}$$

   with boundary conditions:

   $$\left.\frac{\partial c_{s,j}}{\partial r}\right|_{r=0} = 0, \qquad \left.\frac{\partial c_{s,j}}{\partial r}\right|_{r=R_{s,j}} = \frac{-i_{int,j}}{D_{s,j}}$$

   where $c_{s,j}$ is the lithium-ion concentration in the solid phase, $D_{s,j}$ is diffusion coefficient, $a_{s,j} = 3\epsilon_{s,j}/R_{s,j}$ is the specific interfacial surface area, $\epsilon_{s,j}$ is the active

Table 3.2: Electrochemical models overview

	Mass conservation solid phase (3.2)	*Mass conservation liquid phase* (3.4)	*Charge conservation liquid phase* (3.5)	*Charge conservation solid phase* (3.3)	*Phse transition dynamics* (3.16)
(a) **DFN model** (Section 3.1.2.1) 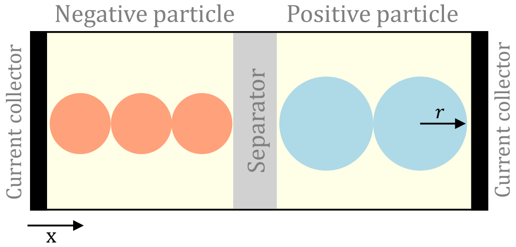 Negative particle Positive particle Current collector Separator Current collector r x	X	X	X	X	
(b) **CS-ESPM** (Section 3.1.2.3) 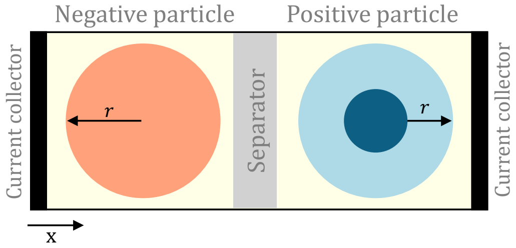 Negative particle Positive particle Current collector r Separator r Current collector x	X	X	X		X
(c) **ESPM** (Section 3.1.2.2) 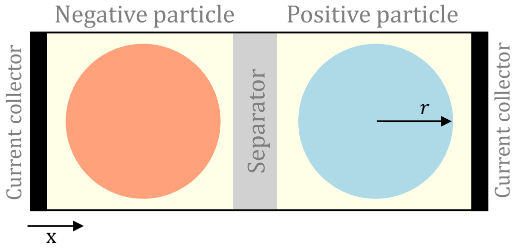 Negative particle Positive particle Current collector Separator r Current collector x	X	X	X		
(d) **SPM** (Section 3.1.2.4) 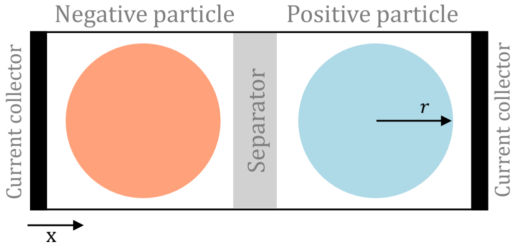 Negative particle Positive particle Current collector Separator r Current collector x	X				

material volume fraction, $R_{s,j}$ is the particles radius, and $i_{int,j}$ is the pore wall flux. The boundary conditions ensure that the ion flux at the particle center is zero, while at the particle surface, it is proportional to the rate of the ion intercalation/deintercalation reaction.

2. **Charge conservation in the solid phase:** The Ohm's law in cartesian coordinates ($x \in [0, L_n + L_s + L_p]$) is used to describe the conservation of charge in the solid phase of each electrode:

$$\frac{\partial}{\partial x}\left(\sigma_{eff,j}\frac{\partial \Phi_{s,j}}{\partial x}\right) - a_{s,j}Fi_{int,j} = 0 \tag{3.3}$$

   with boundary conditions:

$$\left.\frac{\partial \Phi_{s,j}}{\partial x}\right|_{x=L_n} = \left.\frac{\partial \Phi_{s,j}}{\partial x}\right|_{x=L_n+L_s} = 0, \qquad \left.\frac{\partial \Phi_{s,j}}{\partial x}\right|_{x=0} = \left.\frac{\partial \Phi_{s,j}}{\partial x}\right|_{x=L_n+L_s+L_p} = \frac{I_{cell}}{\sigma_{eff,j}}$$

   where $\Phi_{s,j}$ is the solid phase potential and $\sigma_{eff,j}$ is the effective electronic conductivity, obtained as $\sigma_{eff,j} = \sigma_j \epsilon_{s,j}^{brugg}$. The boundary conditions ensure that charge is exchanged through electron movement between the current collectors and the active materials, while preventing any charge movement across the separator.

3. **Mass conservation in the liquid phase:** The conservation of lithium ions in the electrolyte phase, along the thickness of the cell in Cartesian coordinates, is modeled using the following diffusion PDE:

$$\epsilon_{e,j}\frac{\partial c_{e,j}}{\partial t} = \frac{\partial}{\partial x}\left(D_{e,j}^{\text{eff}}\frac{\partial c_{e,j}}{\partial x}\right) + a_{s,j}(1 - t_0^+)i_{int,j} = 0 \tag{3.4}$$

   with boundary conditions:

$$\begin{aligned} \left.\frac{\partial c_{e,n}}{\partial x}\right|_{x=0} &= \left.\frac{\partial c_{e,p}}{\partial x}\right|_{x=L_n+L_s+L_p} = 0 \\ D_{e,n}^{\text{eff}}\left.\left(\frac{\partial c_{e,n}}{\partial x}\right)\right|_{x=L_n} &= D_{e,s}^{\text{eff}}\left.\left(\frac{\partial c_{e,s}}{\partial x}\right)\right|_{x=L_n} \\ D_{e,s}^{\text{eff}}\left.\left(\frac{\partial c_{e,s}}{\partial x}\right)\right|_{x=L_n+L_s} &= D_{e,p}^{\text{eff}}\left.\left(\frac{\partial c_{e,p}}{\partial x}\right)\right|_{x=L_n+L_s} \end{aligned}$$

   where $c_{e,j}$ is the lithium-ion concentration in the liquid phase, $D_{e,j}^{eff}$ is the effective diffusion coefficient in the electrolyte, obtained as $D_{e,j}^{eff} = D_{e,j}\epsilon_{e,j}^{brugg}$, $\epsilon_{e,j}$ is the porosity or the electrolyte volume fraction, and *brugg* is the Bruggeman's number that accounts for electrolyte tortuosity. The boundary conditions ensure concentration continuity across each cell domain and null flux at both current collectors.

4. **Charge conservation in the liquid phase:** The charge conservation in the electrolyte is modeled using the following PDE:

$$\kappa_{e,j}^{\text{eff}}\frac{\partial^2 \Phi_{e,j}}{\partial x^2} - \kappa_{D,j}^{\text{eff}}\frac{\partial^2 \ln c_{e,j}}{\partial x^2} + a_{s,j}Fi_{int,j} = 0 \tag{3.5}$$

with boundary conditions:

$$\frac{\partial \Phi_{e,j}}{\partial x}\bigg|_{x=0} = \frac{\partial \Phi_{e,j}}{\partial x}\bigg|_{x=L_n+L_s+L_p} = 0$$

where $\Phi_{e,j}$ is the liquid phase potential, $\kappa_{e,j}^{\text{eff}} = \kappa_{e,j}\epsilon_{e,j}^{brugg}$ is the liquid phase effective ionic conductivity, and $\kappa_{D,j}^{eff}$ is the electrolyte ionic diffusional conductivity, calculated as $\kappa_{D,j}^{eff} = \frac{2RTk_{e,j}^{eff}}{F}(1-t_0^+)$.

The Butler-Volmer equation is used to model the charge transfer reaction occurring at the surface of the spherical particle at the interface with the electrolyte. Specifically, the rate of the lithium intercalation/de-intercalation reaction is modeled as:

$$i_{int,j} = i_{0,j}\left[\exp\Big(\frac{\alpha_a F\eta_j}{RT}\Big) - \exp\Big(\frac{\alpha_c F\eta_j}{RT}\Big)\right] \tag{3.6}$$

where α_a and α_c are the anodic and cathodic transfer coefficients, respectively. (3.6) relates the electrode intercalation current density $i_{int,j}$ to its overpotential η_j, defined as:

$$\eta_j = \Phi_{s,j} - \Phi_{e,j} - U_j(c_{s,j}^{surf}) \tag{3.7}$$

where U_j is the electrode open circuit potential, calculated as a function of the electrode surface stoichiometry $\theta_{s,j}^{surf} = c_{s,j}^{surf}/c_{s,j}^{max}$. $c_{s,j}^{surf}$ and $c_{s,j}^{max}$ are athe surface and maximum electrode concentration, respectively, and $i_{0,j}$ is the the exchange current density, obtained as:

$$i_{0,j} = k_j\sqrt{c_{e,j}^{avg}c_{s,j}^{surf}(c_{s,j}^{max} - c_{s,j}^{surf})} \tag{3.8}$$

where $c_{e,j}^{avg}$ is the average electrolyte concentration and k_j is the kinetic reaction rate constant. Finally, the cell overall volage is calculated as:

$$V_{cell} = \Phi_{s,p}|_{x=L_n+L_s+L_p} - \Phi_{s,n}|_{x=0} - R_{cell}I_{cell} \tag{3.9}$$

where R_{cell} is the ohmic cell resistanca and I_{cell} is the cell current. Finally, the SOC of each electrode is calculated based on the bulk stoichiometries ($\theta_{s,j}^{bulk}$) as:

$$SOC_n = \frac{\theta_{s,n}^{bulk} - \theta_n^{0\%}}{\theta_n^{100\%} - \theta_{s,n}^{0\%}}, \quad SOC_p = \frac{\theta_p^{0\%} - \theta_{s,p}^{bulk}}{\theta_p^{0\%} - \theta_p^{100\%}} \tag{3.10}$$

where $\theta_{s,j}^{bulk} = c_{s,j}^{bulk}/c_{s,j}^{max}$ in which:

$$c_{s,j}^{bulk} = \frac{1}{\frac{4}{3}\pi R_{s,j}^3}\int_{r=0}^{R_{s,j}} 4\pi r^2 c_{s,j}(r)dr \tag{3.11}$$

3.1.2.2 ESPM

The ESPM is a simplified version of the DFN model. It relies on the assumptions of infinite solid-phase conductivity and uniform current distribution within individual electrodes [52]. The former assumption results in a uniform solid-phase potential, making the governing PDE (3.3) negligible. Additionally, the latter assumption allows all active material particles to be considered in parallel, enabling each electrode to be represented by a single spherical particle with radius $R_{s,j}$. Additionally, a uniform current distribution allows the intercalation/deintercalation current density (3.6) to be rewritten as [53, 54]:

$$i_{int,j} = \frac{I_{cell}}{a_{s,j} A L_j} \tag{3.12}$$

Subsequently, assuming $\alpha_a = \alpha_c = 0.5$ the approximated Butler-Volmer equation (3.6) allows the calculation of the electrode overpotential:

$$\eta_j = \frac{RT}{0.5F} sinh^{-1}\Big(\frac{I_{cell}}{2 a_{s,j} A L_j i_{0,j}}\Big) \tag{3.13}$$

According to [55], the electrolyte overpotential is obtained by integrating the charge conservation in electrolyte phase PDE (3.5):

$$\Delta\Phi_e = \Phi_{e,p} - \Phi_{e,n} = \frac{2RT\nu}{F} ln\Big(\frac{c_{e,j}|_{x=L_n+L_s+L_p}}{c_{e,j}|_{x=0}}\Big) - \frac{I_{cell}}{2A}\Big(\frac{L_n}{k_n^{eff}} + \frac{2L_s}{k_s^{eff}} + \frac{L_p}{k_p^{eff}}\Big) \tag{3.14}$$

Finally, considering the equation (3.7) and the electrolyte and electrode overpotential introduced in this section, the cell voltage is obtained as:

$$V_{cell} = \Phi_{s,p} - \Phi_{s,n} - R_{cell} I_{cell} = U_p + \eta_{s,p} - U_n - \eta_{s,n} + \Delta\Phi_e - R_{cell} I_{cell} \tag{3.15}$$

It is worth noting that the electode SOC is calculated as in (3.10).

3.1.2.3 CS-ESPM

The key aspect of this physics-based electrochemical model is the description of the phase transition undergone by the electrodes during the charge and discharge. Typically, the core-shell ESPM (CS-ESPM) is adopted to described the phase transition exibith by the positive electrode in $LiFePO_4$/graphite batteries [39]. Although, as noted by [56], certain aspects of the lithiation/delithiation description in LFP electrodes using the core-shell model are inconsistent with experimental observations, it is a suitable solution for LFP-based battery model. According to [21], the LFP material experiences three main phases during a charging/discharging cycle: 1) Li-rich phase denoted as β-phase ($LiFePO_4$), 2) two phases transition where the $LiFePO_4$/$FePo_4$ coexist, and 3) Li-poor phase denoted as α-phase ($FePo_4$). Fig. 3.3 provides a schematic representation of these three phases within the model for a constant discharge cycle from 100% to 0% of SOC. Based on the ESPM framework, both electrodes are modeled as spherical particles, where the negative electrode is always in single phase whereas the positive electrode can be in one-phase (1P) or two-phase (2P). Further, $\bar{t}$ and $\bar{t}_f$ highlighted in the Fig. 3.3, refer to the initial and final time of the 2P condition. When the battery is fully charged, the positive electrode is in the α-phase (Li-poor), and it stays in that phase (1P) from when the discharge starts

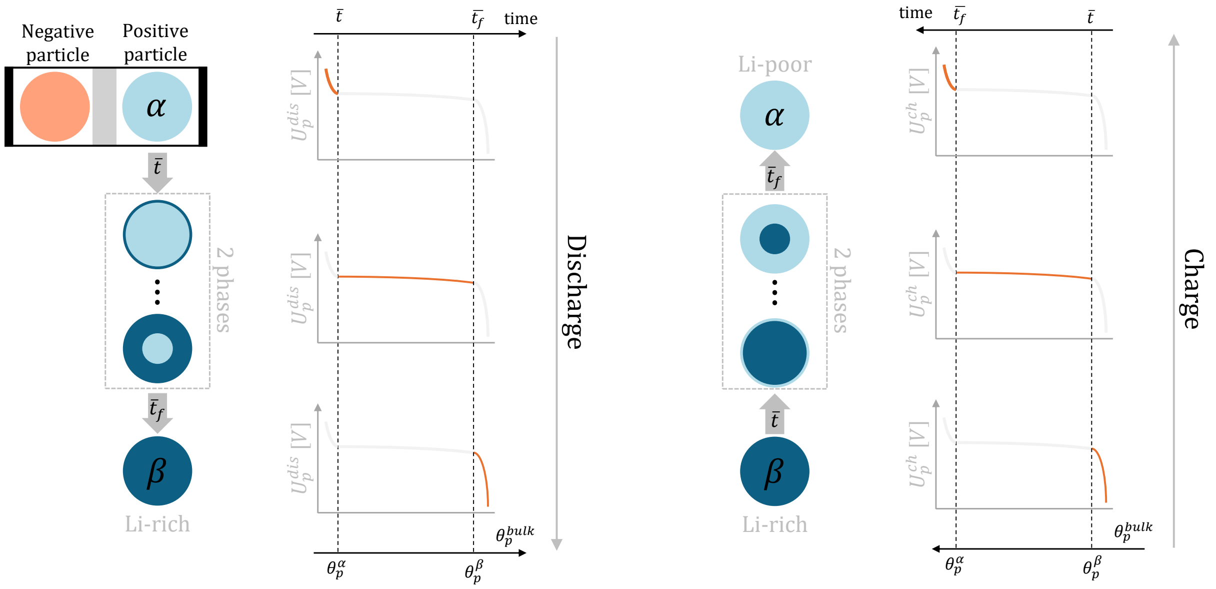
Negative particle
Positive particle
α
$\bar{t}$
2 phases
$\bar{t}_f$
β
Li-rich
$\bar{t}$
$\bar{t}_f$
time
U_p^{dis} [V]
U_p^{dis} [V]
U_p^{dis} [V]
θ_p^{bulk}
θ_p^{α}
θ_p^{β}
Discharge
Li-poor
α
$\bar{t}_f$
2 phases
$\bar{t}$
β
Li-rich
time
$\bar{t}_f$
$\bar{t}$
U_p^{ch} [V]
U_p^{ch} [V]
U_p^{ch} [V]
θ_p^{bulk}
θ_p^{α}
θ_p^{β}
Charge

Figure 3.3: C/4 discharge. The moving boundary (r_p) is plotted to illustate the positive electrode one-phase ($r_p/R_{s,p} = 0$) and two-phase ($r_p/R_{s,p} > 0$) regions.

(Li-ions starts intercalate into the positive electrode) until the positive electrode reaches the normalized concentration θ^{α} at time instant $t = \bar{t}$. At this point, the β-phase starts forming on the outer shell of the positive particle and the two phases (α and β) coexist. The core-region in α-phase is subjected to a shrinking process, while the thickness of the shell-region, in β-phase, increases as the battery is being discharged. When the transition from the α-phase to β-phase is over at time $t = \bar{t}_f$, the entire positive particle remains in β-phase until the end of the discharge. The inverse process takes place during the charging cycle (from β-phase to α-phase). The Li-ion concentration in the negative, as well as in the 1P and in the 2P positive electrode shell-region, is described by the Fick's diffusion law, as shown in eq. (3.2). The core-region of the positive electrode remains at a constant and uniform concentration equal to $c_{s,p}^{\alpha}$ ($c_{s,p}^{\beta}$) during discharging (charging). Further, for $t \in [\bar{t}, \bar{t}_f]$ the dynamics of the moving boundary r_p, describing the distance between the center of the positive particle and the interface between the two phases, is given as:

$$\text{sign}(I_{cell})(c_{s,p}^{\alpha} - c_{s,p}^{\beta})\frac{dr_p}{dt} = D_{s,p}\frac{\partial c_{s,p}}{\partial r}\Big|_{r=r_p} \tag{3.16}$$

The motion of r_p depends on the concentration gradient ($\partial c_{s,p}/\partial r$) across the α-phase and β-phase interface. In dicharge conditions, equation (3.16) is completed with boundary conditions:

$$r_p|_{t=\bar{t}} = R_{s,p}, \quad c_{s,p}|_{r=r_p \wedge t\in[\bar{t},\bar{t}_f]} = \begin{cases} c_{s,p}^{\beta} \text{ Dis.} \\ c_{s,p}^{\alpha} \text{ Ch.} \end{cases}, \quad c_{s,p}|_{t=\bar{t} \wedge r\in[0,R_{s,p}]} = \begin{cases} c_{s,p}^{\alpha} \text{ Dis.} \\ c_{s,p}^{\beta} \text{ Ch.} \end{cases} \tag{3.17}$$

The mass and the charge conservation within the electrolyte, are modeled as in the ESPM adopting the (3.4) and (3.5), respectively. Finally, the overall cell voltage is obtained as in (3.15), while the electode SOC is calculated as in (3.10).

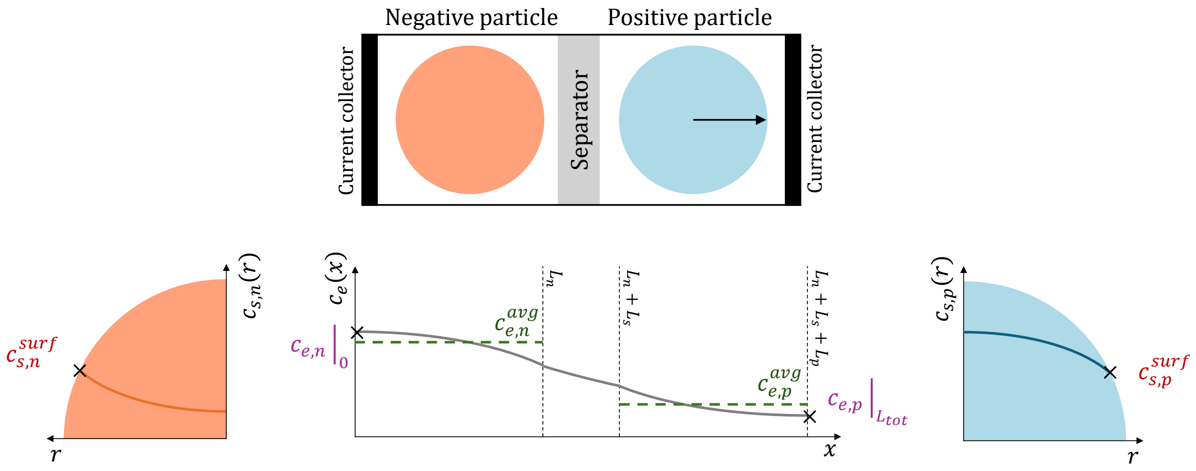

$$V_{cell} = U_p(c_{s,p}^{surf}) + \eta_p(c_{s,p}^{surf}, c_{e,p}^{avg}) - U_n(c_{s,n}^{surf}) - \eta_n(c_{s,n}^{surf}, c_{e,n}^{avg}) + \Delta\Phi_e(c_{e,j}\big|_{0,L_{tot}}) - R_{cell}I_{cell}$$

Figure 3.4: Schematic overview of the key concentration values needed for the voltage calculation in the ESPM.

3.1.2.4 SPM

The SPM is a further approximation of the ESPM. While both models assume uniform current density and infinite conductivity in the electrodes, the SPM further assumes uniform lithium concentration in the electrolyte phase, thereby neglecting electrolyte dynamics (3.4)(3.5). As a result, the conservation of mass in the solid phase is the sole physical law governing the battery dynamics. Considering $\Delta\Phi_e = 0$, the overall cell voltage can be written as:

$$V_{cell} = \Phi_{s,p} - \Phi_{s,n} - R_{cell}I_{cell} = U_p + \eta_{s,p} - U_n - \eta_{s,n} - R_{cell}I_{cell} \tag{3.18}$$

It is worth noting that the electode SOC is calculated as in (3.10).

3.1.3 Model order reduction

In the previous section, the governing PDEAs for EMs, describing the intercalation and deintercalation of lithium ions in both the solid and liquid phases, as well as charge conservation within the cell were detailed. It was shown that the overall cell voltage and electrode SOC are calculated based on specific concentration values obtained from the PDE solutions. This process is schematically illustrated in Figure 3.4 considering as an example the ESPM. The electrode OCPs (U_n and U_p) depend on the particle lithium-ion surface concentration ($c_{s,j}^{surf}$), while the electrode overpotential (η_j), is calculated based both the $c_{s,j}^{surf}$ and the average concentration of the electrolyte ($c_{e,j}^{avg}$). Meanwhile, the electrode SOC is determined by the bulk concentration ($c_{s,j}^{bulk}$) within the electrode.
Various numerical methods for approximating the governing PDAEs were extensively studied in the literature [6]. These techniques focus on calculating the concentration necessary for output model computations values (i.e. $c_{s,j}^{surf}$, $c_{s,j}^{bulk}$, and $c_{e,j}^{avg}$) rather than

providing a complete and detailed description of the spatial concentration distribution within the cell. Further, the considered MOR techniques aim to approximate the PDAEs with highest accuracy while ensuring computational efficiency and preserving the model physical meaning. Figure 3.5 provides a schematic overview of the most commonly used MOR techniques in the context of battery modeling. These methods can be broadly categorized into four types:

- **Spatial discretization techniques** (Section 3.1.3.1) convert PDAEs/PDEs into DAEs/ODEs systems. A commonly used approach is the method of lines, which discretizes only the spatial domain while treating time as a continuous variable [57]. Among spatial discretization techniques, finite-difference methods (FDMs) and finite-volume methods (FVMs) are particularly effective for simplifying the governing equations of EMs [58]. These methods maintain most of the model key properties across various operational conditions. However, the complexity and accuracy of these ROMs depend on the density and distribution of the mesh points or control volumes used, potentially leading to large-scale models that may require further reduction to enhance computational efficiency.

- **Functional approximation methods** (Section 3.1.3.2) approximate the governing equations of electrochemical models as systems of ODEs. One prominent approach is spectral methods [59, 60], which represent spatiotemporal variables as a finite weighted sum of basis functions, typically chosen from orthogonal function spaces such as Fourier series or Chebyshev polynomials [61]. Another approach is parabolic approximation, where the solid-phase concentration is modeled as a polynomial function [62]. This method is particularly effective for applications involving constant, long-duration, low to medium current rates.

- **Frequency domain approximation** (Section 3.1.3.3) is another widely used approach in battery modeling. This method involves applying the Laplace transform to convert the governing PDEs into transcendental transfer functions that describe the system behavior with respect to quantities of interest, such as surface concentration [63]. Once the transfer functions are obtained, MOR techniques are employed to simplify these functions. Methods such as Padé approximation (PA) [63] or Residue Grouping (RG) [64] are commonly used to reduce the complexity of the transfer functions while retaining the essential dynamics of the system. Subsequently, realization algorithms are applied to derive simplified state-space models from the reduced transfer functions. Additionally, direct discretization approaches like Discrete Realization Algorithms (DRA) can be used to obtain discrete-time models from the transcendental transfer functions [23].

- **MOR for high-dimensional ODE systems** (Section 3.1.3.4) addresses the challenge of reducing the complexity of large systems resulting from the spatial discretization of governing PDEs. This approach focuses on identifying and retaining the most significant modes of the system to reduce computational burden while preserving essential dynamic characteristics [65].

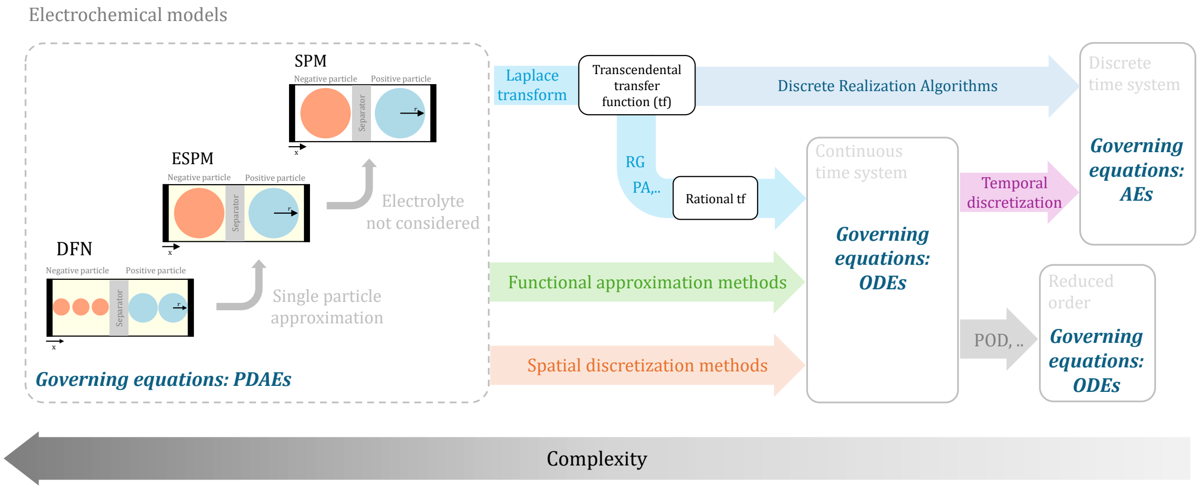
Electrochemical models
SPM
Negative particle
Positive particle
Separator
ESPM
DFN
Electrolyte not considered
Single particle approximation
Governing equations: PDAEs
Laplace transform
Transcendental transfer function (tf)
Discrete Realization Algorithms
Discrete time system
Governing equations: AEs
RG
PA,..
Rational tf
Continuous time system
Governing equations: ODEs
Temporal discretization
Functional approximation methods
Spatial discretization methods
POD, ..
Reduced order
Governing equations: ODEs
Complexity

Figure 3.5: Schematic overview of the most commonly used MOR techniques in the context of battery modeling. Figure inspired by [6].

3.1.3.1 Spatial discretization techniques

Finite Differende Method (FDM)

Given a function $f(x) : \mathbb{R} \rightarrow \mathbb{R}$, the derivative of f at a point x ($f'(x)$) is defined as the limit of the difference quotient:

$$\frac{df(x)}{dx} = \lim_{h\to 0} \frac{f(x+h)-f(x)}{h}. \tag{3.19}$$

In practical applications, $\frac{f(x+h)-f(x)}{h}$ serves as an approximation of $f'(x)$ when h is sufficiently small. To assess the accuracy of this approximation, we analyze the Taylor series expansions of $f(x+h)$ and $f(x-h)$:

$$\begin{aligned} f(x+h) &= f(x) + \frac{df}{dx}h + \frac{h^2}{2!}\frac{d^2 f}{dx^2} + \frac{h^3}{3!}\frac{d^3 f}{dx^3} + \cdots + \mathcal{O}(h^4) \\ f(x-h) &= f(x) - \frac{df}{dx}h + \frac{h^2}{2!}\frac{d^2 f}{dx^2} - \frac{h^3}{3!}\frac{d^3 f}{dx^3} + \cdots + \mathcal{O}(h^4) \end{aligned}$$

From these expansions, we can derive the error associated with the forward and backward difference schemes for approximating the first derivative:

$$\textbf{Forward:} \quad \frac{df(x)}{dx} \approx \frac{f(x+h)-f(x)}{h} = \frac{df(x)}{dx} + \underbrace{\frac{h}{2!}\frac{d^2 f(x)}{dx^2} + \cdots + \mathcal{O}(h^2)}_{\text{Error Term } \mathcal{O}(h)}$$

$$\textbf{Backward:} \quad \frac{df(x)}{dx} \approx \frac{f(x)-f(x-h)}{h} = \frac{df(x)}{dx} - \underbrace{\frac{h}{2!}\frac{d^2 f(x)}{dx^2} + \cdots + \mathcal{O}(h^2)}_{\text{Error Term } \mathcal{O}(h)}$$

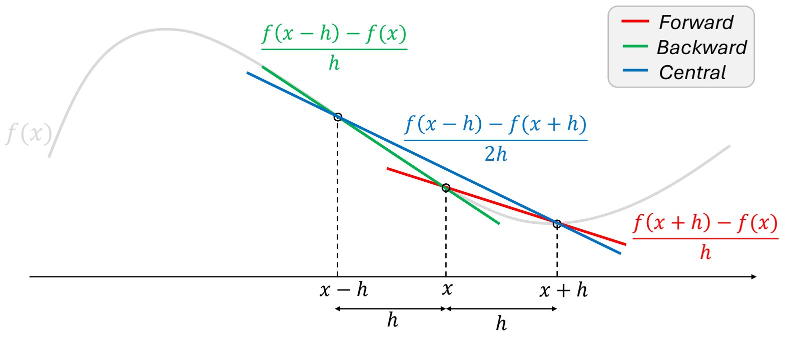

Figure 3.6: Derivative approximation using first-order Forward, Backward and Central FDM scheme

In both schemes, the term $\frac{h}{2!}\frac{d^2f(x)}{dx^2}$ represents the leading error term, which is proportional to h. This implies that the error decreases linearly with h. To achieve higher accuracy, the central difference scheme is often preferred, as it reduces the error term to $\mathcal{O}(h^2)$, providing a more precise approximation of the first derivative:

$$\textbf{Central:} \quad \frac{df(x)}{dx} \approx \frac{f(x+h)-f(x-h)}{2h} = \frac{df(x)}{dx} + \underbrace{\frac{h^2}{3!}\frac{d^3f(x)}{dx^3} + \cdots + \mathcal{O}(h^3)}_{\text{Error Term } \mathcal{O}(h^2)}$$

The central difference scheme significantly reduces the error for small values of h compared to the forward and backward schemes, making it a preferred choice for numerical differentiation. It is important to note that higher approximation accuracy can also be achieved with forward and backward difference schemes by utilizing higher-order approximations, as detailed in Table 3.3. Additionally, Table 3.3 presents the formulations for approximating the second derivative $f''(x)$ using the three different schemes with the corresponding error characteristics.

Example 3.1.1: *FDM for solid phase spatial discretization [46]*

In the context of battery modeling, the FDM is frequently employed to discretize the mass conservation PDE in the solid phase, primarily due to its straightforward implementation. This section provides an overview of the approximation of (3.2) using the FDM, as outlined in [46]. Figure 3.7(a) illustrates the discretization grid employed to partition the particle radius into N_r discrete nodes equally spaced. Firstly, eq. (3.2) is rewritten as follows:

$$\frac{\partial c_{s,j}}{\partial t} = \frac{2D_{s,j}}{r}\frac{\partial c_{s,j}}{\partial r} + D_{s,j}\frac{\partial^2 c_{s,j}}{\partial r^2}. \tag{3.20}$$

FDM scheme	*Derivative*	*Order*	*Formula*	*Error*
Forward	$f'(x)$	First Order	$\frac{f(x+h)-f(x)}{h}$	$\mathcal{O}(h)$
		Second Order	$\frac{-3f(x)+4f(x+h)-f(x+2h)}{2h}$	$\mathcal{O}(h^2)$
	$f''(x)$	First Order	$\frac{f(x+2h)-2f(x+h)+f(x)}{h^2}$	$\mathcal{O}(h)$
		Second Order	$\frac{-f(x+3h)+4f(x+2h)-5f(x+h)+2f(x)}{h^2}$	$\mathcal{O}(h^2)$
Backward	$f'(x)$	First Order	$\frac{f(x)-f(x-h)}{h}$	$\mathcal{O}(h)$
		Second Order	$\frac{3f(x)-4f(x-h)+f(x-2h)}{2h}$	$\mathcal{O}(h^2)$
	$f''(x)$	First Order	$\frac{f(x)-2f(x-h)+f(x-2h)}{h^2}$	$\mathcal{O}(h)$
		Second Order	$\frac{2f(x)-5f(x-h)+4f(x-2h)-f(x-3h)}{h^2}$	$\mathcal{O}(h^2)$
Central	$f'(x)$	Second Order	$\frac{f(x+h)-f(x-h)}{2h}$	$\mathcal{O}(h^2)$
		Fourth Order	$\frac{-f(x+2h)+8f(x+h)-8f(x-h)+f(x-2h)}{12h}$	$\mathcal{O}(h^4)$
	$f''(x)$	Second Order	$\frac{f(x+h)-2f(x)+f(x-h)}{h^2}$	$\mathcal{O}(h^2)$
		Fourth Order	$\frac{-f(x+2h)+16f(x+h)-30f(x)+16f(x-h)-f(x-2h)}{12h^2}$	$\mathcal{O}(h^4)$

Table 3.3: Summary of Finite Difference Method (FDM) Schemes for First and Second Derivative Approximations

Next, the central difference scheme is applied to approximate both the first and second derivatives of $c_{s,j}$ with respect to the particle radius for the internal nodes ($i = 2, \cdots, N_r - 1$). This yields:

$$\begin{aligned} \frac{\partial c_{s,j,i}}{\partial t} &= \frac{2D_{s,j}}{i\Delta r}\frac{c_{s,j,i+1}-c_{s,j,i-1}}{2\Delta r} + D_{s,j}\frac{c_{s,j,i+1}-2c_{s,j,i}+c_{s,j,i-1}}{\Delta r^2}, \\ \frac{\partial c_{s,j,i}}{\partial t} &= \frac{D_{s,j}}{\Delta r^2}\left[\left(1-\frac{1}{i}\right)c_{s,j,i-1} - 2c_{s,j,i} + \left(1+\frac{1}{i}\right)c_{s,j,i+1}\right], \end{aligned} \tag{3.21}$$

where $c_{s,j,i}$ denotes the lithium ion concentration at the i-th node of the j-th electrode, and $\Delta r = R_{s,j}/(N_r - 1)$. For the external nodes, we derive the formulation by considering the boundary conditions of (3.2). Specifically, for the boundary condition at $r = 0$, the spatial derivative $\frac{\partial c_{s,j}}{\partial r}\Big|_{r=0}$ can be approximated using the forward FDM scheme. However, as noted in Table 3.3, the accuracy of the forward scheme is generally lower compared to the central difference scheme. To ensure consistency in accuracy between internal and external nodes, we have two options: either use a second-order forward scheme or employ the ghost node approach [58]. The ghost node method involves adding a fictitious node to the left of the boundary condition (BC), as illustrated in Figure 3.7(a). This approach allows us to approximate

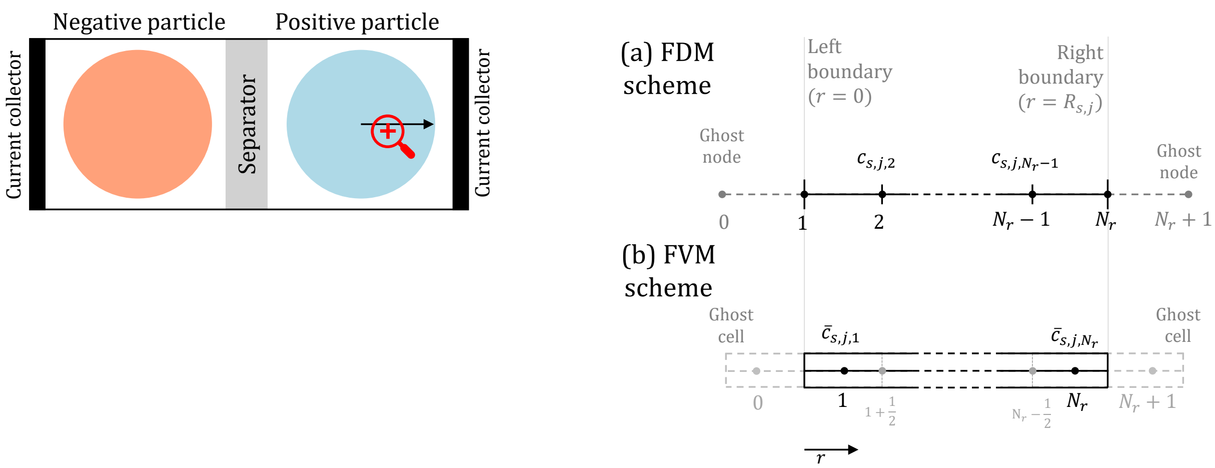
Negative particle
Positive particle
Current collector
Separator
Current collector
(a) FDM scheme
Left boundary ($r = 0$)
Right boundary ($r = R_{s,j}$)
Ghost node
$c_{s,j,2}$
c_{s,j,N_r-1}
Ghost node
0
1
2
$N_r - 1$
N_r
$N_r + 1$
(b) FVM scheme
Ghost cell
$\bar{c}_{s,j,1}$
$\bar{c}_{s,j,N_r}$
Ghost cell
0
1
$1+\frac{1}{2}$
$N_r-\frac{1}{2}$
N_r
$N_r + 1$
r

Figure 3.7: (a) FDM and (b) FVM scheme used to discretized the particle radius of the electrode solid phase.

$\left.\frac{\partial c_{s,j}}{\partial r}\right|_{r=0}$ using the central difference scheme, expressed as:

$$\left.\frac{\partial c_{s,j}}{\partial r}\right|_{r=0} \approx \frac{c_{s,j,2} - c_{s,j,0}}{2\Delta r} = 0 \Longrightarrow c_{s,j,2} = c_{s,j,0}. \tag{3.22}$$

Applying this approximation to the simplified form of (3.20) at $r = 0$ results in:

$$\frac{\partial c_{s,j,1}}{\partial t} = \frac{D_{s,j}}{\Delta r^2}\left[2c_{s,j,2} - 2c_{s,j,1}\right]. \tag{3.23}$$

Similarly, when applying this approximation to the right boundary condition, the overall discretized mass conservation equation can be compactly expressed as:

$$\dot{c}_{s,j} = \alpha_{s,j} A_{s,j} c_{s,j} + \beta_{s,j} B_{s,j} c_{s,j}. \tag{3.24}$$

where $c_{s,j} = [c_{s,j,1}, \cdots, c_{s,j,N_r}] \in \mathbb{R}^{N_r}$, $\alpha_{s,j} = D_{s,j}/\Delta r^2$, $\beta_{s,j} = \pm 1/(AL_j F a_{s,j} \Delta r)$, amd the he matrices $A_{s,j} \in \mathbb{R}^{(N_r)\times(N_r)}$ and $B_{s,j} \in \mathbb{R}^{(N_r)\times(1)}$ are written as:

$$A_{s,j} = \begin{bmatrix} -2 & 2 & 0 & 0 & \cdots & 0 & 0 \\ 1/2 & -2 & 3/2 & 0 & \cdots & 0 & 0 \\ 0 & 2/3 & -2 & 4/3 & \cdots & 0 & 0 \\ \vdots & \vdots & \vdots & \vdots & \ddots & \vdots & \vdots \\ 0 & 0 & 0 & 0 & \cdots & 2 & -2 \end{bmatrix}, \quad B_{s,j} = \begin{bmatrix} 0 \\ 0 \\ 0 \\ \vdots \\ \frac{2N_r}{N_r-1} \end{bmatrix}$$

It is worth mentioning that $c^{surf}_{s,\mathrm{j}} = c_{s,\mathrm{j},N_r}$ and $c^{bulk}_{s,\mathrm{j}} = \frac{3}{R^3_{s,j}} \int_0^{R_{s,\mathrm{j}}} r^2 c_{s,\mathrm{j}} dr$ refer to the electrode surface and bulk concentration, respectively.

Finite Volume Method (FVM)

The FVM is a numerical technique designed for solving PDEs, particularly suited for conservation laws where ensuring mass conservation is essential. The application of FVM consists of three main steps. First, the domain of interest is divided into small control volumes (CVs), with each volume associated with a node that stores the variable of interest (Φ). considering the i-th CV, the volume-averaged value of Φ_i is considered as:

$$\bar{\Phi}_i = \frac{1}{V_i} \int_{CV_i} \Phi_i dV$$

where V_i is the volume of the i-th CV. Next, the PDEs are integrated over each control volume to enforce conservation laws locally. Finally, the divergence theorem is applied to transform the volume integrals into surface integrals, simplifying the equations and enabling the accurate calculation of fluxes across the surfaces of each control volume.

Theorem 1 (Gauss Theorem). Given a vector field f and a closed volume V bounded by a closed surface S, the integral of the divergence of f over V is equal to the flux of f across S. Mathematically, this is expressed as:

$$\int_V \nabla \cdot f \, dV = \oint_S f \cdot n \, dS, \tag{3.25}$$

where $\nabla \cdot$ denotes the divergence operator, and n represents the outward-pointing unit normal vector to the surface S.

In the context of battery modeling, the FVM is employed to discretize the mass conservation PDEs in both the liquid phase and solid phase. Specifically, [66] firstly introduced FVM to the liquid phase, while [67] and [68] use it for the solid phase.

Example 3.1.2: *FVM for solid phase spatial discretization [68]*

This section provides an overview of approximating (3.2) using the FVM; in spherical coordinates, as detailed in [68]. First, the PDE (3.2) is rewritten as:

$$\frac{\partial c_{s,j}}{\partial t} = \nabla \cdot (D_{s,j} \nabla c_{s,j}) \tag{3.26}$$

where $\nabla c_{s,j}$ represents the gradient of the concentration in spherical coordinates [a], and $\nabla \cdot$ denotes the divergence operator [b]. The rewritten PDE is then integrated over the i-th control volume (CV_i) as follows:

$$\int_{CV_i} \frac{\partial c_{s,j}}{\partial t} \, dV = \int_{CV_i} \nabla \cdot (D_{s,j} \nabla c_{s,j}) \, dV \tag{3.27}$$

Applying the Gauss theorem to convert the volume integral on the right-hand side to a surface integral, we obtain:

$$\begin{aligned}\int_{CV_i} \frac{\partial c_{s,j}}{\partial t}\, dV &= \oint_{A_i} (D_{s,j} \nabla c_{s,j} \cdot n)\, dA \\ &= \int_{A_{i+\frac{1}{2}}} D_{s,j} \frac{\partial c_{s,j}}{\partial r}\, dA - \int_{A_{i-\frac{1}{2}}} D_{s,j} \frac{\partial c_{s,j}}{\partial r}\, dA.\end{aligned}$$

Thus, the integral form becomes:

$$\frac{\partial \bar{c}_{s,j,i}}{\partial t} V_i = D_{s,j} \frac{\partial c_{s,j}}{\partial r}\bigg|_{i+\frac{1}{2}} A_{i+\frac{1}{2}} - D_{s,j} \frac{\partial c_{s,j}}{\partial r}\bigg|_{i-\frac{1}{2}} A_{i-\frac{1}{2}}. \tag{3.28}$$

where $A_{i+\frac{1}{2}} = 4\pi r^2_{i+\frac{1}{2}}$ and $A_{i-\frac{1}{2}} = 4\pi r^2_{i-\frac{1}{2}}$ are the the surface areas of the left $(i-1/2)$ and right $(i+1/2)$ boundaries of CV_i, respectively, and $V_i = 4/3\pi(r^3_{i+\frac{1}{2}} - r^3_{i-\frac{1}{2}})$. The central difference scheme is used to approximate the spatial derivative of $c_{s,j}$ for the internal control volumes:

$$\frac{\partial \bar{c}_{s,j,i}}{\partial t} V_i = D_{s,j} \frac{\bar{c}_{s,j,i+1} - \bar{c}_{s,j,i}}{\Delta r} A_{i+\frac{1}{2}} - D_{s,j} \frac{\bar{c}_{s,j,i} - \bar{c}_{s,j,i-1}}{\Delta r} A_{i-\frac{1}{2}}. \tag{3.29}$$

According to [68], the ghost cell approach can be employed to approximate boundary conditions using a central scheme, similar to the FDM discretization scenario. The final FVM-based discretized mass conservation equation can be expressed in state-space form as:

$$\dot{\bar{c}}_{s,j} = A^{FVM}_{s,j} \bar{c}_{s,j} + B^{FVM}_{s,j} I_{cell}. \tag{3.30}$$

where $\bar{c}_{s,j} = [\bar{c}_{s,j,1}, \cdots, \bar{c}_{s,j,N_r}] \in \mathbb{R}^{N_r}$, and the matrices $A^{FVM}_{s,j} \in \mathbb{R}^{N_r \times N_r}$ and $B^{FVM}_{s,j} \in \mathbb{R}^{N_r \times 1}$ are given by:

$$A^{FVM}_{s,j} = \frac{4D_{s,j}}{\Delta r} \begin{bmatrix} -\frac{3}{4} & \frac{3}{4} & 0 & 0 & \cdots & 0 & 0 \\ \frac{3}{28} & -\frac{15}{28} & \frac{12}{28} & 0 & \cdots & 0 & 0 \\ 0 & \frac{12}{76} & -\frac{39}{76} & \frac{27}{76} & \cdots & 0 & 0 \\ \vdots & \vdots & \vdots & \vdots & \ddots & \vdots & \vdots \\ 0 & 0 & 0 & 0 & \cdots & \frac{3(N_r-1)^2}{12N_r^2-12N_r+4} & \frac{-3(N_r-1)^2}{12N_r^2-12N_r+4} \end{bmatrix}, \quad B^{FVM}_{s,j} = \begin{bmatrix} 0 \\ 0 \\ 0 \\ \vdots \\ \beta_3 \end{bmatrix}$$

where $\beta_3 = \frac{3N_r g(I_{cell})}{\Delta r(3N_r^2-3N_r+1)(Fa_{s,j}L_jA)}$, and $g(I_{cell})$ is -1 if $j = p$ and +1 if $j = n$ Unlike the FDM approach, where the surface concentration is directly taken from the last nodal point, in the FVM approach, the surface concentration $c^{surf}_{s,j}$ cannot be calculated directly. Instead, it is typically estimated using linear extrapolation [69]:

$$c^{surf}_{s,j} = \frac{3\bar{c}_{s,j,N_r} - \bar{c}_{s,j,N_r-1}}{2}. \tag{3.31}$$

It is worth noting that the accuracy of this extrapolation can be improved using third-order Hermite extrapolation, as demonstrated in [68].

---

[a] $\nabla c_{s,j} = \frac{\partial c_{s,j}}{\partial r}\hat{r} + 0\hat{\theta} + 0\hat{\phi}$

[b] $\nabla \cdot (D_{s,j} \nabla c_{s,j}) = \frac{D_{s,j}}{r^2}\frac{\partial}{\partial r}\left(r^2 \frac{\partial c_{s,j}}{\partial r}\right)\hat{r} + 0\hat{\theta} + 0\hat{\phi}$

3.1.3.2 Function approximation

Function approximation represents the second major class of techniques used for approximating PDEs within the context of battery modeling. These techniques involve using numerical methods to solve PDEs by assuming a predefined form for the solution and then determining the coefficients of this solution to satisfy the original equation. In this section, we will provide a concise review of the fundamental principles underlying two key methodologies: spectral methods [59, 60] and polynomial approximation [62].

Spectral methods
Spectral methods are advanced numerical techniques designed to approximate solutions of PDEs by leveraging high-order polynomials to represent their solution across the entire computational domain [59, 70]. Unlike FDM, which rely on local approximations where derivatives are estimated based on neighboring grid points, spectral methods utilize global approximations where the value of a derivative at any given point is influenced by the solution across the entire domain. This global approach grants spectral methods a significant advantage in terms of convergence rate, achieving high accuracy with fewer computational points compared to FDM. However, these methods are generally less flexible when dealing with complex geometries or boundary conditions, and can be challenging to implement. The domain of spectral methods is vast and diverse, encompassing a various range of techniques. Key subclasses include Galerkin spectral method, spectral collocation methods (often referred to as pseudospectral methods), and Tau spectral methods. In the context of battery modeling, the Galerkin spectral method and spectral collocation methods are primarily employed to governing PDEs as shown in [71, 72, 73, 61] and [74, 75, 76, 77], respectively. According to [78], let's consider the PDE:

$$PDE[u(x,t)] = 0 \tag{3.32}$$

defined on a domain $\mathcal{D}$ with boundary conditions $B(u) = 0$. In spectral methods, the solution to a PDE is typically approximated as a finite sum of known functions:

$$u_N(x,t) = u_B(x,t) + \sum_{k=0}^{N} a_k(t) \cdot \phi_k(x) \tag{3.33}$$

where $\phi_k(x)$ are the basis functions (or trial functions), and $a_k(t)$ are the time-dependent coefficients. The term $u_B(x,t)$ is included to handle inhomogeneous boundary conditions. It is important to note that in the approximation $u_N(x,t)$, the spatial and temporal dependencies are separated, which simplifies the computation of spatial derivatives. If we assume $u_B = 0$, then:

$$\frac{\partial u_N(x,t)}{\partial x} = \sum_{k=0}^{N} a_k(t) \cdot \frac{d\phi_k(x)}{dx}$$

The coefficients $a_k(t)$ are determined using the method of weighted residuals:

$$\int_{\mathcal{D}} w_j(x) \cdot \mathrm{R}(x,t)\, dx = 0, \quad \text{for } j = 0, \ldots, N \tag{3.34}$$

where $w_j(x)$ represents the weight functions corresponding to the j-th residuals $\mathrm{R}(x,t)$, which is derived by substituting (3.33) into the PDE (3.32). Specifically:

$$\mathrm{R}(x,t) = PDE(u_N(x,t)) \tag{3.35}$$

Eq. (3.34) involves ensuring that the residual is orthogonal to the set of weight functions. It is crucial to recognize that the choice of weight functions distinguishes between the Galerkin and collocation spectral methods. In the Galerkin method, the weight functions are chosen to be equal to the basis functions. In contrast, the collocation method involves selecting $N+1$ collocation points within the domain $\mathcal{D}$ where the residual $\mathrm{R}(x,t)$ is required to vanish, i.e., $\mathrm{R}(x,t) = 0$. In the context of battery modeling, common choices of basis functions include Legendre polynomials, first- and second-order Chebyshev polynomials, and cosine functions [61].

Polynomial approximation

Polynomial approximation is a method used to simplify the microscale diffusion PDE by reducing it to a set of differential algebraic equations (DAEs). This technique assumes that the solid phase concentration within a spherical particle is represented as a polynomial function, enabling the derivation of formulations for both the surface and average particle concentrations [62, 66]. The following example aims to clarity the mass conservation PDE approaximation.

Example 3.1.3: *Polynomial approximation for solid phase*

Considering for instance the two-parameter model [62], the concentration profile within the particle is assumed to take the form of a second-order polynomial, expressed as:

$$c_{s,j}(r,t) = a(t) + b(t)\Big(\frac{r^2}{R_{s,j}^2}\Big)$$

Based on this expression, the surface concentration is calculated by evaluating $c_{s,j}$ at $r = R_{s,j}$:

$$c_{s,j}^{surf}(t) = c_{s,j}(r,t)\big|_{r=R_{s,j}} = a(t) + b(t) \tag{3.36}$$

The bulk concentration is obtained by volume-averaging the particle concentration:

$$c_{s,j}^{bulk}(t) = \frac{1}{\frac{4}{3}\pi R_{s,j}^3}\int_{r=0}^{R_{s,j}} 4\pi r^2 \left[a(t) + b(t)\left(\frac{r^2}{R_{s,j}^2}\right)\right] dr = a(t) + \frac{3}{5}b(t) \tag{3.37}$$

Combining equations (3.36) and (3.37), we can express $a(t)$ and $b(t)$ in terms of $c_{s,j}^{surf}$ and $c_{s,j}^{bulk}$:

$$\begin{cases} c_{s,j}^{surf} & = a(t) + b(t) \\ c_{s,j}^{bulk} & = a(t) + \frac{3}{5}b(t) \end{cases} \longrightarrow \begin{cases} a(t) & = -\frac{3}{2}c_{s,j}^{surf} + \frac{5}{2}c_{s,j}^{bulk} \\ b(t) & = -\frac{5}{2}c_{s,j}^{bulk} + \frac{5}{2}c_{s,j}^{surf} \end{cases} \tag{3.38}$$

Then, the volume-averaged concentration is derived by integrating the governing PDE over the particle volume:

$$\begin{aligned} &\frac{1}{R_{s,j}^3}\int_{r=0}^{R_{s,j}} 3r^2\left(\frac{\partial c_{s,j}}{\partial t} - \frac{D_{s,j}}{r^2}\frac{\partial}{\partial r}\left(r^2\frac{\partial c_{s,j}}{\partial r}\right)\right) dr = 0 \\ &\frac{1}{R_{s,j}^3}\int_{r=0}^{R_{s,j}} 3r^2\left(\frac{da(t)}{dt} + \frac{db(t)}{dt}\frac{r^2}{R_{s,j}^2}\right) dr = \frac{1}{R_{s,j}^3}\int_{r=0}^{R_{s,j}} 18D_{s,j}\frac{r^2}{R_{s,j}^2}b(t)dr \\ &\underbrace{\left(\frac{da(t)}{dt} + \frac{3}{5}\frac{db(t)}{dt}\right)}_{\dot{c}_{s,j}^{bulk}} = \frac{6D_{s,j}}{R_{s,j}^2}b(t) \end{aligned} \tag{3.39}$$

The term $b(t)$ can be calculated using the boundary condition of (3.2) at $r = R_{s,j}$:

$$\begin{cases} \dot{c}_{s,j}^{bulk} = \frac{6D_{s,j}}{R_{s,j}^2}b(t) \\ b(t) = \frac{i_{int,j}}{2D_{s,j}a_{s,j}F} \end{cases} \rightarrow \quad \dot{c}_{s,j}^{bulk} = \frac{i_{int,j}}{a_{s,j}F} \tag{3.40}$$

Finally, $c_{s,j}^{surf}$ is calculated using $b(t)$ from (3.38):

$$\begin{cases} b(t) = 5\left(c_{s,j}^{surf} - c_{s,j}^{bulk}\right) \\ b(t) = \frac{i_{int,j}}{2D_{s,j}a_{s,j}F} \end{cases} \rightarrow \quad c_{s,j}^{surf} = \frac{i_{int,j}}{5D_{s,j}a_{s,j}F} - c_{s,j}^{bulk} \tag{3.41}$$

In summary, the governing PDE (3.2) is approximated into one ODE and one algebraic equation, describing the bulk and surface particle concentrations, respectively. According to [62], higher-order polynomial profile can be used to improve the model approximation for high operating current rates. The polynomial profile concept has also been applied to the approximation of the electrolyte concentration and potential [38].

3.1.3.3 Frequency Domain Approximation

Frequency Domain approximation represents the third major class of techniques used for approximating PDEs in the context of battery modeling. The key idea behind this approach is to apply the Laplace transform to convert PDEs into transcendental transfer functions [1], ultimately enabling their effective conversion into a system of ODEs, which are generally simpler to solve.
Given a function $f(x,t)$ defined for all $t > 0$, the Laplace transform of $f(x,t)$, denoted $\mathcal{L}\big[f(x,t)\big] = F(x,s)$, is given by:

$$\mathcal{L}\big[f(x,t)\big] = \int_0^\infty e^{-st} f(x,t)\, dt = F(x,s) \tag{3.42}$$

where s is the Laplace variable. In the context of PDEs, the differentiation property of the Laplace transform is particularly useful. Specifically, the Laplace transform of the time derivative of $f(x,t)$ is:

$$\mathcal{L}\left[\frac{\partial f(x,t)}{\partial t}\right] = \int_0^\infty e^{-st} \frac{\partial f(x,t)}{\partial t}\, dt = sF(x,s) - f(x,0). \tag{3.43}$$

To enhance reader understanding, the following example shows how to solve the solid phase mass conservation equation using the Laplace transform.

Example 3.1.4: *Laplace trasnform for solid phase PDE [63]*

This section offers an overview of the derivation of the transcendental transfer function for the mass conservation in the solid-phase PDE (3.2), as detailed in [63]. First, we compute the Laplace transform of (3.2). The transformed equation is:

$$SC_{s,j} = D_{s,j} \frac{\partial^2 C_{s,j}}{\partial r^2} + \frac{2D_{s,j}}{r} \frac{\partial C_{s,j}}{\partial r}. \tag{3.44}$$

By substituting $W = C_{s,j} r$, the PDE is transformed into a second-order homogeneous ODE:

$$\frac{D_{s,j}}{r} \frac{\partial^2 W}{\partial r^2} - \frac{S}{r} W = 0 \tag{3.45}$$

The general solution to this ODE is:

$$W = C_{s,j} r = Ae^{r\sqrt{\frac{S}{D_{s,j}}}} + Be^{-r\sqrt{\frac{S}{D_{s,j}}}} \longrightarrow C_{s,j}(S,r) = \frac{Ae^{r\sqrt{\frac{S}{D_{s,j}}}} + Be^{-r\sqrt{\frac{S}{D_{s,j}}}}}{r} \tag{3.46}$$

The coefficients A and B are determined by applying the Laplace transform to the

---

[1] Transfer functions with infinite number of poles

PDE boundary conditions:

$$\begin{cases} \left.\dfrac{\partial C_{s,j}}{\partial r}\right|_{r=0} = 0, \\ D_{s,j}\left.\dfrac{\partial C_{s,j}}{\partial r}\right|_{r=R_{s,j}} = \frac{J_{s,j}}{F} \end{cases} \rightarrow \begin{cases} A = -B, \\ A = \frac{J_{s,j}R_{s,j}}{2F\left[\sinh\left(R_{s,j}\sqrt{\frac{S}{D_{s,j}}}\right) - R_{s,j}\sqrt{\frac{S}{D_{s,j}}}\cosh\left(R_{s,j}\sqrt{\frac{S}{D_{s,j}}}\right)\right]} \end{cases}$$

With the coefficients A and B determined, the transfer function can be calculated for any point of interest within the particle. For example, the transfer function for surface concentration is obtained by evaluating at $r = R_{s,j}$:

$$\frac{C_{s,j}^{\mathrm{surf}}(S)}{J_{s,j}} = \frac{R_{s,j}}{D_{s,j}F}\frac{\sinh\left(R_{s,j}\sqrt{\frac{S}{D_{s,j}}}\right)}{\sinh\left(R_{s,j}\sqrt{\frac{S}{D_{s,j}}}\right) - R_{s,j}\sqrt{\frac{S}{D_{s,j}}}\cosh\left(R_{s,j}\sqrt{\frac{S}{D_{s,j}}}\right)} \tag{3.47}$$

It is worth mentioning that the Laplace transform can be applied to both solid and liquid phase governing PDEs, as demonstrated in [79]. In the context of battery modeling, MOR methods are employed to simplify transfer functions. Specifically, the Pade approximation can linearize the transfer function into a rational form, allowing for direct reduction of the system order through moment matching [63]. Alternatively, residue grouping technique that simplifies complex battery models by grouping transfer function residues into clusters to create a lower-order approximation [64]. Finally, the dynamic realization algorithm generates an reduced-order discrete-time state-space model directly from the orginal transfer fucntion by first determining the discrete-time pulse response and then using the Ho-Kalman algorithm [80, 81].
In the following the besis of pade approximation and residue groupng are briefly explained.

Padé approximation

According to [63], (3.47) can be modeled as a low-pass filter and approximated as:

$$\frac{C_{s,j}^{\mathrm{surf}}(S)}{J_{s,j}} = \frac{a_0 + a_1S + a_2S^2 + \cdots + a_{Q-1}S^{Q-1}}{b_0 + b_2S + b_3S^2 + \cdots + b_QS^{Q-1}}\left(\frac{1}{S}\right) \tag{3.48}$$

where the coefficients can be analytically obtained through the moment matching method [79]. Finally, a linear state-space model can be derived in the form of controllable canonical form, as:

$$\begin{cases} \dot{x} & = \begin{bmatrix} 0 & 1 & 0 & 0 & \cdots & 0 & 0 \\ 0 & 0 & 1 & 0 & \cdots & 0 & 0 \\ \vdots & \vdots & \vdots & \vdots & \ddots & \vdots & \vdots \\ 0 & 0 & 0 & 0 & \cdots & 1 & 0 \\ 0 & 0 & 0 & 0 & \cdots & 0 & 1 \\ 0 & \frac{1}{b_Q} & \frac{b_2}{b_Q} & \frac{b_3}{b_Q} & \cdots & \frac{b_{Q-2}}{b_Q} & \frac{b_{Q-1}}{b_Q} \end{bmatrix} x + \begin{bmatrix} 0 \\ 0 \\ \vdots \\ 0 \\ 0 \\ \frac{1}{b_Q} \end{bmatrix} u \\ \\ c_{s,j}^{\text{surf}} & = \begin{bmatrix} a_0 & a_1 & a_2 & a_3 & \cdots & a_{Q-1} \end{bmatrix} x \end{cases} \tag{3.49}$$

Residue grouping

According to [64], the transcendental transfer function given in (3.47) can be reformulated as:

$$\frac{C_{s,j}^{\text{surf}}(s)}{J_{s,j}} = Z + \sum_{k=1}^{\infty} \frac{\text{Res}_k \, s}{s - p_k} \tag{3.50}$$

where p_k denotes the k-th pole, Res_k is the corresponding residue, and Z represents the steady-state solution. As detailed in [64], the pole p_k, residue Res_k, and steady-state solution Z are given by:

$$p_k = -D_{s,j} \left(\frac{\xi_k}{R_{s,j}} \right)^2, \qquad \text{Res}_k = \frac{-2}{a_{s,j} F R_{s,j} p_k}, \qquad Z = \frac{-R_{s,j}}{5 a_{s,j} F D_{s,j}}$$

where ξ_k satisfies the equation $\tan(\xi_k) = \xi_k$. The residue grouping method involves dividing the frequency range of interest into D bins and calculating the grouped residues within each bin, denoted as $\bar{\text{Res}}_k = \sum_{z=k_{f-1}+1}^{k_f} \text{Res}_z$. Thus, the transfer function (3.50) can be simplified to a D-th order transfer function:

$$\frac{C_{s,j}^{\text{surf}}(s)}{J_{s,j}} = Z + \sum_{k=1}^{D} \frac{\bar{\text{Res}}_k \, s}{s - p_k} \tag{3.51}$$

Finally, the linear model associated with the simplified transfer function is computed as described in [64]. It is important to note that increasing the number of grouped points enhances the accuracy of the reduced-order model but also increases its computational complexity.

3.1.3.4 MOR for high-dimensional ODE systems

In this section, the Balanced Truncation method [65] and the POD-Galerkin method [82] are briefly reviewed. Both methodologies are MOR techniques commonly used to approximate high-dimensional systems of ODEAs that result from the semi-discretization of PDAEs. These methods allow for the reduction of the state space vector of the spatially discretized model while preserving its essential features and accuracy.

Balanced truncation

In this section, we provide a brief overview of the theoretical formulation of balanced truncation, as presented in [65]. Consider a linear system represented in state-space form as:

$$\begin{cases} \dot{x}(t) = Ax(t) + Bu(t) \\ y(t) = Cx(t) + Du(t) \end{cases} \tag{3.52}$$

where $x(t) \in \mathbb{R}^n$ is the state vector, $u(t) \in \mathbb{R}$ is the input vector, and $y(t) \in \mathbb{R}$ is the output vector. It is important to note that the system of ODEs resulting from the FDM discretization of the mass conservation equation in the solid phase (as provided in (3.24)) can be expressed in the same state-space form as the one considered here. According to [65], the controllability (W_c) and observability (W_o) Gramians of the system are defined as:

$$\begin{aligned} W_c &= \int_0^{+\infty} e^{At} B B^T e^{A^T t} \, dt, \\ W_o &= \int_0^{+\infty} e^{A^T t} C C^T e^{At} \, dt, \end{aligned} \tag{3.53}$$

As discussed in [83], a balanced realization of the system is achieved when there exists an invertible transformation matrix $T \in \mathbb{R}^{n \times n}$ such that the Gramians W_c and W_o become equal and diagonal [84]. Specifically, if the system is both controllable and observable, the Gramians can be diagonalized as:

$$W_c = W_o = \begin{bmatrix} \sigma_1 & 0 & \cdots & 0 \\ 0 & \sigma_2 & \cdots & 0 \\ \vdots & \vdots & \ddots & \vdots \\ 0 & 0 & \cdots & \sigma_n \end{bmatrix}, \tag{3.54}$$

where $\sigma_1 \geq \sigma_2 \geq \cdots \geq \sigma_n$ are the singular values of the system. By performing a coordinate transformation $z = Tx$, the system can be converted into a balanced realization, yielding:

$$\begin{cases} \dot{z}(t) = \hat{A}z(t) + \hat{B}u(t) \\ y(t) = \hat{C}z(t) + Du(t) \end{cases} \tag{3.55}$$

where $\hat{A} = TAT^{-1}$, $\hat{B} = TB$, and $\hat{C} = CT^{-1}$. In this balanced form, the states in z are ordered from the highest to the lowest levels of controllability and observability. To obtain a ROM, one can focus on the first $d \ll n$ dominant controllable and observable states by selecting the first d columns of T. The matrices $\hat{A}$, $\hat{B}$, and $\hat{C}$ can then be partitioned as:

$$\hat{A} = \begin{bmatrix} \hat{A}_{11} & \hat{A}_{12} \\ \hat{A}_{21} & \hat{A}_{22} \end{bmatrix}, \quad \hat{B} = \begin{bmatrix} \hat{B}_1 \\ \hat{B}_2 \end{bmatrix}, \quad \hat{C} = \begin{bmatrix} \hat{C}_1 & \hat{C}_2 \end{bmatrix}, \tag{3.56}$$

where $\hat{A}_{11} \in \mathbb{R}^{d\times d}$, $\hat{A}_{12}, \hat{A}_{21} \in \mathbb{R}^{(n-d)\times d}$, $\hat{A}_{22} \in \mathbb{R}^{(n-d)\times(n-d)}$, $\hat{B}_1, \hat{C}_1 \in \mathbb{R}^{d\times 1}$, and $\hat{B}_2, \hat{C}_2 \in \mathbb{R}^{(n-d)\times 1}$. Finally, the ROM can be derived as:

$$\begin{cases} \dot{\tilde{z}}(t) = \hat{A}_{11}\tilde{z}(t) + \hat{B}_1 u(t) \\ y(t) = \hat{C}_1\tilde{z}(t) + Du(t) \end{cases} \tag{3.57}$$

It is noteworthy that the new ROM system, characterized by $d \ll n$ ODEs, retains the most controllable and observable states of the original model.

Proper orthogonal decomposition(POD)-Galerkin projection

In this section, the theoretical formulation of the POD-Galerkin MOR is briefly described, according to [85]. The POD-Galerkin method is particularly suited for a nonlinear dynamical system written as:

$$\begin{cases} \dot{x}(t) & = Ax(t) + f(x(t)) \\ x(t_0) & = x_0 \end{cases} \tag{3.58}$$

where $x \in \mathbb{R}^n$, $A \in \mathbb{R}^{n\times n}$, $f : \mathbb{R}^n \to \mathbb{R}^n$ is a vector field, and $x_0 \in \mathbb{R}^n$ is the initial condition. Note that the considered system consists of a linear part, $Ax(t)$, and a nonlinear part, $f(x(t))$. The solution $x_k \in \mathbb{R}^n$ of (3.58) for a given time instant $t_k \in [0, +\infty]$ is called a **Snapshot**. Given a sequence of Snapshots x_k, obtained for a given time mesh $t_k = t_0 + k \cdot dt$ where dt is the sampling time and $k = 0, 1, \cdots, n_t$, the **Snapshot matrix** $S \in \mathbb{R}^{n\times n_t}$ is constructed as

$$S = \begin{bmatrix} x_0 & x_1 & \cdots & x_{n_t} \end{bmatrix}$$

The key aspect of POD is that it allows the extraction of an orthonormal basis $\begin{bmatrix}\psi_1, \cdots, \psi_z\end{bmatrix}$ of a subspace $\Psi \subset \mathbb{R}^n$ with dimension $z < n$ such that the distance between the Snapshot matrix and its projection onto the new basis functions is minimized:

$$\min_{\psi_1 \cdots \psi_z} \sum_{i=0}^{n_t} \left\| x_i - \sum_{j=1}^{z} \langle x_i, \psi_j \rangle \psi_j \right\|^2, \tag{3.59}$$

where $\langle \cdot, \cdot \rangle$ is an inner product on Ψ such that $\langle \cdot, \cdot \rangle = \| \cdot \|^2$, $\langle \psi_i, \psi_j \rangle = 0$ if $i \neq j$, and $\langle \psi_i, \psi_j \rangle = 1$ if $i = j$. The optimal basis that solves the optimization problem (3.59) can be obtained through the Singular Value Decomposition (SVD) of the Snapshot matrix. Specifically, the SVD allows us to rewrite the Snapshot matrix as

$$S = V \Sigma W^T,$$

where $\Sigma \in \mathbb{R}^{n\times n_t}$, $V \in \mathbb{R}^{n\times n}$, and $W \in \mathbb{R}^{n_t\times n_t}$. The columns of V are called **POD modes** and provide the optimal basis functions $\begin{bmatrix}\psi_1, \cdots, \psi_n\end{bmatrix}$, while the matrix Σ contains a non-null diagonal sub-matrix of dimension $n \times n$, in which the singular values (σ_i) are stored in decreasing order, namely $\sigma_1 > \sigma_2 > \cdots > \sigma_n > 0$. Finally, the truncation of model dynamics is computed by retaining the first r dominant modes $V_r = \begin{bmatrix}\psi_1, \cdots, \psi_r\end{bmatrix}$ of the optimal basis functions, in order to preserve the main features of the system. A common approach to select the truncation order r is by defining the **truncation degree** Θ_r, calculated as

$$\Theta_r = \frac{\sum_{i=1}^{r}\sigma_i^2}{\sum_{i=1}^{n}\sigma_i^2}. \tag{3.60}$$

Note that Θ_r needs to be close to 1 to accurately approximate the solution of the model. Finally, the Galerkin projection of the system (3.58) onto the new subspace V_r is used to reduce the dimension of the state-space model. The ROM is written as:

$$\begin{cases} \dot{\tilde{x}}(t) & = V_r^T A V_r \tilde{x}(t) + f(V_r \tilde{x}(t)) \\ \tilde{x}(t_0) & = V_r^T x_0, \end{cases} \tag{3.61}$$

where $\tilde{x} \in \mathbb{R}^r$ is the state vector of the ROM. It worth mentioning that an approximation ($\bar{x}(t) \in \mathbb{R}^n$) of the original state vector $x(t)$ is reconstructed as $x(t) \approx \bar{x}(t) = V_r^T \tilde{x}(t)$.

3.1.4 Thermal models

Thermal models offer valuable insights into the thermal processes occurring within lithium-ion batteries, such as heat generation, accumulation, and dissipation [47]. For a single battery cell, the heat distribution is governed by the heat conduction PDE, which describes how temperature varies over time and space within the cell. The specific form of the PDE depends on the geometry of the battery cell:

- *Cylindrical Cells [89]:* In spherical coordinates (r, θ), the governing PDE is expressed as:

  $$\rho C_p \frac{\partial T}{\partial t} = \frac{1}{r}\frac{\partial}{\partial r}\left(K_r r \frac{\partial T}{\partial r}\right) + \frac{1}{r^2}\frac{\partial}{\partial \phi}\left(K_\phi \frac{\partial T}{\partial \phi}\right) + \dot{Q} \tag{3.65}$$

  where K_r and K_ϕ are the thermal conductivity in r- and ϕ-direction, respectively, ρ is the density, C_p is the cell heat capacity, and $\dot{Q}$ is heat generated. At the boundary, both convection and radiation are considered:

  $$K_r \frac{\partial T}{\partial r}\bigg|_{r=R_{cell}} = (h_{convection} + h_{rad})\,(T_s - T_{amb})$$

  where R_{cell} is the cell radius, and h_{conv} and $h_{rad} = \epsilon\sigma(T_s^2 + T_{amb}^2)(T_s + T_{amb})$ are the convective and radiative heat transfer coefficients, respectively.

- *Pouch/Prismatic Cells [90]:*

  $$\rho C_p \frac{\partial T}{\partial t} = \frac{\partial}{\partial x}\left(K_x \frac{\partial T}{\partial x}\right) + \frac{\partial}{\partial y}\left(K_y \frac{\partial T}{\partial y}\right) + \frac{\partial}{\partial z}\left(K_z \frac{\partial T}{\partial z}\right) + \dot{Q} \tag{3.66}$$

  Heat exchange at the battery boundaries includes conduction, convection, and radiation [91].

It is important to note that the formulation for heat generation within the cell ($\dot{Q}$) was first introduced in [92]. $\dot{Q}$ depends on several factors, particularly electrochemical reactions,

(a) Two-state lumped thermal model for cylindrical cells [86]

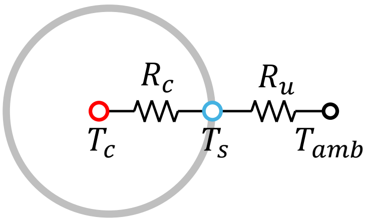
R_c
R_u
T_c
T_s
T_{amb}

$$\begin{aligned} C_c \frac{dT_c}{dt} &= \frac{T_s - T_c}{R_c} + \dot{Q} \\ C_s \frac{dT_s}{dt} &= \frac{T_{amb} - T_s}{R_u} - \frac{T_s - T_c}{R_c} \end{aligned} \tag{3.62}$$

(b) Four-state lumped thermal model for prismatic/pouch cells [87]

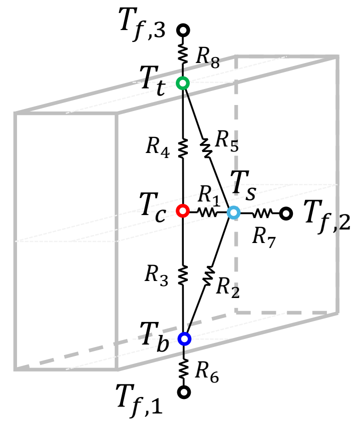
$T_{f,3}$
R_8
T_t
R_4
R_5
T_s
T_c
R_1
$T_{f,2}$
R_7
R_3
R_2
T_b
R_6
$T_{f,1}$

$$\begin{aligned} C_t \frac{dT_t}{dt} &= \frac{T_c - T_t}{R_4} + \frac{T_s - T_t}{R_5} + \frac{T_{f,3} - T_t}{R_8} \\ C_c \frac{dT_c}{dt} &= \frac{T_b - T_c}{R_3} + \frac{T_t - T_c}{R_4} + \frac{T_s - T_c}{R_1} + \dot{Q} \\ C_s \frac{dT_s}{dt} &= \frac{T_b - T_s}{R_2} + \frac{T_c - T_s}{R_1} + \frac{T_t - T_s}{R_5} + \frac{T_{f,2} - T_s}{R_7} \\ C_b \frac{dT_b}{dt} &= \frac{T_{f,1} - T_b}{R_6} + \frac{T_c - T_b}{R_3} + \frac{T_s - T_b}{R_2} \end{aligned} \tag{3.63}$$

(c) Five-state lumped thermal model for prismatic/pouch cells [88]

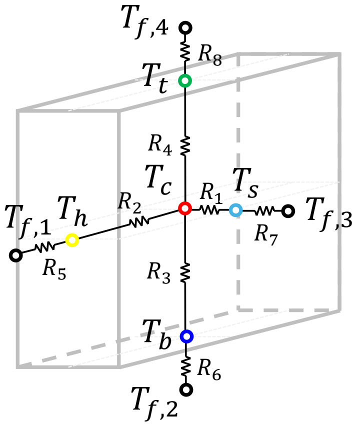
$T_{f,4}$
R_8
T_t
R_4
T_c
T_s
R_2
R_1
$T_{f,1}$
T_h
$T_{f,3}$
R_7
R_5
R_3
T_b
R_6
$T_{f,2}$

$$\begin{aligned} C_t \frac{dT_t}{dt} &= \frac{T_c - T_t}{R_4} + \frac{T_{f,4} - T_t}{R_8} \\ C_c \frac{dT_c}{dt} &= \frac{T_s - T_c}{R_1} + \frac{T_h - T_c}{R_2} + \frac{T_b - T_c}{R_3} + \frac{T_t - T_c}{R_4} + \dot{Q} \\ C_s \frac{dT_s}{dt} &= \frac{T_c - T_s}{R_1} + \frac{T_{f,3} - T_s}{R_7} \\ C_b \frac{dT_b}{dt} &= \frac{T_{f,2} - T_b}{R_6} + \frac{T_c - T_b}{R_3} \\ C_h \frac{dT_h}{dt} &= \frac{T_{f,1} - T_h}{R_5} + \frac{T_c - T_h}{R_2} \end{aligned} \tag{3.64}$$

Table 3.4: Examples of lumped thermal models for cylindrial and prismatic/pouch cells.

phase changes, mixing effects, and Joule heating within the cell. However, calculating $\dot{Q}$ can be complex and often requires calibration of numerous microscopic parameters. Therefore, a simplified equation is typically used, which neglects the enthalpy of mixing and phase change:

$$\dot{Q} = \underbrace{I_{cell}(V_{OCV} - V_{cell})}_{\dot{Q}_{irr}} + \underbrace{I_{cell}T\frac{\partial V_{OCV}}{\partial T}}_{\dot{Q}_{rev}} \tag{3.67}$$

where $\dot{Q}_{irr}$ represents the irreversible heat generation rate, which always leads to heat production and an increase in cell temperature. Whiel, the second term ($\dot{Q}_{rev}$) represents reversible heat generation and can be either positive or negative for the same reaction direction, depending on the sign of the entropy change ($\Delta S = F\partial V_{OCV}/\partial T$) in the electrochemical reactions. It is worth noting that $\partial V_{OCV}/\partial T$ depends on the electrode materials. More details on the experimental procedure and examples for deriving the electrode entropic contribution can be found in [93, 94].

It is important to note that the thermal models introduced so far are based on PDEs. These models are typically solved using numerical methods such as the FVM or the Finite Element Method (FEM), which involve complex three-dimensional discretization meshes. Due to the computational complexity of these models, they are often implemented using Computational Fluid Dynamics (CFD) software, such as COMSOL Multiphysics. This approach allows for accurate visualization of the thermal distribution within the battery cell casing.

However, such detailed and complex model formulations are computationally intensive and are not suitable for real-time applications, such as online temperature estimation of battery cells. The high computational burden of these models makes them impractical for use in dynamic scenarios where quick responses are needed.

To address this limitation, simplified thermal models have been developed. One of the most relevant reduced-order models in the context of battery thermal management is the lumped thermal model. In the lumped thermal model approach, the battery cell is discretized into several nodes, with each node representing an isothermal volume. Heat exchange between these nodes is modeled through thermal resistances, while the heat absorbed or released by each node is represented by its thermal capacitance. The energy balance for each node is governed by a set of ODEs. Table 3.4 presents three examples of lumped thermal models for cylindrical and prismatic/pouch cells. For instance, in the two-state thermal model for cylindrical cells, nodes are placed at the core and on the surface of the cell. In this model, the two key states are the core temperature (T_c) and the surface temperature (T_s). T_c is assumed to be uniformly distributed within the cell core, while T_s is assumed to be uniform across the cell surface. The dynamic behavior of the core and surface temperatures are governed by the equations (3.62). R_c represents the conductive thermal resistance, which models the heat transfer between the cell core and surface. While, R_u represents the convective thermal resistance, which accounts for the heat exchanged between the cell surface and the ambient environment. Despite the simplification of the cell thermal dynamics, this modeling framework offers the significant advantage of flexibility. In particular, for large-format pouch and prismatic cells, as illustrated in examples (b) and (c) in Table 3.4, the lumped nodes can be strategically positioned both inside and on the surface of the cell. By carefully selecting these node locations, the model can effectively capture key aspects of the thermal distribution, ensuring that the simplified model still provides a reliable representation of the cell thermal behavior.

Compared to the more detailed PDE-based thermal models, the lumped thermal model loses some information regarding the spatial distribution of temperature within the cell. However, this simplification significantly reduces computational complexity, making the model easier and faster to simulate. Despite the loss of detailed thermal distribution information, careful selection of node locations can still provide valuable insights into the thermal behavior of the cell.

3.1.4.1 Thermal-dependent parameters

To ensure the robustness of the model, it is crucial to update the transport and kinetic parameters of both the solid particles and the electrolyte based on the cell temperature. Specifically, the Arrhenius equation is commonly employed to update the solid-phase diffusion coefficient ($D_{s,j}$) and the intercalation rate constant (k_j) in the solid phase. The Arrhenius equation is given by:

$$\Phi(T_c) = \Phi^{ref} \exp\left(-\frac{E_{a,\Phi}}{R}\left(\frac{1}{T_c} - \frac{1}{T_{ref}}\right)\right), \quad \text{width: } \Phi = D_{s,j}, k_j \tag{3.68}$$

where $D_{s,j}^{ref}$ and k_j^{ref} are their values at a reference temperature T_{ref}, $E_{a,D_{s,j}}$ and E_{a,k_j} are the activation energies for $D_{s,j}$ and k_j. Conversely, the electrolyte diffusion coefficient ($D_{e,j}$) and conductivity ($k_{e,j}$) are often expressed as functions of both the core temperature and the average electrolyte concentration. These parameters are typically described by empirical relationships, such as those provided in [95, 96].

3.1.5 Aging models

Aging modeling aims to mathematically represent the mechanisms that characterize the degradation of a battery cell over time. According to the literature, there are three primary approaches: empirical, data-driven, and physics-based models. Empirical modeling uses formulas derived from observed data to describe capacity fade and/or resistance increase in a battery cell. These models are developed to address both calendar aging [97, 98, 99] and cycling aging [100, 99, 101, 102], incorporating various stress factors such as C-rate, depth of discharge (DOD), SOC, and temperature. Different empirical models focus on specific conditions and stress factors to estimate degradation. In contrast, data-driven modeling has gained popularity for its flexibility, which is essential for handling the complexity and variability of aging mechanisms. Data-driven approaches predict cell degradation through empirical relationships derived from observed data. These methods use statistical or machine learning techniques to establish correlations between various features and degradation outcomes, as reviewed in [103]. Finally, physics-based models simulate the

electrochemical phenomena responsible for battery degradation. Although these models are more complex to identify and calibrate, they offer a deeper understanding of the underlying mechanisms that influence battery life and performance.
In this chapter, we review four key physics-based modeling approaches for battery aging in accordance with [49].

3.1.5.1 SEI layer growth

This section provides a brief review of the SEI growth model introduced by [55], which represents a simplified version of the model presented by [104]. Particularly, the growth of the SEI layer is identified as the primary source of cell capacity and power degradation. In this model, the SEI layer is assumed to consist of a single layer (i.e. the outer) that grows uniformly around the negative electrode particle due to solvent diffusion within the SEI layer and reduction processes occurring at the particle surface. Specifically, the porous structure of the SEI facilitates the permeation of solvent molecules from the electrolyte to the active particle surface through diffusion and convection mechanisms, as described by the PDE:

$$\frac{\partial c_{\text{solv}}}{\partial t} = D_{\text{solv}} \frac{\partial^2 c_{\text{solv}}}{\partial r^2} - \frac{dL_{\text{SEI}}}{dt} \frac{\partial c_{\text{solv}}}{\partial r} \tag{3.69}$$

where c_{solv} and D_{solv} denote the solvent concentration and diffusivity within the SEI layer, respectively. The solvent subsequently reacts with electrons and lithium ions at the negative electrode surface. The current density of the side reaction is described by:

$$i_s = -2Fk_f (c_{s,n}^{\text{surf}})^2 c_{\text{solv},0} \exp\left[\frac{-\beta F}{R_g T_c}(\Phi_{s,n} - R_{SEI} I_{cell} - U_s)\right] \tag{3.70}$$

where $c_{\text{solv},0}$ is the solvent concentration at the anode surface, and $\Phi_{s,n}$ and U_s represent the electrode potential and the equilibrium potential of the solvent reduction, respectively. Note that, eq. (3.70) is influenced by temperature, applied current, and cell SOC through the term $c_{s,n}^{\text{surf}}$. The side reaction results in SEI growth, which reduces the availability of lithium ions for cycling and is the main cause of cell capacity degradation. This is expressed as:

$$\frac{dL_{\text{SEI}}}{dt} = -\frac{i_s M_{\text{SEI}}}{2F\rho_{\text{SEI}}} \tag{3.71}$$

$$\frac{dQ}{dt} = i_s A L_n a_{s,n} \tag{3.72}$$

where M_{SEI} and ρ_{SEI} are the SEI molar mass and denisity, respectively. The growth of the SEI layer increases the SEI film resistance (R_{SEI}) and affects the variation in anode porosity, as given by:

$$R_{\text{SEI}} = \frac{L_{\text{SEI}}}{a_{s,n} A L_n \kappa_{\text{SEI}}} \tag{3.73}$$

$$\epsilon_{e,n} = 1 - \epsilon_{f,n} - \epsilon_{s,n} \left(1 + \frac{3L_{\text{SEI}}}{R_{s,n}}\right) \tag{3.74}$$

It is important to note that the solvent diffusion coefficient (D_{solv}) is temperature-dependent and described by the Arrhenius equation:

$$D_{\mathrm{solv}} = D_{\mathrm{solv}}^{\mathrm{ref}} \exp\left[\left(\frac{1}{T_{\mathrm{ref}}} - \frac{1}{T_c}\right)\frac{E_{a,D_{\mathrm{solv}}}}{R}\right] \tag{3.75}$$

where $D_{\mathrm{solv}}^{\mathrm{ref}}$ is the reference solvent diffusion coefficient, and it is assumed to depend on I_{cell}, as illustrated in Figure 4 of [55].

3.1.5.2 Lithium plating

The first electrochemical model of lithium (Li) plating and stripping on graphite electrodes was introduced by [105]. This model was later refined and simplified in subsequent works, such as [106] and [107]. However, the process of Li plating is intrinsically connected to lithium stripping and the growth of the SEI. Given the interdependence of these mechanisms, this section provides an overview of a more comprehensive model where the aging mechanisms of Li plating, stripping, and SEI growth are explicitly coupled, as provide in [49].

The concentrations of plated lithium (c_{Li}) and dead lithium (c_{dl}) evolve according to the following ODEs:

$$\begin{aligned} \frac{\partial c_{Li}}{\partial t} &= -a_{s,n} j_{Li} - \frac{\partial c_{dl}}{\partial t}, \\ \frac{\partial c_{dl}}{\partial t} &= \gamma c_{Li}, \end{aligned} \tag{3.76}$$

where γ represents the decay rate of plated lithium into dead lithium, a process that is dependent on the SEI thickness, as defined by:

$$\gamma(L_{SEI}) = \gamma_0 \left(\frac{L_{SEI,0}}{L_{SEI}}\right), \tag{3.77}$$

where $L_{SEI,0}$ is the initial SEI thickness at time $t = 0$, and γ_0 is a fitting parameter that characterizes the rate of transformation of plated lithium into dead lithium under initial SEI conditions. The rate of lithium deposition onto the particle, j_{Li}, is governed by the Butler-Volmer equation:

$$j_{Li} = k_{Li}\left[c_{Li}\exp\left(\frac{F\alpha_{a,Li}\eta_{Li}}{RT}\right) - c_e \exp\left(\frac{F\alpha_{c,Li}\eta_{Li}}{RT}\right)\right], \tag{3.78}$$

where k_{Li} is the rate constant for the lithium deposition reaction, and the term η_{Li} is the overpotential for lithium deposition, defined as:

$$\eta_{Li} = \phi_{s,n} - \phi_e - \eta_{SEI}, \tag{3.79}$$

where $\phi_{s,n}$ and ϕ_e are the solid and electrolyte potentials, respectively, and η_{SEI} represents the additional overpotential due to the SEI layer. Finally, according to [107], the effect of plating/stripping on the negative electrode porosity is given by:

$$\frac{d\epsilon_{e,n}}{dt} = a_{s,n}\frac{M_{Li}}{\rho_{Li}}j_{Li} \tag{3.80}$$

where M_{Li} and ρ_{Li} are the molar mass and denisity of lithium metal.

3.1.5.3 Particle cracking

According to [108], the radial stress (σ_r) and tangetial stress (σ_t) for a speherical electrode are expressed as:

$$\begin{aligned} \sigma_r(r) &= \frac{2\Omega E}{3(1-\nu)}\Big[\frac{1}{R_{s,n}^3}\int_0^{R_{s,n}} c_{s,j}(r)r^2dr - \frac{1}{r^3}\int_0^r c_{s,j}(\zeta)\zeta^2 d\zeta\Big] \\ \sigma_t(t) &= \frac{\Omega E}{3(1-\nu)}\Big[\frac{2}{R_{s,n}^3}\int_0^{R_{s,n}} c_{s,j}(r)r^2dr - \frac{1}{r^3}\int_0^r c_{s,j}(\zeta)\zeta^2 d\zeta - c\Big] \end{aligned} \tag{3.81}$$

where Ω is the partial molar volume, E is the Young modulus, ν is the Poisson ration, and $c_{s,j}^{bulk}|_r$ is the bulk concentration within the electode particle between 0 and r: Then, according to [109], the particle crack length (l_{cr}) growing with each charge-discharge cycle N can be modeled as:

$$\frac{dl_{cr}}{dN} = k_{cr}(\sigma_t b_{cr}\sqrt{\pi l_{cr}})^{m_{cr}} \tag{3.82}$$

where b_{cr} is the stress intensity factor correction, k_{cr} and m_{cr} are constants that are determined from experimental data. Finally, the instantaneous rate of change of the crack area (a_{cr}) can be approximated:

$$\frac{da_{cr}}{dt} = a_{s,j}\rho_{cr}w_{cr}\frac{dl_{cr}}{dN} \tag{3.83}$$

Note that, given the new crack area at each cycles, the loss of lithium-ions are due to growth of SEI thickness in the cracked area, as widley described in [109].

3.1.5.4 Loss of active material

According to [48], similar physical phenomena that cause particle cracks also lead to loss of electrical contact and a reduction of the active material. In particular, combining the radial and tangential stresses defined in (3.81), the hydrostatic stress (σ_h) is defined as:

$$\sigma_h = \frac{2\sigma_t(r) + \sigma_r(r)}{3} \tag{3.84}$$

Finally, the LAM can be approximated as the reduction of the active material volume fraction:

$$\frac{d\epsilon_{s,j}}{dt} = \beta\left(\frac{\sigma_h^{\max} - \sigma_h^{\min}}{\sigma_{\text{yield}}}\right)^{\frac{1}{m_2}} \tag{3.85}$$

3.2 Module-level models

In the previous section, we reviewed the electrochemical, thermal, and aging dynamics of single lithium-ion cells. However, when multiple cells are connected to form a battery module or pack, the influence of electrical and thermal cell-to-cell interconnections must be considered. Electrical interconnections refer to the physical busbars or wires that connect cells in series and/or parallel configurations. Thermal interconnections, on the other hand, pertain to the heat exchanged between cells based on their positions within the module. It is important to distinguish between electrical and thermal interconnections when developing models at the module level, as they are critical for understanding the impact of cell-to-cell variations on the performance and safety of the battery pack.

3.2.1 Electrical submodel

In this section, we review the formulation of the electrical model at the module level for both series-connected and parallel-connected configurations, consisting of N_s and N_p cells, respectively. Additionally, the cell-level dynamics previously described are updated to account for the connection topology. For simplicity, the cell-level dynamics are modeled using a single RC ECM. However, the same conpect is also applicable to electrochemical models, as discussed in the subsequent chapters.

Series-connected module-level model
The electrical dynamics of a series-connected module are straightforward to derive, as the same current (I_{tot}) flows through all interconnected cells. Considering an ideal module with null interconnected resistance among the cells, the overall voltage across the module terminals is given by:

$$V_{mod} = \sum_{i=1}^{N_s} V_{cell}^{[i]} \tag{3.86}$$

where $V_{cell}^{[i]}$ denotes the voltage across the i-th cell in the module. The formulation of $V_{cell}^{[i]}$ can be adjusted based on the cell-level model used. For example, Equation (3.1) and (3.15) should be employed for an ECM and an ESPM model, respectively.

Example 3.2.1: *ECM-based Series-connected module-level model*

Figure 3.8(a) illustrates a schematic representation of the series-connected battery module, emphasizing the interconnection electrical resistance (R_{int}). In the following, the superscript $[k]$ is used to denote a quantity associated with the k-th cell in the module, as shown in Fig. 3.8(a), with $SOC^{[1]}$ and $SOC^{[N_s]}$ denoting the SOC of the closest and farthest cell from the load terminals, respectively. The module's

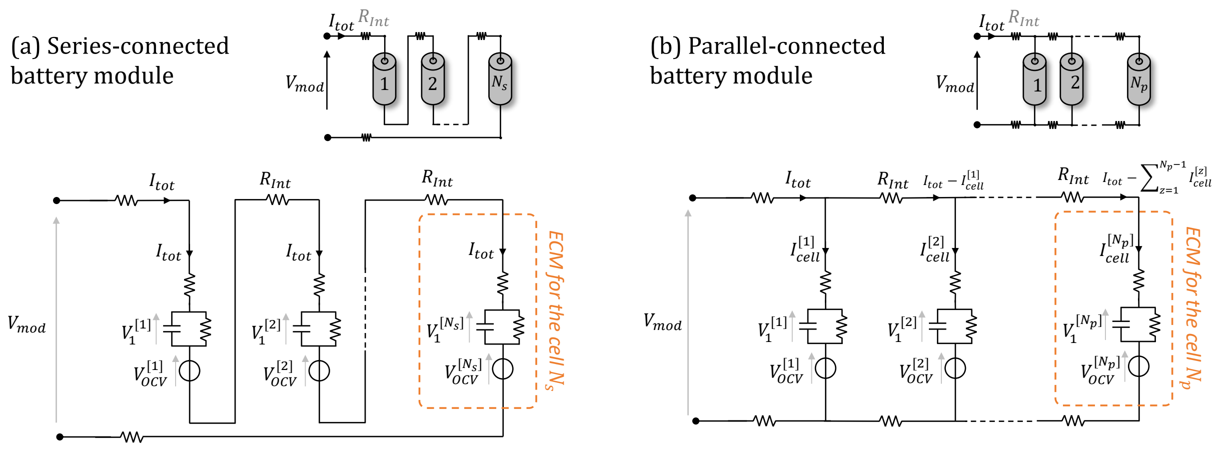

(a) Series-connected battery module
I_{tot}
R_{Int}
V_{mod}
1
2
N_s
R_{Int}
V_{mod}
$V_1^{[1]}$
$V_{OCV}^{[1]}$
$V_1^{[2]}$
$V_{OCV}^{[2]}$
$V_1^{[N_s]}$
$V_{OCV}^{[N_s]}$
ECM for the cell N_s
(b) Parallel-connected battery module
I_{tot}
R_{Int}
V_{mod}
1
2
N_p
$I_{tot} - I_{cell}^{[1]}$
$I_{tot} - \sum_{z=1}^{N_p-1} I_{cell}^{[z]}$
$I_{cell}^{[1]}$
$I_{cell}^{[2]}$
$I_{cell}^{[N_p]}$
$V_1^{[1]}$
$V_{OCV}^{[1]}$
$V_1^{[2]}$
$V_{OCV}^{[2]}$
$V_1^{[N_p]}$
$V_{OCV}^{[N_p]}$
ECM for the cell N_p

Figure 3.8: Schematic representation of the module-level ECM-based model for (a) series-connected and (b) parallel-connected scenarios.

dynamics, derived by integrating N_s ECMs (Section 3.1.1), is expressed as:

$$\dot{x}_{mod} = A_{mod}^{series} x_{mod} + B_{mod}^{series} I_{tot} \tag{3.87}$$

where $x_{mod} = [V_1^{[1]}, SOC^{[1]}, \cdots, V_1^{[N_s]}, SOC^{[N_s]}] \in \mathbb{R}^{2N_s \times 1}$ represents the module state vector, which collects the states of each individual ECM, while, I_{tot} is the overall module input current. The matrices $A_{mod}^{series} \in \mathbb{R}^{2N_s \times 2N_s}$ and $B_{mod}^{series} \in \mathbb{R}^{2N_s \times 1}$ are written as:

$$A_{mod}^{series} = \begin{bmatrix} A^{[1]} & & 0 \\ & \ddots & \\ 0 & & A^{[N_s]} \end{bmatrix} \qquad B_{mod}^{series} = \begin{bmatrix} B^{[1]} \\ \vdots \\ B^{[N_s]} \end{bmatrix}$$

where $A^{[j]} \in \mathbb{R}^{2\times 2}$ and $B^{[j]} \in \mathbb{R}^{2\times 1}$ are the cell-level ECM matrices of the j-th cell, defined as in (3.1).

Parallel-connected module-level model

In a parallel-connected module, the voltage across the module terminals is equal to the voltage across each cell, while the total input current is distributed among the N_p branches. The currents flowing through each cell are determined by solving a system of N_p Kirchhoff's circuit laws. For an ideal module (i.e., $R_{int} = 0$), these laws are expressed as:

$$\begin{cases} V_{cell}^{[k+1]} & = V_{cell}^{[k]} \qquad \text{with } k = 1, \cdots, (N_p - 1) \\ I_{tot} & = \sum_{k=1}^{N_p} I_{cell}^{[k]} \end{cases} \tag{3.88}$$

where $I_{cell}^{[i]}$ denotes the current flowing through the i-th cell in the module. Finally, $V_{mod} = V_{cell}^{[i]}$ is equal to the voltage across the N_p cell in parallel. It is important to note that if the interconnection resistance is not null, as depicted in the scheme of Figure

3.8(b), the Kirchhoff's circuit laws are reformulated as:

$$\begin{cases} V_{cell}^{[k+1]} = V_{cell}^{[k]} - 2R_{int}(\sum_{z=k+1}^{N_p} I_{cell}^{[z]}) \\ I_{tot} = \sum_{k=1}^{N_p} I_{cell}^{[k]} \end{cases} \tag{3.89}$$

where $k \in \{1, \cdots, N_p - 1\}$, and the model output $V_{mod} = V_{cell}^{[1]} + 2R_{int}I_{tot}$.

Example 3.2.2: *ECM-based Parallel-connected module-level model*

Figure 3.8(b) illustrates a schematic representation of the parallel-connected battery module, emphasizing the interconnection electrical resistance (R_{int}). The module's dynamics, derived by integrating N_p ECMs (Section 3.1.1), is expressed as:

$$\dot{x}_{mod} = A_{mod}^{parallel} x_{mod} + B_{mod}^{parallel} I_{mod} \tag{3.90}$$

where $x_{mod} = [V_1^{[1]}, SOC^{[1]}, \cdots, V_1^{[N_p]}, SOC^{[N_p]}] \in \mathbb{R}^{2N_p \times 1}$ represents the module state vector, which collects the states of each individual ECM, while, $I_{mod} = [I_{cell}^{[1]}, \cdots, I_{cell}^{[N_p]}] \in \mathbb{R}^{N_p \times 1}$ contains the cell currents flowing through each parallel branch of the module. The matrices $A_{mod}^{parallel} \in \mathbb{R}^{2N_p \times 2N_p}$ and $B_{mod}^{parallel} \in \mathbb{R}^{2N_p \times 2N_p}$ are written as:

$$A_{mod}^{parallel} = \begin{bmatrix} A^{[1]} & & 0 \\ & \ddots & \\ 0 & & A^{[N_p]} \end{bmatrix} \qquad B_{mod}^{parallel} = \begin{bmatrix} B^{[1]} & & 0 \\ & \ddots & \\ 0 & & B^{[N_s]} \end{bmatrix}$$

where $A^{[j]} \in \mathbb{R}^{2 \times 2}$ and $B^{[j]} \in \mathbb{R}^{2 \times 1}$ are the cell-level ECM matrices of the j-th cell, defined as in (3.1). It is important to note that $I_{cell}^{[k]}$, with $k \in [1, \cdots, N_p]$, is obtained by solving N_p Kirchhoff's circuit laws given in (5.26). Finally, the model output $V_{mod} = V_{cell}^{[1]} + 2R_{int}I_{tot}$ is the voltage across the module terminals. The resulting dynamics at the module level are represented by a system of DAEs (eqs. (3.90) and (3.89)). In [110], the authors proposed a method to integrate the N_p algebraic equations describing the branch currents, with null R_{int}, into the model dynamics, effectively converting the DAEs into a ODEs. Note that, more details are provided in Chapter 9.

3.2.2 Thermal submodel

In this section, the module-level thermal model that will be used in Chapter 5 is introduced. The reader can refer to [47] for a more comprehensive review of module-level thermal models. In particular, a one-state thermal model is considered for cylindrical cells. In Figure 5.6, a schematic representation of the one-dimensional module is depicted, emphasizing the thermal interconnection terms. The single cell model, described in Section 3.1.4, is modified to incorporate the CtC thermal interconnection. The thermal dynamics of the k-th cell in the module ($T_{cell}^{[k]}$ with $k = 1, 2, \cdots, N_p$) are formulated to account for the influence of the upstream and downstream cells, as given by:

$$C_s \frac{dT_{cell}^{[k]}}{dt} = I_{cell}^{[k]}(V_{OCP}^s[k] - V_{cell}^{[k]}) + T_{cell}^{[k]} I_{cell}^{[k]} \frac{dV_{OCP}}{dT_{cell}} + \frac{T_{amb} - T_{cell}^{[k]}}{R_u} - \frac{T_{cell}^{[k]} - T_{cell}^{[k+1]}}{R_m^{[k,k+1]}} - \frac{T_{cell}^{[k]} - T_{cell}^{[k-1]}}{R_m^{[k,k-1]}} \tag{3.91}$$

where $T_{cell}^{[k-1]}$ and $T_{cell}^{[k+1]}$ denote the cell temperature of the preceding cell $(k-1)$ and the following cell $(k+1)$ in the module, respectively. The equation considers the convective thermal resistance between the surface and the ambient (R_u), and the thermal resistances between adjacent cell surfaces ($R_m^{[k,k+1]}$ and $R_m^{[k,k-1]}$). The thermal resistance R_m models heat transfer via conduction through the interconnection tabs (R_m^{tabs}) and the heat transfer via conduction through the air (R_m^{air}), while neglecting the radiative heat transfer. The overall formulation of R_m is derived considering the two thermal resistances in parallel:

$$R_m = (\frac{1}{R_m^{air}} + \frac{1}{R_m^{tabs}})^{-1} \tag{3.92}$$

where R_m^{tabs} and R_m^{air} are calculated as:

$$R_m^{air} = \frac{1}{S_{cell} k_{air}} \tag{3.93}$$

$$R_m^{tabs} = \frac{w}{A_{cell} k_{tabs}} \tag{3.94}$$

where k_{tab} and k_{air} are the tab thermal and air conductivity, respectively, A_{cell} is the cell cross-sectional area, and $w = d + Sp$ is the tab length obtained as the summation of the cell diameter (d) and cell spacing (Sp). Further, according to [111], $S = \frac{2\pi h}{\cosh^{-1}\left(\frac{4w^2 - 2d^2}{2d^2}\right)}$ where h is the cell height. Both R_m^{tabs} and R_m^{air} are inversely proportional to the spacing between the cells; thus, increasing Sp decreases the CtC heat transfer. It is worth noting that R_u is considered constant in this work, as an active cooling system is not taken into account. However, when considering an air-cooled module, R_u is calculated as a function of the air coolant velocity (v_f) [112, 46, 113].

3.3 Conclusion

In this chapter, we have explored the diverse range of battery modeling approaches, spanning from the simple ECMs to the more accurate EMs. Additionally, various flavors of EMs can be developed by applying different model order reduction techniques. Both ECMs and EMs can be further enhanced by incorporating thermal dynamics and aging mechanisms, allowing for more comprehensive representations of battery behavior.

This extensive variety of modeling options can lead to confusion when selecting the appropriate model for a specific application. It is important to remember, as George E.P. Box famously stated, "All models are wrong, but some are useful." A model is a mathe-

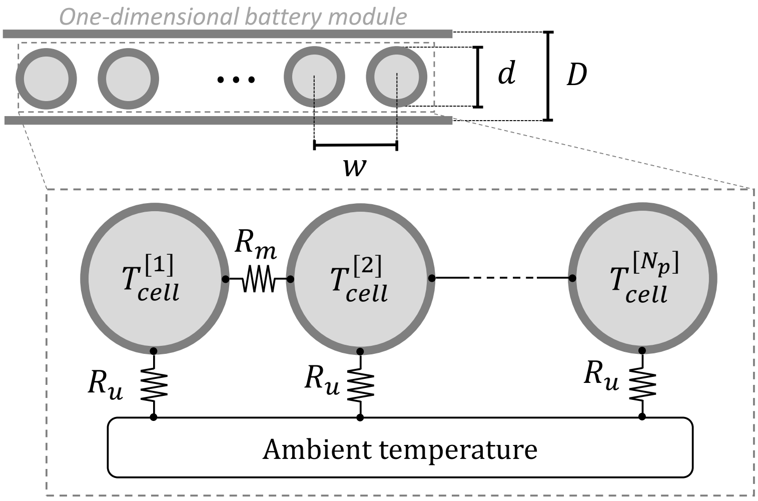

Figure 3.9: Schematic representation of the module-level ECM-based model for (a) series-connected and (b) parallel-connected scenarios.

matical representation of a system that, being an approximation, inevitably comes with limitations and inaccuracies, thus its development should depends on:

1. **Phenomena to be Described:** The specific physical and chemical processes that need to be captured by the model.
2. **Desired Accuracy:** The level of precision required for the model to be effective in its intended application.
3. **Effort Required for Solution and Calibration:** The computational resources and time needed to solve the model equations and calibrate the model parameters against experimental data.

Understanding these factors is paramount to finding the suitable trade-off between accuracy and complexity. A highly detailed model may offer greater accuracy but at the cost of increased computational demand and complexity, which may not be practical for real-time applications or large-scale simulations. Conversely, simpler models may lack the necessary detail but provide sufficient accuracy with lower computational overhead.

Chapter 4

Battery testing

Contents

4.1 Battery cell batches **80**

4.2 Experimental activities **81**

4.2.1 ELISA campaign 81

4.2.2 SECL campaign 86

4.3 Conclusion **92**

The desciption of the experimental campaigns carried out at the Stanford Energy Lab is inspired by the work:

[8] Piombo, G., **Fasolato, S.**, Heymer, R., Hidalgo, M. F., Niri, M. F., Raimondo, D. M., Marco, J., and Onori, S. (2024). *Full factorial design of experiments dataset for parallel-connected lithium-ion cells imbalanced performance investigation.* Data in Brief, 53, 110227.

Introduction

Battery testing is a critical component in the development, optimization, and deployment of energy storage systems. As the demand for reliable and efficient energy solutions continues to grow, especially with the rise of electric vehicles, renewable energy integration, and portable electronics, understanding the performance and limitations of batteries is more crucial than ever. The primary reasons for conducting battery testing include assessing performance metrics such as capacity, energy density, and power output. These tests help in determining if a battery can meet the requirements of specific applications. Additionally, testing is essential for understanding the battery's lifespan and degradation patterns, ensuring that the battery remains reliable over time [114, 115]. Moreover, battery testing provides crutial data needed for several advanced applications. This data is used to calibrate and validate battery models [116, 117], which are the foundation for model-based and data-driven estimation and control algorithms [118]. Additionally, experimental campaigns are essential for accurately assessing battery health through diagnostic tests and predicting the battery remaining useful life [103, 119].

Chapter contribute

This chapter offers an overview of the laboratory experimental campaigns conducted to gather essential battery data, which forms the foundation of the research activities presented in this thesis. It includes detailed information on the specifications of the cell batches used, a comprehensive review of the laboratory equipment, and an outline of the data collection procedures. The experimental activities are primarily divided into three main campaigns:

1. ***ELISA Campaign:*** *Conducted from March 2024 to June 2024 at the Energy Laboratory for Interdisciplinary Storage Applications (ELISA) within the Department of Engineering and Architecture at the University of Trieste.*
2. ***SECL Campaign:*** *Conducted from October 2022 to March 2023 at the Stanford Energy Control Laboratory (SECL) in the Department of Energy Science and Engineering at Stanford University.*
3. ***LGES Campaign:*** *These experimental activities were carried out by the industrial partner of the project, LG Energy Solution, between March 2022 and September 2022.*

Additionally, this chapter significantly contributes by clarifying how experimental data are utilized in subsequent chapters, enhancing reader comprehension of their integration into the research activities.

Chapter structure

- **Section 4.1** summarizes the specifications of the tested cells and the data collected during each experimental campaign.
- **Section 4.2** details the laboratory facilities used and the data collection procedures for the experimental campaigns conducted at the SECL and ELISA labs.
- **Section 4.3** provides a summary of the chapter conclusions.

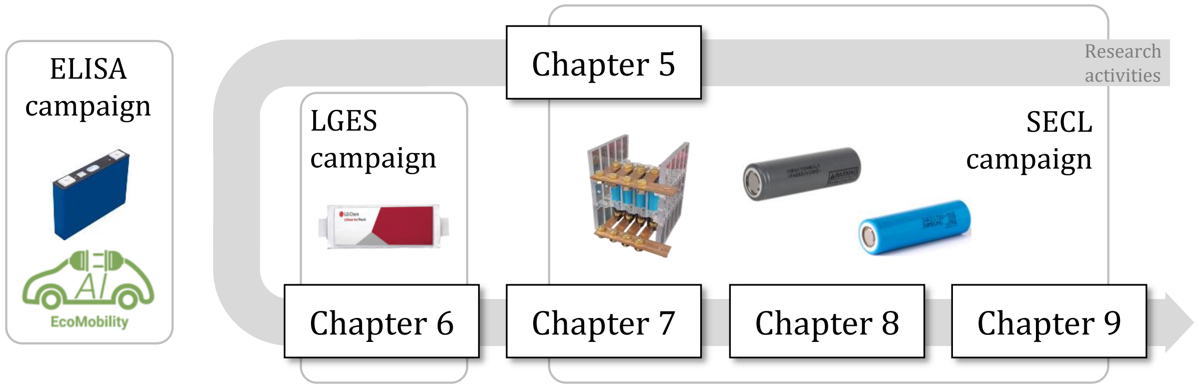

Figure 4.1: A visual flowchart illustrating the data usage in the following chapters

4.1 Battery cell batches

This section provides a detailed overview of the cell batches utilized in this research, specifically outlining the cell specifications and explaining how the collected data are employed in the subsequent chapters of this thesis, as schematically depctide in Figure 4.1. The experimental activities are primarily divided into three campaigns:

1. **ELISA Campaign:**
    - **Tested Cells:** CALB L1248N58, 58 Ah prismatic cells. Technical specifications are provided in Table 4.1.
    - **Number of Cells Tested:** A total of 11 cells were tested.
    - **Brief Data Description:** Single-cell characterization was performed using galvanostatic discharge, Hybrid Pulse Power Characterization (HPPC) tests, and driving cycles on all 11 cells at 10, 25, and 40 °C. Further details are provided in Section 4.2.1.
    - **Data Usage:** The experimental campaign was carried out for the Ecomobility European projects [120]. The collected data will be employed in future research activities and are not utilize in this thesis.
    - **Data Availability:** [121] https://data.mendeley.com/datasets/ycx459r5c3/1
2. **SECL Campaign:**
    - **Tested Cells:** LG INR21700-M50T and Samsung INR21700-50E, cylindrical cells with nominal capacities of 4.85 Ah and 4.90 Ah, respectively. Technical specifications are provided in Table 4.1.
    - **Number of Cells Tested:** A total of 39 cells were tested, including 19 new LG INR21700-M50T cells, 18 new Samsung INR21700-50E cells, and 2 pre-aged cells of the same chemistries.
    - **Brief Data Description:** Single-cell characterization was performed using galvanostatic discharge, HPPC tests, and MultiSine profiles on all 39 cells

at 23 °C. Further details are provided in Section 4.2.2.1. Additionally, 54 experiments were conducted on a 4-cells parallel-connected battery module, based on a full factorial design of experiments. More details can be found in Section 4.2.2.2.

- **Data Usage:** The collected data are used for identifying module-level ECM- and ESPM-based models, which are employed for the state estimation algorithm in Chapter 9 and for the model-based statistical analysis in Chapter 8, respectively. Furthermore, both module-level and cell-level experiments are used in Chapter 7, where the data-driven statistical analysis is performed to analyze the effects of cell-to-cell variation on module performance.
- **Data Availability:** [8] https://data.mendeley.com/datasets/zh58byr53c/1

3. **LGES Campaign:**

   - **Tested Cells:** Two LFP-graphite pouch cells with capacities of 49 Ah and 56 Ah are considered in this campaign. Technical specifications, provided by the industrial partner, are provided in Table 4.1.
   - **Number of Cells Tested:** A total of 2 cells were tested, one for each type.
   - **Brief Data Description:** Discharge tests at different C-rates and driving cycles were conducted at 25 °C.
   - **Data Usage:** The provided data are used in Chapter 6 for the identification and validation of reduced-order models for the CS-ESPM.
   - **Note:** The data were directly collected and provided by the industrial partner. Details on laboratory equipment and cell specifications are confidential. Information reported in this thesis is based on publicly available literature.
   - **Data Availability:** The collected data for the 49 Ah cell are available at: [28] https://data.mendeley.com/datasets/68rs3d99zc/2

4.2 Experimental activities

Section 4.2.1.1 describes the test protocols conducted during the ELISA lab campaign and provides a brief visualization of the results. Similarly, Section 4.2.2 outlines the procedures for both cell-level and module-level experiments carried out at the SECL.

4.2.1 ELISA campaign

This experimental campaign is part of experimental battery tests for the Ecomobility projects [120] and are available at [121].

Table 4.1: Technical specifications of the tested cell

Manufacturer	LG Chem	LG Chem	CALB
Model	-	-	L148N58
Type	Pouch	Pouch	Prismatic
Positive electrode	$LiFePO_4$	$LiFePO_4$	$Li(NiCoMn)O_2$
Negative electrode	Graphite	Graphite	Graphite
Size (W × L × H)	99.7×301.5× ×14.8mm	- -	148.2×26.6× ×105.9mm
Weight	850g	-	926g
Nominal capacity	49Ah	56Ah	58Ah
Nominal voltage	3.2V	-	3.6V
Charge cutoff voltage	3.6V	-	4.35V
Discharge cutoff voltage	2.5V	-	2.2-2.75V
Cutoff current	-	-	50mA
Reference	[28]	-	[122]

Manufacturer	LG Chem	Samsung
Model	INR21700-M50T	INR21700-50E
Type	Cylindrical	Cylindrical
Positive electrode	$Li(NiCoMn)O_2$	$Li(NiCoAl)O_2$
Negative electrode	Graphite and Silicon	Graphite and Silicon
Size (diameter × length)	21.44×70.80mm	21.25×70.80mm
Weight	69.25g	69.00g
Nominal capacity	4.85Ah	4.90Ah
Nominal voltage	3.63V	3.63V
Charge cutoff voltage	4.2V	4.2V
Discharge cutoff voltage	2.5V	2.5V
Cutoff current	50mA	50mA
Reference	[123]	[124]

Table 4.2: ELISA campaign: cell-level characterization procedure

	Step	**Action**	**Exit condition**
C/20 cycles	1	CC charge at 0.33 C-rate	4.2V reached
	2	CV charge	Supplied current below 50mA
	3	Rest	60 minutes limit reached
	4	CC discharge at 1/20 C-rate	2.5V reached
	5	Rest	30 minutes limit reached
	6	CC charge at 1/20 C-rate	4.2V reached
	7	CV charge	Supplied current below 50mA
HPPC tests	8	Rest	60 minutes limit reached
	9	HPPC	10s charge and 10s discharge pulses
	10	Repeat Steps 10-11	2.5V reached
	11	CC charge at 0.33 C-rate	4.2V reached
	12	CV charge	Supplied current below 50mA
	13	Rest	60 minutes limit reached
	14	HPPC	10s charge and 10s discharge pulses
	15	Repeat Steps 15-16	2.5V reached
Driving cycles	16	CC charge at 0.33 C-rate	4.2V reached
	17	CV charge	Supplied current below 50mA
	18	DV1	DV1 minutes limit reached or 2.5V reached
	19	Rest	60 minutes limit reached
	20	CC charge at 0.33 C-rate	4.2V reached
	21	CV charge	Supplied current below 50mA
	22	DV2	DV2 minutes limit reached or 2.5V reached
	23	Rest	60 minutes limit reached
	24	CC charge at 0.33 C-rate	4.2V reached
	25	CV charge	Supplied current below 50mA
	26	DV3	DV3 minutes limit reached or 2.5V reached
	27	Rest	60 minutes limit reached

4.2.1.1 Testing procedure

The cell characterization process for the 11 CALB L148N58 is divided into three main steps, as outlined in Table 4.2. It is important to note that these steps are repeated at three different ambient temperatures: 10, 25, and 40 °C. The steps are:

1. **C/20 Constant Current (CC) Discharge and Charge Cycles** (Steps 1-7 in Table 4.2): This procedure involves both discharging and charging the battery at a C/20 rate using a constant current. Initially, each cell undergoes a conditioning phase where it is charged using a constant current-constant voltage (CCCV) protocol at a rate of C/3. The charging continues until the voltage reaches 4.2 V during the CC phase, and the charging current decreases to 50 mA during the CV phase. During the C/20 CC discharge phase, the cell is discharged from a fully charged state (4.2 V, corresponding to 100% SOC) down to a cutoff voltage of 2.5 V, which is considered 0% SOC. The total capacity extracted during this discharge (Q_{dis}) is

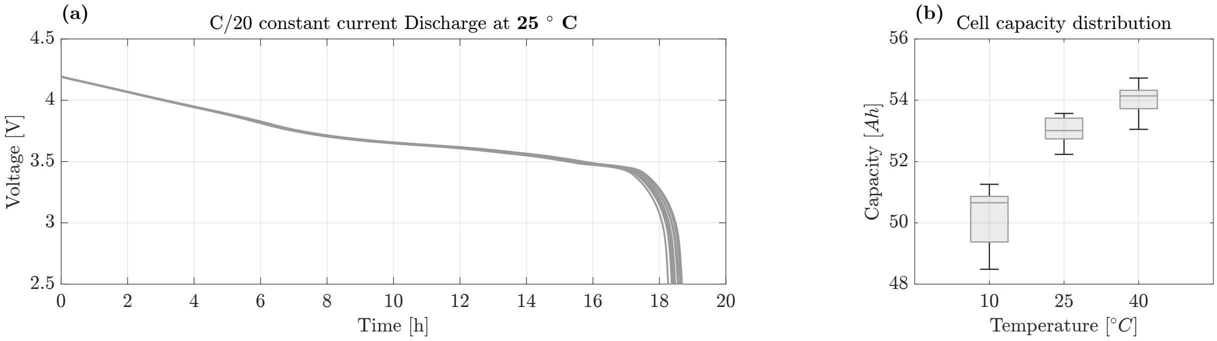

Figure 4.2: (a) Pseudo OCV curves of the fresh 11 cells under C/20 discharge test procedure (Steps 4 in Table 4.2). (b) Boxplot of cell capacities under different temperatures.

calculated using the formula [125]:

$$Q_{dis} = \frac{1}{3600}\int_{t_{in}}^{t_{fin}} I_{cell}\, dt = \frac{I_{cell}(t_{fin} - t_{in})}{3600} \tag{4.1}$$

where t_{in} and t_{fin} are the start and end times of the discharge period, and I_{cell} is the discharge current. It is important to note that the discharged capacity (Q_{dis}) varies with temperature. Figure 4.2(b) shows a box plot depicting the capacity distribution of the 11 tested cells at three different temperatures. The average discharged capacity increases with temperature, recording 50.23 Ah, 52.99 Ah, and 54.03 Ah at 10°C, 25°C, and 40°C, respectively. Additionally, the standard deviation of the capacity is 0.914 Ah, 0.471 Ah, and 0.474 Ah at 10°C, 25°C, and 40°C, respectively.

2. **Hybrid Pulse Power Characterization (HPPC) test at various C-rates** (Steps 8-15 in Table 4.2): The HPPC test was designed to assess the impact of the SOC on the internal properties of the cells. This test involves applying a series of discharge and charge current pulses at evenly spaced SOC intervals while the battery is discharging, as illustrated in Figure 4.3(a). To establish the desired SOC, the battery is discharged at a 1C rate for 6 minutes. Following this, a 1-hour rest period is allowed to stabilize the cell voltage. Then, at each SOC level, a sequence of 10-second discharge and charge pulses is applied, with a 10-minute rest period between each pulse [114]. This sequence continues until the cutoff voltage is reached. Note that the test are repeated considering two different C-rates for the discharge pulses: C/3 and 1C.

   According [126], the HPPC test is used to extract the high-frequency cell resistance, commonly referred to as the cell's ohmic resistance. As shown in Figure 4.3(b), the discharge ohmic resistance ($R_{0,dis}$) is determined by the ratio of the instantaneous voltage drop (ΔV_{pulse}) to the instantaneous current drop (ΔI_{pulse}) that occurs at the moment of the current pulse. The $R_{0,dis}$ can be calculated using the formula:

$$R_{0,dis} = \frac{\Delta V_{pulse}}{\Delta I_{pulse}} \tag{4.2}$$

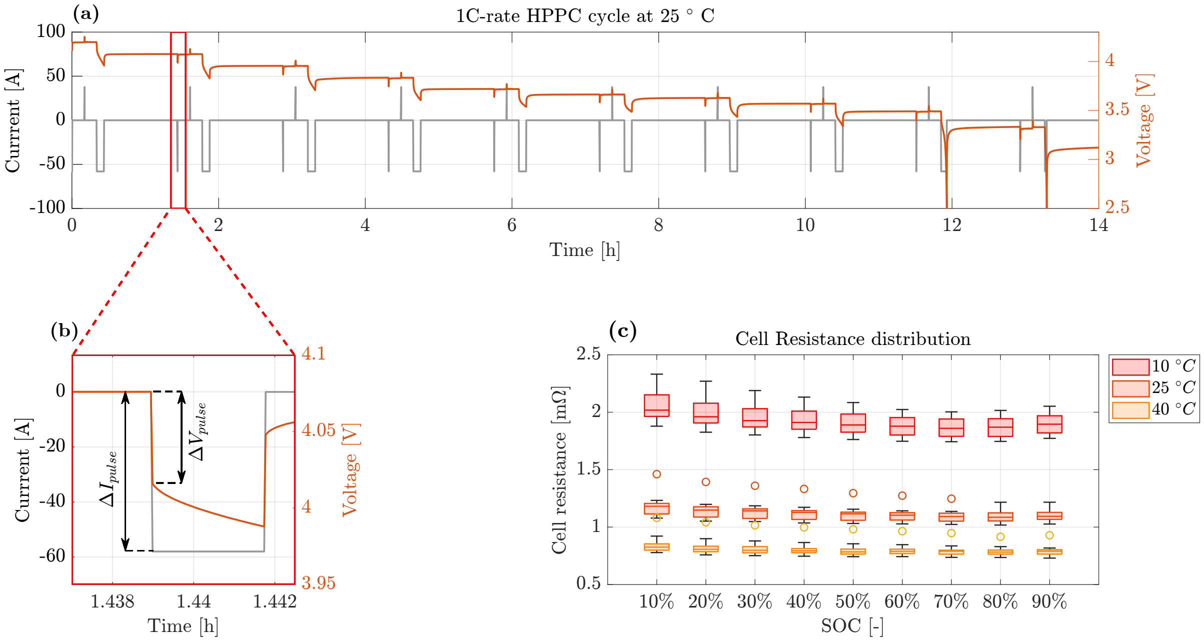

Figure 4.3: (a) HPPC test procedure showing the voltage and current profiles during the test. (b) Detailed view of a discharge pulse highlighting the voltage drop (ΔV_{pulse}) and current drop (ΔI_{pulse}) used to calculate the ohmic resistance ($R_{0,dis}$). (c) Boxplot illustrating the distribution of $R_{0,dis}$, calculated using (4.2), at various SOC and temperatures.

Finally, Figure 4.3(c) presents a boxplot of $R_{0,dis}$ across different SOC levels at three ambient temperatures (i.e. 10°C, 25°C, and 40°C). The data reveal two notable trends: 1) As expected, the ohmic resistance increases with decreasing temperature; 2) The standard deviation of $R_{0,dis}$ also increases at lower temperatures, indicating greater cell-to-cell resistance heterogenities under cooler conditions.

3. **Driving Cycles** In this study, three different driving cycles are analyzed: the Worldwide Harmonized Light Vehicles Test Procedure (WLTP), the Urban Dynamometer Driving Schedule (UDDS), and the US06 cycle. Each cycle represents a standardized speed profile over time and is typically used to compare fuel consumption and performance in conventional combustion vehicles. In the context of EVs, time-varying current profiles are generated from an electric vehicle simulator to simulate the battery pack input current in real driving conditions. These profiles are then scaled for a single cell based on battery pack topology, providing a realistic representation of actual current patterns. The WLTP and UDDS are global driving cycle standards, each lasting 30 minutes, while the US06 duration is 12 minutes. In this campaign, to extend the experimental duration and cover a broader SOC range, multiple WLTP, UDDS, and US06 cycles are concatenated, as shown in Figure 4.4. Additionally, the current profiles are scaled to achieve a maximum peak current of 1C-rate, and different initial conditions are considered. Specifically, the initial SOC is fixed at approximately 100% for the WLTP, 80% for the UDDS, and 60% for the US06 cycle.

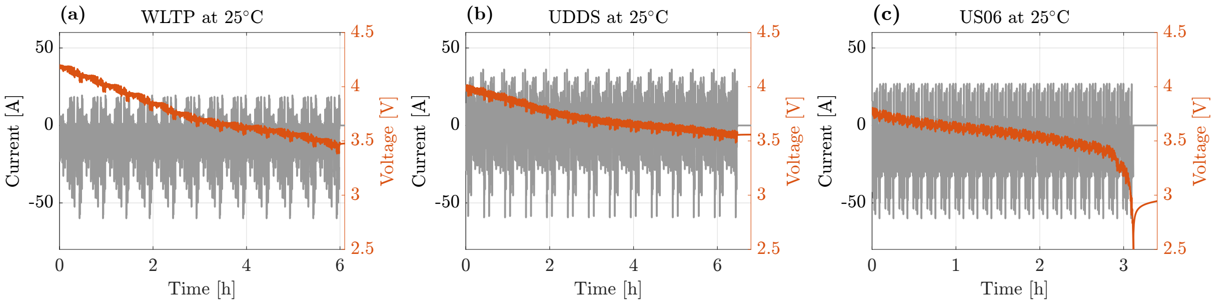

Figure 4.4: Voltage and current profiles for the (a) WLTP, (b) UDDS, and (c) US06 driving cycles at 25 $°C$.

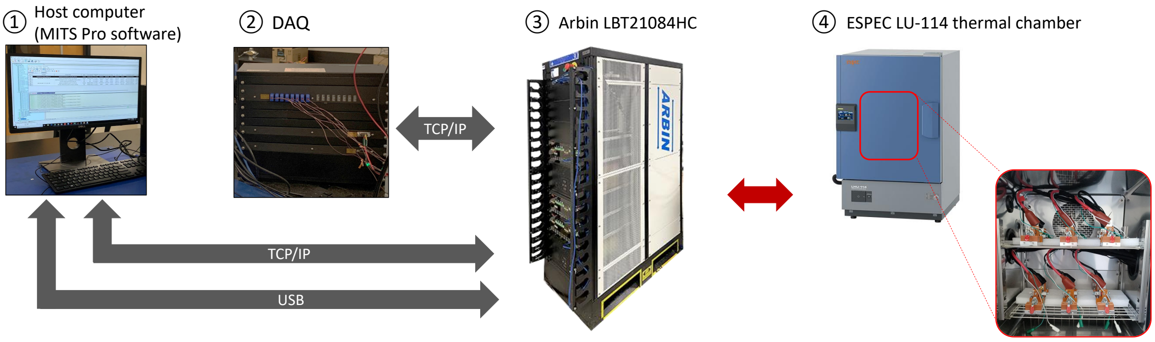

Figure 4.5: Equipment available at the Energy Laboratory for Interdisciplinary Storage Applications (ELISA)

4.2.1.2 Laboratory facilities

The equipment available at the Energy Laboratory for Interdisciplinary Storage Applications and employed in the experimental campaign is shown in Figure 4.5. Cell-level tests are configured using MITS Pro software ①, which defines the testing protocols and sequences. To supply the battery cell with the desired current profile and to collect sensor data (e.g., cell voltage, and cell surface temperatures), the Arbin LBT21084HC ③ is used in conjunction with the Dat Acquisition System (DAQ) ②. During testing, each cell ⑤ is placed inside the ESPEC LU-114 thermal chamber ④ and is equipped T-type thermocouples to measure the surface temperatures at the surface of each cell as well as the ambient temperature.

4.2.2 SECL campaign

The experimental campaign is composed of two complementary phases. The first phase involves the characterization of 39 individual cells to assess their sample properties and distribution post-manufacture, as detailed in Section 4.2.2.1. The second phase focuses on conducting 0.75C constant current (CC) discharge tests on four cells connected in parallel within a ladder configuration, as described in Section 4.2.2.2.

To aid the reader's understanding of the experimental procedures, a high-level flowchart depicting the steps for both campaigns is provided in Figure 4.6. This flowchart highlights

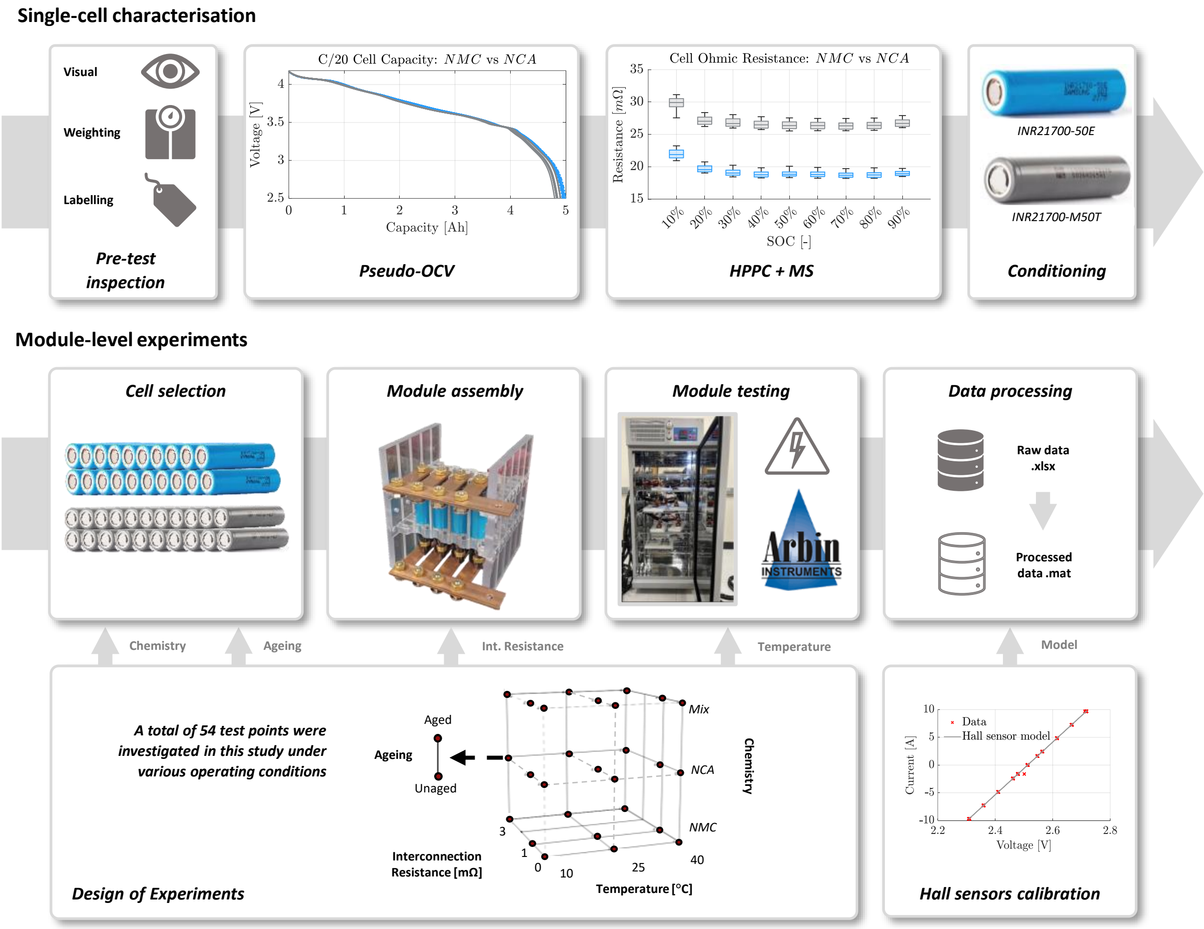
Single-cell characterisation
Visual
Weighting
Labelling
Pre-test inspection
C/20 Cell Capacity: NMC vs NCA
Voltage [V]
4
3.5
3
2.5
0
1
2
3
4
5
Capacity [Ah]
Pseudo-OCV
Cell Ohmic Resistance: NMC vs NCA
Resistance [mΩ]
35
30
25
20
15
10%
20%
30%
40%
50%
60%
70%
80%
90%
SOC [-]
HPPC + MS
INR21700-50E
INR21700-M50T
Conditioning
Module-level experiments
Cell selection
Module assembly
Module testing
Arbin INSTRUMENTS
Data processing
Raw data .xlsx
Processed data .mat
Chemistry
Ageing
Int. Resistance
Temperature
Model
A total of 54 test points were investigated in this study under various operating conditions
Aged
Ageing
Unaged
Mix
NCA
NMC
Chemistry
3
1
0
Interconnection Resistance [mΩ]
10
25
40
Temperature [°C]
Design of Experiments
10
5
0
-5
-10
Current [A]
Data
Hall sensor model
2.2
2.4
2.6
2.8
Voltage [V]
Hall sensors calibration

Figure 4.6: A visual flowchart of the implemented experimental procedures, selected steps, and design of experiments. Single-cell characterization (top) is performed before module-level testing (bottom).

the primary steps involved in both the cell-level and module-level testing, which are described in detail in the subsequent sections.

4.2.2.1 Cell-level testing

To characterize the 39 cells, the testing protocol was conducted in two phases: a Pseudo-OCV test and an HPPC test augmented by a Multi-Sine (MS) procedure [127]. Details of the testing procedures are outlined in Table 4.3. The initial conditioning for all tests involved a constant CCCV charge at a rate of C/3, continuing until the charging current fell to 50 mA and the voltage reached 4.2 V. The Pseudo-OCV test consisted of discharging the cells at a constant current of C/20 until the voltage dropped to 2.5 V. The combined HPPC and MS tests aimed to explore the effects of SOC on the cells internal properties. Dynamic current profiles were applied at SOC intervals of 10%, each preceded by a discharge at a 1C rate and a 60-minute rest period. At each SOC level, an HPPC pulse with a charge/discharge ratio of 0.75 and a duration of 10 seconds was applied [114]. This was followed by MS dynamic current profiles designed as per the methodology in [127], using an alpha (α) value of 0.6 and a pulse duration of 10 seconds.

Table 4.3: SECL campaign: cell-level characterization procedure

Step	Action	Exit condition
1	CC charge at 0.33 C-rate	4.2V reached
2	CV charge	Supplied current below 50mA
3	Rest	60 minutes limit reached
4	CC discharge at 1/20 C-rate	2.5V reached
5	Rest	30 minutes limit reached
6	CC charge at 0.33 C-rate	4.2V reached
7	CV charge	Supplied current below 50mA
10	Rest	60 minutes limit reached
11	HPPC	10s charge and 10s discharge pulses
12	MS	Time-dependent current profile
13	Rest	2.5V reached or go to Step 10

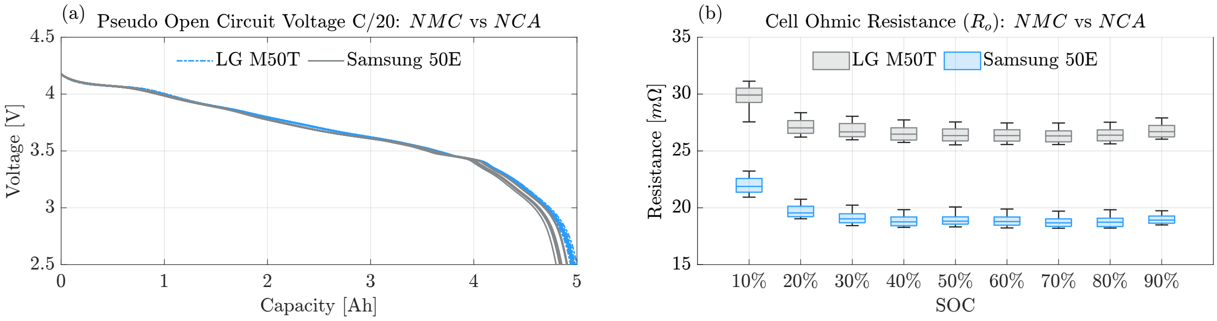

Figure 4.7: (a) Pseudo OCV curves of the fresh 37 cells under C/20 discharge test procedure. (b) Boxplot of cells internal resistances at 10% SOC intervals.

The experimental campaign aimed to assess the distribution of internal features of the cells post-manufacturing. As illustrated in Figure 4.7(a), a C/20 CC discharge test was used to measure variations in cell capacities, calculated in accordance with eq. (4.1). For the two batches, consisting of 19 LG M50T cells and 18 Samsung 50E cells, the mean cell capacity was 4.86 Ah and 4.96 Ah, respectively. The standard deviations were 0.033 Ah for the LG M50T cells and 0.013 Ah for the Samsung 50E cells. Additionally, the distribution of cell ohmic resistance at different SOC levels was evaluated using the HPPC cycle, as shown in Figure 4.7(b). The cell ohmic resistance was determined from the ratio of the voltage drop to the current drop immediately following the current pulse, according to eq. (4.2).

4.2.2.2 Module-level testing

The module-level campaign aimed to enhance our understanding of how various factors affect the inconsistent performance of parallel-connected cells. This study builds on insights from the single-cell characterization campaign, which provides valuable data on the distribution of electrical properties. The module-level tests further explore characteristics related to design choices and operating conditions. The tests involved a four-cell parallel string configured in a ladder setup, with terminals connected on the same side as depicted

Table 4.4: SECL campaign: module-level testing steps

Step	Action	Exit condition
①	Rest	90 minutes limit reached
②	CC charge at 0.33 C-rate	4.2V reached
③	CV charge	Supplied current below 200mA
④	Rest	30 minutes limit reached
⑤	CC discharge at 0.75 C-rate	2.5V reached
⑥	Rest	60 minutes limit reached
⑦	CC charge at 0.33 C-rate	4.2V reached
⑧	CV charge	Supplied current below 200mA

in Figure 4.8. Based on the DOE cube shown in Figure 4.6, different battery module are built and tested under different operating temperature (10, 25, and 40 $^{\circ}C$), cell-to-cell interconnection resistance (0, 1, and 3 mΩ), cell chemistry (NCA, NMC, and Mixed), and aging status (Aged vs. Unaged). It is important to note, a "Mixed" chemistry configuration refers to a parallel string of two NMC cells and two NCA cells. The NCA cells are positioned closest to the terminals to represent a worst-case load imbalance scenario, given their lower ohmic resistance compared to NMC cells. The "NMC" and "NCA" configurations consist of modules with cells of uniform chemistry. The "Unaged" configuration includes four new cells, while the "Aged" configuration involves one aged cell among four new cells. The aged cell is placed in position 4 to maximize load imbalance, due to its higher ohmic resistance and reduced discharge capacity compared to unaged cells. Additionally, the mixed and aged case includes both mixed chemistries and two aged cells. To manage variability in cell characteristics over the experimental campaign, a randomized sampling methodology was developed. At each instance, a random combination of four cells from the batch of twenty is selected and assigned a position (1-4) in the module, minimizing repetitive testing of the same cells. Stat-Ease Design Expert software version 22.0.2 is used to design a full-factorial DOE, resulting in 54 testing points as detailed in Table 5 of [8]. The module-level test protocol consists of eight consecutive steps, as listed in Table 4.4 . Each cycle begins with a 90-minute resting period (Step ①) to allow the cells to self-balance and reach thermal and electrochemical equilibrium, eliminating initial state variations. Steps ② and ③ involve charging the module with a CC at a C/3 rate up to 4.2V, followed by a CV phase until the module current drops below 200 mA. The module then rests for 30 minutes (Step ④). A 0.75C constant current discharge profile is applied until the terminal voltage reaches 2.5V (Step ⑤). The module undergoes a one-hour rest phase for self-balancing (Step ⑥). The protocol concludes with Steps ⑦ and ⑧, which repeat Steps ② and ③. This procedure is repeated for each of the 54 testing points as highlighted in [8].

4.2.2.3 Laboratory facilities

The equipment available at the Stanford Energy Control Lab [7] and employed in the experimental campaign for module cycling is shown in Figure 4.8 [1] Module-level tests are configured using MITS Pro software ①, which defines the testing protocols and sequences. To supply the battery module with the desired current profile and to collect sensor data (e.g., module voltage, Hall sensor voltages, and cell surface temperatures), the Arbin LBT22013 ③ is used in conjunction with the Data Acquisition System (DAQ) ②. During testing, each battery module ⑤ is placed inside the Amerex IC500R thermal chamber ④ and is equipped with five T-type thermocouples to measure the surface temperatures at the center of each cell as well as the ambient temperature. Additionally, four Honeywell SS495A Hall sensors are installed in each module to measure parallel path currents. Hall-effect sensors were preferred over standard shunt resistors due to their superior accuracy and lack of influence on the module's current distribution. Hall sensors operate with an external 5V circuit, and they are mechanically secured and glued into ferrite rings to improve the signal-to-noise ratio and enhance the reading accuracy. These rings are fixed around the current-carrying connector at the negative terminal of each cell, ensuring that sensor placement remains consistent throughout testing. Shielded cables are used for signal enclosure, and terminal legs are soldered and insulated to stabilize them and prevent shorts during operation. A 1 mF capacitor is soldered across the 5V power supply to stabilize the input signal and minimize its impact on readings. Raw data from each test are exported in Excel spreadsheets (.xlsx) format. For more details on the setup, please refer to [128].

---

[1] A description of the equipment used for single-cell testing can be found in [128].

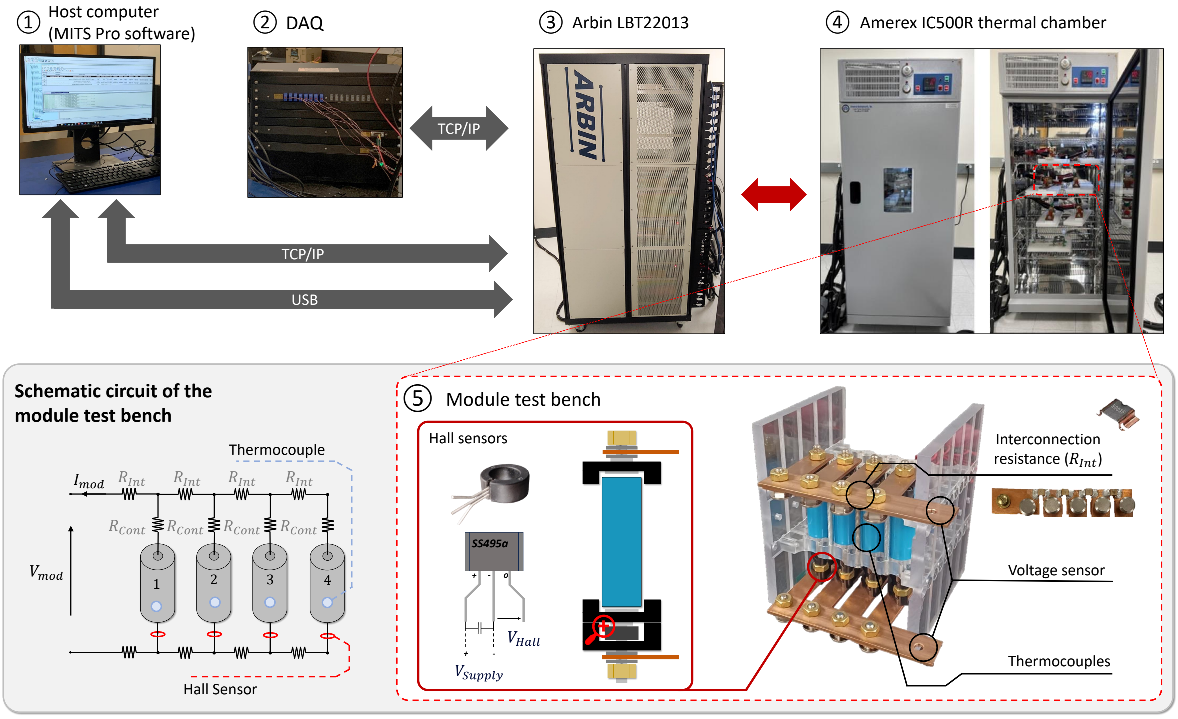
① Host computer (MITS Pro software)
② DAQ
③ Arbin LBT22013
④ Amerex IC500R thermal chamber
TCP/IP
TCP/IP
USB
ARBIN
Schematic circuit of the module test bench
Thermocouple
I_{mod}
R_{Int}
R_{Int}
R_{Int}
R_{Int}
R_{Cont}
R_{Cont}
R_{Cont}
R_{Cont}
V_{mod}
1
2
3
4
Hall Sensor
⑤ Module test bench
Hall sensors
SS495a
V_{Hall}
V_{Supply}
Interconnection resistance (R_{Int})
Voltage sensor
Thermocouples

Figure 4.8: Equipment available at the Stanford Energy Control Lab [7]

4.3 Conclusion

In this chapter, a comprehensive description of the experimental campaigns conducted is presented. Specifically, the specifications of the tested cells, the laboratory facilities employed, and the data collection procedures implemented are detailed.
Additionally, the usage of the collected data throughout the remainder of the manuscript is presented in alignment with the schematic flowchart shown in Figure 4.1.

Chapter 5

EM parametrization

Contents

5.1 EMs parameters identification 97

5.1.1 Cell teardown method 97

5.1.2 Parameter sensitivity analysis 99

5.2 ESPM identification and validation for LG M50T 103

5.2.1 Single cell ESPM identifiction and validation 103

5.2.2 ESPM-based module-level model validation 108

5.3 Conclusion 115

Introduction

According to Chapter 3, electrochemical models for lithium-ion batteries involve numerous physical parameters that span across each cell domain and the electrolyte. These models estimate the internal variables of battery cells based on physical principles, but accurate predictions are contingent upon proper parameter identification.

Currently, the most advanced method for identifying electrochemical parameters involves cell teardown analyses, which allows to directly measure the physical, chemical, and electrochemical properties of the cell [129, 96]. However, this method is complex, costly, time-consuming, and requires sophisticated equipment. Consequently, it is not always feasible for use in model parametrization.

Alternatively, non-destructive optimization-based techniques that use cell input-output data have gained popularity in battery modeling to address these limitations [130]. These methods involve aligning experimentally measurable cell quantities, such as voltage and/or temperature, with those predicted by the model [131]. However, several key challenges remain to be addressed. Firstly, certain parameters in EMs are interdependent, as they are either multiplied or summed within the model. Consequently, these parameters cannot be individually identified using input-output data, instead, only their combined effects can be assessed. A common solution to this issue is to reformulate the model to utilize uncorrelated lumped parameters, thereby simplifying the identification process [132]. The second key challenge is that attempting to identify all parameters simultaneously may lead to overfitting, negatively affecting the model predictive accuracy and generalizability. A commonly adopted solution is to group parameters based on their sensitivity to the model output. Each parameter subset is then identified using the corresponding model input, ensuring proper identifiability of the parameters[117, 116]. This strategy is based on the principle that parameter sensitivity depends not only on the model structure but is also significantly influenced by the model inputs [133, 134, 135]. Consequently, parameters that exhibit low sensitivity are less likely to be uniquely determined from the output measurements. For instance, in [117], the identification of a DFN model is presented. The authors clustered the 21 model parameters into three groups: the first group was sensitive to low-rate CC cycles, the second to high-rate CC cycles, and the third to time-varying current profiles. Dividing the identification process into multiple steps is a valuable alternative to destructive methodologies.

However, hybrid approaches that combine both teardown and optimization-based techniques are generally preferred over using either method in isolation. In particular, according to [130], a practical solution involves directly extracting electrode open-circuit potential (OCP) curves from half-cell experiments and measuring electrode geometrical dimensions, as these tasks require minimal effort after cell teardown and provide high accuracy. This approach simplifies the optimization problem for determining the remaining parameters, making it more manageable and straightforward by adopting the parameter grouping mentioned above.

Chapter contribute

This chapter aims to provide a high-level overview of the cell teardown methodology for parameterizing electrochemical models, referencing the process described in [96] for the LG Chem M50. Additionally, the chapter briefly reviews parameter sensitivity analysis methods, which are crucial in optimization-based parameter identification. Readers can refer to [130] for detailed numerical optimization methods used in solving the nonlinear minimization problem.

Finally, an example of model identification is presented. Specifically, an ESPM is identified for the LG M50T cells tested at the SECL laboratory, as described in Section 4.2.2.1. A hybrid approach, combining cell teardown methods and optimization-based techniques, is utilized. Parameters measured in [96] for the LG M50 model are used as a starting point for model development for the LG M50T, an updated version of the M50. Then, a subset of high-sensitivity parameters, selected based on ESPM parameter sensitivity analysis from the literature, is refined using optimization methods to fit the cell voltage response. Subsequently, based on the identified ESPMs and in accordance with the module-level experimantes conducted at the SECL (Section 4.2.2.2), the validation of a model consisting of four parallel-connected ESPM cells is reported. This model is central to the high-fidelity *offline simulation described in Chapter 8.*

Chapter structure

- **Section 5.1** provides a high-level overview of electrochemical model identification, focusing on the cell teardown method for assessing the physical, chemical, and electrochemical properties of the cell, and on parameter sensitivity analysis methods to evaluate the identifiability of electrochemical model parameters.
- **Section 5.2** details the identification and validation procedure for the ESPM-based cell-level model of the LG Chem M50T. It also illustrates the formulation and validation of a module-level model consisting of four cells connected in parallel.
- **Section 5.3** summarizes the conclusions.

5.1 EMs parameters identification

5.1.1 Cell teardown method

In this section, we present a high-level overview of parameter identification through cell teardown. For a more detailed understanding, readers are encouraged to refer to [129, 136] and to Figure 4(a) of [116] which provided a complete overview of the process. The parameter identification procedure is revisited based on the methodology described in [96]. The authors disassembled the LG Chem M50 cell and measured its physical, chemical, and electrochemical properties to parameterize a DFN model.

This review is conducted here for two primary reasons. First, it provides a comprehensive overview of model identification for a commercially available cell. Second, and equally important, our experimental campaign focuses on the LG M50T, an updated version of the M50. Consequently, the parameters measured for the M50 in [96] will serve as a baseline for the ESPM parameterization discussed in the following sections.

Physical cell properties

The physical properties of the cell involve measuring dimensions such as the electrode thickness (L_j), surface area (A), and overall cell dimensions. Material properties include the electrode porosity ($\epsilon_{e,j}$), which determines the active material volume fraction ($\epsilon_{s,j}$), particle radius ($R_{s,j}$), and the Bruggeman constant ($brugg$) which refers to the material tortuosity. To obtain these properties, the cell is disassembled after being fully discharged. The layer thicknesses of the electrode foils and separator, and the electrode area are typically measured using precision instruments such as micrometers or other high-accuracy devices. For example, [96] used an incremental length gauge to measure the thickness and electrode areas of the LG M50, as reported in Table 5.1. On the other hand, electrode microstructure and morphology properties as the porosity, particle shape, density, and tortuosity can be investigated using various techniques, including mercury porosimetry, X-ray tomography, and scanning electron microscopy (SEM). In [96], the electrode morphology was analyzed using SEM. Specifically, the $R_{s,j}$ was obtained from the average particle size measured in 2D SEM images, while the $\epsilon_{e,j}$ and tortuosity were assessed using focused ion beam SEM (FIB-SEM). Finally, the active material volume fraction is derived using the relationship $\epsilon_{s,j} = 1 - \epsilon_{e,j}$.

Chemical cell properties

In terms of chemical properties, the elemental composition of the active materials is considered. This can be analyzed using techniques such as inductively coupled plasma optical emission spectroscopy (ICP-OES), energy-dispersive X-ray spectroscopy (EDS), and X-ray diffraction for determining the material's crystal structure and theoretical density. In particular, in [96], EDS was employed to determine the percentage of nickel, cobalt, manganese, and aluminum in the positive electrode, as well as the percentage of silicon in the graphite of the negative electrode. In the context of electrochemical battery modeling, such information is not directly utilized; however, it provides important insights into

Table 5.1: ESPM parameters for the LG 21700 M50T

	Param.	Unit	Cathode ($j = p$)	Sep. ($j = s$)	Anode($j = n$)	Ref.
Physical param.	L_j	m	$75.6 \cdot 10^{-6}$	$12 \cdot 10^{-6}$	$85.2 \cdot 10^{-6}$	[96]
	$R_{s,j}$	m	$5.22 \cdot 10^{-6}$	$-$	$5.86 \cdot 10^{-6}$	[96]
	$\epsilon_{s,j}$	$-$	$1 - \epsilon_{e,n}$		$1 - \epsilon_{e,p}$	
	$\epsilon_{e,j}$	$-$	0.335	0.47	0.25	[96]
	$brug$	$-$	2.43	2.57	2.91	[96]
	A	m^2	$(0.1027 + 0.10465)/2$			[96]
Electrochemical param.	$D_{s,j}$	m^2/s	$1.48 \cdot 10^{-15}$	$-$	$1.74 \cdot 10^{-15}$	[96]
	$k_{s,j}$	$m^{2.5}/(mol^{0.5}s)$	$3.42 \cdot 10^{-6}$	$-$	$6.48 \cdot 10^{-7}$	[96]
	$c_{s,j}^{max}$	mol/m^3	51765	$-$	29583	[96]
	θ_j^0	$-$	0.9084	$-$	0.0279	[96]
	θ_j^{100}	$-$	0.2661	$-$	0.9014	[96]
Electrolyte	$D_{e,j}$	m^2/s	$8.794 \cdot 10^{-11} c_{e,j}^2 - 3.972 \cdot 10^{-10} c_{e,j} + 4.862 \cdot 10^{-10}$			[96]
	$\kappa_{e,j}$	S/m	$0.1297 c_{e,j}^3 - 2.51 c_{e,j}^{1.5} + 3.329 c_{e,j}$			[96]
	t^+	$-$	0.2594			[96]
	$c_{e,0}$	mol/m^3	1000			[96]

electrode composition and for the calculation of the maximum ion concentration in the active material.

Electrochemical cell properties

Electrochemical parameterization involves identifying the thermodynamic and kinetic properties of the materials and electrodes. This can be accomplished using various configurations, such as two-electrode full cells, half cells, and three-electrode setups, in combination with experimental techniques such as Galvanostatic Intermittent Titration Technique (GITT) and Electrochemical Impedance Spectroscopy (EIS) [137, 138].

Specifically, in [96], the electrode open-circuit potentials (OCPs) were measured using both three-electrode and half-cell configurations, applying GITT and a pseudo-OCP test with a CC discharge at a C/20 rate. The fitted electrode potentials are given by:

$$\begin{aligned}U_p =&4.4875 - 0.8090\theta_p^{\text{surf}} - 0.0428\tanh(18.5138(\theta_p^{\text{surf}} - 0.5542))+\\&- 17.7326\tanh(15.7890(\theta_p^{\text{surf}} - 0.3117))+\\&+ 17.5842\tanh(15.9308(\theta_p^{\text{surf}} - 0.3120))\\U_n =&0.2482 + 1.9793e^{-39.3631\theta_p^{\text{surf}}} - 0.0909\tanh(29.8538(\theta_p^{\text{surf}} - 0.1234))+\\&- 0.04478\tanh(14.9159(\theta_p^{\text{surf}} - 0.2769))+\\&- 0.0205\tanh(30.4444(\theta_p^{\text{surf}} - 0.6103))\end{aligned} \tag{5.1}$$

It is worth noting that combining half-cell and full-cell three-electrode tests, along with information regarding the elemental composition of the active materials obtained from chemical analysis, enables the analysis of cell stoichiometry ($\theta_j^{100\%}$ and $\theta_j^{0\%}$) and maximum lithium content within each electrode ($c_{s,j}^{max}$), as reported in Table 5.1. Similarly, GITT was used to calculate the diffusion coefficients for both electrodes as a function of stoichiometry, with the average values for $D_{s,j}$ provided in Table 5.1. Finally, EIS was employed to determine the intercalation rate constants (k_j) for both electrodes.

5.1.2 Parameter sensitivity analysis

The parameter sensitivity analysis (PSA) is a mathematical tool used to assess how changes in parameters affect the model output. It provides essential insights into parameter identifiability, since parameters with low sensitivity are less likely to be uniquely determined from the output measurements. PSA can be performed locally (LPSA) by perturbing the parameters around their nominal values (p^*), or globally (GPSA) by considering the entire range of physical parameter variations.

Consider a general non-linear system of ODEs denoted by Σ, expressed as:

$$\Sigma : \begin{cases}\dot{x}(t) = f(x(t), u(t), p)\\ y(t) = g(x(t), u(t), p)\end{cases} \tag{5.2}$$

where $x(t) \in \mathbb{R}^w$ represents the state vector, $p \in \mathbb{R}^m$ denotes the parameter vector, $u(t) \in \mathbb{R}$ is the input, $y(t) \in \mathbb{R}$ represents the model output, and $f : \mathbb{R}^w \times \mathbb{R} \longrightarrow \mathbb{R}^w$ and $g : \mathbb{R}^w \times \mathbb{R} \longrightarrow \mathbb{R}$ are a vector field and a scalar function, respectively. For the system described in (5.2), the LPSA of Σ with respect to the v-th parameter p_v, where $v = 1, 2, \cdots, m$, is calculated as $(\partial y/\partial p_j)|_{p=p^*}$, where p^* represents the nominal values of the parameters.

Determining the LPSA around p^* is relatively easy and computationally efficient. However, this approach provides limited information as it focuses only on the neighborhood of the nominal parameter values.

On the other hand, the GPSA is more computationally demanding. It requires a large number of simulations to explore the entire range of parameter space, but it yields more robust and comprehensive results. Among the most adopted GPSA methods in the battery modelling context variance-based Sobol coefficients [139] and elementary effect method (EEM) can be distinguished [140, 141] The latter, also known as the Morris method, offers a feasible computational approach for conducting GPSA. To implement EEM, the first step involves selecting the physical variation interval for each parameter p_v, where $v = 1, 2, \cdots, m$, thus defining a m-dimensional variation space $\Omega \subset \mathbb{R}^m$. Next, the parameter variation ranges are normalized to the dimensionless range of $[0, 1]$ and uniformly divided into l levels, thereby partitioning Ω. Starting from an initial parameter combination $P = [p_1, p_2, \cdots, p_m]$ randomly selected from Ω, a trajectory of $m+1$ points is constructed. At each point, one parameter of P is incrementally increased by a predefined value $\Delta = l/(2(l-1))$, while keeping the other parameters constant. This incremental parameter variation is performed sequentially, one parameter at a time (AOT). For each point along the trajectory, the model output is computed, and an elementary effect (EE_v) is calculated for each parameter p_v using the following equation:

$$EE_v = \frac{y(p_1, p_2, \cdots, p_v + \Delta, \cdots, p_m) - y(p_1, p_2, \cdots, p_v, \cdots, p_m)}{\Delta} \tag{5.3}$$

This process is repeated for a total of r different trajectories. The mean value (μ_v) and standard deviation (σ_v) of EE_v are then computed for each parameter using the following equations:

$$\mu_v^* = \frac{1}{r}\sum_{z=1}^{r} |EE_v^z|, \qquad \sigma_v = \sqrt{\frac{1}{r-1}\sum_{z=1}^{r}(EE_v^z - \mu_v)^2} \tag{5.4}$$

The parameter μ_v^* represents the overall impact of the parameter on the model output, while a high value of σ_v suggests that the parameter is involved in interactions with other parameters. To ensure thorough coverage of Ω, the starting point for each trajectory is selected using the Latin Hypercube Sampling (LHS) method [142]. It is important to note that the GPSA evaluation of the model requires a total of $r(m+1)$ simulations when employing the EEM with the LHS method. Finally, the model parameter importance is evaluated in terms of μ_v^*, as shown in [143].

Parameter sensitivity analysis of the ESPM at the cell level has been widely analyzed in the literature under both local [144] and global [134] approaches, considering various input current profiles, such as Constant Current (CC) [133], CC Constant Voltage (CCCV) [134], and driving cycles (DV) [135].

Example 5.1.1: *Morris method for module-level models*

The application of the Morris method is demonstrated for the module-level electrochemical-aging-thermal model, which will be presented in Section 5.2.2 [a]. The main goal is to examine the influence of variations in 18 electrochemical cell parameters on the module voltage. To streamline the computational process, we assume that the parameters are identical for each cell within the module.

Note that, our analysis goes beyond previous works that focused on individual cells only. We take into account the coupling terms arising from the module's thermal and electrical models. This allows us to capture the interactions and dependencies between cells within the module, providing a more comprehensive understanding of the system's behavior. It is important to note that the GPSA in this study is conducted using the EEM using 20 trajectories for each cycle, following the approach outlined in [134]. To ensure comprehensive coverage of the parameter variation range, we employ the Latin Hypercube Sampling (LHS) method to randomly select the starting parameter set for each trajectory [142]. This approach enables us to capture the overall behavior and sensitivity of the system under different parameter configurations. In the analysis, the parallel-connected modules, composed of 6 cells, are subjected to a charging cycle at a constant current of 1C-rate, from 0% to 100% SOC, followed by a resting period. Additionally, a dynamic driving cycle discharge is performed from 100% to 20% SOC. The physical variation bounds for the parameters are obtained from the literature and are provided in Table 3.1. Figure 5.1 (a-b) depicts the module voltage responses obtained from the simulations conducted using the GPSA method. These simulations encompass various parameter variations, and the corresponding module voltage profiles are shown. To assess the sensitivity of the parameters, statistical measures such as the mean of the absolute value of EE_v ($\mu^*_{EE_v}$) and the standard deviation of EE_v (σ_{EE_v}) are calculated at each time instant using Equation (5.4). These measures provide valuable information regarding the magnitude and variability of the module voltage due to the parameter change. Figures 5.1 (c-d) and (e-f) present these statistical measures for each time instant, allowing for a comprehensive analysis of parameter sensitivity. Finally, the average value of $\mu^*_{EE_v}$ over time, shown in Figure 5.1 (g), is used to determine the highly influential parameters. Parameters with an average $\mu^*_{EE_v}$ value exceeding the threshold of 0.05 are considered to have a significant influence on the module voltage. Based on the obtained results, it can be noticed that the capacity-related cathode parameters, the active material volume fraction ($\epsilon_{s,p}$) and thickness (L_n), exhibit the highest sensitivity under both the constant current and driving cycle scenarios. This indicates that variations in these parameters have a substantial impact on the module voltage. Additionally, the parameters $\epsilon_{s,n}$ and L_n show a high influence, particularly at the end of the discharge and charge phases. On the other hand, the particle radius ($R_{s,j}$) and the reaction rate constant (k_j) appear to have a significant influence only in the dynamic scenario, suggesting that they play an important role during dynamic discharging processes. Note that the GPSA results obtained at the module level in our study are consistent with the sensitivity analysis conducted at the cell-level in existing literature [145].

---

[a] Readers are encouraged to consult Sections 5.2.1 and 5.2.2 for a detailed description of the model

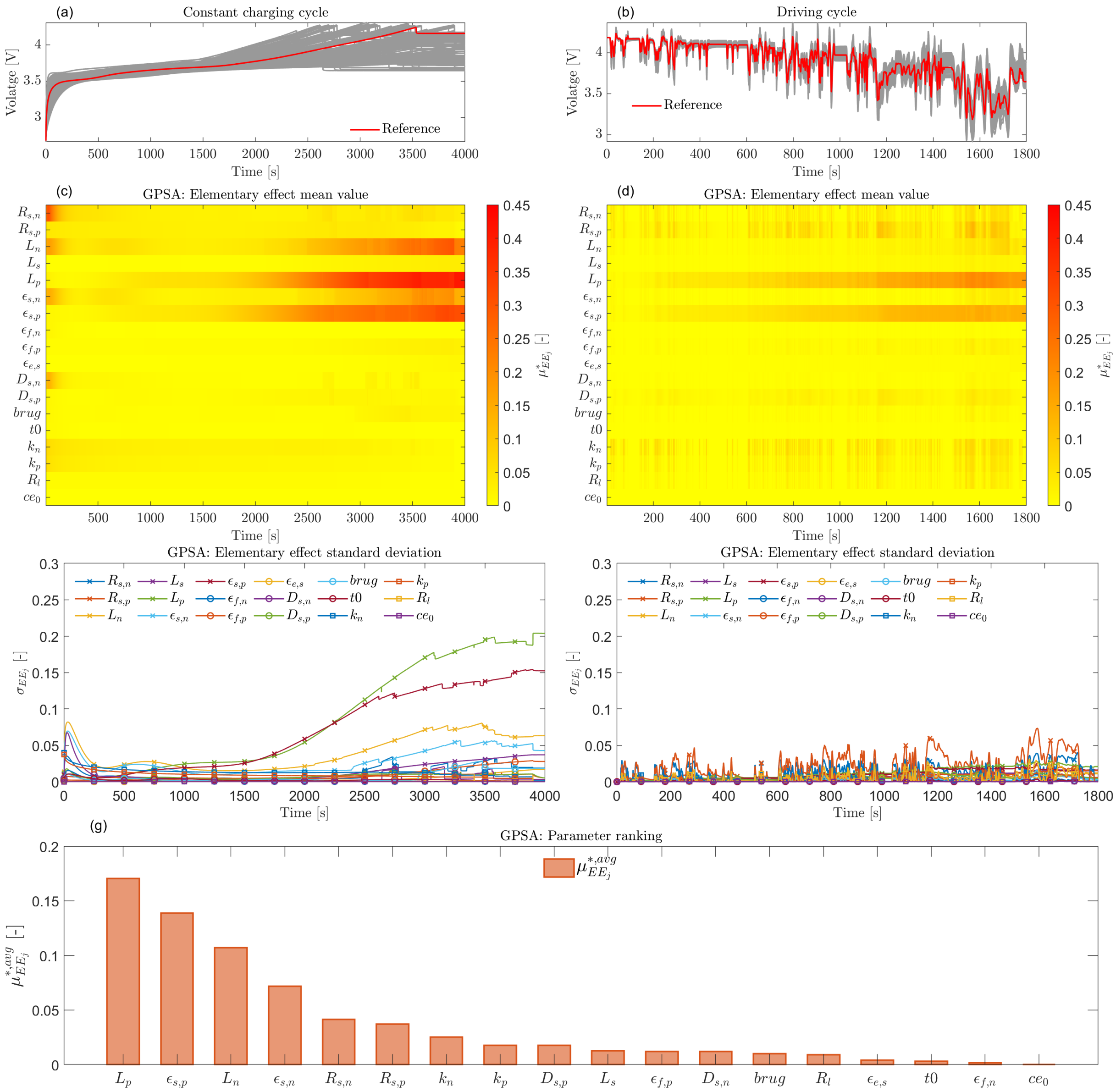

Figure 5.1: GPSA results: (a-b) show the module voltage responses resulting from the GPSA for a CC+rest and DV scenarios, respectively. (c-d) and (e-f) reports the mean value (μ_{EE_j}) and standard deviation (σ_{EE_j}) of the Elementary Effect (EE) at each time instant for each parameter in both scenarios. (g) shows the average mean value ($\mu^{avg}_{EE_j}$) calculated over the entire operating cycles (CC+rest and DV cycles) for each parameter.

5.2 ESPM identification and validation for LG M50T

This section presents two distinct contributions and is divided into the following two main parts as schematically depicted in Figure 5.2: In particular:

1. *Section 5.2.1 demonstrates the development of an electrochemical model using a commercially available cell as an example, as schematically highlighted in Figure 5.2(a).*

   Based on the SECL experimental campaign described in Section 4.2.2 of Chapter 4, the ESPM framework is calibrated for the LG Chem M50T. Starting from the parameter sets provided by [96] for the LG M50, detailed in Table 5.1, the ESPM for the LG M50T cell model is adjusted using single-cell characterization data from 19 tested LG M50T cells. Specifically, a subset of highly influential parameters, identified through parameter sensitivity analysis from the literature, is fine-tuned using an optimization-based approach during C/20 CC cycles. This procedure is repeated for all 19 cells to further analyze parameter distribution. The resulting models are then validated for each cell using the HPPC+MS cycle.

2. *Section 5.2.2 focuses on the validation of a module-level model consisting of cells connected in parallel as illustrated in Figure 5.2(b), which is central to the model-based analysis presented in **Chapter 8**.*

   Specifically, the identified ESPMs are combined to construct modules comprising four cells connected in parallel, in accordance with the module-level experiments described in Section 4.2.2.2 of Chapter 4. The goal is to demonstrate that module-level performance and heterogeneities, such as current and thermal distribution within the module, can be predicted by appropriately scaling up the single-cell model to the module level. To this end, both thermal and cell current distributions within the module are validated against experimental data.

5.2.1 Single cell ESPM identifiction and validation

Table 5.2 provide a summari of the ESPM-based electrochemical-thermal-aging model adopted for the LG M50T governing equation, derived in accordance with Chapter 3.
The governing PDEs of the ESPM are solved numerically using different methods. Specifically, the FDM is employed to solve the solid phase mass conservation, as detailed in Section 3.1.3.1. In contrast, following the approach of [66], the FVM is used to solve the mass conservation in the liquid phase. The resulting ODE systems are listed in (5.5) and (5.6) for the solid and liquid phases, respectively. Meanwhile, the overall cell voltage (V_{cell}), electrode overpotential (η_j), electrode exchanged current density ($i_{0,j}$), electrolyte potential ($\Delta\Phi_e$), and electrode SOC (SOC_j) are formulated as described in Section 3.1.2.2 and reported in eqs. (5.7) to (5.13). The thermal dynamics of the cell are modeled using a lumped one-state model specifically tailored for cylindrical cells, as reviewed in Section 3.1.4. The cell temperature, governed by the ODE (5.14), is assumed to be uniform

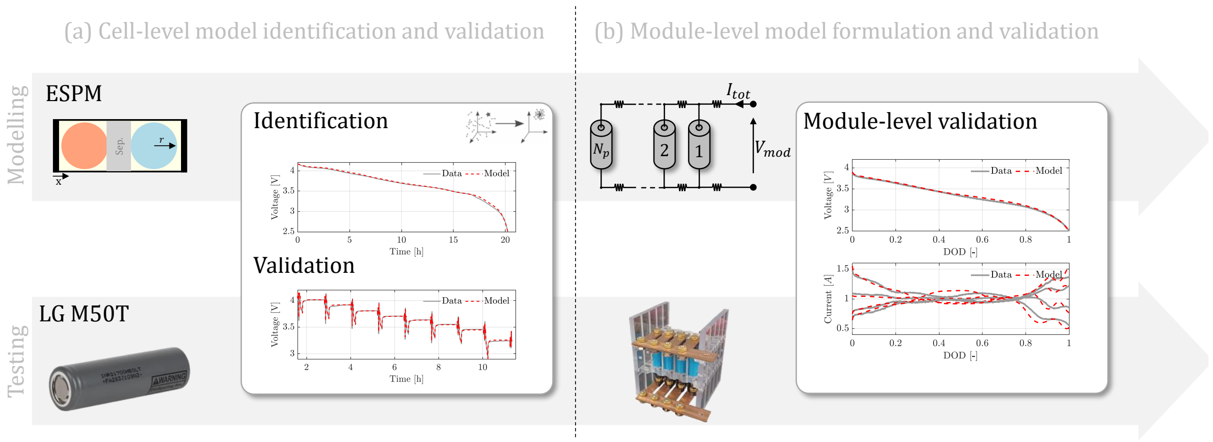
(a) Cell-level model identification and validation
(b) Module-level model formulation and validation
Modelling
Testing
ESPM
Sep.
r
x
LG M50T
Identification
Validation
Data
Model
Voltage [V]
Time [h]
I_{tot}
V_{mod}
N_p
2
1
Module-level validation
Current [A]
DOD [-]

Figure 5.2: Schematic overview of the identification and validation procedure described in this section. (a) 19 different ESPMs are identified and validated using single-cell characterization data from a batch of LG M50T cells. (b) The single-cell model dynamics are scaled up to the module level, and the resulting current and thermal distributions are validated against experimental data.

within the cell casing and across its surface. Additionally, a physics-based aging model, described in Section 3.1.5.1 and based on SEI layer growth, is utilized. This model is detailed in equations eqs. (5.15) to (5.20). Following the approach in [46], the governing PDE (5.15) is numerically solved using the FDM, with the SEI thickness discretized into N_{SEI} points, as shown in equation (5.16). It is important to note that as the SEI layer grows, maintaining N_{SEI} constant results in a time-varying grid size.

Once the model equations and initial parameter guesses (i.e., Table 5.1) are defined, a prior verification must be performed before proceeding to the optimization-based model adjustment for the LG M50T. Specifically, it needs to be confirmed whether the electrode OCPs and stoichiometry limits provided for the M50 in [96] are suitable for the M50T. Thus, the remaing of the section is divided in two steps: 1) Verification of electrode OCPs and stoichiometry limits, and 2) Identification and validation of ESPM parameters.

Step 1: Electrode OCPs and stoichiometry limits check

This verication is inspire by the works presented in [146, 147, 148] where procedures to identify the electrode stoichietry limit is provided.

Generally, the open-circuit voltage (OCV) of a full cell is determined by combining the open-circuit potentials (OCP) of each electrode, as given by:

$$V_{OCV} = U_p(\theta_{s,p}^{surf}) - U_n(\theta_{s,n}^{surf}) \tag{5.21}$$

where $\theta_{s,p}^{surf} \in [\theta_p^{0\%}, \theta_p^{100\%}]$ and $\theta_{s,n}^{surf} \in [\theta_n^{0\%}, \theta_n^{100\%}]$. The stoichiometric limits define the maximum and minimum levels to which the active materials in the electrodes can be charged or discharged while preserving their integrity and performance. Therefore, battery manufacturers specify voltage limits to prevent overcharging and over-discharging. To that

Table 5.2: Cell-level electrochemical-thermal-aging dynamics for the LG M50T.

Electrochemical dynamics [*Spatially discretized*] ($A_{s,j}$, $B_{s,n}$, A_e, B_e, $\alpha_{s,j}$, $\beta_{s,j}$, $\alpha_{es,j}$ and β_e defined in [46])

Solid phase mass conservation, $j \in [n,p]$

$$\dot{c}_{s,j} = \alpha_{s,j} A_{s,j} c_{s,j} + \beta_{s,j} B_{s,j} [I_{cell} - g_{s,j}] \tag{5.5}$$

Liquid phase mass conservation, $j \in [n,s,p]$

$$\dot{c}_e = \alpha_e A_e c_e + \beta_e B_e I_{cell} \tag{5.6}$$

Cell Voltage

$$V_{cell} = U_p + \eta_p - U_n - \eta_n + \Delta\Phi_e - I_{cell}(R_{cell} + R_{\mathrm{SEI}}) \tag{5.7}$$

Anode OCP [96]

$$\begin{aligned} U_n = {} & 0.1493 + 0.8493 e^{-61.79\theta_n^{surf}} + 0.3824 e^{-665.8\theta_n^{surf}} - e^{39.42\theta_n^{surf} - 41.92} \\ & - 0.03131 \arctan(25.59\theta_n^{surf} - 4.099) - 0.009434 \arctan(32.49\theta_n^{surf} - 15.74) \end{aligned} \tag{5.8}$$

Cathode OCP [96]

$$\begin{aligned} U_p = {} & 10188.54(\theta_p^{surf})^9 - 66535.82(\theta_p^{surf})^8 + 189316.65(\theta_p^{surf})^7 - 307780.79(\theta_p^{surf})^6 + 314825.52(\theta_p^{surf})^5 + \\ & - 209988.26(\theta_p^{surf})^4 + 91295.30(\theta_p^{surf})^3 - 24944.01(\theta_p^{surf})^2 + 3884.75(\theta_p^{surf})^1 - 258.27 \end{aligned} \tag{5.9}$$

Electrode overpotential, $j \in [n,p]$

$$\eta_j = \frac{R_g T_c}{0.5F} \sinh^{-1}\Big(\frac{I_{cell}}{2Aa_{s,j} L_j i_{o,j}}\Big) \tag{5.10}$$

Exchanged current density, $j \in [n,p]$

$$i_{o,j} = k_j F \sqrt{c_{e,j}^{avg} c_{s,j}^{surf} (c_{s,j}^{max} - c_{s,j}^{surf})} \tag{5.11}$$

Electrolyte overpotential

$$\Delta\Phi_e = \frac{2 R_g T_c v(c, T_c)}{F} \ln\left(\frac{c_e(L_n + L_s + L_p)}{c_e(0)}\right) \tag{5.12}$$

Electrode SOC

$$SOC_n = \frac{\theta_n^{bulk} - \theta_{n,0\%}}{\theta_{n,100\%} - \theta_{n,0\%}}, \quad SOC_p = \frac{\theta_{p,0\%} - \theta_p^{bulk}}{\theta_{p,0\%} - \theta_{p,100\%}} \tag{5.13}$$

Thermal dynamics

Cell heat balance

$$C_s \frac{dT_{cell}}{dt} = I_{cell}(V_{OCP} - V_{cell}) + T_{cell} I_{cell} \frac{dV_{\mathrm{OCP}}}{dT_{cell}} + \frac{T_{amb} - T_{cell}}{R_u} \tag{5.14}$$

Aging dynamics — *Boundary conditions*

Solvent conservation in the SEI layer [*governing PDE*]

$$\frac{\partial c_{\mathrm{solv}}}{\partial t} = D_{\mathrm{solv}} \frac{\partial^2 c_{\mathrm{solv}}}{\partial r^2} - \frac{dL_{\mathrm{SEI}}}{dt} \frac{\partial c_{\mathrm{solv}}}{\partial r}$$

$$\begin{aligned} - D_{\mathrm{solv}} \frac{\partial c_{\mathrm{solv}}}{\partial r}\Big|_{r=R_{s,n}} + \frac{dL_{\mathrm{SEI}}}{dt} c_{\mathrm{solv}}^{\mathrm{surf}} &= \frac{i_s}{F} \\ c_{\mathrm{solv}}\big|_{r=R_n+L_{\mathrm{SEI}}} &= \epsilon_{\mathrm{SEI}} C_{\mathrm{solv}}^{\mathrm{bulk}} \end{aligned} \tag{5.15}$$

Solvent conservation in the SEI layer [*Spatially discretized*]

$$\dot{c}_{\mathrm{solv}} = \begin{cases} 2\alpha_{\mathrm{solv}}(c_{solv,2} - c_{solv,1}) + \beta_{\mathrm{solv}}\Big(\frac{i_s}{F} - \frac{dL_{\mathrm{SEI}}}{dt} c_{\mathrm{solv}}\Big) & \text{if} \quad i = 1 \\ \alpha_{\mathrm{solv}}(c_{solv,i+1} - 2c_{\mathrm{solv},i} + c_{solv,i-1}) + \gamma_{\mathrm{solv}}(c_{solv,i+1} - c_{solv,i-1}) & \text{if} \quad 1 < i < N_{\mathrm{SEI}} \\ 0 & \text{if} \quad i = N_{\mathrm{SEI}} \end{cases} \quad \begin{cases} \alpha_{\mathrm{solv}} = \frac{D_{\mathrm{solv}}}{(L_{\mathrm{SEI}}\Delta\xi)^2} \\ \beta_{\mathrm{solv}} = \Big(\frac{\xi - 1}{2L_{\mathrm{SEI}\Delta\xi}} \frac{dL_{\mathrm{SEI}}}{dt}\Big) \\ \gamma_{\mathrm{solv}} = \Big(\frac{2}{L_{\mathrm{SEI}\Delta\xi}} + \frac{1}{D_{\mathrm{solv}}} \frac{dL_{\mathrm{SEI}}}{dt}\Big) \end{cases} \tag{5.16}$$

Side reaction current density

$$i_s = -2Fk_f (c_{s,n}^{surf})^2 c_{solv}^{surf} exp\Big[\frac{-\beta F}{R_g T_c}(\Phi_{s,n} - R_{SEI} I_{cell} - U_s)\Big] \tag{5.17}$$

Electrolyte porosity

$$\epsilon_{e,n} = 1 - \epsilon_{f,n} - \epsilon_{s,n}\Big(1 + \frac{3L_{SEI}}{R_{s,n}}\Big) \tag{5.18}$$

SEI layer growth

$$\frac{dL_{SEI}}{dt} = -\frac{i_s M_{SEI}}{2F\rho_{SEI}} \tag{5.19}$$

SEI resistance

$$R_{sei} = \frac{L_{SEI}}{a_{s,n} A L_n \kappa_{SEI}} \tag{5.20}$$

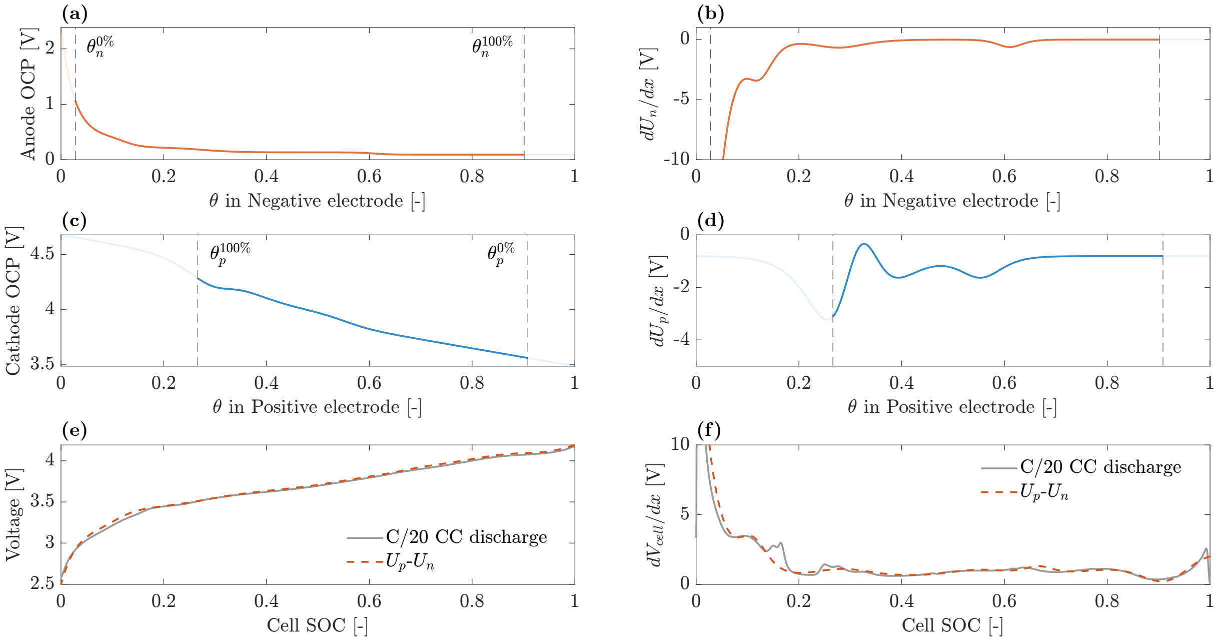

Figure 5.3: Comparison between the modeled cell OCV (i.e., $U_p - U_n$) for the LG M50, obtained using equations (5.8) and (5.9), and the measured OCV obtained through a pseudo-OCV test for the LG M50T (Section 4.2.2.1).

end, it is essential to verify that:

$$\begin{aligned} V_{OCV}^{max} &= U_p(\theta_p^{100\%}) - U_n(\theta_n^{100\%}) \\ V_{OCV}^{min} &= U_p(\theta_p^{0\%}) - U_n(\theta_n^{0\%}) \end{aligned} \tag{5.22}$$

By ensuring that the stoichiometric limits fall within these voltage constraints, one can verify the proper operation of the cell and maintain its safety and efficiency.

Here, the condition given in equation (5.22) is checked by comparing the values of U_j, $\theta_j^{0\%}$, and $\theta_j^{100\%}$ provided by [96] for the M50 electrode with the full cell OCV of the M50T, as obtained from the experimental campaign[1]. The verification results are presented in Figure 5.3. Specifically, Figures 5.3(a) and (c) show the U_n and U_p, as described in equations (5.8) and (5.9), respectively, with the corresponding stoichiometric limits highlighted. The measured full cell OCV, obtained through the C/20 discharge pseudo-OCV test, is compared to the modeled OCV (i.e., $U_p - U_n$) as illustrated in FIugre 5.3(e). Two main trends are observed: 1) The minimum and maximum voltages are within the expected limits. 2) Despite some discrepancies at low SOC, the modeled OCV is in good agreement with the measured one.

Additionally, to further evaluate the accuracy of the modeled OCV, the derivative $\frac{dV_{OCV}}{d\theta}$ is calculated for both the measured and modeled OCV, as shown in Figures 5.3(b), (d), and (f). This comparison further confirms the suitability of the OCP profiles provided by [96] for the LG M50T.

---

[1] The full cell OCV is determined using a pseudo-OCV test at C/20 constant current discharge, as described in Section 4.2.2.1

Step 2: **ESPM parameters identifiction and validation**

All parameters for the ESPM are sourced from [96] (see Table 5.1), with the exception of the active material volume fractions for both electrodes ($\epsilon_{s,j}$). These parameters are individually determined for each of the 19 tested M50T cells using a C/20 constant current discharge cycle. It is important to highlight that $\epsilon_{s,n}$ and $\epsilon_{s,p}$ are particularly influential due to their high sensitivity in battery electrochemical models under constant current conditions, as documented in the literature [145, 117]. Additionally, variations in $\epsilon_{s,j}$ directly affect electrode porosity, which is calculated using the formula $\epsilon_{e,j} = 1 - \epsilon_{s,j}$. Following the approach outlined in [144], the subset of parameters $\Theta = [\epsilon_{s,n}, \epsilon_{s,p}]$ is identified by solving the following optimization problem:

$$\begin{aligned} \min_{\Theta} \quad & J_1(\Theta) + J_2(\Theta) + J_3(\Theta) \\ \text{subject to} \quad & \text{ESPM governing equations} \end{aligned} \tag{5.23}$$

Here, $J_1(\Theta) = \sqrt{\frac{1}{N}\sum_{i=1}^{N}(V_{cell}^{data} - V_{cell}^{model})^2}$ represents the root mean squared error (RMSE) between the measured and simulated cell voltages, as given by equation (5.7). $J_2(\Theta) = \sqrt{\frac{1}{N}\sum_{i=1}^{N}(SOC^{ref} - SOC_n)^2}$ and $J_3(\Theta) = \sqrt{\frac{1}{N}\sum_{i=1}^{N}(SOC^{ref} - SOC_p)^2}$ denote the RMSE between the Coulomb counting SOC and the bulk SOC for the anode and cathode, respectively. It is important to note that the optimization problem given in equation (5.23) is solved for each of the 19 tested cells under the corresponding C/20 discharging cycle.
The identification results are summarized in Figure 5.4. Overall, the performance of the 19 identified ESPMs are satisfactory, as demonstrated by the voltage RMSEs (Figure 5.4(b)), which remains between 15 and 21 mV. Additionally, Figure 5.4(a) compares the simulated and measured voltage profiles for cells P12 and P13. This comparison highlights that the only re-identification of $[\epsilon_{s,n}, \epsilon_{s,p}]$ effectively capture CtC variations in capacity among fresh cells. Figure 5.4(c) shows that the ESPM accurately reflects the cell SOC. Moreover, Figure 5.4(d) presents the identified values for $\epsilon_{s,n}$ and $\epsilon_{s,p}$ against the corresponding cell capacities (Q_{cell}), calculated as described in Section 4.2.2.1. The identified $\epsilon_{s,n}$ and $\epsilon_{s,p}$ exhibit a mean value and standard deviation $[\mu_{\epsilon_{s,j}}, \sigma_{\epsilon_{s,j}}]$ equal to [0.801, 0.006] and [0.702, 0.005], respectively. Furthermore, a significant linear correlation is evident between both $\epsilon_{s,j}$ and Q_{cell} is evident:

$$\begin{aligned} \epsilon_{s,n} &= 0.0091055 + 0.16312 \cdot Q_{cell} \\ \epsilon_{s,p} &= 0.011719 + 0.14208 \cdot Q_{cell} \end{aligned} \tag{5.24}$$

showing a R^2 values of 0.993 and 0.967, respectively. This trend, expected due to the linear dependence of electrode capacity (Q_j) on the active material volume fraction ($Q_j = FAL_j\epsilon_{s,j}c_{s,j}^{max}(\theta_j^{100\%} - \theta_j^{0\%})/3600$, as pointed out in eq. (7) of [149]), confirms the physical-meaning of the identified parameter values.
Lastly, the identified ESPMs are validated against the corresponding HPPC+MS cycle. Figure 5.5 summarizes the model validation results. Specifically, Figures 5.5(a) and (c) offer a visual comparison between the measured and simulated voltages, and between the

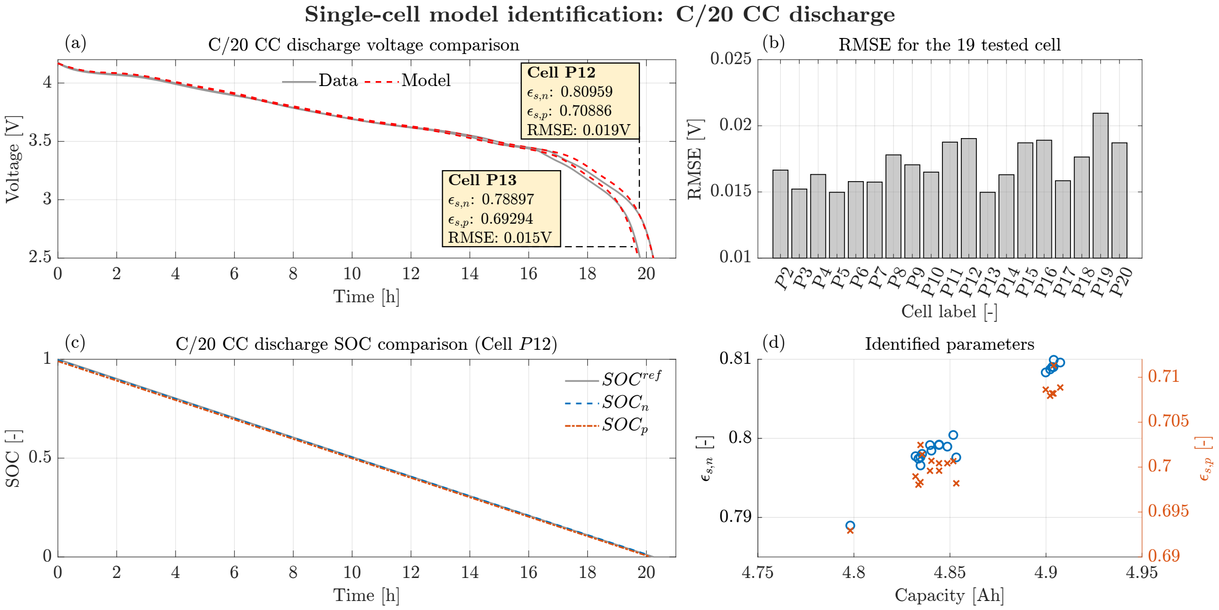

Figure 5.4: Single-cell parameter identification results at C/20 for the 19 LG M50T cells. (a) Voltage profile comparison between experimental CC discharge and model simulations for cells P12 and P13. (b) RMES between experimental data and model predictions during CC C/20 discharge for all cells. (c) SOC comparison between model predictions and experimental measurements for cell P12. (d) identified parameters (i.e. $\epsilon_{s,n}$ and $\epsilon_{s,p}$) for the 19 tested cells against cell capacity.

Coulomb counting SOC and the electrode SOC for cell P12, respectively. Overall, the ESPMs demonstrate a good fit for both cell voltage and SOC. This accuracy is underscored by the voltage RMSE for all tested cells (shown in Figure 5.5(b)), which ranges between 0.012 and 0.018 V. Additionally, the bar chart in Figure 5.5(c) displays the SOC RMSE for both electrodes across all cells, with a maximum RMSE of 0.9% for the negative electrode and 0.51% for the positive electrode.

5.2.2 ESPM-based module-level model validation

Based on the inegrated ESPM identified and validated in the previous section, whose formualtion id reported in Tabele 5.2, the aging model described in Section 3.1.5.1, and the module thermal and electrical models discussed in Sections 3.2.2 and 3.2.1 and schematically depicted in Figure 5.6, respectively, the state-space model for the parallel module can be expressed as follows:

$$\begin{cases} \dot{c}_{s,j}^{mod} = A_{s,j}^{mod} c_{s,j}^{mod} + B_{s,j}^{mod} I_{cell}^{mod} - G_{s,j}^{mod} \\ \dot{c}_{e}^{mod} = A_{e}^{mod} c_{e}^{mod} + B_{e}^{mod} I_{cell}^{mod} \\ \dot{T}_{state}^{mod} = A_{therm}^{mod} T_{state}^{mod} + B_{therm}^{mod} I_{cell}^{mod} - G_{therm}^{mod} \\ \dot{c}_{solv}^{mod} = F_{solv}^{mod} \\ \dot{L}_{sei}^{mod} = G_{sei}^{mod} \end{cases} \tag{5.25}$$

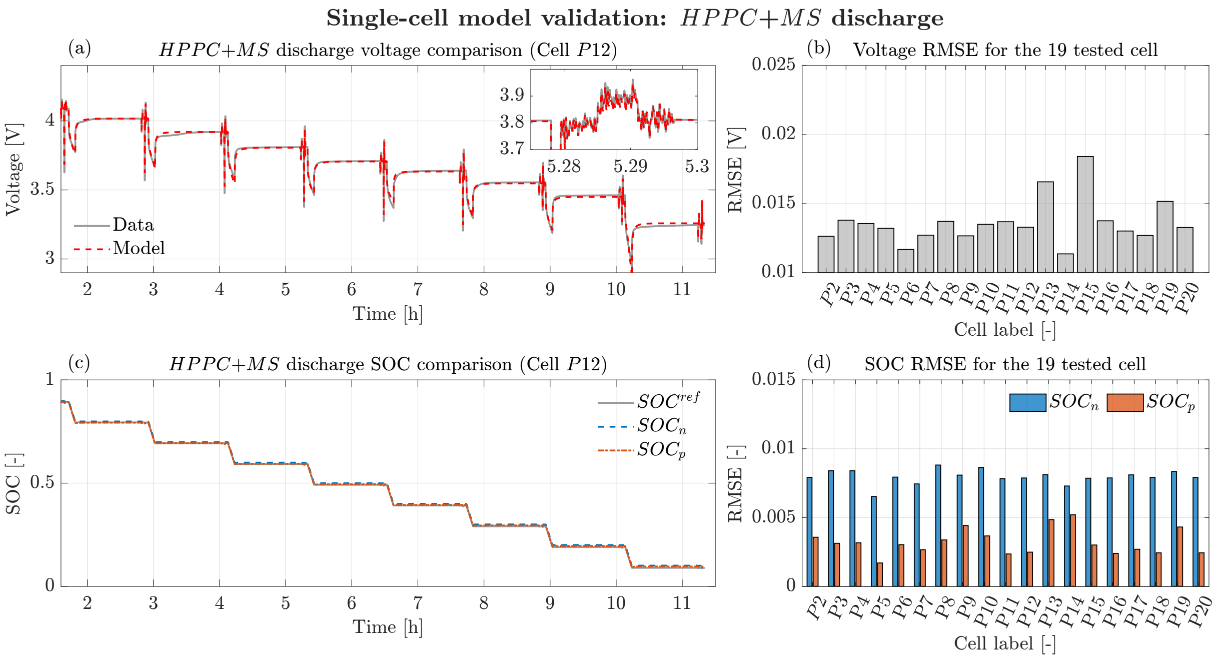

Figure 5.5: Single-cell parameter validation for the 19 LG M50T cells under HPPC+MS testing protocol. (a) and (c) Voltage profile and SOC comparison between experiments and model simulations for cell P12, respectively. (b) RMES between experimental voltage and model predictions for all cells. (d) RMES between reference SOC and electrode SOC for all the cells.

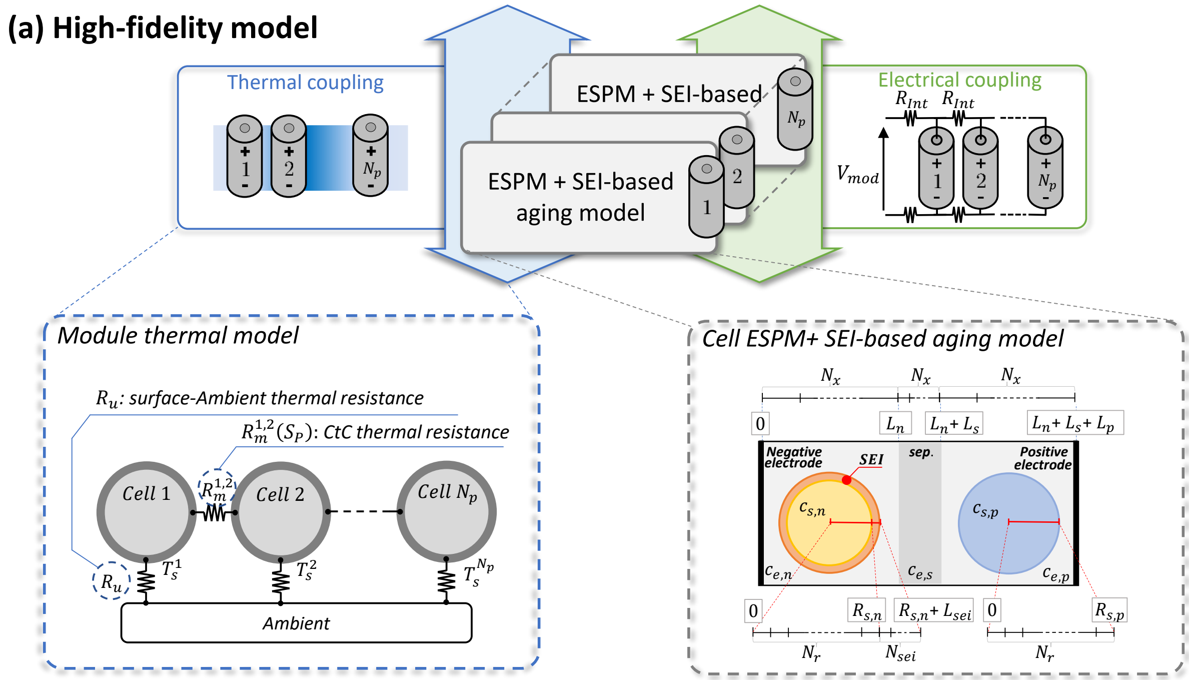
(a) High-fidelity model
Thermal coupling
ESPM + SEI-based
ESPM + SEI-based aging model
Electrical coupling
R_{Int}
V_{mod}
Module thermal model
R_u: surface-Ambient thermal resistance
$R_m^{1,2}(S_P)$: CtC thermal resistance
Cell 1
Cell 2
Cell N_p
T_s^1
T_s^2
$T_s^{N_p}$
Ambient
Cell ESPM+ SEI-based aging model
N_x
L_n
$L_n + L_s$
$L_n + L_s + L_p$
Negative electrode
SEI
sep.
Positive electrode
$c_{s,n}$
$c_{s,p}$
$c_{e,n}$
$c_{e,s}$
$c_{e,p}$
$R_{s,n}$
$R_{s,n} + L_{sei}$
$R_{s,p}$
N_r
N_{sei}

Figure 5.6: Schematic representation of the physics-based electrochemical-aging-thermal model for the battery module, where the module thermal model and the ESPM coupled with the SEI-based aging model are highlighted.

In this model, the state variables $c_{s,j}^{mod} \in \mathbb{R}^{N_p\cdot(N_r-1)}$, $c_e^{mod} \in \mathbb{R}^{N_p\cdot 3N_x}$, $c_{solv}^{mod} \in \mathbb{R}^{N_p\cdot N_{sei}}$, $T_{state}^{mod} \in \mathbb{R}^{3N_p}$, and $L_{sei}^{mod} \in \mathbb{R}^{N_p}$ represent the combined solid, liquid, and solvent concentrations, cell temperatures, and SEI thickness of each cell within the module, as shown in eq. (5.31). The matrices and non-linear input terms of the state-space model, namely $A_{s,j}^{mod}$, $B_{s,j}^{mod}$, A_e^{mod}, B_e^{mod}, A_{therm}^{mod}, B_{therm}^{mod}, $G_{s,j}^{mod}$, G_{therm}^{mod}, and G_{sei}^{mod}, are provided in Table 5.3. It should be noted that the model input is I_{mod}, while $I_{cell}^{mod} = \begin{bmatrix} I_{cell}^{[1]} & \cdots & I_{cell}^{[N_p]} \end{bmatrix}^T \in \mathbb{R}^{N_p}$ represents the currents delivered by each cell, which are obtained by solving the system of N_p equations:

$$\begin{cases} V_{cell}^{[k+1]} = V_{cell}^{[k]} - 2R_{int}(\sum_{z=k+1}^{N_p} I_{cell}^{[z]}) \\ I_{tot} = \sum_{k=1}^{N_p} I_{cell}^{[k]} \end{cases} \tag{5.26}$$

where $k \in \{1, \cdots, N_p - 1\}$, and the model output $V_{mod} = V_{cell}^{[1]} + 2R_{int}I_{tot}$.

Module-level model identification and validation

In this section, the validation of the module-level electrical model, as well as the identification and validation of the thermal model, is discussed. Notably, we consider nine different configurations of four cells connected in parallel, under various combinations of interconnection resistance (R_{int} = 0, 1, and 3 $m\Omega$) and ambient temperature (T_{amb} = 10, 25, and 40 $°C$). It is important to clarify that the thermal model of the individual cell was not identified in the previous section. This omission is due to the characteristics of the testing methods used: the Pseudo-OCV involves a very low discharging rate, and the HPPC tests include long rest periods. Both factors limit the ability to evaluate the thermal dynamics of the single cell effectively since the cell temperature does not rise. Therefore, the thermal dynamics of the cell are identified at the module level considering a CC discharge at 0.75C-rate, considering the scenario with $R_{int} = 1$ mΩ at 25$°C$, while reserving the other eight case studies as validation cycles. Specifically, the parameters $\Theta_{th} = [R_u, R_m, C_s]$, introduced in Section 3.2.2 for the module thermal model, are identified by solving the following optimization problem:

$$\begin{aligned} \min_{\Theta_{th}} \quad & \sum_{k=1}^{N_p} \left(\sqrt{\frac{1}{N} \sum_{i=1}^{N} \left(T_{cell}^{[k],data} - T_{cell}^{[k],model} \right)^2} \right) \\ \text{subject to} \quad & \text{Model governing equations (5.25)} \end{aligned} \tag{5.27}$$

where the cost function is defined as the sum of the RMSE between the measured and simulated temperatures for each cell in the module. Following the identification of the set of parameters, the model's ability to accurately represent the thermal distribution within the module is assessed. This evaluation involves comparing the mean temperature standard deviation ($\sigma_{T_{cell}}$) and the average cell temperature ($\mu_{T_{cell}}$) across different experimental scenarios:

$$\sigma_{T_{cell}} = \frac{1}{N}\sum_{z=1}^{N}\left(\sqrt{\frac{1}{N_p-1}\sum_{k=1}^{N_p}\left(T_{cell}^{[k]}|_{t=z} - \sum_{q=1}^{N_p}\bar{T}_{cell}^{[q]}|_{t=z}\right)^2}\right) \tag{5.28}$$

$$\mu_{T_{cell}} = \frac{1}{N}\sum_{z=1}^{N}\left(\sqrt{\frac{1}{N_p}\sum_{k=1}^{N_p}T_{cell}^{[k]}|_{t=z}}\right) \tag{5.29}$$

Further, the model ability to predict the cell current imbalance is analyse throught the mean cell current standard deviation ($\sigma_{I_{cell}}$), calculated as:

$$\sigma_{I_{cell}} = \frac{1}{N}\sum_{z=1}^{N}\left(\sqrt{\frac{1}{N_p-1}\sum_{k=1}^{N_p}\left(I_{cell}^{[k]}|_{t=z} - \sum_{q=1}^{N_p}\bar{I}_{cell}^{[q]}|_{t=z}\right)^2}\right) \tag{5.30}$$

Note that, the mean value for the current distribution is not considered since the simulated and experimental currents are identical (I_{mod}/N_p) due to the constraints imposed by Kirchhoff's circuit laws (5.26).
Figure 5.7 (a-d) presents a comparison between the simulated temperatures and those experimentally measured during the identification cycle. Two main observations emerge: firstly, the thermal measurements exhibit significant noise, and secondly, the thermal model successfully captures the dynamics of each cell. Furthermore, the comparison between $\sigma_{T_{cell}}$ and $mu_{T_{cell}}$ calculated for the experimental and simulated data are presented in Figures 5.7(e-g) and 5.7(h-l) respectively. It is evident that the model satisfactorily predicts the average temperature within the module, as shown in Figures 5.7(h-l), though it tends to slightly overestimate it. On the other hand, the model performance declines in predicting the module thermal distribution, particularly when the interconnection resistance is low. This trend can be attributed to the low accuracy of the thermal sensors, which leads to imprecise thermal readings especially when thermal gradients are minimal, and to parasitic resistance introduced during module assembly that is not fully accounted for in the model formulation. Future work will explore the possibility of enhancing model accuracy with a more complex model. However, for this study, the overall performance of the model is considered satisfactory, particularly in light of the additional results that are presented for the current distribution in the following. In particular, Figure 5.8 presents the module-level model validation in terms of predictive accuracy for both overall module voltage and cell current distribution. It is important to note that the electrochemical parameters for each cell within the model remain consistent with those identified at the cell level in the previous Section. This validation approach not only tests the model's capability to predict overall module performance and heterogeneities but also evaluates whether the model can predict module imbalances by scaling up cell CtC variations to the module level. Figure 5.8 (a-b) presents a comparison between the measured and simulated voltages for $R_{int} = 0, 1,$ and 3 mΩ at $25°C$. along with the voltage RMSE for all module experiment scenarios considered. While the overall model performance slightly deterio-

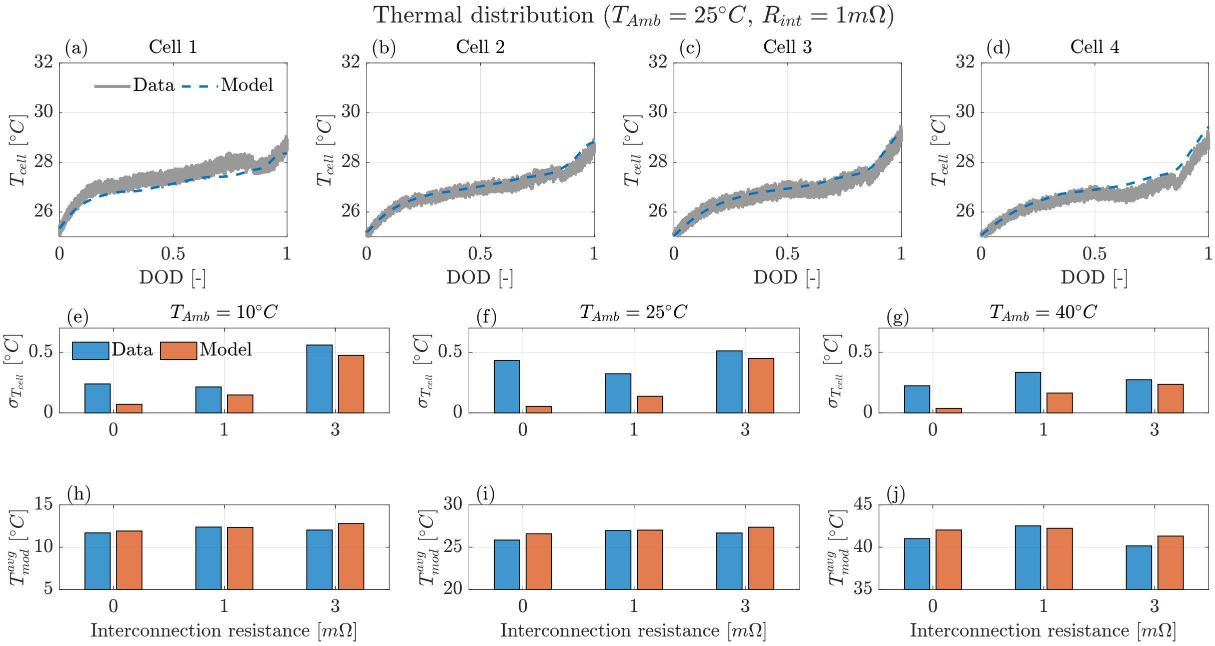

Figure 5.7: Module-Level thermal model results for four parallel-connected cells under $R_{int} = 0, 1,$ and 3 mΩ and $T_{amb} = 10, 25,$ and $40°C$. (a-d) Comparison of cell temperatures between experimental data and model simulations for the battery module subjected to a 1 mΩ of R_{int} at 25°C. (e-g) Comparisons between $\sigma_{T_{cell}}$ calculated using the simulated and measured cell theraml distribution. (h-l) Comparisons between $\mu_{T_{cell}}$ calculated using the simulated and measured cell theraml distribution.

rates compared to the single-cell results, it remains acceptable with the voltage RMSE still within the same order of magnitude as observed in the single-cell campaign. The performance degradation could be attributed to the fact that parameters were identified under a very low discharging rate (i.e. C/20) at a constant temperature ($25°C$), whereas the module-level validation was conducted at higher discharging rates and varying ambient temperatures. Nevertheless, the model accurately predicts cell current imbalances, as demonstrated by Figure 5.8 (g-i). It is evident that the $\sigma_{I_{cell}}$ calculated using the cell currents measured by the Hall sensor closely aligns with those calculated from the simulated current distribution.

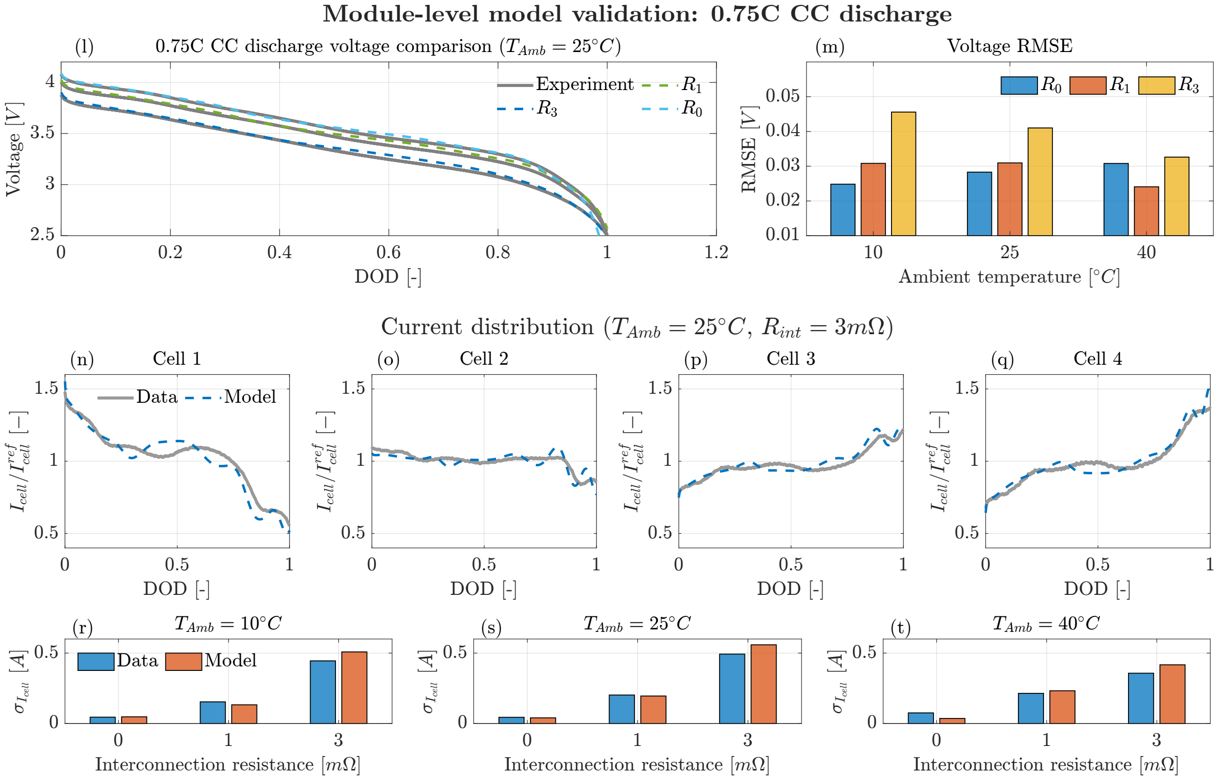

Figure 5.8: Module-Level model validation for four parallel-connected cells under $R_{int} = 0, 1, \text{and } 3$ mΩ and $T_{amb} = 10, 25, \text{and } 40°C$. (a) Comparison of voltage profiles between experimental data and model simulations for $R_{int} = 0, 1, \text{and } 3$ mΩ at $25°C$. (b) Voltage RMSE across all module experiment scenarios considered. (c-f) Comparison of cell currents between experimental data and model simulations for the battery module subjected to a 3 mΩ of R_{int} at 25°C. (g-i) Comparisons between $\sigma_{I_{cell}}$ calculated using the simulated and measured cell currents.

Table 5.3: Parallel-module state-space model matrices and coefficients of state-space model (5.25)

State-space model, State vectors

$$c_{s,j}^{\text{mod}} = \begin{bmatrix} c_{s,j}^{[1]} \\ c_{s,j}^{[2]} \\ \vdots \\ c_{s,j}^{[N_p]} \end{bmatrix} \qquad c_e^{\text{mod}} = \begin{bmatrix} c_e^{[1]} \\ c_e^{[2]} \\ \vdots \\ c_e^{[N_p]} \end{bmatrix} \qquad c_{\text{solv}}^{\text{mod}} = \begin{bmatrix} c_{\text{solv}}^{[1]} \\ c_{\text{solv}}^{[2]} \\ \vdots \\ c_{\text{solv}}^{[N_p]} \end{bmatrix} \qquad T_{cell}^{\text{mod}} = \begin{bmatrix} T_{cell}^{[1]} \\ T_{cell}^{[2]} \\ \vdots \\ T_{cell}^{[N_p]} \end{bmatrix} \tag{5.31}$$

Mass Conservation in the solid phase ($j \in [n,p]$), Matrices and Coefficients

$$A_{s,j}^{\text{mod}} = \begin{bmatrix} (\alpha_{s,j} A_{s,j})^{[1]} & & 0 \\ & \ddots & \\ 0 & & (\alpha_{s,j} A_{s,j})^{[N_p]} \end{bmatrix}_{N_r N_p \times N_r N_p} \qquad B_{s,j}^{\text{mod}} = \begin{bmatrix} (\beta_{s,j} B_{s,j})^{[1]} & & 0 \\ & \ddots & \\ 0 & & (\beta_{s,j} B_{s,j})^{[N_p]} \end{bmatrix}_{N_r N_p \times N_r N_p}$$

Mass Conservation in the electrolyte ($j \in [n,s,p]$), Matrices and Coefficients

$$A_e^{\text{mod}} = \begin{bmatrix} (\alpha_e A_e)^{[1]} & & 0 \\ & \ddots & \\ 0 & & (\alpha_e A_e)^{[N_p]} \end{bmatrix}_{3N_x N_p \times 3N_x N_p} \qquad B_e^{\text{mod}} = \begin{bmatrix} (\beta_e B_e)^{[1]} & & 0 \\ & \ddots & \\ 0 & & (\beta_e B_e)^{[N_p]} \end{bmatrix}_{3N_x N_p \times 3N_x N_p}$$

Module Thermal Model: Matrices and Coefficients

Air conductive heat thermal resistance

$$R_m^{air} = \frac{1}{S_{cell} k_{air}} \tag{5.32}$$

Tabs conductive heat thermal resistance

$$R_m^{tabs} = \frac{w}{A_{cell} k_{tabs}} \tag{5.33}$$

$$A_{\text{therm}}^{\text{mod}} = \begin{bmatrix} \frac{-1}{C_s}\left(\frac{1}{R_u} + \frac{1}{R_m}\right) & \frac{1}{R_m C_s} & 0 & 0 & \dots & 0 & 0 \\ \frac{1}{R_m C_s} & \frac{-1}{C_s}\left(\frac{1}{R_u} + \frac{2}{R_m}\right) & \frac{1}{R_m C_s} & 0 & \dots & 0 & 0 \\ 0 & \frac{1}{R_m C_s} & \frac{-1}{C_s}\left(\frac{1}{R_u} + \frac{2}{R_m}\right) & \frac{1}{R_m C_s} & \dots & 0 & 0 \\ \vdots & \vdots & \vdots & \vdots & \ddots & \vdots & \vdots \\ 0 & 0 & 0 & 0 & \dots & \frac{1}{R_m C_s} & \frac{-1}{C_s}\left(\frac{1}{R_u} + \frac{1}{R_m}\right) \end{bmatrix}_{N_p \times N_p}$$

$$B_{\text{therm}}^{\text{mod}} = \begin{bmatrix} \frac{1}{C_c}\left(V_{\text{OCP}}^{[1]} - V_{\text{Cell}}^{[1]}\right) + T_{cell}^{[1]} \frac{dV_{OCP}}{dT_{cell}} & \cdots & 0 \\ \vdots & \ddots & \vdots \\ 0 & \cdots & \frac{1}{C_c}\left(V_{\text{OCP}}^{[N_p]} - V_{\text{Cell}}^{[N_p]}\right) + T_{cell}^{[N_p]} \frac{dV_{OCP}}{dT_{cell}} \end{bmatrix}_{N_p \times N_p}$$

Aging matrices and Nonlinear input vectors

$$G_{\text{SEI}}^{\text{mod}} = \begin{bmatrix} (\beta_{\text{SEI}} g_{s,n})^{[1]} \\ \vdots \\ (\beta_{\text{SEI}} g_{s,n})^{[N_p]} \end{bmatrix}_{N_p \times 1} \qquad G_{s,j}^{\text{mod}} = \begin{bmatrix} (\beta_{s,j} B_{s,j} g_{s,j})^{[1]} \\ \vdots \\ (\beta_{s,j} B_{s,j} g_{s,j})^{[N_p]} \end{bmatrix}_{N_p N_r \times 1} \qquad g_{s,j} = \begin{cases} a_{s,n} L_n A i_s, & \text{if j=n} \\ 0, & \text{otherwise} \end{cases}$$

5.3 Conclusion

This chapter has presented a comprehensive methodology for cell teardown and its application in the parameterization of electrochemical models. Additionally, it reviewed parameter sensitivity analysis techniques, which, when combined with optimization methods, form the foundation of an effective strategy for parameter identification.

A practical application of this methodology was demonstrated through the model identification of the LG M50T cell, tested at the SECL laboratory. Starting with parameters derived from the LG M50 model, as described in [96], the identification process focused on refining high-sensitivity parameters, determined through a sensitivity analysis of the ESPM. The adjusted parameters were optimized to ensure a closer alignment with the experimental cell voltage response, thereby improving model accuracy.

The chapter concluded with the validation of a module-level model comprising four parallel-connected ESPM cells. This model, pivotal to the high-fidelity offline simulations described in Chapter 8, provides a robust framework for simulating the behavior of parallel-connected cells and serves as a foundation for further simulation studies.

Chapter 6

CS-ESPM model order reduction

Contents

6.1 CSa-ESPM numerical solution 120
6.1.1 FDM-based CSa-ESPM: 2P-Region Approximation 120
6.1.2 CSa-ESPM: State-space formulation 123
6.2 CSa-ESPM moder order reduction 125
6.2.1 POD-Galerkin ROM 126
6.2.2 FVM-based CSa-ESPM 132
6.3 Conclusion 136

This contribution is based on the following works:

- [29] **Fasolato, S.**, Allam, A., Li, X., Lee, D., Ko, J., and Onori, S. (2022). *Reduced-order model of lithium-iron phosphate battery dynamics: A POD-Galerkin approach.* IEEE Control Systems Letters, 7, 1117-1122.
- [30] Xu, L., **Fasolato, S.**, and Onori, S. (2024). *Finite-volume method and observability analysis for core-shell enhanced single particle model for lithium iron phosphate batteries.* IEEE 2024 Conference on Decision and Control (CDC), **Accepted**.

Introduction

Cobalt- and nickel-free positive electrode materials for LIBs in the form of Lithium Iron Phosphate (LFP) are currently being considered for mass production in electric vehicle batteries. Despite their lower energy density, LFP batteries offer good electrochemical stability, thermal performance, and cycle life making them a suitable candidate for cobalt- and nickel-free batteries [16]. Olivine structured LFP batteries are characterized by a flat open circuit voltage due to the phase transition [21] and are accompanied by a significant hysteresis between the open circuit voltage during charge and discharge and strong path dependence dynamics [150], making it challenging to model and predict their internal behavior accurately. In particular, the dreaded flat voltage plateau is a major challenge to designing algorithms for real-time BMS. Owing to that, an electrochemical model that can accurately capture the battery dynamics, especially the phase transition behavior, would prove to be a good basis for designing advanced BMS algorithms.

Among the electrochemical models addressing the phase transition behavior of LFP batteries, the core-shell approach stands out as a key method. This model, initially developed by [39], is revisited in Chapter 3. As detailed in Section 3.1.2.3, the dynamics of the core-shell model are governed by PDEs coupled with an ODE that describes the movement of the phase transition boundary. This problem falls under the category of one-phase Stefan problem [151]. Such problems are common in various scientific and engineering applications, such as melting of a solid (i.e. ice into water). Numerous numerical methods have been proposed in the literature to address the Stefan problem [152, 153]. In core-shell models, Variable Space Grid (VSG) methods are frequently employed to numerically approximate the phase transition [154]. These methods involve dividing the shell region of the particle into a fixed number of points, with the spacing between grid points adjusted dynamically to reflect the movement of the phase transition interface, while maintaining a constant number of grid points. Coordinate transformations can further simplify the problem by converting the moving boundary into fixed coordinates. For example, the Landau transformation [155] is commonly used to address such issues, as demonstrated in [10, 156, 18]. Additionally, [157] utilized the Arbitrary Lagrangian-Eulerian (ALE) formulation, implemented in COMSOL, to solve the problem. In contrast, [158] approached the phase transition problem by maintaining a constant grid size over time, while introducing new points into the discretization grid based on the dynamics of the moving boundary.

Chapter contribute

This chapter summarizes two different ROMs developed for the Core-Shell Models developed in [10, 9, 28]. In [10], the CS-ESPM was discretized into an ODE system using the Landau transformation and FDM, resulting in a high-dimensional model with 169 state variables. Subsequently, [9] introduced the average CS-ESPM (CSa-ESPM), an advanced version of the CS-ESPM. This model eliminates discontinuities in the positive OCP and overpotential during the phase transition. Notably, while the concentration dynamics in both electrodes are identical, the models differ in their cell voltage calculations only. Finally, in [28], the CSa-ESPM was combined with a machine learning-based hysteresis model to form a hybrid model. This hybrid approach accurately captures hysteresis-induced voltage behavior and path dependence dynamics under real-world drive cycles. However, the discretized CSa-ESPM model, with its 169 state variables, remains complex and challenging to implement on hardware-constrained microcontrollers. Consequently, there is a need for a low-dimensional model that captures the system's dominant behavior while being accurate and computationally efficient.

The main contributions of this chapter are divided into two categories as follows:

1. *Based on the models presented in [10, 9, 28], a ROM is developed for the 49 Ah LFP/graphite cell based on the Proper Orthogonal Decomposition (POD)-Galerkin method.*

2. *A FVM-based ROM is formulated and identified for the 56 Ah LFP/graphite cell.*

Chapter structure

- **Section 6.1** provides an overview of the numerical techniques used to approximate the CSa-ESPM in the previous works [10, 9]. Specifically, Section 6.1.1 revisits the FDM-based discretization for the Stefan problem in the CSa-ESPM. Section 6.1.2 summarizes the overall cell state-space representation of the CSa-ESPM for the LG Chem LFP cell with a nominal capacity of 49 Ah [1].

- **Section 6.2** presents the ROMs for the CSa-ESPM. It covers the formulation, validation results, and limitations of the POD-Galerkin ROM designed for the 49 Ah cell in Sections 6.2.1, 6.2.1.1, and 6.2.1.2, respectively. Further the formulation, parameter identification and validation results of the FVM-based CSa-ESPM are provided in Sections 6.2.2 and 6.2.2.1, respectively.

- **Section 6.3** summarizes the conclusions drawn and outlines future research opportunities.

---

[1] Cell specifications given in Chapter 4

6.1 CSa-ESPM numerical solution

In previous studies [10, 9], the CSa-ESPM was numerically solved and identified for a 49 Ah LFP pouch cell. This section provides an overview of the techniques originally used to approximate the CSa-ESPM. Specifically, Section 6.1.1 reviews the numerical approximation of the cell's solid-phase dynamics during two-phase (2P) operating scenarios, as described in [10]. Following that, Section 6.1.2 presents the overall cell model. It is important to note that this model serves as a benchmark for the development of the ROMs.

6.1.1 FDM-based CSa-ESPM: 2P-Region Approximation

In [10, 9], the Landau transformation was utilized to numerically solve the Stefan problem outlined in Section 3.1.2.3. This transformation involved remapping the shell region from $[r_p, R_p]$ to $[0, 1]$, thus rendering the shell calculation domain stationary while accommodating boundary movement, as shown in Figure 6.1(a). The coordinate transformation is given by:

$$\chi = \frac{r - r_p}{R_p - r_p} \in [0, 1] \tag{6.1}$$

where r denotes the radial position within the particle, and r_p is the moving boundary. Applying this transformation, the governing equation for solid-phase diffusion in the two-phase region (3.2) is reformulated as:

$$\frac{\partial c_{s,p}}{\partial t} = \frac{\partial^2 c_{s,p}}{\partial \chi^2}\left[\frac{D_{s,p}}{(R_p - r_p)^2}\right] + \frac{\partial c_{s,p}}{\partial \chi}\left[\frac{2D_{s,p}}{r(R_p - r_p)}\right] - \frac{\partial c_{s,p}}{\partial \chi}\frac{\partial r_p}{\partial t}\left[\frac{\chi - 1}{R_p - r_p}\right] \tag{6.2}$$

The corresponding boundary conditions (3.17) in the χ coordinate are expressed as:

$$\left.\frac{\partial c_{s,p}}{\partial \chi}\right|_{\chi=1} = \frac{I_{cell}(R_p - r_p)}{D_{s,p} a_p A_{cell} F L_p}$$

$$\left.c_{s,p}\right|_{\chi=0} = g(I_{cell}) = \begin{cases} c^{\beta}_{s,p} & \text{Discharge} \\ c^{\alpha}_{s,p} & \text{Charge} \end{cases} \qquad \left.c_{s,p}\right|_{t=\bar{t}} = \mathrm{ic}_k$$

where $\chi = 0$ corresponds to the moving boundary r_p, and $\chi = 1$ corresponds to the surface R_p. Furthermore, the dynamics of the moving boundary (3.16) are rewritten as:

$$\text{sign}(I_{cell})(c^{\alpha}_{s,p} - c^{\beta}_{s,p})(R_p - r_p)\frac{dr_p}{dt} = D_{s,p}\left.\frac{\partial c_{s,p}}{\partial \chi}\right|_{\chi=0} \tag{6.3}$$

According to Section 3.1.3, various numerical methods can be employed to solve the governing PDEs of electrochemical models. In [10], the FDM was utilized to approximate lithium-ion diffusion dynamics within the electrodes under both 1P and 2P operating conditions. Specifically, during two-phase operation, the shell region is discretized into N_r points, as illustrated in Figure 6.1(a). The first and second spatial derivatives of the

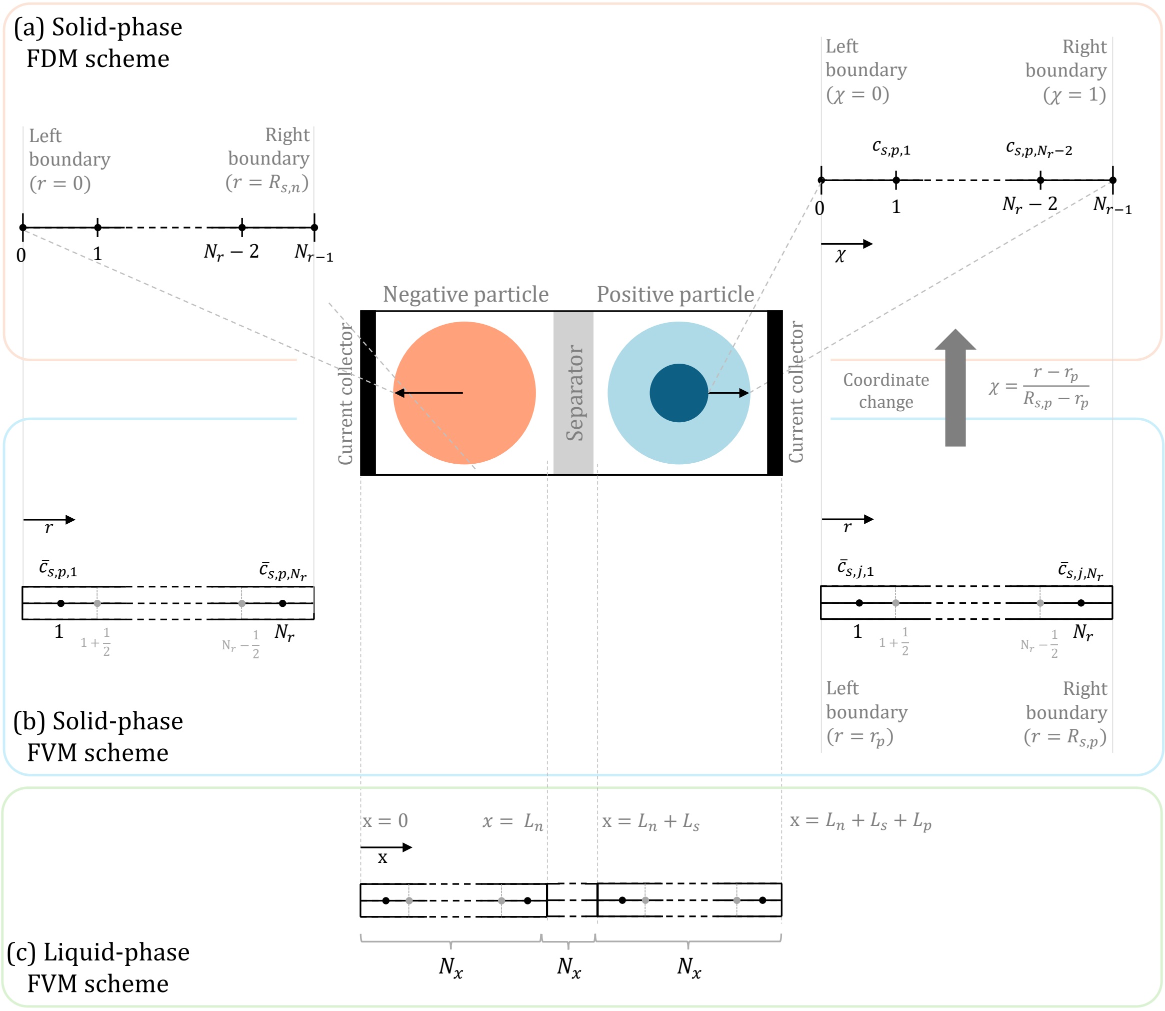
(a) Solid-phase FDM scheme
Left boundary (r = 0)
Right boundary (r = R_{s,n})
0
1
N_r − 2
N_{r−1}
Left boundary (χ = 0)
Right boundary (χ = 1)
c_{s,p,1}
c_{s,p,N_r−2}
χ
Negative particle
Positive particle
Current collector
Separator
Current collector
Coordinate change
χ = (r − r_p)/(R_{s,p} − r_p)
r
c̄_{s,p,1}
c̄_{s,p,N_r}
1 + 1/2
N_r − 1/2
N_r
c̄_{s,j,1}
c̄_{s,j,N_r}
Left boundary (r = r_p)
Right boundary (r = R_{s,p})
(b) Solid-phase FVM scheme
x = 0
x = L_n
x = L_n + L_s
x = L_n + L_s + L_p
x
N_x
N_x
N_x
(c) Liquid-phase FVM scheme

Figure 6.1: Overview of discretization grids used to numerically solve the diffusion PDE in the CSa-ESPM: (a) FDM grid for the solid particles, (b) FVM grid for the solid particles, and (c) FVM mesh for the liquid phase of the CSa-SPM.

equations (6.2) and (6.3) are approximated using forward and central difference schemes, respectively. As outlined in Section 3.1.3.1, these approximations are given by:

$$\frac{\partial c_{s,p,l}}{\partial \chi} \approx \frac{c_{s,p,l+1} - c_{s,p,l}}{\Delta_\chi} \tag{6.4}$$

$$\frac{\partial^2 c_{s,p,l}}{\partial \chi^2} \approx \frac{c_{s,p,l+1} - 2c_{s,p,l} + c_{s,p,l-1}}{\Delta_\chi^2} \tag{6.5}$$

where l denotes the index of the discretization point χ_l, defined as:

$$\chi_l = \frac{r_l - r_p}{R_p - r_p}, \quad \Delta_\chi = \chi_l - \chi_{l-1} \tag{6.6}$$

Applying these derivative approximations to (6.3), the dynamics of the moving boundary are approximated as:

$$\begin{aligned} \frac{dr_p}{dt} &= \frac{M_1}{\Delta_\chi}\left(c_{s,p_1} - \mathrm{g}(I_{cell})\right) \\ M_1 &= \frac{\mathrm{sign}(I_{cell})D_{s,p}}{(c^{\alpha}_{s,p} - c^{\beta}_{s,p})(R_p - r_p)} \end{aligned} \tag{6.7}$$

Similarly, the approximation is applied to eq. (6.2), and the discretized lithium-ion concentration at the internal nodes $l \in [1, N_{r,p} - 2]$ of the shell region is formulated as:

$$\frac{\partial c_{s,p,l}}{\partial t} = \frac{M_3}{\Delta_\chi^2}\left(c_{s,p_{l+1}} - 2c_{s,p_l} + c_{s,p_{l-1}}\right) + \frac{M_4}{\Delta_\chi}\left(c_{s,p_{l+1}} - c_{s,p_l}\right) \tag{6.8}$$

where M_3 and M_4 are defined as:

$$\begin{aligned} M_3 &= \frac{D_{s,p}}{(R_p - r_p)^2} \\ M_4 &= \frac{2D_{s,p}}{[\chi_l(R_p - r_p) + r_p](R_p - r_p)} - \frac{\chi_l - 1}{R_p - r_p}\frac{M_1}{\Delta_\chi}\left(c_{s,p_1} - \mathrm{g}(I_{cell})\right) \end{aligned} \tag{6.9}$$

According to [10], the discretized solid-phase mass transport equation at the shell surface ($l = N_{r,p} - 1$) is written as:

$$\left.\frac{\partial c_{s,p}}{\partial t}\right|_{N_{r,p}-1} = \frac{M_3}{\Delta_\chi^2}\left(M_2 I_{cell} - c_{s,p_{N_{r,p}-1}} + c_{s,p_{N_{r,p}-2}}\right) + \frac{M_2 M_4}{\Delta_\chi} I \tag{6.10}$$

where M_2 is defined as:

$$M_2 = \frac{(R_p - r_p)\Delta_\chi}{D_{s,p} a_p A_{cell} F L_p} \tag{6.11}$$

It is worth noting that, as indicated by Equation (3.17), at $l = 0$, the time derivative $\frac{\partial c_{s,p_0}}{\partial t}$ is zero, since c_{s,p_0} remains constant.
Finally, let the state vector $c_{s,p} = [c_{s,p,1}, \dots, c_{s,p,N_r-1}]^T \in \mathbb{R}^{N_r-1}$ represent the concentration at each point within the particle shell region, and considering the coefficients:

$$\eta_1 = \frac{M_3}{\Delta_\chi^2}, \quad \eta_2 = \frac{M_4}{\Delta_\chi}, \quad \eta_3 = \frac{M_2}{\Delta_\chi}\left(M_4 + \frac{M_3}{\Delta_\chi}\right), \quad \eta_4 = \frac{M_1}{\Delta_\chi} \tag{6.12}$$

the overall discretized mass conservation equation in 2P condition can be compactly expressed as:

$$\dot{c}_{s,p} = \eta_1 A_1 c_{s,p} + \eta_2 A_2 c_{s,p} + \eta_3 B I_{cell} + \eta_1 G \tag{6.13}$$

where the matrices $A_1 \in \mathbb{R}^{(N_r-1)\times(N_r-1)}$ and $A_2 \in \mathbb{R}^{(N_r-1)\times(N_r-1)}$ are given by:

$$A_1 = \begin{bmatrix} -2 & 1 & 0 & 0 & \dots & 0 \\ 1 & -2 & 1 & 0 & \dots & 0 \\ 0 & 1 & -2 & 1 & \dots & 0 \\ 0 & 0 & 1 & -2 & \dots & 0 \\ \vdots & \vdots & \vdots & \vdots & \ddots & \vdots \\ 0 & 0 & 0 & 0 & \dots & -1 \end{bmatrix}, \quad A_2 = \begin{bmatrix} -1 & 1 & 0 & 0 & \dots & 0 \\ 0 & -1 & 1 & 0 & \dots & 0 \\ 0 & 0 & -1 & 1 & \dots & 0 \\ 0 & 0 & 0 & -1 & \dots & 0 \\ \vdots & \vdots & \vdots & \vdots & \ddots & \vdots \\ 0 & 0 & 0 & 0 & \dots & 0 \end{bmatrix}$$

Similarly, the vectors $\mathbf{B} \in \mathbb{R}^{(N_r-1)\times 1}$ and $\mathbf{G} \in \mathbb{R}^{(N_r-1)\times 1}$ are defined as:

$$B = \begin{bmatrix} 0 \\ 0 \\ \vdots \\ 0 \\ 1 \end{bmatrix}, \quad G = \begin{bmatrix} g(I_{cell}) \\ 0 \\ \vdots \\ 0 \\ 0 \end{bmatrix}$$

6.1.2 CSa-ESPM: State-space formulation

This section summarizes the final state-space model for the CSa-ESPM as outlined in [10]. The mass conservation in the solid phase is numerically solved using the FDM in both 1P and 2P regions [46]. The discretization meshes used to approximate the Li-ion diffusion dynamics within the electrodes are depicted in Figure 6.1. The radius of the negative electrode particle, and the radius of the positive electrode particle for the 1P and the shell-region, are divided into N_r discretization points. Following [46], the mass conservation in the solid phase is approximated by a system of $N_r - 1$ ODEs, as shown in (6.14) and (6.16) for the negative electrode and 1P positive electrode, respectively. In contrast, (6.17) and (6.18) approximate the diffusion dynamics in the 2P positive electrode shell region and the moving boundary motion, as detailed in the previous section. On the other hand, FVM is employed for the liquid phase. Each cell domain is discretized into N_x volumes for approximating the electrolyte dynamics, as illustrated in Figure 6.1(c), resulting into a system of $3N_x$ ODEs (6.15), following the approach discussed in [66]. The model state vectors include the Li-ion concentration in the electrodes, represented as $c_{s,\text{j}} = [c_{s,\text{j},1}, \dots, c_{s,\text{j},N_r-1}]^T \in \mathbb{R}^{N_r-1}$, and in the electrolyte, denoted as $c_e = [c_{e,n}, c_{e,s}, c_{e,p}]^T \in \mathbb{R}^{3N_x}$, where $c_{e,\text{j}} = [c_{e,\text{j},1}, \dots, c_{e,\text{j},N_x}]^T \in \mathbb{R}^{N_x}$. Here, $c_{s,\text{j},\text{i}}$ refers to the Li-ion concentration at the i-th discretization point within the j-th electrode (where $\text{j} \in \{n, p\}$ for the solid phase), while $c_{e,\text{j},\text{i}}$ represents the Li-ion concentration in the i-th volume of the j-th cell domain (where $\text{j} \in \{n, s, p\}$ for the electrolyte phase). Additionally, $c_{s,\text{j}}^{\text{surf}} = c_{s,\text{j},N_r-1}$ and $c_{s,\text{j}}^{\text{bulk}} = \frac{3}{R_{s,j}^3} \int_0^{R_{s,j}} r^2 c_{s,\text{j}} \, dr$ denote the electrode surface and bulk concentrations, respectively.

The overall cell voltage (V_{cell}^{CC} for constant current and V_{cell}^{DV} for dynamic voltage) is computed as described in (6.19). Notably, V_{cell}^{DV} includes an additional term V_h to model hysteresis and path dependence dynamics during real driving cycles. This term V_h is

Table 6.1: Core-shell ESPM discretized electrochemical governing dynamics [9][10]

Model state-space formulation ***(The model matrices and coefficients are reported in [10])***

Negative electrode mass conservation

$$\dot{c}_{s,n} = \alpha_{s,n} A_{s,n} c_{s,n} + \beta_{s,n} B_{s,n} I_{cell} \tag{6.14}$$

1P positive electrode mass conservation

$$\dot{c}_{s,p} = \alpha_{s,p} A_{s,p} c_{s,p} + \beta_{s,p} B_{s,p} I_{cell} \tag{6.16}$$

Electrolyte mass conservation

$$\dot{c}_e = \alpha_e A_e c_e + \beta_e B_e I_{cell} \tag{6.15}$$

2P positive electrode mass cons. and r_p dynamics

$$\dot{c}_{s,p} = \eta_1 A_1 c_{s,p} + \eta_2 A_2 c_{s,p} + \eta_3 B I_{cell} + \eta_1 G \tag{6.17}$$

$$\dot{r}_p = \eta_4 (c_{s,p,1} - g(I)) \tag{6.18}$$

Model output: Cell voltage and SOC

Cell voltage

$$\begin{cases} V_{cell}^{CC} = U_p + \eta_p - U_n - \eta_n + \Delta\Phi_E - R_l I_{cell} \\ V_{cell}^{DV} = (U_p^{ch} + U_p^{dis})/2 + \eta_p - U_n - \eta_n + \Delta\Phi_E - R_l I_{cell} + V_h \end{cases} \tag{6.19}$$

Negative electrode OCP

$$\begin{aligned} U_n = {} & 0.1459 + 0.8442 \exp(-48.68\theta_n^{surf}) + 87.49 \exp(-665.8\theta_n^{surf}) - \exp(39.42\theta_n^{surf} - 41.92) + \\ & - 0.02975 \arctan(25.59\theta_n^{surf} - 4.099) - 0.012 \arctan(32.49\theta_n^{surf} - 15.74) \end{aligned} \tag{6.20}$$

Positive electrode OCP

$$\begin{cases} \textbf{Discarge} & U_p^{dis} = 3.382 - 0.2955 \exp\left[-44.99(1-z)^{0.8707}\right] + \\ & \quad + 10^{-20.71} \exp\left[14.17(1-z)^{8.128}\right] + 10^{-40.82} \exp\left[100(1-z)^{1.213}\right] \\ \textbf{Charge} & U_p^{ch} = 3.442 - 0.1774 \exp\left[-127.7(1-z)^{0.7921}\right] + \\ & \quad + 10^{-2.123} \exp\left[16.56(1-z)^{24.08}\right] + 10^{-10.29} \exp\left[99.91(1-z)^{22.17}\right] \end{cases} \quad \text{with: } \begin{cases} \textbf{One-phase (1P):} \\ \quad z = \theta_p^{surf} = \frac{c_{s,p}^{surf}}{c_{s,p}^{max}} \\ \textbf{Two-phase (2P):} \\ \quad z = \theta_p^{bulk} = \frac{c_{s,p}^{bulk}}{c_{s,p}^{max}} \end{cases} \tag{6.21}$$

Elelctrode overpotential

$$\eta_j = \frac{R_g T_c}{0.5F} \sinh^{-1}\left(\frac{I_{cell}}{2A a_{s,j} L_j i_{o,j}}\right) \tag{6.22}$$

Electrolyte overpotential

$$\begin{aligned} & \Delta\Phi_e = \frac{2RTv(c,T)}{F} \ln\left(\frac{c_e(L)}{c_e(0)}\right), \text{ with } L = L_n + L_s + L_p \\ & \rightarrow v(c,T) = 0.601 - 0.24(c_e^{avg}/1000)^{1/2} + \\ & \qquad + 0.982[1 - 0.0052(T - 273)](c_e^{avg}/1000)^{3/2} \end{aligned} \tag{6.23}$$

Exchange current density

$$\begin{cases} \textbf{negative electrode} & i_{o,n} = k_n F \sqrt{c_{e,n}^{avg} c_{s,n}^{surf} (c_{s,n}^{max} - c_{s,n}^{surf})} \\ \textbf{positive electrode} & i_{o,p} = k_p F \sqrt{c_{e,p}^{avg} k (c_{s,p}^{max} - k)} \text{ with: } \begin{cases} \text{1P: } k = c_{s,p}^{surf} \\ \text{2P: } k = c_{s,p}^{bulk} \end{cases} \end{cases} \tag{6.24}$$

State of charge

$$\begin{cases} \textbf{negative electrode} & SOC_n = \frac{\theta_n^{bulk} - \theta_{n,0\%}}{\theta_{n,100\%} - \theta_{n,0\%}} \\ \textbf{positive electrode} & SOC_p = \frac{\theta_{p,0\%} - \theta_p^{bulk}}{\theta_{p,0\%} - \theta_{p,100\%}} \end{cases} \tag{6.25}$$

provided by a physics-informed feedforward neural network (FNN), which was trained and validated in [28]. The FNN consists of 9 hidden layers with 17 neurons each and uses I_{cell}, $\theta_p^{\mathrm{bulk}} = c_{s,p}^{\mathrm{bulk}}/c_{s,p}^{\mathrm{max}}$, and c_e^{avg} from the CSa-ESPM solution as input features [28]. U_{j} and η_{j} are the electrode OCP and overpotential, respectively, I_{cell} is the input cell current, $\Delta\Phi_e$ is the electrolyte overpotential and R_l is the lumped cell resistance. U_n and η_n reported in (6.20) and (6.22) depend only on the particle surface concentration, while the positive electrode quantities (U_p and η_p) are calculated as a function of $c_{s,p}^{bulk}$ during the 2P condition and $c_{s,p}^{surf}$ during the 1P one, as shown in (6.21) and (6.22). According to [9], the $c_{s,p}^{bulk}$ is utilized during the 2P postive electrode to address the discontinuity in the output due to the surface concentration during the phase transition. Finally, the average positive OCP ($(U_p^{ch} + U_p^{dis})/2$) is used in V_{cell}^{DV} as opposed to U_p used in V_{cell}^{CC}. The SOC of each electrode is calculated based on the normalized bulk concentration ($\theta_{\mathrm{j}}^{bulk}$), as in (6.25).

It is important to note that the transition from one to two-phase region ($t = \bar{t}$) occurs when θ_p^{bulk} reaches $\theta_p^{\alpha} = c_{s,p}^{\alpha}/c_{s,p}^{max}$ ($\theta_p^{\beta} = c_{s,p}^{\beta}/c_{s,p}^{max}$) for discharging (charging). At the following time instant, the moving boundary switches from 0 to $R_{s,p} - \epsilon$ since the two-phase interface is on the particle surface, where ϵ is a small constant utilized to prevent singularities in the model formulation. The r_p then begins to decrease as a result of the core-region shrinking process.

6.2 CSa-ESPM moder order reduction

According to Sectin 3.1.3 of Chapter 3, various MOR techniques have been proposed in the literature for battery electrochemical model. It is to be noted that a core-shell ESPM for LFP is governed by nonlinear coupled dynamics due to the inclusion of one ODE in the positive electrode that models the moving boundary indicating the phase transition. Such an additional moving boundary ODE makes the model unsuitable for popular reduction methods. In [18], the solid state diffusion dynamics of a core-shell model is approximated by a polynomial to obtain a ROM. Another alternative approach is to utilize coarse-grained spatial grid points, instead of fine-grained, while discretizing battery governing PDAEs into ODAEs. However, fewer grid points result in a low-dimensional feeble system that is not only inaccurate but also susceptible to lack of numerical convergence while solving the moving boundary ODE that indicates the phase transition [10].

Here the CSa-ESPM is reduced using two different approaches: a POD-Galerkin method and the Finite Volume Method. It is important to note that the POD-based ROM is derived from the full model identified in [10, 9, 28] for the 49 Ah LFP cell. On the other hand, the FVM-based model is designed for the 56 Ah LFP cell, and therefore, the cell parameters are adjusted in accordance with the industrial partner's specifications based on provided experimental data.

6.2.1 POD-Galerkin ROM

In this section, the POD-Galerkin based ROM is formulated for the discretized CSa-ESPM (Table 6.1), according to Section 3.1.3.4. Fig. 6.2 provides a schematic representation of the steps required to develop the ROM and Table 6.2 reports the mathematical formulation of the model. According to eqs. (6.27) to (6.30), four different Snapshot matrices are generated solving eqs. (6.14) to (6.17) for a given constant input current. The columns of S_n and S_e contain the solution vectors $c_{s,n}$ and c_e of (3.2) and (3.4), for each time instant from the beginning (t_0) to the end (t_{end}) of the charge/discharge. Meanwhile, $S_{p,1P}$ and $S_{p,2P}$ are constructed considering the positive electrode concentration ($c_{s,p}$) during 1P ($t \in [t_0, \bar{t}-1] \vee [\bar{t}_f+1, t_{end}]$) and 2P ($t \in [\bar{t}, \bar{t}_f]$), respectively. Then, the truncated POD basis functions ($V_n^r, V_{p,1P}^r, V_{p,2P}^r$ and V_e^r) are obtained by keeping the first dominant columns of the basis functions ($V_n, V_{p,1P}, V_{p,2P}$ and V_e) that were previously generated by computing the SVD of the snapshot matrices, as reported in (6.31). Different truncation orders $[r_e, r_n, r_{p,1P}, r_{p,2P}]$ are selected for the electrolyte, negative and postive electrode in both 1P and 2P, respectively, such that the truncation degrees result close to 1, $r_e < N_x$ and $r_n, r_{p,1P}, r_{p,2P} < N_r$. Finally, the original state-space model eqs. (6.14) to (6.17) is projected onto new subspaces as shown in (6.32) in accordance with (3.61). The new state vectors, indicated with $\tilde{c}_{s,n} \in \mathbb{R}^{r_n}, \tilde{c}_{s,p} \in \mathbb{R}^{r_{p,P-2P}}$ and $\tilde{c}_e \in \mathbb{R}^{r_e}$, correspond to the projection of the Li-ion concentration in both electrodes and in the electrolyte onto the new subspaces. Note that the reduced-order state-space model is composed by $(r_n + r_{p,1P-2P} + r_e + 1)$ ODEs, instead of $(2(N_r - 1) + 3N_x + 1)$ ones as the original CSa-ESPM. Further, considering the POD truncated basis function and the solution of the (6.32), an approximation of the original state vectors ($\bar{c}_{s,j} \in \mathbb{R}^{N_r}$ and $\bar{c}_e \in \mathbb{R}^{3N_x}$) of the same dimension is reconstructed as:

$$\bar{c}_{s,n} = V_n^r \tilde{c}_{s,n} \quad \bar{c}_{s,p} = V_{p,(1P-2P)}^r \tilde{c}_{s,p} \quad \bar{c}_e = V_e^r \tilde{c}_e. \tag{6.26}$$

The $\bar{c}_{s,\mathrm{j}} = \begin{bmatrix} \bar{c}_{s,\mathrm{j},1} & \cdots & \bar{c}_{s,\mathrm{j},N_r-1} \end{bmatrix}^T$ are then used to obtain an approximation of the particle surface ($\bar{c}_{s,\mathrm{j}}^{surf} = \bar{c}_{s,\mathrm{j},N_r-1}$) and bulk concentration ($\bar{c}_{s,\mathrm{j}}^{bulk} = \frac{3}{R_{s,\mathrm{j}}^3} \int_0^{R_{s,\mathrm{j}}} r^2 \bar{c}_{s,\mathrm{j}} dr$) of each electrode. The $\bar{c}_{s,\mathrm{j}}^{surf}$, $\bar{c}_{s,\mathrm{j}}^{bulk}$ and $\bar{c}_e^{avg}$ are employed, in turn, for the calculation of the approximated cell voltage ($\bar{V}_{cell}$), SOC ($S\bar{O}C_{\mathrm{j}}$) and as input features for the FNN, in accordance with eqs. (6.19) to (6.25) in Table 6.1.

6.2.1.1 Simulation results

In this section, the POD-Galerkin ROM is compared against both the high-dimensional CSa-ESPM and experimental data. The experiments are carried out on a 49.9 Ah LFP pouch cell and consist of CC discharging cycles at C/3, C/6, C/10 and C/12 rate. The high dimensional CSa-ESPM is simulated considering the electrochemical parameters identified in [10] for a C/6-rate cycle and using $N_r = 70$ and $N_x = 10$ for the PDAE discretization. It should be noted that in [9], it was demonstrated that the configuration $[Nr, Nx] = [70, 10]$ provides the best trade-off in terms of simulation accuracy. The high dimensional CSa-ESPM is employed for the snapshot matrix generation for each input value, in accordance

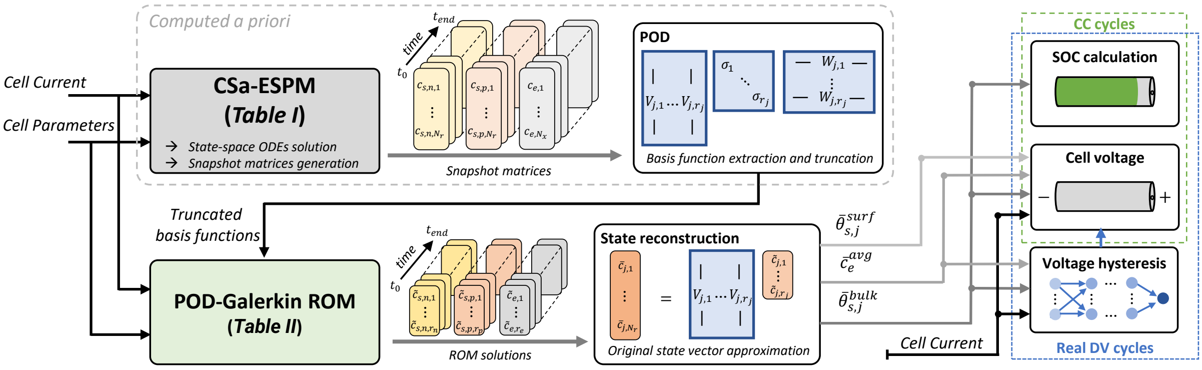
Computed a priori
Cell Current
Cell Parameters
CSa-ESPM
(Table I)
→ State-space ODEs solution
→ Snapshot matrices generation
time
t_0
t_{end}
$c_{s,n,1}$
c_{s,n,N_r}
$c_{s,p,1}$
c_{s,p,N_r}
$c_{e,1}$
c_{e,N_x}
Snapshot matrices
POD
$V_{j,1} \cdots V_{j,r_j}$
σ_1
σ_{r_j}
$W_{j,1}$
W_{j,r_j}
Basis function extraction and truncation
Truncated
basis functions
POD-Galerkin ROM
(Table II)
$\tilde{c}_{s,n,1}$
$\tilde{c}_{s,n,r_n}$
$\tilde{c}_{s,p,1}$
$\tilde{c}_{s,p,r_p}$
$\tilde{c}_{e,1}$
$\tilde{c}_{e,r_e}$
ROM solutions
State reconstruction
$\bar{c}_{j,1}$
$\bar{c}_{j,N_r}$
=
$\tilde{c}_{j,1}$
$\tilde{c}_{j,r_j}$
Original state vector approximation
$\bar{\theta}_{s,j}^{surf}$
$\bar{c}_e^{avg}$
$\bar{\theta}_{s,j}^{bulk}$
Cell Current
CC cycles
SOC calculation
Cell voltage
−
+
Voltage hysteresis
Real DV cycles

Figure 6.2: Model reduction flowchart applied to the CSa-ESPM

Table 6.2: POD-Galerkin average core-shell ESPM: Snapshot matrices and ROM state-space formulation

Snapshot matrices

Electrolyte dynamics

$$S_e = \begin{bmatrix} c_e^{t_0} & \cdots & c_e^{t_{end}} \end{bmatrix} \tag{6.27}$$

1P positive electrode solid phase dynamics

$$S_{p,1P} = \begin{bmatrix} c_{s,p}^{t_0} & \cdots & c_{s,p}^{\bar{t}-1} & c_{s,p}^{\bar{t}_f+1} & \cdots & c_{s,p}^{t_{end}} \end{bmatrix} \tag{6.28}$$

Negative electrode solid phase dynamics

$$S_n = \begin{bmatrix} c_{s,n}^{t_0} & \cdots & c_{s,n}^{t_{end}} \end{bmatrix} \tag{6.29}$$

2P positive electrode solid phase dynamics

$$S_{p,2P} = \begin{bmatrix} c_{s,p}^{\bar{t}} & \cdots & c_{s,p}^{\bar{t}_f} \end{bmatrix} \tag{6.30}$$

Snapshot matrices SVD an d POD basis functions truncation

$$S_\square = V_\square \Sigma_\square W_\square^T \quad \longrightarrow \quad V_\square = \begin{bmatrix} V_{\square,1} & \cdots & V_{\square,N_r} \end{bmatrix} \quad \longrightarrow \quad V_\square^r = \begin{bmatrix} V_{\square,1} & \cdots & V_{\square,r_\square} \end{bmatrix} \tag{6.31}$$

with: $\square = [e, n, (p, 1P), (p, 2P)]$

POD-Galerkin ROM state-space formulation

$$\left\{ \begin{array}{ll} \text{negative electrode} & \dot{\tilde{c}}_{s,n} = V_n^{r,T}(\alpha_{s,n} A_{s,n}) V_n^r \tilde{c}_{s,n} + V_n^{r,T}(\beta_{s,n} B_{s,n}) I_{cell} \\ \text{positive electrode} & \begin{cases} \text{1P: } \dot{\tilde{c}}_{s,p} = V_{p,1P}^{r,T}(\alpha_{s,p} A_{s,p}) V_{p,1P}^r \tilde{c}_{s,p} + V_{p,1P}^{r,T}(\beta_{s,p} B_{s,p}) I_{cell} \\ \text{2P: } \begin{cases} \dot{\tilde{c}}_{s,p} & = V_{p,2P}^{r,T}(\eta_1 A_1) V_{p,2P}^r \tilde{c}_{s,p} + V_{p,2P}^{r,T}(\eta_2 A_2) V_{p,2P}^r \tilde{c}_{s,p} + V_{p,2P}^{r,T}(\eta_3 B) I_{cell} + V_{p,2P}^{r,T}(\eta_1 G) \\ \dot{\tilde{r}}_p & = \eta_4(\bar{c}_{s,p,1} - g(I)) \end{cases} \end{cases} \\ \text{electrolyte} & \dot{c}_e = V_e^{r,T}(\alpha_e A_e) V_e^r c_e + V_e^{r,T}(\beta_e B_e) I_{cell} \end{array} \right. \tag{6.32}$$

POD-Galerkin ROM truncation orders and degrees

$$r_n = 2, \qquad r_{p,1P} = 3, \qquad r_{p,2P} = 3, \qquad r_e = 3 \tag{6.33}$$

$$\begin{array}{ll} \theta_n = 0.999999 & \theta_{p,1P} = 0.999997 \\ \theta_e = 0.999996 & \theta_{p,2P} = 0.999994 \end{array} \tag{6.34}$$

Table 6.3: %RMSEs between the ROM and the CSa-ESPM

	Discharging cycle			
C-rate:	$V_{cell}^{\%RMS}$	$SOC_n^{\%RMS}$	$SOC_p^{\%RMS}$	$r_p^{\%RMS}$
C/3	0.5149	0.0066	1.1373	2.0572
C/6	0.5542	0.0194	1.3857	1.4735
C/10	0.5728	0.0959	1.2745	1.9672
C/12	0.5561	0.0066	1.4434	1.2145
	Real driving cycle			
-	0.1209	0.0023	0.0053	0.0030

with Section 6.1.2. The POD truncation orders used in the ROM simulation, illustrated in (6.33), are selected to obtain truncation degrees close to unity, as shown in (6.34). Finally, the comparison between both models and the experimental data, in terms of cell voltage, SOC, and moving boundary is presented in Fig. 6.3 and 6.4 for both CC discharging profiles and real driving cycles. The discrepancies between the two models are evaluated through the percentage root mean squared error (%RMSE) between Ψ^{POD} (quantity from ROM) and Ψ (quantity from the high-dimensional CSa-ESPM):

$$\Psi^{\%RMS} = \sqrt{\frac{1}{t_{end}} \int_0^{t_{end}} (\Psi^{POD} - \Psi)^2 dt} \frac{100 t_{end}}{\int_0^{t_{end}} \Psi dt} \tag{6.35}$$

where $\Psi^{POD} \in [\bar{V}_{cell}, \bar{SOC}_j, \bar{r}_p]$ and $\Psi \in [V_{cell}, SOC_j, r_p]$. It is observed that the ROM matches the dynamics of the original model well, as depicted in Fig. 6.3 and 6.4. In particular, it provides an accurate approximation of the cell voltage (%RMSE consistently below 0.6%) and negative SOC, as indicated by $V_{cell}^{\%RMS}$ and $SOC_n^{\%RMS}$ in Table 6.3. In contrast, the %RMSE of positive SOC and moving boundary r_p are slightly higher, but still within 2.1%, showing that the ROM conserves the phase transition information. It needs to be stressed that the ROM results shown in Fig. 6.3 and 6.4 are obtained by solving a system of 9 ODEs (i.e. 2: negative electrode, 3+1: positive electrode + moving boundary, 3: electrolyte), instead of the 169 ODEs used for the CSa-ESPM. This stunning reduction in model-order results in low usage of memory during simulation, wherein the ROM requires only one-third of the peak memory needed by CSa-ESPM to simulate the cell dynamics for the CC profiles listed in Table 6.3. The simulation time of the ROM, though, is in the same order of magnitude as that of CSa-ESPM, which is expected when the POD-Galerkin method is applied to reduce the order of a non-linear model [159]. Overall, the primary advantage of the POD-Galerkin ROM is the considerable reduction of the number of ODEs (from 169 to 9) describing the cell electrochemical dynamics while accounting for the phase transition, easing the computational burden, and still maintaining accuracy.

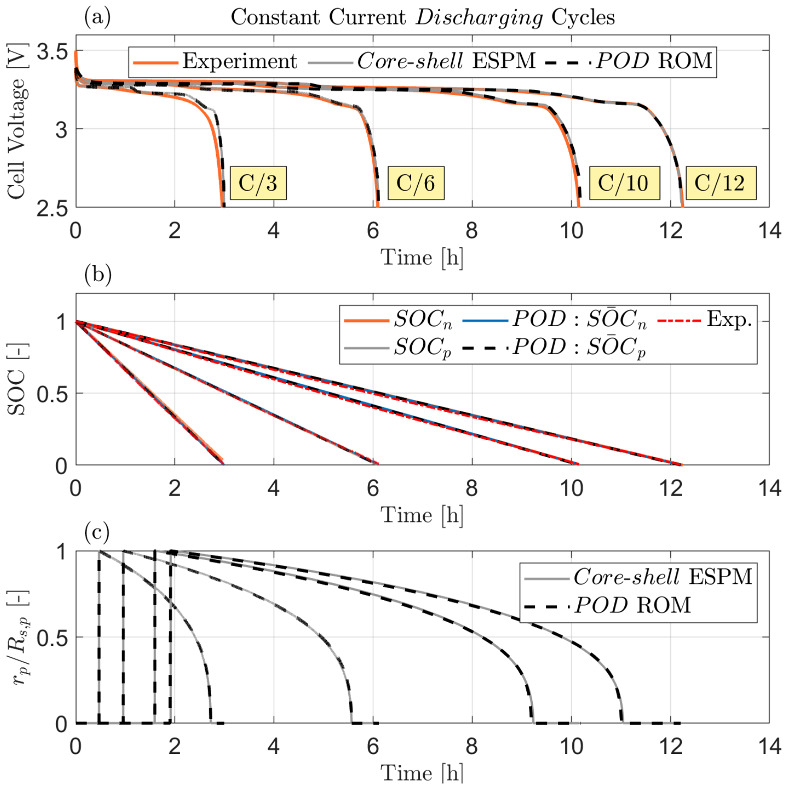

Figure 6.3: Constant current discharge cycles at C/3, C/6, C/10 and C/12: Cell voltage(a), SOC (b) and moving boundary (c).

6.2.1.2 POD-Galerkin ROM limitations

In this section, a ROM is proposed to approximate the electrochemical dynamics of LFP batteries. The POD-Galerkin technique is employed to reduce the dimensionality of the state-space model derived from the spatial discretization of the CSa-EPSM governing equations. This ROM achieves a significant reduction in dimensionality, from 169 to just 9 state variables. Validation results for CC and real DV scenarios, compared against both experimental data and CSa-ESPM simulations, demonstrate that the POD-based ROM accurately captures cell voltage and electrode SOC. Nevertheless, two significant limitations might affect the model's performance and accuracy:

- **Sensitivity to Snapshot Generation**
  A significant limitation of the POD-Galerkin method is its sensitivity to the current values used for generating the snapshots, since the performance of the ROM is influenced by these snapshot values. To address this issue, our ongoing research is focused on eliminating the need for ad-hoc snapshot matrices in the ROM formulation.
  One promising strategy involves constructing a combined set of snapshot matrices that integrate snapshots generated at multiple current levels. For instance, snapshot matrices for current values of $\pm C/3$, $\pm C/6$, $\pm C/10$, and $\pm C/12$ are combined as

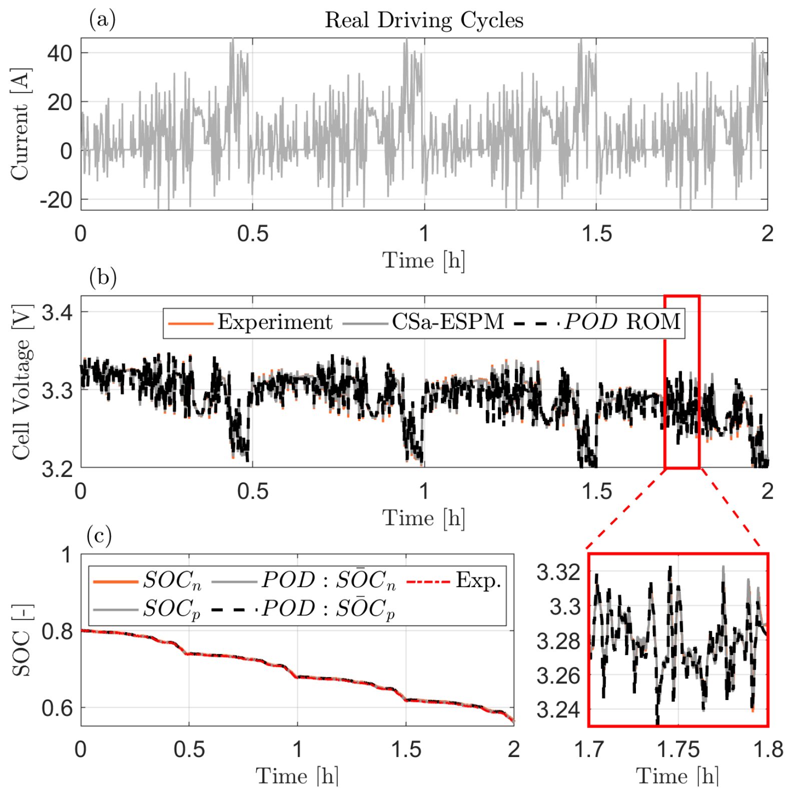

Figure 6.4: Real driving cyle results comparison: Cell current profile (a), voltage (b) and SOC (c).

follows:

$$\begin{aligned}
S_e^{comb} &= \begin{bmatrix} S_e^{C/3} & S_e^{-C/3} & S_e^{C/6} & S_e^{-C/6} & S_e^{C/10} & S_e^{-C/10} & S_e^{C/12} & S_e^{-C/12} \end{bmatrix} \\
S_n^{comb} &= \begin{bmatrix} S_n^{C/3} & S_n^{-C/3} & S_n^{C/6} & S_n^{-C/6} & S_n^{C/10} & S_n^{-C/10} & S_n^{C/12} & S_n^{-C/12} \end{bmatrix} \\
S_{p,2P}^{comb} &= \begin{bmatrix} S_{p,2P}^{C/3} & S_{p,2P}^{-C/3} & S_{p,2P}^{C/6} & S_{p,2P}^{-C/6} & S_{p,2P}^{C/10} & S_{p,2P}^{-C/10} & S_{p,2P}^{C/12} & S_{p,2P}^{-C/12} \end{bmatrix} \\
S_{p,1P}^{comb} &= \begin{bmatrix} S_{p,1P}^{C/3} & S_{p,1P}^{-C/3} & S_{p,1P}^{C/6} & S_{p,1P}^{-C/6} & S_{p,1P}^{C/10} & S_{p,1P}^{-C/10} & S_{p,1P}^{C/12} & S_{p,1P}^{-C/12} \end{bmatrix}
\end{aligned} \tag{6.36}$$

The truncated basis functions $V_e^{r,comb}$, $V_n^{r,comb}$, $V_{p,1P}^{r,comb}$, and $V_{p,2P}^{r,comb}$ are then extracted from these combined snapshot matrices. This approach aims to provide a more robust and generalizable set of basis functions. Figure 6.5 illustrates the comparison of cell voltage, SOC, and moving boundary dynamics using these combined truncated basis functions considering input currents not present in the combined snapshot matrices.

- **Conservation of Mass and Numerical Stability**
  Another limitation of the proposed ROM relates to the conservation of mass within the reduced-order framework, as well as of the original FDM-based model. The ROM may not fully ensure mass conservation, potentially leading to numerical errors, especially in long-term simulations.

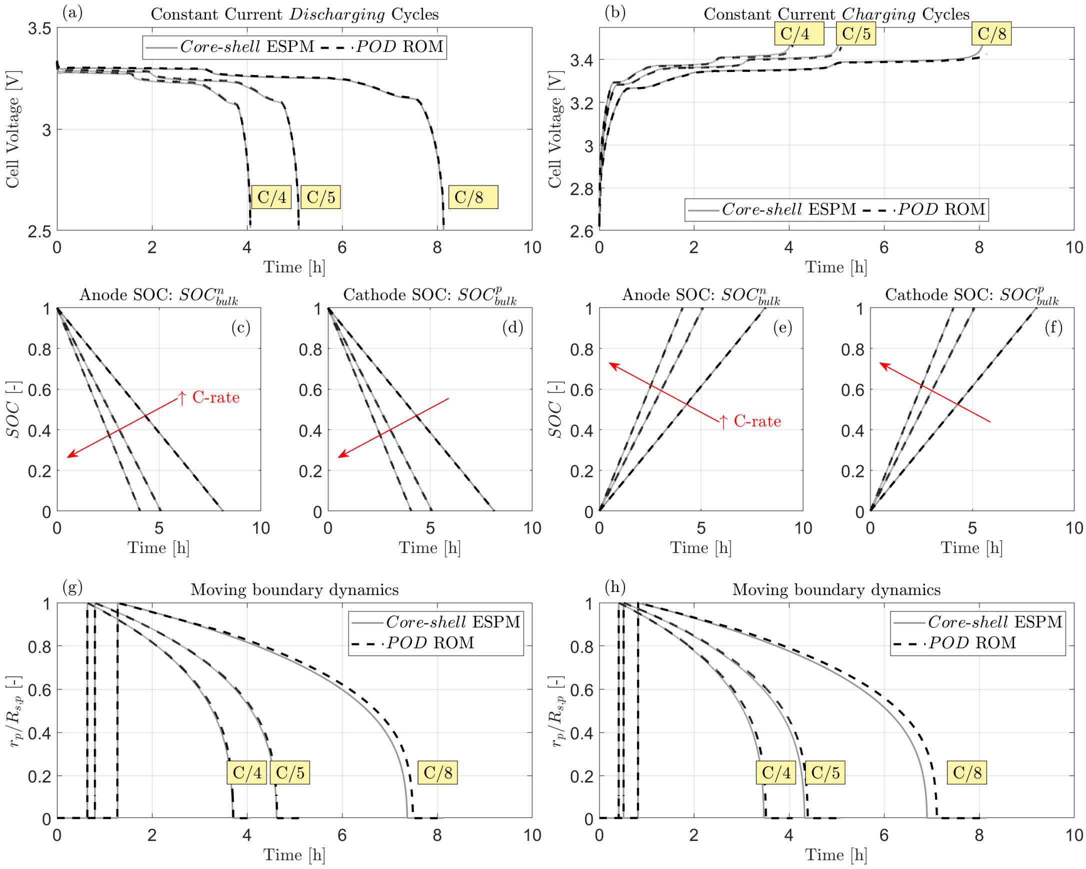

Figure 6.5: Constant current discharge results comparison using the combined trucated basis function: Cell voltage(a-b), SOC (c-f) and moving boundary (g-h).

Keeping these factors in mind, the following section introduces an alternative approach for reducing the dimensionality of the original model: the FVM-based ROM. Unlike the POD-Galerkin ROM, which focuses on reducing the FDM-based discretized ODE model, the FVM-based ROM approximates the original cell dynamics as described by the PDEs. We will demonstrate that the FVM effectively discretizes the Stefan problem characteristic of the CSa-ESPM, providing accurate solutions with fewer than four control volumes while ensuring mass conservation across multiple operational cycles. The resulting control-oriented, reduced-order FVM-based CSa-ESPM is validated experimentally using various C-rate load profiles.

6.2.2 FVM-based CSa-ESPM

In Section 6.1.1, the Stefan problem was discretized using the FDM following the application of a Landau transformation to modify the coordinates. Unlike FDM, which directly discretizes the governing equations, the FVM approaches the problem by solving the equations in their integral form, ensuring mass conservation. However, the complexity introduced by coordinate transformation renders FVM less effective for this approach.
Consequently, this section is dedicated to the numerical solution of the CSa-ESPM using FVM, where the original coordinate system remains unchanged.
As discussed in Section 3.1.3.1, the FVM divides the computational domain into control volumes (CVs). The volume-averaged value of the solid-phase concentration within each CV, denoted by $\bar{c}_{s,p,j}$, is calculated as:

$$\bar{c}_{s,p,j} = \frac{1}{V_i}\int_{CV_i} c_{s,p,j}\,dV \tag{6.37}$$

Here, V_i represents the volume of the i^{th} CV. By integrating Eq. 3.26 over a control volume CV_i and applying the Gauss theorem in a spherical coordinate system, we obtain:

$$\left.\frac{\partial \bar{c}_{s,p}}{\partial t}V_i\right|_i = D_{s,p}\left.\left(\frac{\partial c_{s,p}}{\partial r}\right)\right|_{i+\frac{1}{2}} A_{i+\frac{1}{2}} - D_{s,p}\left.\left(\frac{\partial c_{s,p}}{\partial r}\right)\right|_{i-\frac{1}{2}} A_{i-\frac{1}{2}} \tag{6.38}$$

Where $V_i = \frac{4}{3}\pi\left(r^3_{i+\frac{1}{2}} - r^3_{i-\frac{1}{2}}\right)$ is the volume of CV_i, and $A_{i+\frac{1}{2}} = 4\pi r^2_{i+\frac{1}{2}}$ and $A_{i-\frac{1}{2}} = 4\pi r^2_{i-\frac{1}{2}}$ are the surface areas of the left and right boundaries of CV_i, respectively. The indices $i+\frac{1}{2}$ and $i-\frac{1}{2}$ refer to the interfaces between CV_i/CV_{i+1} and CV_{i-1}/CV_i, respectively.
The central difference scheme is then employed to approximate the diffusive terms in Eq. 6.38:

$$\begin{aligned}\left.\frac{\partial c_{s,p}}{\partial r}\right|_{i+\frac{1}{2}} &\approx \frac{\bar{c}_{s,p,i+1} - \bar{c}_{s,p,i}}{\Delta r}\\ \left.\frac{\partial c_{s,p}}{\partial r}\right|_{i-\frac{1}{2}} &\approx \frac{\bar{c}_{s,p,i} - \bar{c}_{s,p,i-1}}{\Delta r}\end{aligned} \tag{6.39}$$

Substituting Eq. 6.39 into Eq. 6.38, the discrete form of the solid-phase diffusion equation for CV_i becomes:

$$\frac{\partial \bar{c}_{s,p,i}}{\partial t} V_i = D_{s,p} \frac{\bar{c}_{s,p,i+1} - \bar{c}_{s,p,i}}{\Delta r} A_{i+\frac{1}{2}} - D_{s,p} \frac{\bar{c}_{s,p,i} - \bar{c}_{s,p,i-1}}{\Delta r} A_{i-\frac{1}{2}} \tag{6.40}$$

where $\Delta r = \frac{R_p - r_p}{N_{r,p}}$ represents the length of each CV. For $i = 1$, using the boundary condition $c_{s,p,0} = g\left(I_{cell}\right)$, Eq. 6.41 can be expressed as:

$$\frac{\partial \bar{c}_{s,p,1}}{\partial t} V_1 = D_{s,p} \frac{\bar{c}_{s,p,2} - \bar{c}_{s,p,1}}{\Delta r} A_{1+\frac{1}{2}} - D_{s,p} \frac{\bar{c}_{s,p,1} - \bar{c}_{s,p,0}}{\Delta r/2} A_{1-\frac{1}{2}} \tag{6.41}$$

For the internal control volumes CV_i, the equation is:

$$\frac{\partial \bar{c}_{s,p,i}}{\partial t} V_i = D_{s,p} \frac{\bar{c}_{s,p,i+1} - \bar{c}_{s,p,i}}{\Delta r} A_{i+\frac{1}{2}} - D_{s,p} \frac{\bar{c}_{s,p,i} - \bar{c}_{s,p,i-1}}{\Delta r} A_{i-\frac{1}{2}} \tag{6.42}$$

For the last control volume CV_i, the equation becomes:

$$\frac{\partial \bar{c}_{s,p}}{\partial t} V_i = D_{s,p} \left(\frac{\partial \bar{c}_{s,p}}{\partial r} \right) \Bigg|_{surface} A_{surface} - D_{s,p} \frac{\bar{c}_{s,p,i} - \bar{c}_{s,p,i-1}}{\Delta r} A_{i-\frac{1}{2}} \tag{6.43}$$

Applying the boundary condition $D_{s,p} \frac{\partial c_{s,p}}{\partial r} \Big|_{r=R_p} = -I_{cell}/(AFL_p a_{s.p})$ to Eq. 6.43, we get:

$$\frac{\partial c_{s,p,N_r}}{\partial t} V_i = -j A_{surface} - D_{s,p} \frac{c_{s,p,i} - c_{s,p,i-1}}{\Delta r} A_{i-\frac{1}{2}} \tag{6.44}$$

Finally, the state-space representation of Eq. 6.44 is given as:

$$\dot{\bar{c}}_{s,p} = A_s \bar{c}_{s,p} + B_s I_{cell} + G_s \tag{6.45}$$

where the matrices A_s, B_s and G_s are reported in Table 6.4.

6.2.2.1 Parameters identification and results

Following the identification strategy proposed in [10], CSa-ESPM model parameters are identified. These parameters are shown in Table 6.2. First, C/4 charge and discharge data are employed to identify the parameter vector, denoted as $\lambda_{C/4}$, which comprises:

$$\lambda_{C/4} = \begin{aligned} &\big[\theta^{ch}_{p,\alpha}, \theta^{ch}_{p,\beta}, \theta^{ch}_{p,\alpha}, \theta^{ch}_{p,\beta}, \epsilon_{s,p}, \epsilon_{s,n}, \\ &R_{s,n}, R_{s,p}, D_{s,n}, D_{s,p}, A, k_n, k_p\big] \end{aligned} \tag{6.54}$$

Then, the following parameter vector is identified using C/2 and 1C charge data.

$$\lambda_{C/2} = \lambda_{1C} = \left[\ D_{s,p}, \quad D_{s,n}, \quad k_p, \quad k_n\ \right] \tag{6.55}$$

The identified values are shown in Table 6.5, and the identification results are shown in Fig. 6.6(a)-(c). Here, only 4 CVs are used to discretize the CSa-ESPM (FVM with $N_r = 4$). Model validation is conducted using C/2 discharge and 1C discharge data. As

Table 6.4: CSa-ESPM discretized electrochemical governing dynamics

FVM-based state-space formulation (The matrices and coefficients are reported in [10] and [68])

Negative electrode and 1P positive electrode concentration [68]

$$c_{s,j} = A_j c_{s,j} + B_j I_{cell}, \quad \text{with:} \quad j = n, p \tag{6.46}$$

Electrolyte concentration [10]

$$c_e = A_e c_e + B_e I_{cell} \tag{6.47}$$

Positive electrode in two-phase

$$c_{s,p} = A_s \bar{c}_{s,p} + B_s I_{cell} + G_s \tag{6.48}$$

$$c_{s,p} = \left[\bar{c}_{s1,p}, \bar{c}_{s2,p} \cdots \bar{c}_{sN_r,p}\right]^T \in \mathbb{R}^{N_r \times 1} \tag{6.49}$$

$$\dot{r}_p = \frac{2\,\text{sign}\,(I)\, D_{s,p}}{\Delta r_{2\text{P}} \left(c_{s,p}^{\alpha} - c_{s,p}^{\beta}\right)} \left(\bar{c}_{s1,p} - g\left(I_{cell}\right)\right) \tag{6.50}$$

$$g\left(I\right) = \begin{cases} c_{s,p}^{\beta} = \theta_{p,\beta} \cdot c_{s,p}^{\max}, & \text{if} \quad I_{cell} > 0 \\ c_{s,p}^{\alpha} = \theta_{p,\alpha} \cdot c_{s,p}^{\max}, & \text{if} \quad I_{cell} < 0 \\ 0, \quad \text{otherwise} & \end{cases} \tag{6.51}$$

$$A_s = \frac{3D_{s,p}}{\Delta r_{2\text{P}}} \begin{bmatrix} -\frac{(\Delta r_{2\text{P}} + r_p)^2 + 2r_p^2}{(\Delta r_{2\text{P}} + r_p)^3 - r_p^3} & \cdots & 0 \\ \vdots & \ddots & \vdots \\ 0 & \cdots & \frac{((N_r - 1)\Delta r_{2\text{P}} + r_p)^2}{((N_r - 1)\Delta r_{2\text{P}} + r_p)^3 - R_{s,p}^3} \end{bmatrix}_{(N_r \times N_r)} \tag{6.52}$$

$$B_s = \frac{3}{AFL_p a_p} \begin{bmatrix} 0 \\ \vdots \\ \frac{R_{s,p}^2}{((N_r - 1)\Delta r_{2\text{P}} + r_p)^3 - R_{s,p}^3} \end{bmatrix}_{(N_r \times 1)}, G_s = \begin{bmatrix} -\frac{6 D_{s,p} g(I) r_p^2}{\Delta r_{2\text{P}} \left((\Delta r_{2\text{P}} + r_p)^3 - r_p^3 \right)} \\ \vdots \\ 0 \end{bmatrix}_{(N_r \times 1)} \tag{6.53}$$

Model output shown in Table 6.1

Table 6.5: Identified parameters at different C-rates.

Current profiles	Charge			Discharge
C-rates	C/4	C/2	1C	C/4
$\theta_{n,100\%}$ [-]	0.832	-	-	0.831
$\theta_{n,0\%}$ [-]	0.011	-	-	0.009
$\theta_{p,100\%}$ [-]	0.065	-	-	0.066
$\theta_{p,0\%}$ [-]	0.910	-	-	0.925
$\theta_{p,\alpha}$ [-]	0.220	-	-	0.196
$\theta_{p,\beta}$ [-]	0.817	-	-	0.804
$R_{s,n}$ [m]	8.10e-07	-	-	8.10e-07
$R_{s,p}$ [m]	1.67e-08	-	-	1.67e-08
ε_n [-]	0.655	-	-	0.655
ε_p [-]	0.681	-	-	0.681
A_{cell} [m^2]	2.125	-	-	2.125
R_l [Ω]	1.54e-03	-	-	1.54e-03
$D_{s,n}$ [m^2/s]	1.28e-15	1.00e-10	1.42e-15	-
$D_{s,p}$ [m^2/s]	4.05e-18	5.45e-18	2.74e-18	-
k_n [m$^{2.5}$/(mol$^{0.5}$s)]	2.02e-12	2.56e-12	4.71e-12	-
k_p [m$^{2.5}$/(mol$^{0.5}$s)]	9.50e-13	6.00e-13	1.45e-12	-

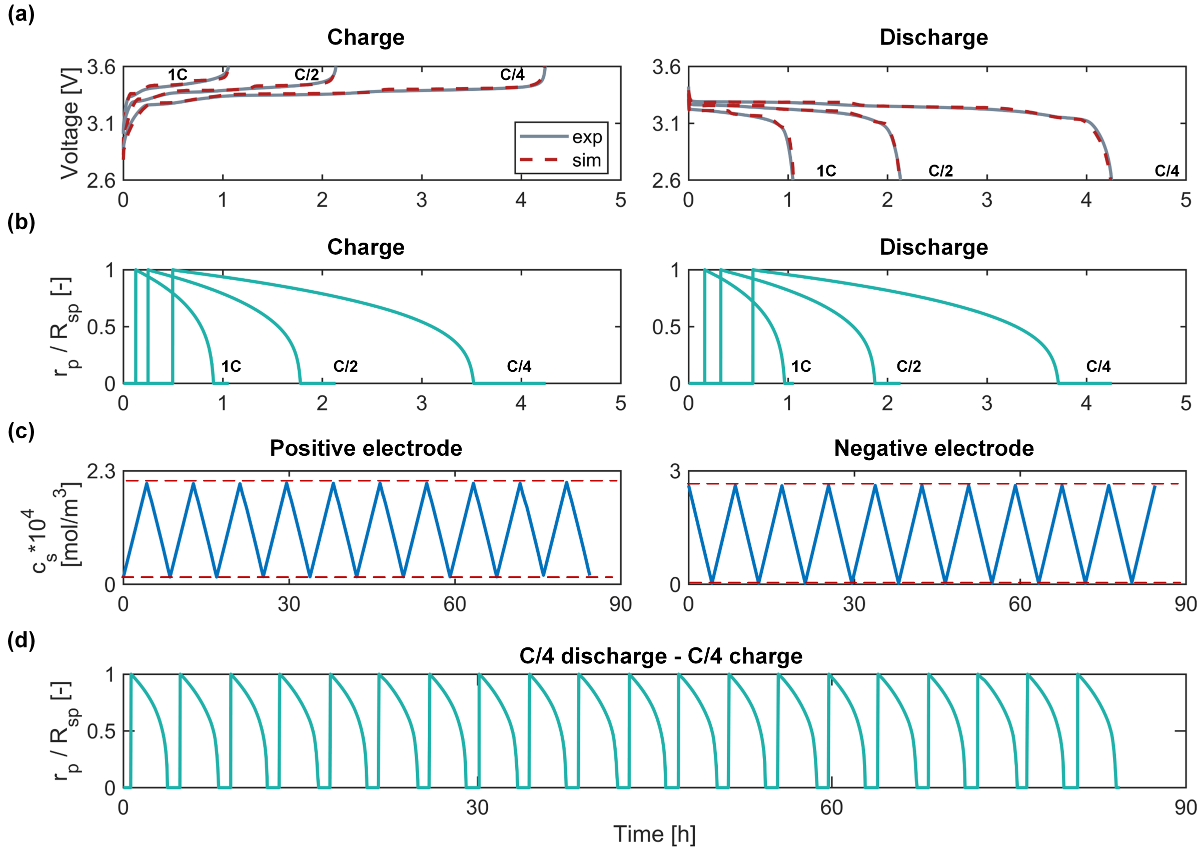

Figure 6.6: Comparison results at C/4, C/2, and 1C for (a) voltage, (b) moving boundary, (c) volume-average concentraion, (d) moving boundary during cycling.

can be seen from Fig. 6.6(a), the simulated voltage matches well with the measured data. The root-mean-square-error (RMSE) of voltage under C/2 and 1C discharge are 14.96 mV and 23.89 mV, respectively. Above results show that FVM-based CSa-ESPM has high accuracy with only 4 CVs. To the best of our knowledge, it is the first time that CSa-ESPM solved by FVM is validated using experimental data. Besides accuracy, the mass conservation property is also checked. Following the approach presented in [68], we used a C/4 charge – C/4 discharge profile for multiple cycles simulation, which ensures the total ampere-hour throughput are the same for charge and discharge. Fig. 6.6(d) shows that the peak values for positive and negative electrodes volume-average concentration remain constant, which proves the mass is conserved when using FVM for solving CSa-ESPM. Also, Fig. 6.6(e) shows that the moving boundary changes continuously between one-phase and two-phase regions.

6.3 Conclusion

In this chapter, we explore two distinct reduction techniques applied to the physics-based CSa-ESPM formulated by [10] for modeling the electrochemical dynamics of graphite/LFP batteries.

First, the POD-Galerkin method is employed to reduce the dimensionality of the state-space model derived from the spatial discretization of the CSa-ESPM electrochemical governing equations. This approach achieves a significant reduction in the number of state variables, from 169 to just 9. Validation results from comparison with both experimental data and CSa-ESPM simulations demonstrate that the POD-based ROM accurately predicts cell voltage and electrode SOC. Additionally, the ROM successfully captures phase transition dynamics, voltage hysteresis, and path dependence effects.

Second, the FVM is utilized to spatially discretize the CSa-ESPM model for LFP batteries. This technique substantially reduces the number of solid-phase state variables to fewer than 6, while ensuring mass conservation. Experimental validation confirms that the FVM-based reduced-order CSa-ESPM provides a good match for both cell voltage and electrode SOC.

It is worth noting that the observability of the FVM-based CSa-ESPM model is analyzed and quantified through rank tests and condition numbers as discussed in [30]. The results indicate that model observability is influenced by different current inputs and the number of discrete equations, providing crucial insights for the further development of electrode-based observers in BMS applications.

Chapter 7

Data-driven analysis of CtC variation impact on parallel-connected module

Contents

7.1 Methodology 142
7.1.1 Design of Experiments 142
7.1.2 Data-driven model 144
7.1.3 Feature importance analysis 147
7.2 Results and discussion 149
7.2.1 MLR models analysis 149
7.2.2 ML models analysis 152
7.2.3 Models comparison 155
7.2.4 Limitations 157
7.3 Conclusion 158

This contribution is based on the following work:

- [31] Piombo, G., **Fasolato, S.**, Heymer, R., Hidalgo, M., Niri, M. N., Onori, S., Marco, J. (2024). *Unveiling the performance impact of module level features on parallel-connected lithium-ion cells via explainable machine learning techniques on a full factorial design of experiments*, Journal of Energy Storage, 84, 110783.

Introduction

Depending on the application, individual cells are combined using various series and/or parallel architectures to form modules and packs that meet specific power and energy requirements [160]. Series connections are employed to achieve higher voltages, which helps to mitigate voltage-related losses [46]. In contrast, parallel connections enable the pack to store a larger amount of energy by increasing the overall capacity [161]. However, a critical challenge in enhancing the performance, safety, and longevity of battery modules is understanding the causes and effects of cell-to-cell (CtC) heterogeneity [24].

CtC variations causes

Prior research has effectively identified and synthesized the key factors that significantly impact the efficacy of bettery modules [162].

Heterogeneities in batch of fresh cells are typically attributed to manufacturing tolerances during production processes and/or differences in material composition [163]. Manufacturing-related CtC variations can manifest as variations in internal resistance [164, 165, 166], capacity [167, 168], or a combination of both [169, 170, 171]. Examples of distributions of cell characteristics outside of manufacturer specifications can be found in [163] and [172, 173] for LFP/graphite and NCA/graphite fresh cell batches, respectively. Not only single-cell level features but also module-level characteristics strongly contribute to introduced CtC variation. According to [162], uneven electrical resistance among the cell interconnections [174, 175, 176] stands as the second leading factor contributing to heterogeneity in a battery module. This type of CtC heterogeneity can be attributed to several factors, including weld cracks or faulty connections between cells and the module busbar [177, 178]. Similarly, contact imperfections among electrodes, current collectors, and the busbar [179] also play a role. These defects might arise from surface irregularities of materials and uneven contact pressure within battery systems. Furthermore, improper dimensioning of electrical connections between cells might result in increased local resistance [180]. Additionally, the number of cells in parallel [181, 182], topology selection [183, 184], and chemistry combination [185, 186] have a non-negligible impact on pack performance. Finally, operating temperature [187, 188, 189] and poor cooling design-induced thermal gradients [190, 191] can also affect the uniformity of pack performance.

CtC variations effects

The effect of CtC heterogeneity on the operation of a battery module or pack varies based on the interconnection configuration, whether connected in series or parallel.

In the **series-connected cells** scenario, the overall capacity of the module is constrained by the weakest cell [192], which is the one with the lowest capacity. Additionally, the module's degradation is accelerated by thermal gradients among the cells [26], resulting from uneven heat generation due to heterogeneous cell internal and/or interconnection resistances, as well as a suboptimal cooling system. On the other hand, in a **parallel-connected module**, dissimilar cell capacities, resistances, and temperatures result in heterogeneous current distribution [193], which in turn leads to thermal and SOC imbalances [194]. This results in cell-to-cell fluctuations in internal resistance, capacity [172, 195, 190], and aging rate [196, 162, 197] over time. In particular, the phenomenon of performance imbalance leading to non-uniform aging of individual cells has been reported in the literature. Specifically, it has been noted that the prolongation of imbalances is a contributing factor to this phenomenon. The existing literature presents divergent views on this matter. While some researchers [170, 169, 198, 199] affirm that there exists a convergence and self-balancing tendency among parallel-connected cells over time, others' [24, 200, 171, 201] findings oppose this theory. So far, most research has focused on individual cells' behavior, with some experimental assessments of module connections reported in [162, 174]. Consequently, the issue of parallel cell connections leaves gaps in the knowledge and necessitates further investigation.

Considering these factors, it is important to highlight that CtC variations in real parallel-connected battery modules are closely interdependent and, in practical terms, challenging to eliminate.
One approach to gain insights into these issues is to systematically conduct multiple tests at the module and pack levels across a wide range of scenarios. However, in systems that exhibit complexity and involve multiple variables, it is imperative to establish a structured and controlled experimental design to guarantee the precision and dependability of outcomes. The recent interest in implementing Design of Experiment (DOE) in the battery community [202] is attributed to its capability to identify the most significant factors in a system, resulting in cost savings through reduced experimentation time and resources [203]. DOE can be defined as the branch of statistics involved in the planning, collection, and analysis of experimental data to ensure valid and objective engineering conclusions. DOE involves a series of methodical steps, beginning with the definition of the problem and the objectives of the experimental study. This is followed by performing the experiments as dictated by the experimental design. Once the data has been collected, it is processed using statistical methods. In this step, an empirical model can be used to interpret the results and to represent the relationship between the factors and the response. Finally, the evidence provided by the statistical analysis serves as a basis for arriving at objective conclusions. This structured approach ensures that the experimental outcomes are both precise and dependable, facilitating informed decision-making in complex battery systems.
Note that, an effective alternative is the use of digital twins, as discussed in next Chapter.

Chapter contribute

This chapter aims to analyze the effect of CtC variations on the performance of a paralle–connected battery moduel based on DOE approach. The ability to anticipate anomalous behaviors of parallel cells is crucial for ensuring the longevity and safety of battery packs. Understanding the predominant factors contributing to the inconsistent performance of a module is essential for developing predictive models that optimize system performance. To the best of the authors' knowledge, there have been no previous attempts to apply DOE at the module level for purposes beyond thermal design optimization [204, 205].
The main contributions of this chapter can be mainly divided in two as follows:

1. *Based on the DOE-based experimental campaign on parallel-connected modules, described in Section 4.2.2.2, a comprehensive statistical analysis is conducted. This analysis methodically isolated and ranked the impact of key factors such as intercon-*

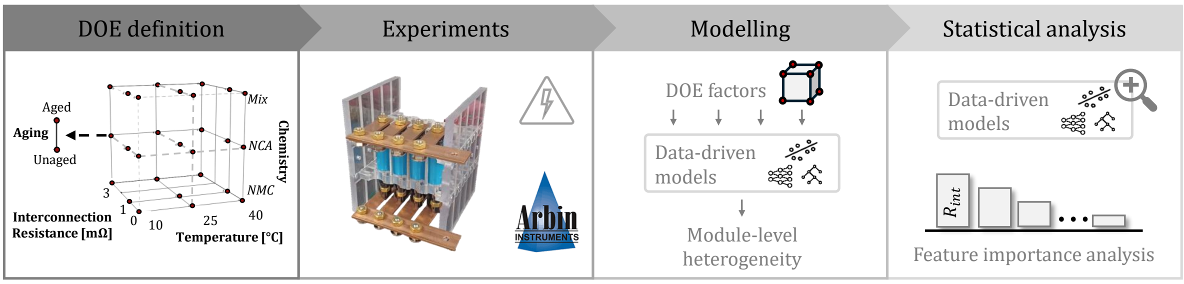
DOE definition
Experiments
Modelling
Statistical analysis
Aged
Aging
Unaged
Mix
NCA
NMC
Chemistry
3
1
0
10
25
40
Interconnection Resistance [mΩ]
Temperature [°C]
Arbin INSTRUMENTS
DOE factors
Data-driven models
Module-level heterogeneity
Data-driven models
R_{int}
Feature importance analysis

Figure 7.1: Visual overview of the DOE-based CtC variations analysis described in this chapter.

nection resistance, operating temperature, cell chemistry combinations, and aging on heterogeneities propagation in parallel strings current, temperature, SOC distribution, and time-to-self balance.

2. *The combination of novel interpretable machine learning techniques with established linear regression strategies. Specifically, the statistical analysis is based on multilinear regression (MLR) models and machine learning (ML) models. Neural Networks (NNs) and Random Forest (RF) models are trained and optimized to provide complementary insights to MLR, outlining their benefits and drawbacks in identifying the key contributors to heterogeneous performance in parallel-connected cells. It is important to note that while MLR models offers interpretability, ML models are often considered black boxes. Therefore, novel explainable machine learning (XML) techniques are applied to enhance ML model predictability by capturing non-linear relationships and improving interpretability.*

Chapter structure

- **Section 7.1** provides a comprehensive description of the methodology employed in this study. Specifically, Section 7.1.1 illustrates the full factorial DOE approach used, highlighting the control and response variables involved. Section 7.1.2 reviews both MLR and ML models considered in the analysis. Additionally, Section 7.1.3 details the XML techniques utilized to analyze feature importance within the ML models.

- **Section 7.2** presents the results of the statistical analysis. Specifically, Sections 7.2.1 and 7.2.2 present the results for the MLR and ML models, respectively. Furthermore, the two approaches are compared in Section 7.2.3.

- **Section 7.3** summarizes the conclusions and outlines future research opportunities.

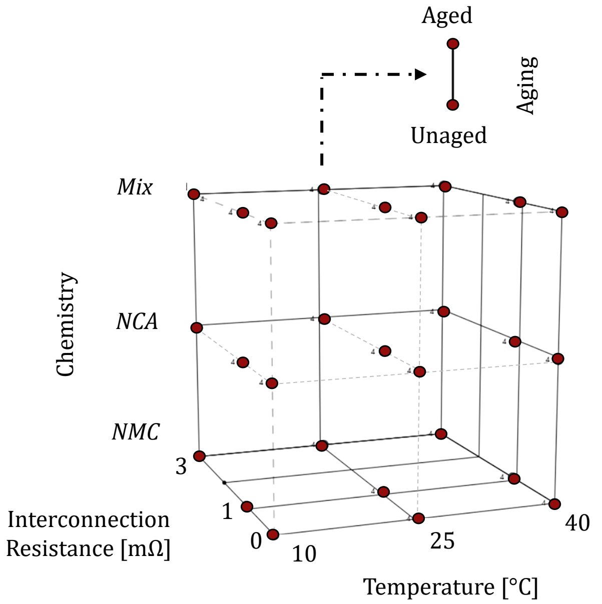

Figure 7.2: Graphical representation resulting from the four factors and respective levels of the full-factorial DoE.

7.1 Methodology

7.1.1 Design of Experiments

This study employs a full factorial DOE [202] to identify and rank key module-level features affecting module performance responses. Figure 7.2 visually represents the DOE cube utilized in this study, detailing the four control parameters and their respective ranges as outlined in Table 7.1. These ranges were selected based on the literature and practical considerations. Specifically, the interconnection resistance ranges from 0.1 to 3 mΩ, chosen to maintain a 2.5% ratio relative to the energy cell's internal resistance [206]. Testing temperatures vary between 10°C, 25°C, and 40°C. The cell chemistry is categorized into three levels: "NMC," "NCA," and "Mix." The "NMC" and "NCA" configurations consist of modules with cells of uniform chemistry, while the "Mix" configuration involves a parallel string of two NMC cells and two NCA cells. Although combining chemistries is unconventional, this approach is selected due to the comparable characteristics of NMC and NCA cells and their potential for repurposing in second-life applications [185, 207]. Finally, including a cell with low SOH helps to better understand cell behavior under conditions of failed contact, high resistance, and capacity gradients.

Subsequently, based on the described full factorial DOE, the module-level experiments are conducted as detailed in Section 4.2.1.1 of Chapter 4. It is important to note that the module responses, defined in the following of section, are calculated considering the 0.75 C-rate CC discharge cycle from 100% to 0% of the module SOC.

Finally, a set of eight response variables, categorized into four distinct groups based on the analyzed phenomena, is reported in Table 7.1 and visualized in Figure 7.3. These categories are:

Table 7.1: Overview of the control and response variables included in the study. N_p refers to the number of cells connected in parallel (in this study, $N_p = 4$). I_{Cellk} denotes the current delivered by the k-th cell, I_{Mod} is the module input current. T_{Amb} is the ambient temperature, SoC_{Cellk} and T_{Cellk}^{Surf} are the SoC and surface temperature of the k-th cell, respectively. t_1, t_2, and t_{end} are the time instants used to split the cell current distribution, as depicted in Figure 7.3.

Control variables	*Levels*	**Response variables**
Interconnection resistance [$m\Omega$]	[0, 1, 3]	$\sigma I_{Start} = \frac{1}{t_1} \int_0^{t_1} \left(\sqrt{\frac{1}{N_p - 1} \sum_{k=1}^{N_p} (I_{Cellk} - I_{Mod}/N_p)^2} \right) dt$ (7.1)
Temperature [$°C$]	[10, 25, 40]	$\sigma I_{Mid} = \frac{1}{t_2 - t_1} \int_{t_1}^{t_2} \left(\sqrt{\frac{1}{N_p - 1} \sum_{k=1}^{N_p} (I_{Cellk} - I_{Mod}/N_p)^2} \right) dt$ (7.2)
Chemistry [$-$]	[NMC, NCA, Mix]	$\sigma I_{End} = \frac{1}{t_{End} - t_2} \int_{t_2}^{t_{End}} \left(\sqrt{\frac{1}{N_p - 1} \sum_{k=1}^{N_p} (I_{Cellk} - I_{Mod}/N_p)^2} \right) dt$ (7.3)
Ageing [$-$]	[Aged, Unaged]	$\Delta SoC_{Max} = \max(SoC_{Cellk}) - \min(SoC_{Cellk})$ (7.4)
		$\Delta SoC_{End} = \max(SoC_{Cellk}\vert_{t=t_{End}}) - \min(SoC_{Cellk}\vert_{t=t_{End}})$ (7.5)
		$\Delta T_{Net}^{Max} = \max(T_{Cellk}^{Surf} - T_{Amb}) - \min(T_{Cellk}^{Surf} - T_{Amb})$ (7.6)
		$\sigma T_{Mean} = \frac{1}{t_{End} - t_1} \int_{t_1}^{t_{End}} \left(\sqrt{\frac{1}{N_p - 1} \sum_{k=1}^{N_p} (T_{Cellk}^{Surf} - T_{Amb})^2} \right) dt$ (7.7)
		TTSB

- **Current Heterogeneities:** Figure 7.3(a) illustrates the three stages of current distribution among the four cells during discharge considered in this study. To quantify deviations in current relative to the reference, the average standard deviation at the beginning, middle, and end of the cycle ($\sigma I_{\mathrm{Start}}$, σI_{Mid}, σI_{End}) is calculated using (7.1), (7.2), and (7.3), respectively.

- **Thermal Heterogeneities:** Figure 7.3(b) displays the matrices used to assess thermal distribution heterogeneities within the module. Specifically, ΔT_{Max} and σT_{Mean} denote the maximum temperature increase and the mean standard deviation of the temperature gradient across cells during discharge, respectively. These metrics are calculated using (7.6) and (7.7).

- **SOC Heterogeneities:** Figure 7.3(c) shows the maximum absolute SOC difference and the SOC difference at the end of the cycle between cells ($\Delta \mathrm{SoC}_{\mathrm{Max}}$ and $\Delta \mathrm{SoC}_{\mathrm{End}}$), computed as described in (7.4) and (7.5).

- **Time to Self-Balance (TTSB):** This measures the time required for the cumulative balancing currents to stabilize at 200 mA during the post-discharge period, as illustrated in Figure 7.3(d).

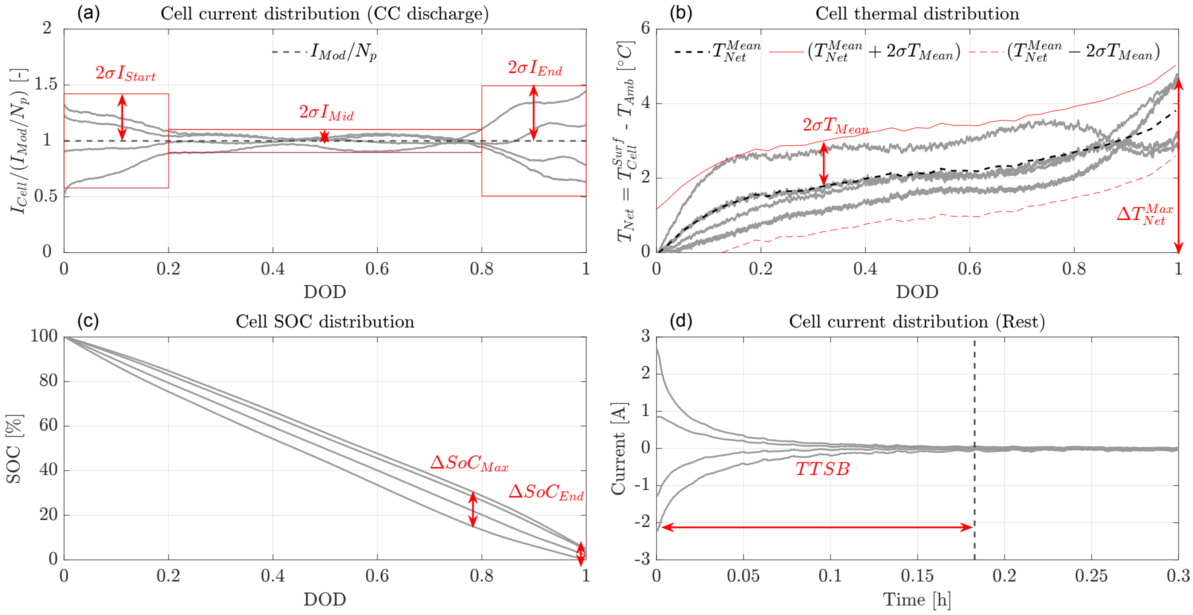

Figure 7.3: Visual representation of the eight response variables considered in this study for one of the 54 experiments. The variables are illustrated based on (a) current distribution, (b) thermal distribution, (c) SOC distribution, and (d) TTSB.

7.1.2 Data-driven model

The aim of conducting a systematic DOE is to develop a comprehensive empirical model that identifies and elucidates the relationship between control variables (x) and response variables (y). This section reviews the formulation of the models used in this analysis, including multi-linear regression models and machine learning approaches such as Neural Networks (NN) and Random Forests (RF). Before identifying the model, input feature scaling is conducted to ensure a reliable comparison of coefficients in multi-linear regression models and to minimize input sensitivity in machine learning models. This step is essential for accurately assessing the importance of each feature by normalizing the data, which facilitates a clearer understanding of how each term influences the model and improves the stability and performance of the analysis. In particular, the input features are rescaled as:

$$z = \frac{(x - \mu)}{\sigma} \tag{7.8}$$

where μ represents the feature mean and σ represents its standard deviation.

7.1.2.1 Multilinear-regression (MLR) models

The statistical analysis is conducted using a technique called multi-linear regression (MLR). MLR is a statistical method employed to determine the influence of a set of independent variables (predictors) on a response variable, assuming a linear relationship between the inputs and the output. Consider a set of N observations, denoted as $\Theta = \{(X_1, y_1), (X_2, y_2), \cdots, (X_N, y_N)\}$, where $X_k = [x_1, \cdots, x_q] \in \mathbb{R}^q$ and $y_k \in \mathbb{R}$ (with $k = 1, \cdots, N$) represent the vector containing the q predictors ($x_j, j = 1, \cdots, q$) and the response variable for the k-th sample, respectively. According to [208], the MLR model can be formulated as follows:

$$\hat{y} = f(x_1, x_2, \cdots, x_q) = \beta_0 + \sum_{z=1}^{q}(\beta_z x_z + \beta_{zz} x_z^2) + \sum_{z=1}^{q-1}\sum_{y=i+1}^{q}(\beta_{z,y} x_z x_y) \tag{7.9}$$

where β_0 represents the intercept, β_z and β_{zz} are constant coefficients associated with the linear and quadratic terms, while $\beta_{z,y}$ corresponds to the interactions between variables. It is worth noting that the MLR model can also include nonlinear terms, such as polynomials or interactions between variables, as they can be considered equivalent to additional predictors impacting the response variable linearly. The coefficients of the MLR model in eq. (7.9) are estimated using a least square approach that minimizes the sum of squared residuals:

$$\min_{\beta_0,\beta_z,\beta_{zz},\beta_{z,y}} \sum_{k=1}^{N} \epsilon_k = \min_{\beta_0,\beta_z,\beta_{zz},\beta_{z,y}} \sum_{k=1}^{N}(y_k - \beta_0 - \sum_{z=1}^{q}(\beta_z x_z + \beta_{zz} x_z^2) - \sum_{z=1}^{q-1}\sum_{y=i+1}^{q}(\beta_{z,y} x_z x_y)) \tag{7.10}$$

Since not all terms in the MLR model may be statistically significant, their relevance is examined by testing the null hypothesis (NH) for each coefficient using p-value analysis [209]. For example, considering the coefficient β_z, the NH assumes that there is no relationship between y and x_z, meaning $\beta_z = 0$. The p-value represents the probability of observing the NH, and it is calculated based on the t-statistic of β_z [208]. A high p-value indicates that the NH is likely true, suggesting that the term associated with β_z is not statistically significant and can be disregarded. In this study, a reduced-order model (ROM) of Eq. (7.9) is derived by considering only the significant terms with a p-value greater than 0.05 [209]. The ROM formulation is a crucial step in the statistical analysis as it enables the identification of the most relevant predictors, thereby highlighting potential significant nonlinear relationships between the inputs and outputs, as well as important interactions among the predictors. One limitation of this methodology is its inflexibility, as it relies on a predefined structure for the regression model, which may introduce potential inaccuracies.

7.1.2.2 Machine learning (ML) models

To unveil non-linear relationships, ML models such as RF and NN allow to approximate more complex shapes, to the detriment of features importance understanding.

Random forest (RF)

The Random Forest model is an ensemble learning technique used for both classification and regression tasks, consisting of multiple decision trees (DTs) [208]. In this context, Random Forests with N_{DT} decision trees are specifically employed for regression purposes. Consider a dataset with N observations, denoted as $\Theta = \{(X_1, y_1), (X_2, y_2), \cdots, (X_N, y_N)\}$. Here, $X_k = [x_1, \cdots, x_q] \in \mathbb{R}^q$ represents the vector of q predictors (x_j, $j = 1, \cdots, q$), and $y_k \in \mathbb{R}$ is the response variable for the k-th sample. The development of the Random Forest model begins with dataset preparation. Specifically, N_{DT} bootstrap samples, denoted as Θ_j^*, are created by randomly sampling n instances from Θ with replacement. For each bootstrap sample Θ_j^*, a decision tree T_j is trained by minimizing a splitting criterion, such as the Root Mean Squared Error (RMSE). Once all N_{DT} decision trees are trained, the Random Forest model makes predictions by averaging the outputs of all N_{DT} trees. For a new observation X_{new}, the final prediction is computed as follows:

$$\hat{y}_{new} = \frac{1}{N_{DT}} \sum_{j=1}^{N_{DT}} T_j(X_{new}). \tag{7.11}$$

This ensemble approach reduces variance and enhances the model's ability to generalize compared to individual decision trees, resulting in more accurate and robust predictions. In summary, the Random Forest algorithm aggregates multiple decision trees to create a robust model for regression tasks. By leveraging the diversity introduced through bootstrap sampling and feature randomness, this method improves prediction accuracy and mitigates overfitting issues commonly associated with individual decision trees.

Neural Network (NN)

Multilayer Perceptron (MLP) neural networks are a type of feedforward neural network, consisting of multiple layers of neurons, where each neuron in a given layer is fully connected to all neurons in the subsequent layer.

An MLP typically includes three types of layers: The **Input Layer** consists of neurons that receive input features from the dataset. Each neuron in the input layer corresponds to a feature in the input vector. There are one or more **Hidden Layers** situated between the input and output layers. Each neuron in a hidden layer computes a weighted sum of its inputs and then applies a non-linear activation function. The weighted sum for a neuron j is given by:

$$z_j = \sum_i w_{ji} x_i + b_j \tag{7.12}$$

where z_j is the weighted sum for neuron j, w_{ji} is the weight connecting input i to neuron j, x_i is the input value, and b_j is the bias term for neuron j. After computing this weighted sum, the non-linear activation function σ is applied:

$$a_j = \sigma(z_j) \tag{7.13}$$

where a_j is the output of neuron j after applying the activation function σ. Finally, the **Output Layer** produces the final prediction of the network. For regression tasks, this layer typically contains a single neuron with a linear activation function, which directly outputs the predicted value.

7.1.2.3 Performance matrices

To evaluate and compare the performance of the identified models, the coefficient of determination (R^2) and the Root Mean Squared Error (RMSE) are computed as using the follows:

$$R^2 = 1 - \frac{\sum_{i=1}^{N}(y_i - \hat{y}_i)^2}{\sum_{i=1}^{N}(y_i - \frac{1}{N}\sum_{j=1}^{N} y_j)^2} \tag{7.14}$$

$$\text{RMSE} = \sqrt{\frac{1}{N}\sum_{i=1}^{N}(y_i - \hat{y}_i)^2} \tag{7.15}$$

where, y_i represents the observed values, $\hat{y}_i$ denotes the predicted values, and N is the number of observations. The R^2 value indicates the proportion of variance explained by the model, while RMSE measures the average magnitude of the prediction errors. Note that, R^2 ranges between 0 and 1, indicating the proportion of variability in the response variable captured by the MLR model. A value of 1 signifies that the model precisely captures the variability, while lower values indicate a lesser degree of captured variability. To reduce estimation bias and provide a more generalizable assessment of model accuracy, a K-fold cross-validation approach is employed. Although K can vary between 2 and the number of samples minus 1, a value of $K = 5$ is chosen here for simplicity. This choice ensures that each fold contains a sufficient number of samples for both training and validation phases. Specifically, the dataset is divided into 80% for training and 20% for validation/testing, and the cross-validation process is performed across all five folds with randomly selected samples.

7.1.3 Feature importance analysis

In this study the feature important is analyszed odobting traditional statistic method and XML techniques.

- **Akaike Information Criterion (AIC):** In the context of MLR models, the AIC is utilized to guide the selection of linear, interaction, and quadratic terms. Specifically, the corrected Akaike Information Criterion (AICc) is minimized to optimize the model formulation [210]. The AIC and AICc coefficients are defined as follows:

  $$AIC(M_k) = -2\log L(M_k) + 2k \tag{7.16}$$

  $$AICc(M_k) = AIC(M_k) + \frac{(2k^2 + 2k)}{(n - k - 1)} \tag{7.17}$$

  where $\log L(M_k)$ represents the logarithm of the likelihood function for the model M_k, k denotes the number of features included in the model, and n is the sample size. Among a set of candidate models, the model with the lowest AIC value is preferred. The AIC balances goodness of fit, as measured by the likelihood function, with a penalty for the number of estimated parameters. The AICc extends the AIC by incorporating an additional penalty term for the number of parameters, making it more suitable for smaller sample sizes. In this study, the feature importance analysis for the MLR model is conducted through the examination of the resulting weights.

- **SHapley Additive exPlanations (SHAP) values** are a technique for interpreting machine learning models by quantifying the contribution of each feature to the model's predictions. They are derived from Shapley values in cooperative game theory, which provide a fair allocation of a total payout among players based on their individual contributions. The SHAP value for the i-th feature in a model $\hat{y}$ is calculated as:

$$\phi_i = \sum_{S \subseteq N \setminus \{i\}} \frac{|S|!(|N| - |S| - 1)!}{|N|!} \left[\hat{y}(S \cup \{i\}) - \hat{y}(S)\right] \tag{7.18}$$

where N is the set of all features, and S is a subset of N that excludes the feature i. The term $\hat{y}(S \cup \{i\}) - \hat{y}(S)$ represents the marginal contribution of feature i when added to a subset S of features. It measures how the prediction changes with the inclusion of feature i in various subsets. Meanwhile, the weight $\frac{|S|!(|N|-|S|-1)!}{|N|!}$ adjusts the marginal contribution by considering the number of possible permutations of features. This ensures that each feature's contribution is fairly averaged over all possible feature combinations. SHAP values ensure that each feature's contribution to a model prediction is fairly attributed by considering all possible combinations of features. This method provides a robust and interpretable measure of feature importance, making it a powerful tool for understanding model predictions and ensuring transparency in machine learning models.

The SHAP method facilitates the identification of feature importance, however, it exhibits limitations in terms of visualising of the results. To that end, Individual Conditional Expectation (ICE) and Partial Dependence Plot (PDP) are computed as detailed in the following.

- **Individual Conditional Expectation (ICE) and Partial Dependence Plot (PDP)**: ICE plots are used to illustrate how the prediction for a single instance changes as a specific feature varies, while keeping other features fixed. In contrast, PDPs show the relationship between a feature and the predicted outcome averaged across all instances in the dataset. Unlike ICE plots, which focus on individual instances, PDPs provide a global view by aggregating the feature's effect across the entire dataset.

  To PDP function for a given feature i, is calcualated as:

$$\text{PDP}_i(x_i) = \frac{1}{N} \sum_{j=1}^{N} \hat{y}(x_i, x_{-i}^{(j)}) \tag{7.19}$$

  In this formula, x_i represents the value of the feature i for which the partial dependence is being computed, while $x_{-i}^{(j)}$ denotes the values of all other features (excluding feature i) for the j-th instance in the dataset. The total number of instances in the dataset is denoted by N, and $\hat{y}$ is the model's prediction function. This formula computes the average prediction of the model when feature i is set to x_i, while averaging out the effects of all other features. According to [211], the use of PDPs enables the visualization of the feature of interest and response variable are

Table 7.2: Multivariate linear regression model equations with 3 most influencing β coefficients underlined ($\underline{1^{st}}$, $\underset{-\,-\,-}{2^{nd}}$, $\underset{\cdots}{3^{rd}}$) and resulting R^2 values.

Multivariate linear regression models

$$\begin{aligned}\hat{y} =& \beta_0 + \beta_1 \mathrm{Chem}_{NCA} + \beta_2 \mathrm{Chem}_{MIX} + \beta_3 \mathrm{Ageing} + \beta_4 R_{Int} + \beta_5 T_{amb} + \beta_6 R_{Int}^2 + \\ &+ \beta_7 T_{amb}^2 + \beta_8 \mathrm{Chem}_{NCA} \cdot \mathrm{Ageing} + \beta_9 \mathrm{Chem}_{MIX} \cdot \mathrm{Ageing} + \beta_{10} \mathrm{Chem}_{NCA} \cdot T_{amb} + \\ &+ \beta_{11} \mathrm{Chem}_{MIX} \cdot T_{amb} + \beta_{12} \mathrm{Ageing} \cdot R_{Int} + \beta_{13} \mathrm{Ageing} \cdot T_{amb} + \beta_{14} R_{Int} \cdot T_{amb}\end{aligned} \tag{7.20}$$

Response variable	β_0	β_1	β_2	β_3	β_4	β_5	β_6	β_7
$\%\sigma I_{\mathrm{Start}}$ $[-]$	0.153	-0.002	$\underset{-\,-\,-}{0.044}$	0.014	$\underline{0.098}$	$\underset{\cdots}{0.020}$	-	-
$\%\sigma I_{\mathrm{Mid}}$ $[-]$	0.041	$\underset{\cdots}{-0.014}$	$\underline{0.021}$	0.005	$\underset{-\,-\,-}{0.020}$	0.003	0.005	-
$\%\sigma I_{\mathrm{End}}$ $[-]$	0.151	-0.003	$\underset{-\,-\,-}{0.032}$	0.009	$\underline{0.098}$	$\underset{\cdots}{0.025}$	-	-
$\Delta SoC_{\mathrm{Max}}$ [%]	9.430	-0.795	$\underset{-\,-\,-}{2.600}$	0.659	$\underline{6.764}$	0.807	$\underset{\cdots}{1.093}$	-
$\Delta SoC_{\mathrm{End}}$ [%]	2.648	-0.939	$\underset{\cdots}{0.981}$	0.287	$\underline{1.402}$	-0.683	$\underset{-\,-\,-}{1.384}$	-
$\Delta T_{\mathrm{Net}}^{Max}$ $[°C]$	0.147	-	-	0.313	$\underset{\cdots}{0.477}$	$\underline{-0.941}$	-	$\underset{-\,-\,-}{0.552}$
σT_{Mean} $[-]$	0.384	-0.052	$\underset{-\,-\,-}{0.089}$	0.030	$\underline{0.171}$	-0.051	-	-
TTSB $[-]$	318.575	58.834	-42.268	82.158	$\underline{359.093}$	$\underset{-\,-\,-}{-210.082}$	$\underset{\cdots}{-135.242}$	86.642

Response variable	β_8	β_9	β_{10}	β_{11}	β_{12}	β_{13}	β_{14}	R^2
$\%\sigma I_{\mathrm{Start}}$ $[-]$	0.018	-0.010	-0.005	0.020	-	0.005	-	**0.93**
$\%\sigma I_{\mathrm{Mid}}$ $[-]$	-	-	-	-	-	-	0.003	**0.91**
$\%\sigma I_{\mathrm{End}}$ $[-]$	0.016	-0.008	-0.005	0.018	-	-	0.015	**0.90**
$\Delta SoC_{\mathrm{Max}}$ [%]	0.729	-0.439	-	-	-	0.498	-	**0.97**
$\Delta SoC_{\mathrm{End}}$ [%]	-	-	0.328	-0.651	-	0.551	-0.478	**0.78**
$\Delta T_{\mathrm{Net}}^{Max}$ $[°C]$	-	-	-	-	-	- 0.247	-	**0.61**
σT_{Mean} $[-]$	-	-	-	-	-	-	$\underset{\cdots}{-0.055}$	**0.67**
TTSB $[-]$	-	-	-55.121	82.870	43.473	-46.775	-107.180	**0.94**

related, thereby facilitating the identification of whether the relationship is linear, monotonic, or more intricate in nature. However, the principle of PDPs based on averages does not necessarily eliminate the possibility of interference from interacting variables. This limitation is circumvented by the complementary character of PDPs and ICE plots, which perform optimally when combined as in the presented research.

7.2 Results and discussion

Sections 7.2.1 and 7.2.2 present the results for the MLR and ML models, respectively. Additionally, the two approaches are compared in Section 7.2.3, and the limitations are summarized in Section 7.2.4.

7.2.1 MLR models analysis

Table 7.2 presents the MLR models for the eight response variables under consideration, as detailed in Equation (7.9), in which the three most significant predictors are highlighted.

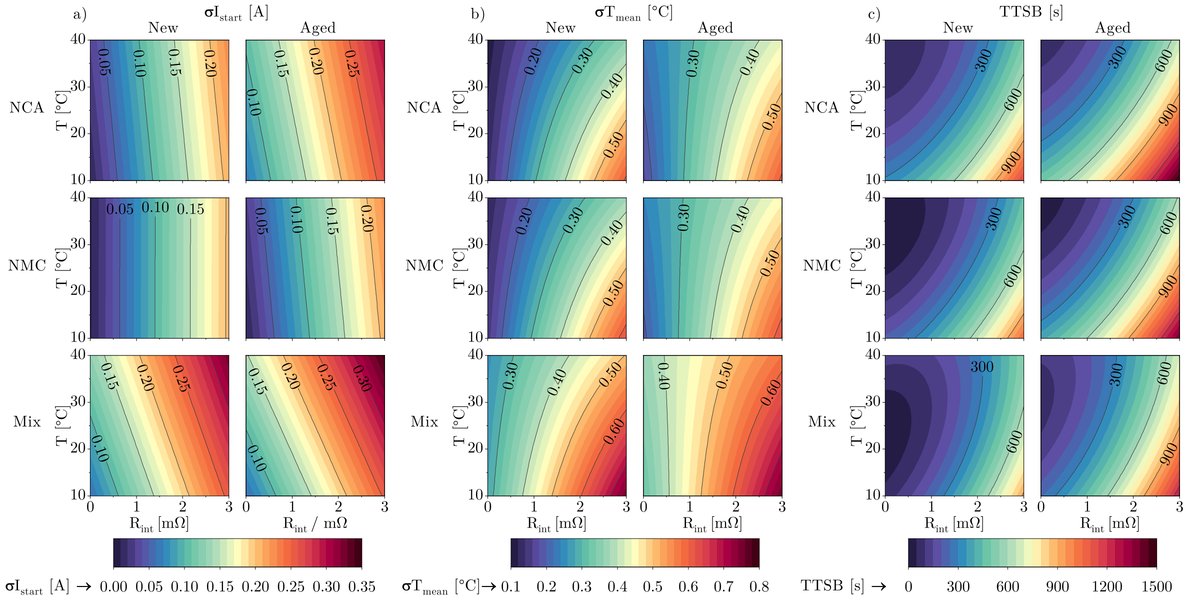

Figure 7.4: Contour plots derived from the multivariate linear models simulated space for (a) σI_{Start}, (b) σT_{Mean}, (c) $TTSB$. The horizontal and vertical axes of individual contour plots are the interconnection resitance and the test temperature, respectively. The columns of each group of six contour plots have new and aged cells configurations, respectively, while the rows differ upon chemistry (NMC, NCA, Mix).

Note that, the reported models have been refined by excluding statistically irrelevant terms using the AIC method. Additionally, the chemistry features are categorized into two groups: $Chem_{NCA}$ and $Chem_{Mix}$. This categorization is necessary because the three levels in the DOE (i.e. NCA, NMC, and Mix) are treated as two binary pairs in the MLR model.

Interconnection resistance emerges as the most influential factor for both the initial and final current distributions, with the effects of chemistry and its combinations following closely. For σI_{mean}, chemistry again plays a significant role. Further analysis will explore how chemistry and aging contribute to the internal characteristics of the cells. In terms of the maximum and final SOC differences, both interconnection resistance and its square, as well as the inclusion of different chemistries, are crucial factors. The models generally perform well, with five out of eight response variables achieving an R^2 of 0.9. The predictive models for temperature yield less satisfactory results, primarily due to the measurement uncertainty associated with temperature itself. Nevertheless, the MLR coefficients suggest that interconnection resistance, operating temperature, and its square influence both the net surface temperature increase and its gradient between the cells. Finally, the TTSB variability can be predominantly attributed to interconnection resistance, its square, and operating temperature.

The MLR model formulations, detailed in Table 7.2, are further illustrated using contour plots, as shown in Figure 7.4. This figure includes three of the eight response variables from the MLR model: σI_{Start}, σT_{Mean}, and TTSB. The x and y axes represent interconnection resistance and test temperature, respectively. The columns indicate different aging levels, while the rows display tests with NCA, NMC, and mixed chemistries.

A common trend observed across all three plots is that as interconnection resistance increases, the performance of cells connected in parallel deteriorates. Figure 7.4(a) illustrates that higher interconnection resistance leads to increased initial current heterogeneity, potentially exceeding 300 mA. While temperature has a minimal effect on individual NCA and NMC cells, it significantly influences combinations of different chemistries. The bottom row of the figure shows that resistance and temperature have nearly equal relevance. Higher temperatures exacerbate current distribution issues, with a 70 mA difference observed between 10 $°C$ and 40 $°C$ at constant resistance. Additionally, the presence of an aged cell adversely affects the current distribution in other cells. The contour plot for σT_{Mean} is shown in Figure 7.4(b). It is visible that the ambient temperature significantly influences the temperature gradient, exhibiting a non-linear relationship with interconnection resistance. The reduction in temperature gradient ranges from 0 $°C$ at 1 mΩ resistance to 0.2$°C$ at 3 mΩ, with similar trends observed for both NMC and NCA cells. When combining different chemistries, the temperature difference between cells can exceed 0.7$°C$. An aged cell has minimal impact on temperature distribution in single-chemistry scenarios but increases the gradient to 0.35-0.75$°C$ in mixed-chemistry situations. Finally, Figure 7.4(c) illustrates a pronounced curvature in the TTSB with respect to interconnection resistance and operating temperature, while aging level and cell mixture have a less pronounced impact.

Despite the MLR analysis of the performance of the parallel-connected battery module, this analysis provides additional insights. It confirms that combining NMC and NCA cells in parallel is feasible. However, it also highlights a detrimental effect on both current and temperature distribution. This issue is primarily due to the differing internal characteristics of the two cell types. Although the discharge capacity difference is approximately 2%, the internal resistance of NCA cells is 30% lower than that of NMC cells, leading to increased heterogeneity when cells are connected in parallel. Similarly, the inclusion of an aged cell adversely affects the balance between the cells.

As briefly mentioned in the previous paragraph, linearizing categorical variables poses significant challenges. To overcome this, the categorical variables representing chemistry and aging are transformed into numerical variables. These numerical variables provide detailed information on internal resistance and cell capacity distribution within the module. Specifically, ΔR_0 *and* ΔC_n *are introduced to quantify the differences in resistance and capacity between the stronger and weaker cells within the module. This approach is physically justified, as the primary distinctions between NMC, NCA, and Mix configurations lie in their internal parameter values under both aged and fresh scenarios. Furthermore, by replacing categorical variables with numerical counterparts, a higher level of granularity is achieved in the variation of control variables. This transformation allows for a more nuanced analysis, as the variables are no longer confined to two or three discrete levels but can capture a continuous range of values. To ensure the robustness of the model and to prevent potential multicollinearity among the predictors, a Variance Inflation Factor*

(VIF) analysis is conducted prior to modifying the predictors. This step is crucial in identifying and mitigating any correlated predictors, thereby enhancing the reliability of the regression results.

7.2.2 ML models analysis

Figures 7.5, 7.6, 7.7 present contour plots resulting from the MLR, NN and RF models for TTSB, respectively. The x and y axes are replaced by the new control variables ΔR_0 and ΔC_n. The columns indicate the interconnection resistance, while the rows represent the ambient temperatures. Note that, each contour plots are constrained by ΔR_0 and ΔC_n obtained in the tests. The key difference between conventional linear models and ML models is their interpretability. As illustrated in Figures 7.6 and 7.7, the ML models exhibit a higher sensitivity to the dataset used. This is evident from the distinct island-like countrs in the NN plots and the square-shaped contours observed in the RF plots. Consequently, this high sensitivity makes ML models more challenging to interpret compared to traditional linear models.

The initial method applied is the SHAP technique [212], as shown in Figure 7.8 for the eight response variables in the RF model. Similar findings are observed with the NN model, though these results are omitted here for conciseness. As detailed in Section 7.1.3, SHAP values facilitate the ranking of feature importance, highlighting key factors influencing model performance. Consistent with findings from linear models, the interconnection resistance emerges as the most significant factor affecting parallel string performance, with the exception of ΔT_{Net}^{MAx}. Figure 7.8 (g) demonstrates that cell temperature inversely impacts the increase in temperature during operation. This inverse relationship is attributed to the fact that lower operating temperatures lead to a greater temperature rise during discharge due to heightened ohmic losses. Additionally, the internal resistance of the cell is known to vary with operating temperature. The ranking of the remaining three features fluctuates depending on the specific response variable considered. Among the notable trends, Figure 7.8 (b) reveals a strong influence of ΔC_n on σI_{Mid}, suggesting that discrepancies in nominal capacity between cells affect the current distribution during the discharge's central phase. Meanwhile, variations in internal resistance at both the start and end of discharge exert a more pronounced effect, as shown in Figures 7.8 (a) and (c). Operating temperature also significantly impacts the TTSB, as illustrated in Figure 7.8 (h). Interpreting the differences in SOC, as depicted in Figures 7.8 (e) and (f), is more complex. The model demonstrates greater stability in predicting ΔSoC_{Max} compared to ΔSoC_{End}, suggesting a more substantial influence of ΔR_0 on the maximum SoC differences. Conversely, Figure 7.8 (f) does not reveal a distinct order of importance among the features.

Although SHAP analysis is effective in ranking controllable variables, it does not address how their effects are distributed spatially. To address this limitation and enhance model interpretability, PDP and ICE plots are employed. Figure 7.8 presents these plots for both the Neural Network (NN) and Random Forest (RF) models, covering five of the eight re-

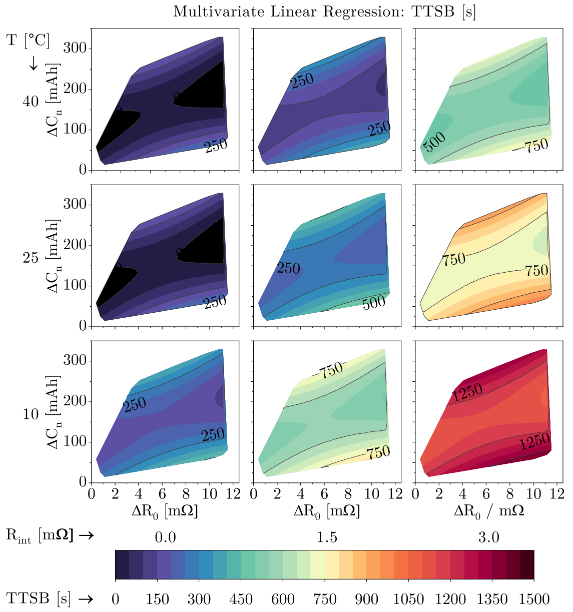

Figure 7.5: Contour plots derived from the MLR model for TTSB.

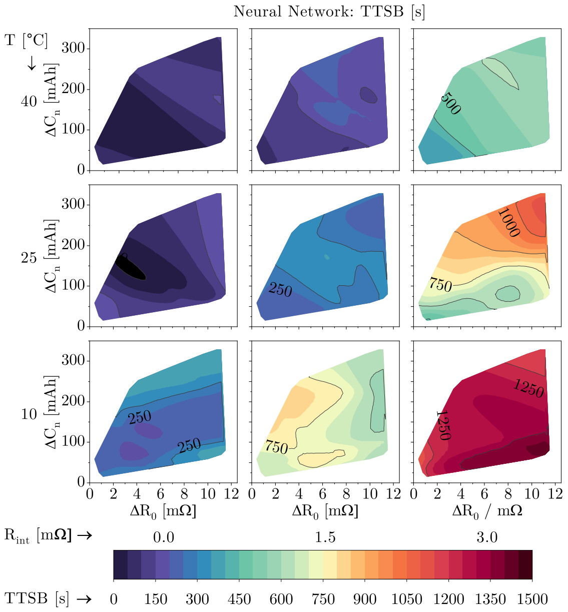

Figure 7.6: Contour plots derived from the NN model for TTSB.

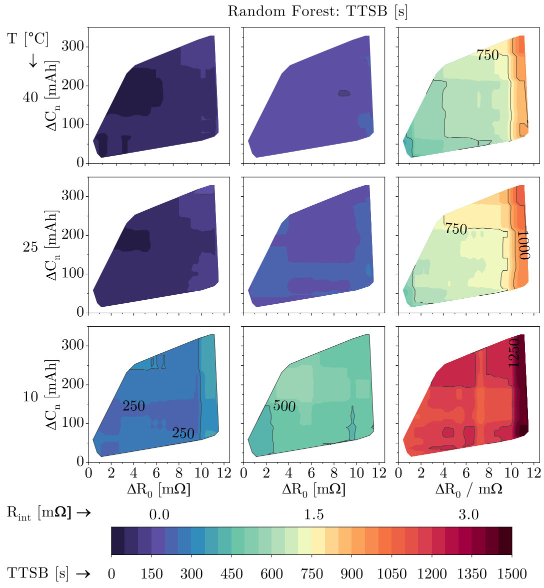

Figure 7.7: Contour plots derived from the RF model for TTSB.

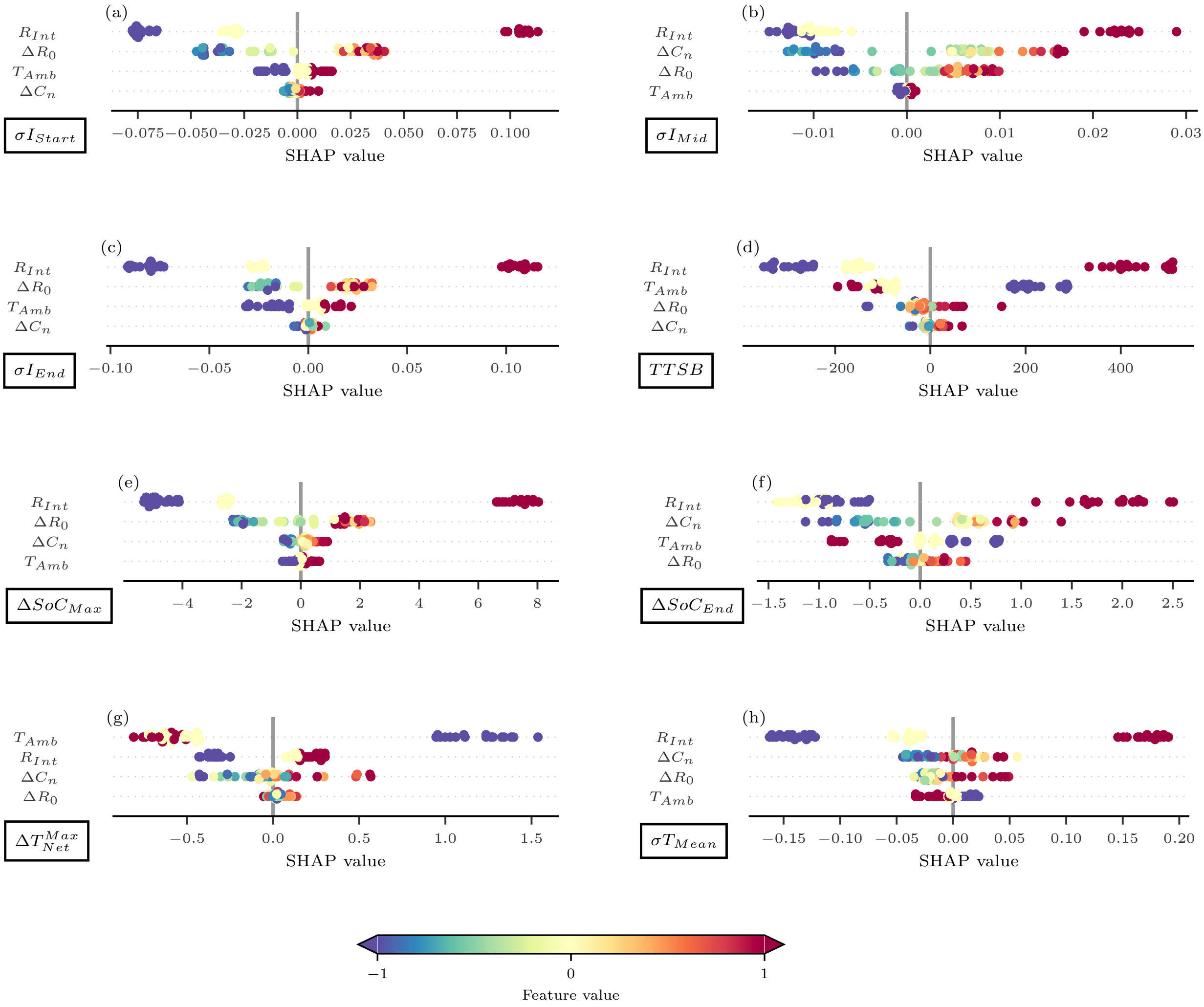

Figure 7.8: Random Forest model simulated Shap values for the eight considered response variables (a-h). On the left side of individual graphs the resulting feature importance ranking is reported, while the circles' colour shades indicate their absolute value.

sponse variables. [1] The angular coefficient of the curves provides insights analogous to those given by the normalized coefficients in linear models. It becomes evident that interconnection resistance is the most significant factor, as it yields the highest angular coefficient, consistent with previous analyses. Both ML models shows similar results. As predicted by the SHAP analysis, ΔC_n plays a crucial role alongside interconnection resistance when addressing σI_{Mid}, as illustrated in Figure 7.9 (b). For σI_{Start} shown in Figure 7.9 (a), the interconnection resistance and ΔR_0 are the most significant factors. In the NN model, a strong linear relationship between ΔR_0 and σI_{Start} is observed. Conversely, in the RF model, ΔR_0 shows notable increases only near the median values, a pattern that is also evident for ΔSoC_{Max} in Figure 7.9 (c). On the other hand, the dependency of σT_{Mean} on ΔR_0 and ΔC_n in Figure 7.9 (d) is less clear, with oscillations suggesting a high sensitivity to the dataset. Finally, Figure 7.9 (e) shows that TTSB is directly correlated with interconnection resistance and inversely correlated with operating temperature.

Note that PDP and ICE plots offer insights into the impact of each individual feature included in the analysis, but they do not capture interactions between features. To examine the interactions between control variables, two-dimensional PDP plots can be used. For those interested in a more detailed analysis of 2D PDPs, please refer to [31].

These graphs help determine whether the machine learning model employs linear, monotonic, or non-linear relationships between the control and response variables. In the investigated scenario, the relationships appear to be only slightly non-linear. In such cases, a linear model may be adequate for predicting both the responses and the importance of the features, as will be further demonstrated in the next section.

7.2.3 Models comparison

The predictive performances of the three models, expressed in terms of R^2 with the corresponding standard deviation reported in parentheses, are detailed in Table 7.3. This evaluation utilizes 5-fold cross-validation.

Overall, the performance of the modeling frameworks is comparable for σI_{Start}, σI_{End}, and ΔSOC_{max}, each exhibiting R^2 values greater than 0.85. On the other hand, a performance decrease is observed for the remaining response variables, with R^2 values ranging from 0.43 to 0.89. However, no single modeling framework consistently outperforms the others across these variables. RF models are particularly effective for predicting σI_{Mid}, while NN demonstrate superior performance in modeling the variability of the maximum thermal gradient. In contrast, MLR models offers the best predictions for the TTSB. Finally, the standard deviation is a critical metric as it reflects the stability of the model outcomes across different datasets. It is evident that for variables such as temperature and final SoC variation, both the absolute predictive performance and repeatability are limited.

---

[1] The response variables, including initial and final current, maximum and final SoC variation, ΔT_{Net}^{Max}, and σT_{Mean}, are pairwise correlated.

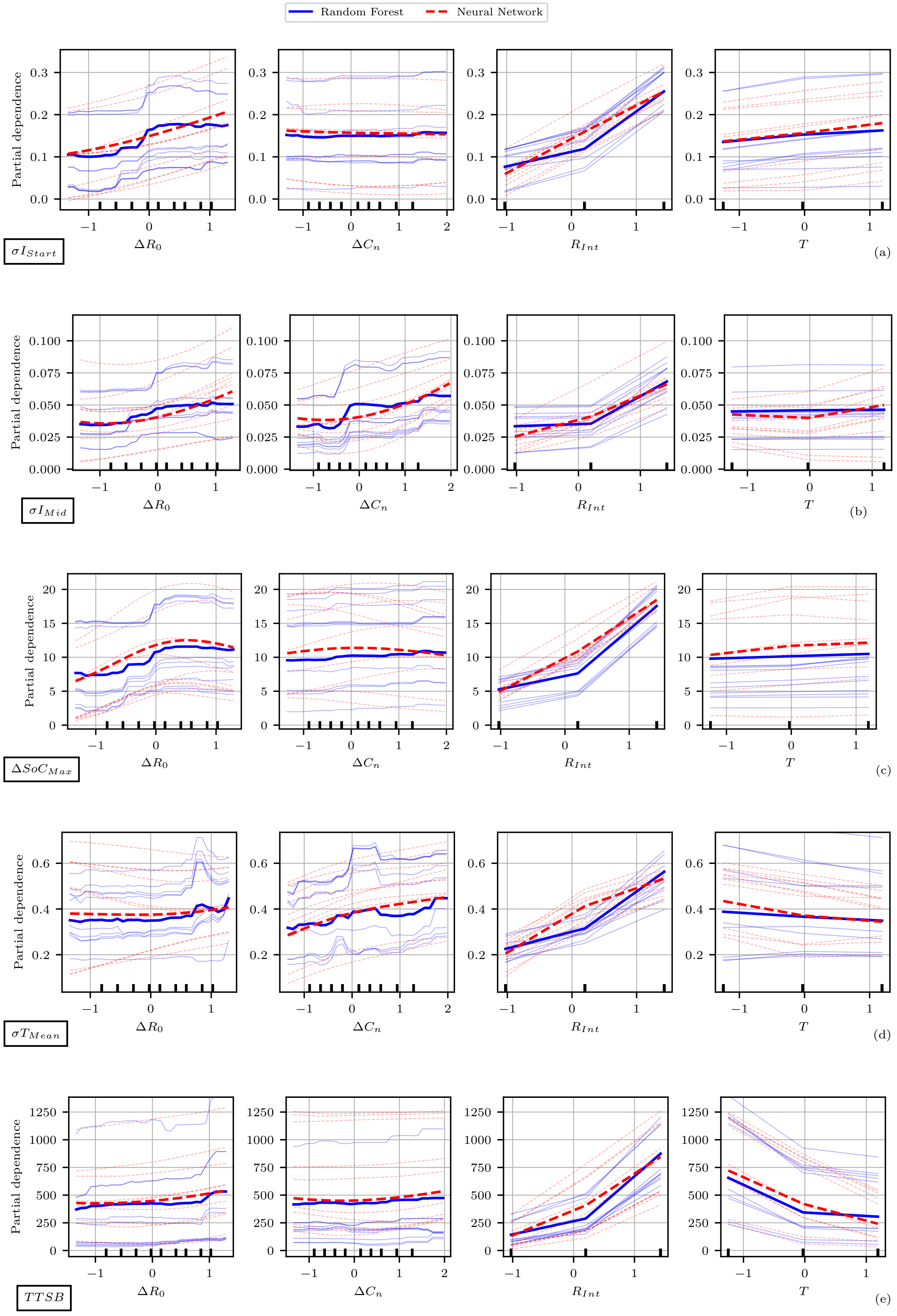

Figure 7.9: Random Forest (red) and Neural Network (blue) models PDP and ICE plots for five out of the eight response variables (a-e). Each column reports the PDP and ICE plots resulting from one individual feature.

Table 7.3: Evaluated 5-fold cross-validation models performance mean values and standard deviations.

	Model Mean (Std) R^2		
Response Variable	*MLR*	*NN*	*RF*
σI_{Start}	0.91(0.03)	0.90(0.13)	0.90(0.04)
σI_{Mid}	0.73(0.19)	0.74(0.13)	0.89(0.05)
σI_{End}	0.86(0.08)	0.90(0.04)	0.85(0.16)
ΔSoC_{Max}	0.91(0.04)	0.87(0.14)	0.93(0.02)
ΔSoC_{End}	0.47(0.24)	0.59(0.73)	0.53(0.11)
ΔT_{Net}^{Max}	0.43(0.25)	0.70(0.60)	0.46(0.27)
σT_{Mean}	0.49(0.23)	0.56(0.28)	0.55(0.43)
$TTSB$	0.73(0.19)	0.65(0.20)	0.66(0.13)

7.2.4 Limitations

This study presents certain limitations. Despite efforts to minimize and monitor the influence of the experimental setup, parallel-connected cells remain particularly sensitive to the quality of their connections. While industry-level busbars typically use soldered connections rather than bolted ones, the results of this research remain applicable to such contexts, though the impact of interconnection resistance is expected to be lower due to its reduced magnitude. Although the proposed methodology is data-agnostic, the tuning of machine learning model hyperparameters is not. Careful tuning will be necessary when applying this approach to other scenarios. Further research is needed to explore a broader range of input and output variables. Future studies could examine different architectures (such as Z or mixed), chemistries (e.g., LFP, LMO), form factors (18650, 4650, pouch), and real-world load cycles. Additionally, module configurations with optimized cell spacing and arrangement should be considered. While this study focuses on performance-related heterogeneities, the long-term effects of imbalances on cell aging remain an open question in the literature. Their influence on SOH distribution and aging rates also requires further investigation.

It is important to note that conducting full-factorial DOE with numerous input features is both expensive and time-consuming. A more efficient alternative is the use of high-fidelity, module-level digital twins. In the next chapter, an experimentally validated electrochemical battery model is introduced for this purpose. By employing high-fidelity mathematical models that account for Ctc interactions and replicate cell heterogeneity, we can gain deeper insights into the propagation of heterogeneity within parallel battery modules. This approach has the potential to enhance module performance, ensure safety, and ultimately support battery recyclability.

7.3 Conclusion

In this chapter, the influence of cell- and module-level properties on the performance of parallel-connected strings was investigated through a combination of non-invasive experiments and data-driven modeling techniques. A comprehensive 54-condition full-factorial DOE was conducted on four ladder-parallel connected modules. This allowed for the independent evaluation of various factors to quantify their impact on overall module performance. The experiments provided insights into how variations in cell current, SOC, temperature heterogeneity, and TTSB respond to different interconnection resistances, operating temperatures, combinations of cell chemistries, and levels of aging. These conditions were examined under a CC discharging scenario. Three different modeling frameworks were employed to predict performance outcomes and assess the importance of various predictors. Specifically, MLR was applied in combination with the AIC, while RF and NN were used alongside SHAP values, PDP, and ICE plots.
The main findings are summarized as follows:

1. **Interconnection Resistance**: The interconnection resistance was identified as the most significant factor contributing to performance heterogeneity within parallel-connected strings. In the early and middle stages of discharge, internal resistance and capacity distribution respectively influenced load imbalances across the cells. An increase in operating temperature exacerbated the temperature gradient within the string. To mitigate self-balancing currents post-discharge, optimized busbar design and effective thermal management are crucial.

2. **Mixed Chemistries**: Statistical analysis from the DoE indicates that combining NMC and NCA cells in parallel is feasible. However, this results in a twofold increase in current deviation between the cells compared to using a single chemistry. While temperature gradients increase, the TTSB remains largely unaffected by this combination.

3. **Aging Effects**: The introduction of an aged cell into the string worsened the overall homogeneity of the cells performance. Additionally, the impact of operating temperature on performance imbalances increased, underscoring the need for improved thermal management in such cases.

4. **Modeling Performance**: Both traditional linear regression and machine learning models demonstrated comparable predictive accuracy, with R^2 values exceeding 0.85 for most response variables, except for $\Delta\text{SoC}_{\text{End}}$ and temperature-related signals. While the machine learning models exhibited strong performance, their interpretability remained limited, thus, XML techniques demonstrated their value in addressing this limitation.

Chapter 8

Model-based analysis of CtC variation impact on parallel-connected module

Contents

8.1 Model and method 163
- 8.1.1 High-fidelity model 163
- 8.1.2 CtC variation effect: MLR analysis 163

8.2 Results and discussion 165
- 8.2.1 MLR analysis: short term CtC heterogeneity effects 165
- 8.2.2 MLR analysis: long term CtC heterogeneity effects 169
- 8.2.3 Cell arrangement strategy for thermal gradient reduction 172

8.3 Conclusion 174

This contribution is based on the following work:

- [27] **Fasolato, S.**, Allam, A., Onori, S., and Raimondo, D. M. (2024). *Cell-to-Cell Heterogeneities and Module Configurations analysis in Parallel-Connected Battery Modules via physics-based modeling*, Journal of Energy Storage, **Submitted**.

Introduction

As outlined in the introduction of Chapter 7, CtC variations arise from multiple sources and their effects are intricately interrelated within parallel battery modules. Furthermore, it was emphasized that the effective implementation of a DOE is essential for establishing a well-structured experimental campaign, to ensures the reliable results while optimizing the utilization of available resources.

However, considering the multitude of factors involved in module and pack design, along with the long-term effects of CtC variations on battery system aging, utilizing digital twins presents an effective alternative approach. Digital twins employ high-fidelity mathematical models that capture CtC interactions and replicate both cell heterogeneity and module responses. This methodology provides valuable insights into how heterogeneity propagates within parallel battery modules, especially under stringent economic, temporal, and facility constraints that hinder the execution of complex experimental campaigns. In this chapter, this efficient approach by utilizing an experimentally validated electrochemical battery model, with the final aim to investigate the impact of CtC variation on parallel-connected battery modules through a model-based statistical approach. Within this framework, high-fidelity electrochemical models are preferred over ECMs due to their ability to accurately capture the intricate electrochemical dynamics of each cell. Unlike ECMs, which simplify the battery behavior using electrical components, high-fidelity models provide a more detailed representation of the underlying electrochemical processes, and, in turn, are better suited for offline high-fidelity simulations.

Chapter contribute

The physics-based modeling framework for parallel-connected cells, identified and validated in Section 5.2 of Chapter 5, is adopted in this chapter. Specifically, the electrochemical dynamics of each cell are modeled using ESPM, coupled with a thermal model. This thermal model has been identified and validated using single-cell characterization data from a batch of 19 cells and module-level experiments. The framework incorporates both Cell-to-Cell (CtC) thermal and electrical interactions, along with a physics-based aging model. Compared to several ECM-based parallel-connected modules proposed in the literature [200, 194, 169, 213, 191, 214, 164, 215, 171], the present model accurately monitors the electrochemical states of each cell and is better suited for offline high-fidelity simulations. Additionally, the preference for the ESPM over the more complex DFn-based parallel-connected module models [189, 186, 216, 176] is due to its demonstrated comparable performance at C-rates below 3 [217]. Furthermore, the ESPM significantly reduces the computational burden when dealing with a large number of cells and conducting long-term simulations. Subsequently, a statistical analysis is performed using multi-linear regression to examine the influence of CtC parameter uncertainties and module configuration on cell current and temperature distributions, as well as on the module's energy and capacity in both fresh and aged conditions. Unlike the previous chapter, this analysis incorporates the effects of varying cell spacing, cell location, and manufacturing-induced CtC variations within the module, investigating their impacts under both short-term and long-term operations. Conversely, ambient temperature and the effects of mixed chemistry are excluded from this analysis. Finally, a simple cell arrangement strategy is proposed to mitigate thermal gradients in parallel-connected battery modules, thereby reducing the aging gradient between cells by the end of the simulations.

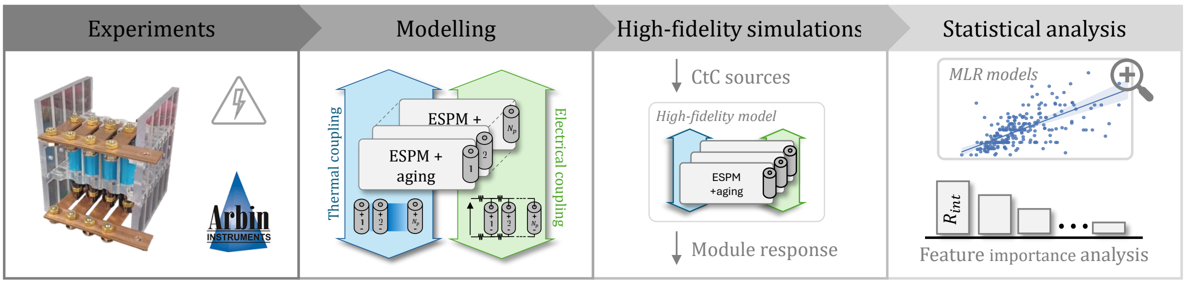
Experiments
Modelling
High-fidelity simulations
Statistical analysis
Arbin INSTRUMENTS
Thermal coupling
Electrical coupling
ESPM +
ESPM + aging
CtC sources
High-fidelity model
ESPM +aging
Module response
MLR models
R_{int}
Feature importance analysis

Figure 8.1: Visual overview of the model-based CtC variations analysis described in this chapter.

Chapter structure

- **Section 8.1** provides a comprehensive description of the model and methods employed in this study. Specifically, Section 8.1.1 directs readers to Chapter 5, where the model is thoroughly described. Additionally, Section 8.1.2 details the MLR-based statistical analysis conducted.

- **Section 8.2** presents the results of the MLR-based analysis. Specifically, Sections 8.2.1 and 8.2.2 detail the outcomes for the short-term and long-term scenarios, respectively. Furthermore, Section 8.2.3 outlines the cell arrangement strategy.

- **Section 8.3** summarizes the conclusions drawn and outlines future research opportunities.

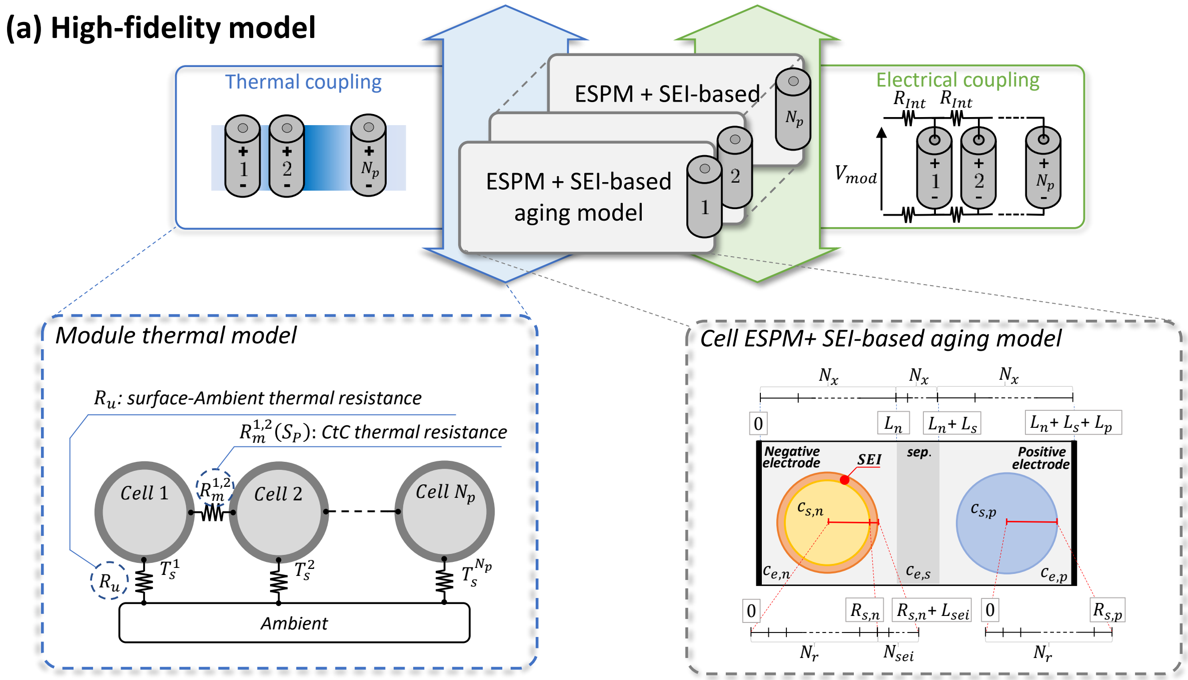
(a) High-fidelity model
Thermal coupling
1
2
N_p
ESPM + SEI-based
ESPM + SEI-based aging model
Electrical coupling
R_{Int} R_{Int}
V_{mod}
Module thermal model
R_u: surface-Ambient thermal resistance
$R_m^{1,2}(S_p)$: CtC thermal resistance
Cell 1
Cell 2
Cell N_p
$R_m^{1,2}$
R_u
T_s^1
T_s^2
$T_s^{N_p}$
Ambient
Cell ESPM+ SEI-based aging model
N_x N_x N_x
0
L_n
$L_n + L_s$
$L_n + L_s + L_p$
Negative electrode
SEI
sep.
Positive electrode
$c_{s,n}$
$c_{s,p}$
$c_{e,n}$
$c_{e,s}$
$c_{e,p}$
$R_{s,n}$
$R_{s,n} + L_{sei}$
$R_{s,p}$
N_r N_{sei} N_r

Figure 8.2: Schematic representation of the physics-based electrochemical-aging-thermal model for the battery module, where the module thermal model and the ESPM coupled with the SEI-based aging model are highlighted.

8.1 Model and method

8.1.1 High-fidelity model

At the core of the analysis lies a mathematical model, schematically depicted in Figure 8.2, capable of accurately capturing the electrochemical, thermal, and aging dynamics of each cell within the module. Particularly, the ESPM-baed module-level model described in Section 5.2 is employed in this Chapter. The cell-level dynamics, described by the ESPM in conjunction with a physics-based degradation model, was identified and validated using characterization data (i.e. Pesudo-OCV test and HPPC) from a batch of 19 LG Chem INR 21700 M50T cells, as described in Section 5.2.1. Subsequently, the parallel-connected module model was developed by integrating the cell-level dynamics with module-level electrical and thermal models, as validated and presented in Section 5.2.2.

8.1.2 CtC variation effect: MLR analysis

In this study, MLR analysis is used to assess the impact of a set of independent variables (predictors) on a response variable, assuming a linear relationship between predictors and the response, as reviewed in Section 7.1.2.1. The predictors selected for the MLR model represent common sources of CtC variations in battery modules at the beginning of their lifecycle. Subsequently, a relative importance analysis evaluates their contributions to cell current and thermal heterogeneities, as well as to the energy and capacity of parallel-connected modules under both fresh and aged conditions.

To achieve our objective, we simulate a population of battery modules by sampling values of highly influential parameters (i.e. $[\epsilon_n, \epsilon_p]$), electrical interconnection resistances (R_{int}), cell spacing (Sp), and their respective locations. Variations in ϵ_n and ϵ_p stem from tolerances in various electrode production steps—mixing, coating, calendaring, and sliding [218]. The parameter set $[\epsilon_n, \epsilon_p]$ is chosen based on sensitivity analysis results for the ESPM present in the literature (Section X) and from the identification procedure outlined in Section 5.2.1, where it was shown that the variation of $[\epsilon_n, \epsilon_p]$ can effectively capturing capacity variations across batches of fresh cells. Given the numerous physical parameters in the ESPM, addressing this issue solely through simulations would be computationally demanding. In contrast, differences in R_{int} and Sp are influenced by module design and manufacturing precision.

Note that, ϵ_n and ϵ_p are simultaneously perturbed for each cell in the module, inducing capacity gradients among interconnected branches. As mentioned earlier, auxiliary variables, specifically the mean value ($\mu_{\epsilon_{s,j}}$) and standard deviation ($\sigma_{\epsilon_{s,j}}$) of both parameters, are considered as predictors to account for the parameter distribution within the module. These are calculated as follows:

$$\mu_{\epsilon_{s,j}} = \frac{1}{N_p}\sum_{i=1}^{N_p} \epsilon_{s,j}^{[i]}, \qquad \sigma_{\epsilon_{s,j}} = \sqrt{\frac{1}{N_p - 1}\sum_{i=1}^{N_p}(\epsilon_{s,j}^{[i]} - \mu_{\epsilon_{s,j}})^2}, \qquad \text{with: } j \in [n,p] \tag{8.1}$$

It is important to note that assuming that cell capacity can deviate by up to 2.5% from the nominal value (i.e. 4.85 Ah for the LG M50T battery), the lower and upper bounds for ϵ_n and ϵ_p are determined based on the relationships identified in Section 5.2.1 considering the batch of 19 tested cells. Specifically, the values of ϵ_n and ϵ_p are randomly sampled for each cell assuming a uniform probability distribution for both parameters. Besides $\mu_{\epsilon_{s,j}}$ and $\sigma_{\epsilon_{s,j}}$, the other predictors for the multi-linear regression models are Sp, assumed identical between all cells and highlighted in Figure 8.2, R_{int}, and cell location (Loc) within a module of N_p parallel-connected cells, as detailed in Table 8.1. Specifically, Sp and R_{int} are randomly sampled within the intervals $[1, 10]$ mm and $[0.1, 0.5]$ $m\Omega$, respectively. The introduction of the predictor Loc aims to consider the effect of cell arrangement on the thermal gradient. Specifically, for each perturbed parameter, Loc is calculated as a weighted mean value of $min({\epsilon_{s,n}^{-}}^{[i]}, {\epsilon_{s,p}^{-}}^{[i]})$, as shown in (8.5). Here, ${\epsilon_{s,j}^{-}}^{[i]}$ is the normalized value of $\epsilon_{s,j}^{[i]}$ within the interval [0,1], and w_i is the weight depending on the position of the cell ($P_i = 1, 2, \cdots N_p$) within the module.

A total of 500 battery modules are generated, each of them undergoes 500 cycles at an ambient temperature of $T_{amb} = 25°C$. Each cycle consists of the following steps: 1) CCCV charge at a C/3-rate, 2) 30 minutes of rest, 3) CC discharge at a 1C-rate, starting from 100% SOC down to 0% SOC, 4) another 30 minutes of rest to allow for the balancing of any SOC heterogeneity within the module. The quantities of interest for the CtC analysis (i.e. response variables) that are computed for all the conducted simulations are presented in Table 8.1. In particular, $\%\Delta E$ and $\%\Delta Q$, calculated as in (8.11) and (8.12), indicate the percentage deviation of the module energy (E_{mod}) and capacity (Q_{mod}) from their reference values E_{mod}^{ref} and Q_{mod}^{ref}, respectively. The reference module is composed by 4 unperturbed cells, cycled considering $R_{int} = 0.25m\Omega$ and $Sp = 5mm$, where E_{mod} and Q_{mod} are calculated as:

$$E_{mod} = \int_{t_{in}^{ch}}^{t_{end}^{ch}} V_{mod} I_{mod} dt, \qquad Q_{mod} = \int_{t_{in}^{ch}}^{t_{end}^{ch}} I_{mod} dt \tag{8.2}$$

and t_{in}^{ch} and t_{end}^{ch} are the initial and final time instant of the CC discharging cycle. Further, $\sigma_{I_{cell}}$ is the mean of the cell current standard deviation, calculated as in (8.14). ΔT_{max} is maximum thermal gradient (8.13) and $\sigma_{T_{cell}}$ is the mean of the cell temperature standard deviation. E_{lost} measures the energy lost experienced from the first charging cycle (i.e., the Beginning Of Simulation - BOS) until the End of the Simulation (EOS), after a total of 500 cycles. σR_{SEI}^{EOS}, reported in Eq. (8.16), represents the standard deviation of SEI resistance of the cells within the module at the EOS. Finally, $\Delta\mu_{\epsilon_{s,n}}$ and $\Delta\sigma_{\epsilon_{s,n}}$ are, respectively, the difference between the $\mu_{\epsilon_{s,j}}$ and $\sigma_{\epsilon_{s,j}}$ calculate at the BOS and EOS, as in (8.18) and (8.17).

8.2 Results and discussion

In this section, the results of the MLR statistical analysis are discussed. Specifically, the outcomes of the short-term and long-term analyses are presented in Sections 8.2.1 and 8.2.2, respectively.

8.2.1 MLR analysis: short term CtC heterogeneity effects

In this section, the short-term impacts of CtC heterogeneities on fresh battery cells are investigated. We focus on the previously mentioned response variables, specifically $\%\Delta Q$, $\%\Delta E$, $\sigma_{I_{cell}}$, $\sigma_{T_{cell}}$ and ΔT_{max}, while excluding those affected by aging, such as E_{lost}, σR_{SEI}^{EOS}, $\Delta\mu_{\epsilon_{s,n}}$ and $\Delta\sigma_{\epsilon_{s,n}}$. Before constructing the multilinear regression models, we conduct both correlation and Variance Inflation Factor (VIF) analyses on the model predictors to mitigate multicollinearity. Multicollinearity occurs when independent variables in a regression model are correlated, leading to unstable coefficient estimates and unreliable statistical tests on these coefficients [208]. A VIF value of 1 indicates no correlation between a given predictor and the other predictors, whereas VIF values exceeding 5 or 10 suggest significant multicollinearity. It is important to note that the set of predictors previously introduced (i.e. $\Gamma_1 = [\mu_{\epsilon_{s,n}}, \mu_{\epsilon_{s,p}}, \sigma_{\epsilon_{s,n}}, \sigma_{\epsilon_{s,p}}, R_{int}, Sp, Loc]$) are uncorrelated, as demonstrated in Figure 8.3(a-b), making them well-suited for MLR model construction. The MLR models are then constructed using the structure defined in Equation (7.9), focusing on terms that exhibit statistical significance (p-value < 0.05). To evaluate the relative importance of each predictor, a comprehensive relative importance analysis was performed, and the results are presented in Figure 8.3 for each considered response variable. This analysis assesses the contribution of each predictor to the increase in the corresponding model's R^2 value. The first column of Figure 8.3(c.1-g.1) visually represents the

Table 8.1: Multi linear regression model predictor aand response variable

MLR models: Predictors

$$\mu_{\epsilon_j} = \frac{1}{N_p}\sum_{i=1}^{N_p}\epsilon_{s,j}^{[i]}, \quad \text{with: } j \in [n,p] \tag{8.3}$$

$$\sigma_{\epsilon_j} = \sqrt{\frac{1}{N_p-1}\sum_{z=1}^{N_p}(\epsilon_{s,j}^{[z]} - \mu_{\epsilon_j})^2}, \quad j \in [n,p] \tag{8.4}$$

$$Loc = \sum_{i=1}^{N_p} w_i \cdot \min(\epsilon^{-}_{s,n}{}^{[i]}, \epsilon^{-}_{s,p}{}^{[i]}), \qquad \text{where} \qquad w_i = \begin{cases} (\frac{N_p}{2}+1) - P_i & \text{if: } 1 \leq P_i \leq \frac{N_p}{2} \\ \frac{N_p}{2} - P_1 & \text{if: } \frac{N_p}{2} < P_i \leq N_p \end{cases} \tag{8.5}$$

$$\mu_{comb} = \frac{1}{N_p}\sum_{i=1}^{N_p} min(\epsilon^{-}_{s,n}{}^{[i]}, \epsilon^{-}_{s,p}{}^{[i]}) \tag{8.6}$$

$$\sigma_{comb} = \sqrt{\frac{1}{N_p-1}\sum_{z=1}^{N_p}(min(\epsilon^{-}_{s,n}{}^{[i]}, \epsilon^{-}_{s,p}{}^{[i]}) - \mu_{comb})^2} \tag{8.7}$$

$$Loc_j = \sum_{i=1}^{N_p} w_i \cdot \min(\epsilon_{s,j}^{[i]}), \quad j \in [n,p] \tag{8.8}$$

Cell spacing (Sp)

$$\sigma I_{cell} = \frac{1}{t_{end}-t_0}\int_{t_0}^{t_{end}} \sqrt{\frac{1}{N_p-1}\sum_{z=1}^{N_p}(I_{cell}^{[z]} - I_{mod}/N_p)^2 dt} \tag{8.9}$$

$$\sigma T_{cell} = \frac{1}{t_{end}-t_0}\int_{t_0}^{t_{end}} \sqrt{\frac{1}{N_p-1}\sum_{z=1}^{N_p}\Big(T_{cell}^{[z]} - \frac{1}{N_p}\sum_{i=1}^{N_p}T_{cell}^{[i]}\Big)dt} \tag{8.10}$$

MLR models: Response variables

$$\%\Delta E = 100\frac{E_{mod} - E_{mod}^{ref}}{E_{mod}^{ref}} \tag{8.11}$$

$$\%\Delta Q = 100\frac{Q_{mod} - Q_{mod}^{ref}}{E_{mod}^{ref}} \tag{8.12}$$

$$\Delta T_{max} = max(T_s^{mod}) - min(T_s^{mod}) \tag{8.13}$$

$$\%\Delta I_{max} = 100\frac{max(I_{cell}^{mod}) - min(I_{cell}^{mod})}{I_{mod}/N_p} \tag{8.14}$$

$$E_{lost} = E_{mod}^{EOS} - E_{mod}^{BOL} \tag{8.15}$$

$$\sigma R_{SEI}^{EOS} = \sqrt{\frac{1}{N_p-1}\sum_{z=1}^{N_p}\Big(R_{SEI}^{[z],EOS} - \frac{1}{N_p}\sum_{i=1}^{N_p}R_{SEI}^{[i]}\Big)^2} \tag{8.16}$$

$$\Delta\sigma_{\epsilon_{s,n}} = \sigma_{\epsilon_{s,n}}^{EOS} - \sigma_{\epsilon_{s,n}}^{BOS} \tag{8.17}$$

$$\Delta\mu_{\epsilon_{s,n}} = \mu_{\epsilon_{s,n}}^{EOS} - \mu_{\epsilon_{s,n}}^{BOS} \tag{8.18}$$

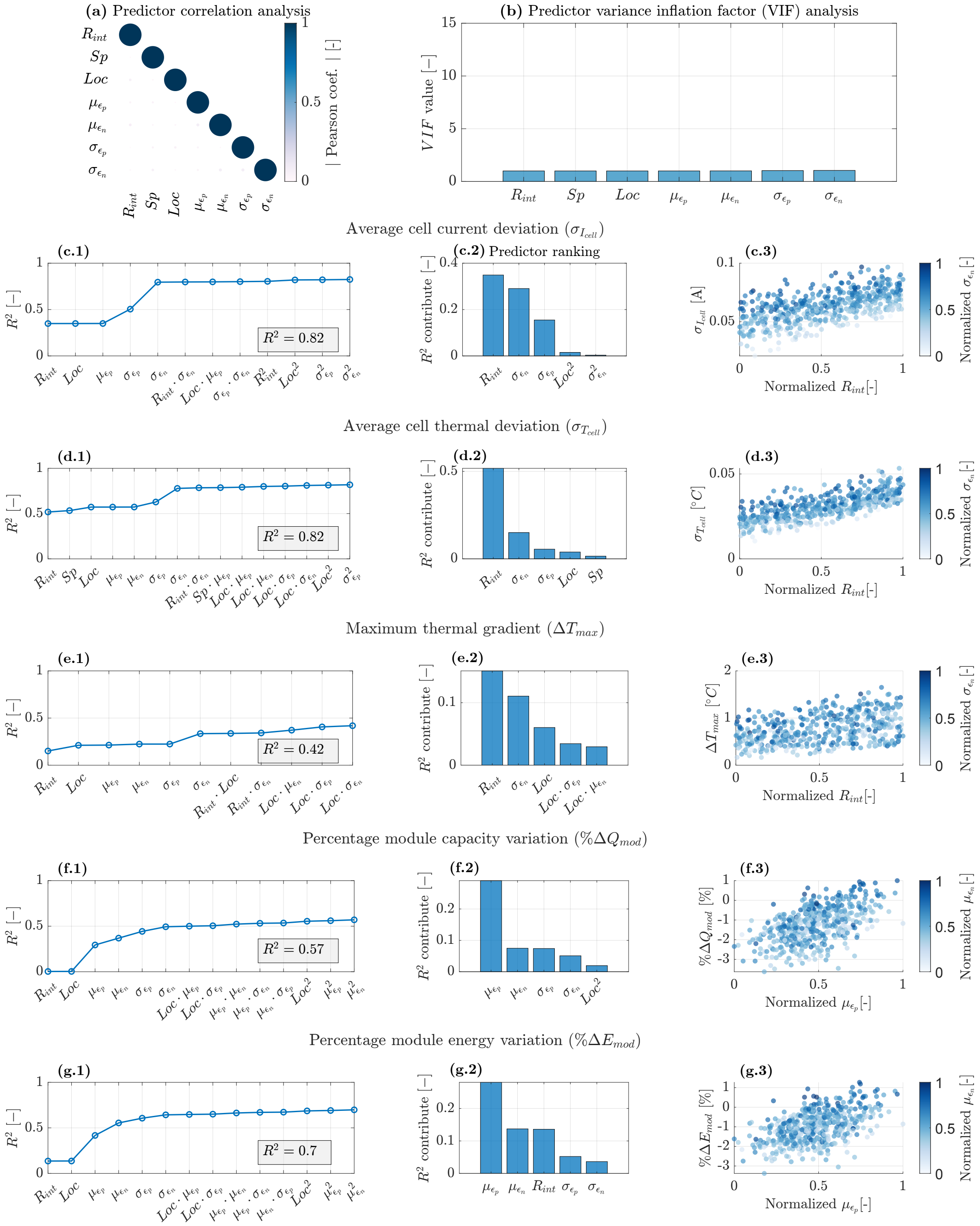

Figure 8.3: Figure (a) and (b) report the correlation and VIF analyses for the model predictors, respectively. Figures (c.1-g.1) depict the impact of each term in the multilinear regression (MLR) model on the model's R^2. Figures (c.2-g.2) rank the terms of the MLR model according to their influence on increasing R^2. Finally, Figures (c.3-g.3) visually demonstrate the contributions of the two most influential predictors to the corresponding response variable.

contribution of each term in the MLR model, highlighting their individual impact. The second column (Figure 8.3(c.2-g.2)) ranks the five most significant predictors based on their contribution to the increase in R^2, providing a clear view of the key drivers of model performance. The third column (Figure 8.3(c.3-g.3)) illustrates the response variation over the most important predictor on the x-axis, with colors indicating the influence of the second most important predictor.

In the following section, to enhance the explanation of the variability in the module response and to capture the key factors influencing the module's behavior, an additional seven predictors are added to the MLR model depending on the response variable considered. These additional predictors are: μ_{comb}, σ_{comb}, Loc_n, Loc_p, σSOC, μSOC, and ΔT_{max}. μ_{comb} and σ_{comb} represent the lumped mean and standard deviation of $\epsilon_{s,j}$, accounting for the fact that cell capacity is limited by the weakest electrode. The $\epsilon_{s,j}$ values are normalized to the [0,1] range, and the average is calculated by taking the minimum $\epsilon_{s,j}$ value for each cell, as detailed in equation (8.6). $Loc_j = \sum_{i=1}^{N_p} w_i \epsilon_{s,j}^{[i]}$ with $j \in [n, p]$ stands for the location index for each perturbed cell-level parameter. σSOC and μSOC are the standard deviation and mean value of the SOC of the N_p cells at the end of the discharge cycle. The main trends resulting form the MLR analysis are the following:

1. **Current distribution standard deviation (σI_{cell}):** R_{int} and $\sigma_{\epsilon_{s,j}}$ (with $j \in [n, p]$) emerge as the primary drivers influencing the heterogeneous current distribution among the parallel branches. Specifically, the current gradient increases at the beginning of the operation as the R_{int} value rises. In contrast, a higher $\sigma_{\epsilon_{s,j}}$ results in larger current heterogeneities in the middle and final SOC range. The significance of $\sigma_{\epsilon_{s,j}}$ as a predictor is primarily due to a key reason. When cells with unmatched $\epsilon_{s,j}$ are connected, the electrode particles experience different lithium-ion intercalation and deintercalation fluxes during operation. This discrepancy leads to varying surface concentrations across the cells, causing them to operate at different U_j and η_j. With the same overall current injected into the module, this imbalance in U_j and η_j results in an uneven distribution of current among the different branches, exacerbating current heterogeneities. Although the R^2 value of the model using the Γ_1 predictor set is satisfactory (i.e. 0.82), the model fitting can be further enhanced by including the ΔT_{max} and σSOC as additional predictors. A high thermal gradient causes significant variations in the temperature-dependent parameters within the cell-level ESPMs, particularly increasing heterogeneity in the particle diffusion coefficient among the cells. This exacerbates the differences in surface concentration ($c_{s,j}^{surf}$), further impacting the current distribution. Similarly, large σ_{SOC} indicates that the cells have operated at different SOC, resulting in dissimilar OCV values.

2. **Percentage variation in the module capacity and energy ($\%\Delta Q$ and $\%\Delta E$):** The $\mu_{\epsilon_{s,j}}$ with $j \in [n, p]$ emerge as the primary drivers influencing the overall module capacity and energy of the battery modules, as highlighted by both $\%\Delta Q$ and $\%\Delta E$. According to [146], the capacity of a single cell is directly proportional to the $\epsilon_{s,j}$ values. Therefore, in parallel-connected modules, an higher $\mu_{\epsilon_{s,j}}$ values, indicating larger magnitudes of $\epsilon_{s,j}$, substantially influence the module's total capacity, as it

depends on the cumulative energy of its individual cells [200]. Furthermore, R_{int} plays a significant role, particularly in affecting $\%\Delta E$, as the R_{int} increases, the Joule losses within the module also rise, thereby reducing the overall energy efficiency. To further improve the fitting performance of the MLR models for both response variables, which currently show R^2 values lower than 0.6 using the predictor set Γ_1, two variations are introduced in the predictor list. First, the $\mu_{\epsilon_{s,j}}$ and $\sigma_{\epsilon_{s,j}}$ are replaced with a lumped mean and standard deviation (μ_{comb} and σ_{comb}) to account for the fact that cell capacity is limited by the weakest electrode. Specifically, the $\epsilon_{s,j}$ values are normalized to the [0,1] range for comparability, and the average is then calculated by taking the minimum $\epsilon_{s,j}$ value for each cell, as in eq. (8.6). Secondly, the predictor list is enhanced by integrating the mean state of charge μSOC. A high value of this index indicates that the energy extracted from the module during the cycle is not entirely depleted, even when the cutoff voltage is reached, as the cells remain slightly charged. As evident from Figure 8.4, the updated predictors μ_{comb} and μSOC significantly impact the variability of the module responses. This improvement is also highlighted by the R^2 values, which increased from 0.57 and 0.7 to 0.99 and 0.99, respectively.

3. **Thermal distribution standard deviation (σT_{cell}) and maximum thermal gradient (ΔT_{max}):** R_{int} and the $\sigma_{\epsilon_{s,j}}$ with $j \in [n,p]$ emerge as the primary factors influencing the heterogeneous thermal distribution among parallel cells. It is important to note that σI_{cell} and σT_{cell} share the same most significant predictors. This is because heterogeneous temperatures are primarily driven by uneven current distribution, especially in the absence of a thermal management system. Although this trend is confirmed by ΔT_{max}, the R^2 value of 0.42 highlights that we are not fully able to describe the response variability using the predictor set Γ_1. As will become clear in Section 8.2.3, ΔT_{max} occurs at low SOC values primarily due to variations in the anode OCV, leading to significant current gradients. This effect is exacerbated by the positions of cells with the highest and lowest capacity of the negative electrodes. To better capture this behavior in the MLR analysis, the predictor set has been modified. The Loc index is now divided into Loc_n and Loc_p to specifically account for the perturbation positions of the negative and positive electrodes, respectively. This adjustment ensures that the model more accurately reflects the influence of electrode location on thermal distribution and current gradients, as shown in Figure 8.4(c.1-c.3). In particular, the R^2 which increased from 0.82 and 0.41 to 0.98 and 0.90 for σT_{cell} and σI_{cell}, respectively.

8.2.2 MLR analysis: long term CtC heterogeneity effects

The long-term impact of CtC variation on the performance and health of a battery module over 500 cycles is thoroughly investigated. This evaluation focuses on four critical response: E_{lost}, $\Delta\mu_{\epsilon_{s,n}}$, $\Delta\sigma_{\epsilon_{s,n}}$ and σR_{SEI}^{EOS}. It is important to note that E_{lost}, $\Delta\mu_{\epsilon_{s,n}}$, and $\Delta\sigma_{\epsilon_{s,n}}$ are determined by calculating the difference between their initial values at

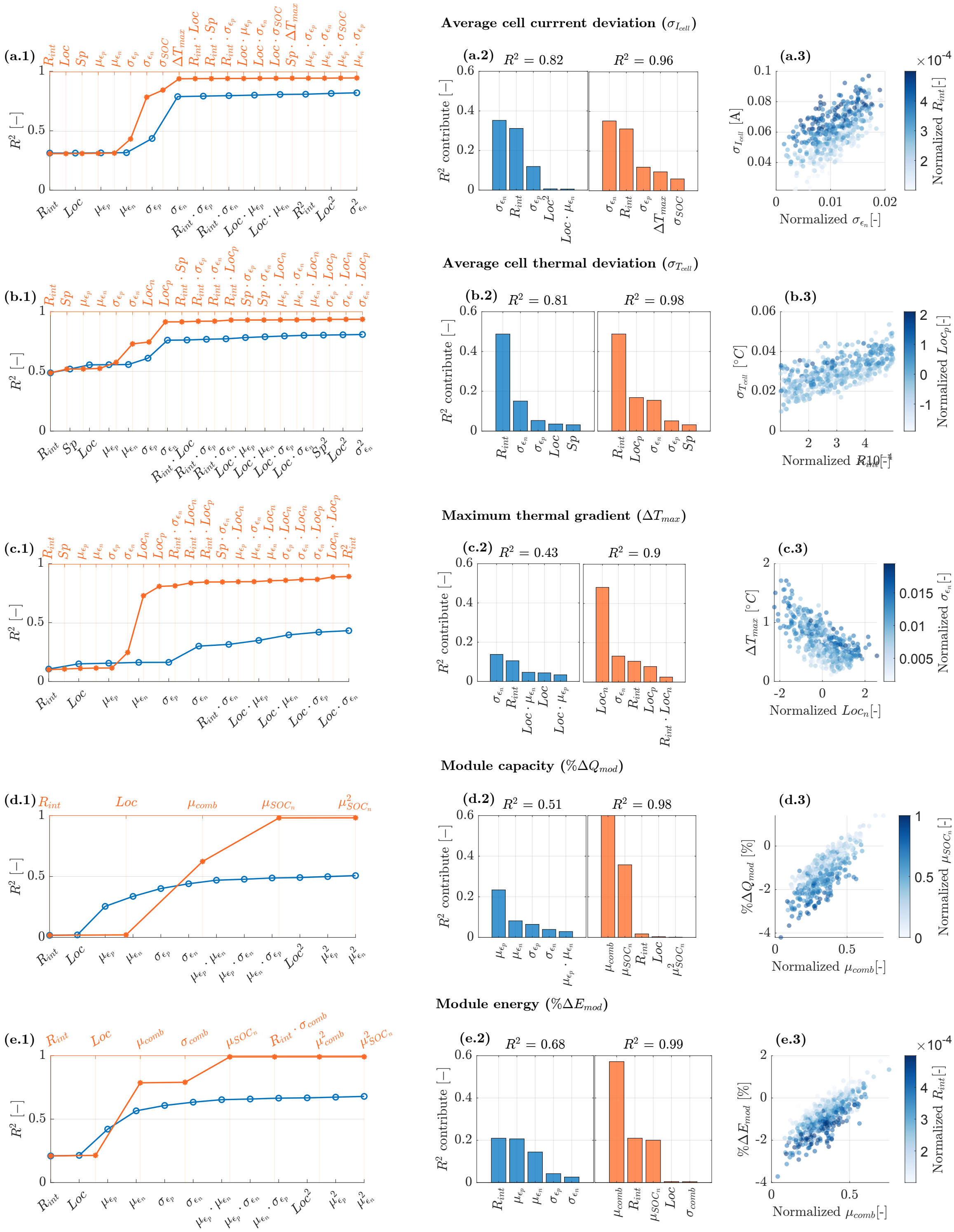

Figure 8.4: Figures (a.1-e.1) illustrate the impact of each term in two MLR models. The blue line represents the predictors set Γ_1, while the orange solid line represents the enhanced model. Figures (a.2-e.2) rank and compare the terms of both MLR models based on their influence on increasing R^2. Figures (a.3-e.3) visually demonstrate the contributions of the two most influential predictors to the corresponding response variable.

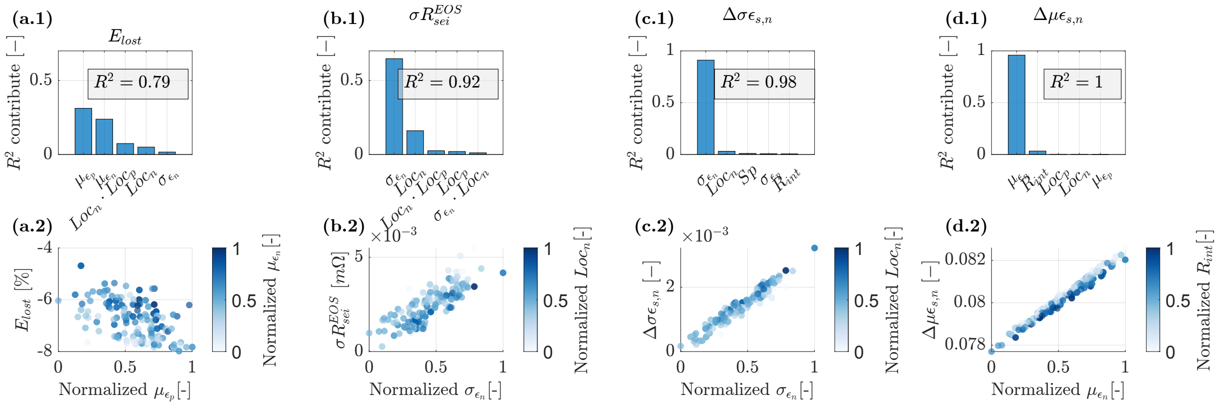

Figure 8.5: MLR analysis long-term simulation results. Figures (a.1-d.1) rank and compare the terms of both MLR models based on their influence on increasing R^2. Figures (a.2-d.2) visually demonstrate the contributions of the two most influential predictors to the corresponding response variable.

the BOL and their final values at the EOS. A positive value for $\Delta\mu_{\epsilon_{s,n}}$ and $\Delta\sigma_{\epsilon_{s,n}}$ signifies an increase in heterogeneity over time, indicating that the module is not benefiting from the cell aging self-balancing effect. While E_{lost} and σR_{SEI}^{EOS} underscore the loss of energy and the increase in heterogeneity related to cell SEI film resistance throughout the simulation. The Pareto analysis results, derived from the MLR models based on the simulated data, are presented in Figure 8.5. Overall, the results suggest that electrode-based manufacturing-induced heterogeneities (i.e. $\mu_{\epsilon_{s,n}}$ and $\sigma_{\epsilon_{s,n}}$) significantly influence the aging behavior of the parallel-connected module. $\Delta\mu_{\epsilon_{s,n}}$ and $\Delta\sigma_{\epsilon_{s,n}}$ are directly proportional to the initial heterogeneity, showing a larger magnitude as $\mu_{\epsilon_{s,n}}$ and $\sigma_{\epsilon_{s,n}}$ at BOL rises. σR_{SEI}^{EOS} strongly depends on the initial $\sigma_{\epsilon_{s,n}}$, while E_{lost} depends on $\mu_{\epsilon_{s,j}}$. The cell location emerges as the second most important factors, especially for the E_{lost} and σR_{Sei}^{EOS}. As emphasized in Section 8.2.1, the primary reason for this outcome is the strong correlation of Loc_n and Loc_p with the thermal gradient within the parallel-connected branches, which is responsible for triggering the aging mechanisms within the system. Indeed, our findings are consistent with previous experiments conducted in this field. For instance, [219] demonstrated that a 6 parallel-connected cells battery module subjected to a thermal gradient of $20°C$ experienced a 5.2% higher degradation rate compared to the isothermal case. This trend was further validated through experimental evidence by [190], who observed an accelerated aging rate in 2 parallel-connected cells exposed to a thermal gradient of $25°C$. Furthermore, the authors highlighted that a high thermal gradient within the module led to divergent capacity fade among the parallel-connected cells. Another intriguing observation is that, both $\Delta\mu_{\epsilon_{s,n}}$ and $\Delta\sigma_{\epsilon_{s,n}}$ show positive values, underlying that the initial CtC heterogeneities diverge over time, confirming the results of [24] [162].

8.2.3 Cell arrangement strategy for thermal gradient reduction

According to the previous section, the degradation and propagation of heterogeneity in parallel-connected battery modules are significantly influenced by the initial heterogeneity characteristics of the fresh cells (i.e $\mu_{\epsilon_{s,j}}$ and $\sigma_{\epsilon_{s,j}}$). The $\mu_{\epsilon_{s,j}}$ and $\sigma_{\epsilon_{s,j}}$ of the initial cell parameters are primarily determined by the manufacturing process and cannot be optimized post-production. However, the arrangement of cells within the module, which emerged as the second most critical predictors, provides an opportunity to enhance the overall performance and longevity of the battery module. The necessity of an optimized cell arrangement to mitigate thermal gradients within the module casing and improve the uniformity of cell aging has been discussed in the literature over the past decade. Among the most relevant studies, the authors in [220] proposed an innovative cell spacing distribution optimization strategy, where cells are non-uniformly spaced within the module. This optimization resulted in a substantial reduction of T_{max} by $3°C$, and an impressive 60% decrease in ΔT_{max} when compared to the conventional uniform cell placement. Further, [221] compares three module configurations: inline, offset, and staggered cell arrangements, in terms of thermal gradient and power consumption of the battery thermal management system (BTMS). It was demonstrated that adopting an offset cell arrangement leads to a remarkable 43.1% reduction in power consumption for the BTMS compared to using inline and staggered cell arrangements.

This study introduces a straightforward cell arrangement strategy for a parallel-connected battery module. The primary approach to tackle thermal inconsistencies within the module revolves around taking into account CtC variations resulting from the manufacturing process and the dissimilar R_{int}. To mitigate these issues, the proposed strategy involves positioning cells with larger capacities at the beginning of the module, where the interconnection resistance is lower due to the proximity to the module terminals. A lower R_{int} results in higher delivered currents during the initial phase of operation. By locating the cells with the highest capacity at the beginning of the module, it can effectively manage higher currents and mitigate SOC differences during operation. This arrangement results in a lower thermal gradient at low SOC levels, as the cells experience more uniform SOC. Practically, the proposed cell arrangement strategy involves characterizing the individual cells before building the module. Then, the cells with higher capacity should be placed in locations where the interconnection resistance is expected to be lower. In situations where budget and/or time constraints make the preliminary single-cell testing infeasible, a sub-optimal alternative could be arranging the parallel cells according to their weight. In [222], a linear correlation between cell capacity and weight was demonstrated for a batch of 5300 5.3Ah cells.

A visual representation of the cell arrangement strategy is provided in Figure 8.6. To demonstrate this approach, a 4-cell battery module (M1) is randomly selected from the MLR analysis simulations conducted in the previous section. The thermal and current distribution of M1 is compared with that of M2, which is achieved by rearranging the cells in descending order based on their capacity, in Figure 8.6(d) and (e), respectively. The cell with the highest capacity delivered the largest current at high SOC and effectively

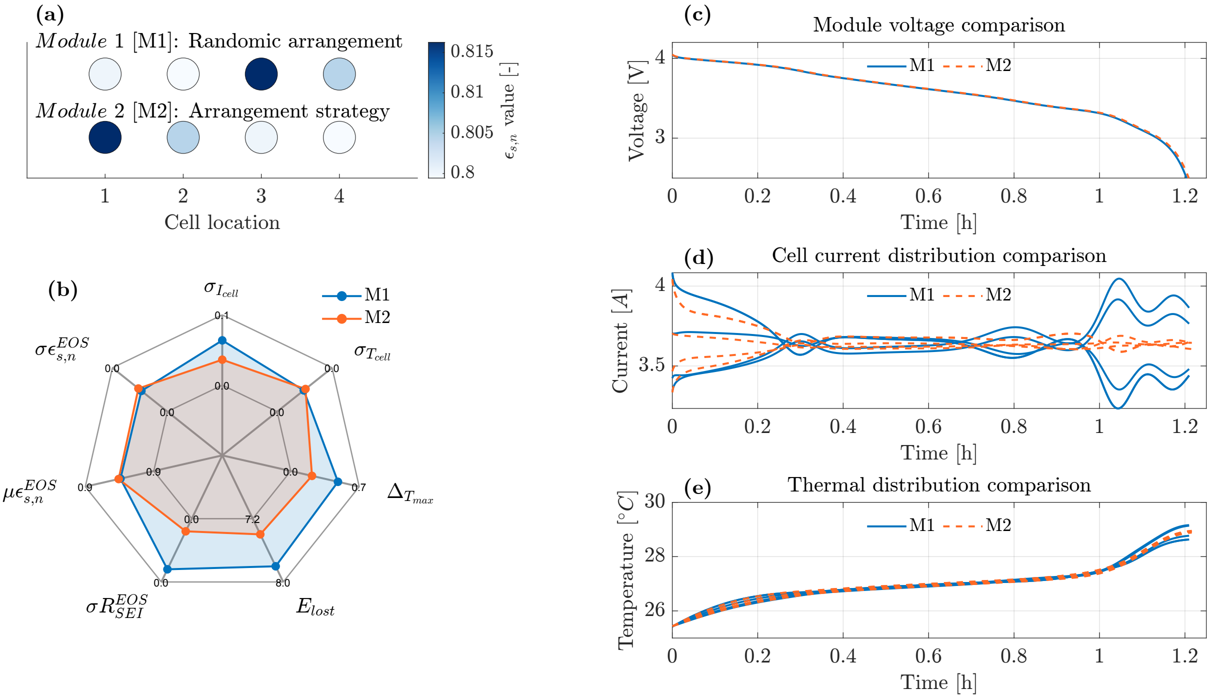

Figure 8.6: Cell arrangement strategy for parallel-connected module graphical overview. (a) shows the battery module with randomly arranged cells (M1) and the optimized cell arranged(M2). (b) compare the modules' response variables. (c), (d), and (e) report the module voltage, the cell current distribution, and the thermal distribution comparison between M1 and M2, respectively.

managed higher currents, mitigating large SOC gradients, resulting in homogeneous current and thermal distribution toward the end of the cycle. Specifically, σI_{cell} and ΔT_{max} decrease from 0.0649 A and 0.471°C to 0.0573 A and 0.227°C, as highlighted in Figure 8.6(b). This results in a reduction of 5.2% (from -7.83% to -7.42%) and 60.9% (from 2.4643e-06 to 9.641e-07) in E_{lost} and σR_{SEI}^{EOS}, respectively. On other hand a slight increase of both $\mu_{\epsilon_{s,n}}^{EOS}$ and $\sigma_{\epsilon_{s,n}}^{EOS}$ of 0.01% and 3.3%, respectively, is reported. Overall, the benefits of the arrangement strategy, such as decreased energy loss and improved uniformity in SEI resistance, substantially outweigh the minor increase in $\mu_{\epsilon_{s,n}}^{EOS}$ and $\sigma_{\epsilon_{s,n}}^{EOS}$, demonstrating its effectiveness.

8.3 Conclusion

This study assessed the impact of heterogeneity among parallel cells, resulting from manufacturing tolerances and various module configurations, on the module's performance. To the best of our knowledge, this article is the first to consider this type of analysis for parallel cells. Additionally, unlike other studies relying on empirical evaluations, our approach employs a model-based method to carry out the analysis and interpret the resulting performance. Leveraging the high interpretability and low computational demands of multi-linear regression models, the analysis was conducted focusing on the identified key cell-level parameters, as well as various model configurations. The objective was to assess their relative importance concerning overall capacity, energy, heterogeneity distribution, and aging propagation in a parallel-connected module. In the short-term MLR analysis, electrode active material volume fractions and the interconnection resistance significantly impact module performance and the propagation of heterogeneities. Modules with high overall capacity and energy tend to have a higher average value of single-cell capacities, as highlighted by the effect of the predictors μ_{comb} on the responses $\%\Delta E$ and $\%\Delta Q$. Conversely, the standard deviation in the capacities of interconnected cells strongly affects both current distribution and thermal inconsistencies within the module. In the long-term MLR analysis, it is demonstrated that a high thermal gradient accelerates the module's aging rate and increases the SEI resistance variation across interconnected cells. It is worth noting that favoring more uniformly aged cells at the end of their first life is desirable also for creating durable and secure second-life battery modules and packs. To address this, a simple cell arrangement strategy is presented to reduce the CtC thermal gradient, thereby decreasing aging heterogeneities in the long-term scenario. The key idea is to leverage the cell current resulting from the manufacturing-induced CtC variation to mitigate the module's thermal gradient by placing cells with higher capacity at the beginning of the module, where the interconnection resistance is lower. From an implementation perspective, a cost-effective solution could involve arranging the cells based on their weight. According to simulation results, this method allows for a thermal gradient reduction of 51.8% and a consequent decrease of 5.2% of the module energy loss after 500 aging cycles. In summary, our findings demonstrate the importance of considering electrode manufacturing-dependent parameters and the potential benefits of the proposed cell arrangement strategy in enhancing the performance, safety, and longevity of parallel-connected battery modules.

Chapter 9

States estimation for parallel-connected battery module

Contents

9.1 ECM-based Cell model 180
  9.1.1 Single cell first order ECM identification 180
  9.1.2 Module-level model formulation 180
9.2 Non-linear observability analysis 184
  9.2.1 Nonlinear observability analysis: results from the module-level model 188
9.3 Moving horizon estimation 190
  9.3.1 MHE for parallel-connected module 191
9.4 Conclusion 198

This contribution is based on the following works:

- [32] **Fasolato, S.**, Acquarone, M. and Raimondo, D. M. (2024). *States estimation for parallel-connected battery module: a moving horizon approach*, IEEE Transaction on Control System Technology, **Submitted**
- [33] **Fasolato, S.**, and Raimondo, D. M. (2022). *Observability analysis of a li-ion cell equivalent circuit model based on interval arithmetic*, 2022 IEEE Vehicle Power and Propulsion Conference (VPPC), 1-7.

Introduction

One of the main tasks of a BMS is to estimate the internal states of the batteries [23]. Significant efforts have been dedicated to accurately estimating the battery SOC, which provides important information about the remaining driving range of the vehicle [223]. Although the battery pack is a complex system composed of series and/or parallel connected cells, most works focus on estimating the SOC of individual cells through isolated testing, rather than considering their interaction with other cells. Several SOC estimation algorithms have been developed under both data-driven and model-based approaches. The former approach is based on establishing empirical correlations between measurable battery signals and SOC [118]. However, this kind of algorithm often requires substantial amounts of training data to obtain accurate and generalizable estimation results. Conversely, model-based methods rely on physics-based battery models, e.g., electrochemical models or ECMs, providing deeper insights into battery dynamics and delivering accurate estimates across a wide range of conditions. Among the most notable model-based approaches, we can distinguish different variants of Kalman filters [224], particle filters [225], sliding mode techniques [149], Luenberger observers [226], set-based approaches [227], and Moving horizon estimation (MHE) [228]. MHE is an optimization-based technique, suitable for non-linear system, which employs a moving horizon of measurements instead of a single instantaneous measurement to reconstruct the model states. Compared to traditional [224, 225, 149, 226, 227] estimation methods, MHE helps avoid the "short-horizon syndrome", providing smoother estimations in the presence of disturbances [228], while ensuring compliance with state bounds. Further, it proves to be more robust against poor initial SOC guesses and achieves faster convergence [229], at the expense of a higher computational time. To mitigate its high computational cost in the context of SOC estimation, [230] implemented a sequential quadratic programming strategy, while [231] utilized an event-triggered approach.

One of the main limitations of the mentioned works is that their estimation methods have been applied to the case of single cells only. However, in BEVs, the individual cells are combined in modules to satisfy the driver power requests, and, hence, the energetic efficiency of the pack is also dependent on their collective behavior. Cell-to-cell variation in battery modules may originate from various factors, including manufacturing tolerances, as well as inadequacies in pack architecture and cooling design [162]. Those heterogeneities in parallel-connected modules lead to uneven current distribution among the parallel branches, resulting in undesired SOC and thermal gradients, as widely discussed in Chapters 7 and 8. Although quantifying CtC variations would be beneficial for enhancing the BMS, parallel-connected modules are often treated as single lumped cells neglecting internal heterogeneity.

In recent years, only a handful of studies have delved into SOC estimation for parallel-connected modules. In [232] and [233], the authors tackled the estimation challenge with a module comprising two cells, employing an observer with linear output error injection and an interval observer, respectively. Likewise, [234] and [235] investigated SOC estimation for the same battery module setup, employing the Extended Kalman filter and functional observer methods, respectively. [233] was extended in [236] to include battery modules with both serial and parallel connections, incorporating thermal measurements. All of the aforementioned approaches for parallel-connected battery modules are grounded in ECM models. It is important to highlight that none of these SOC observer algorithms were validated using real experimental data in the referenced studies; instead, they relied on the model output as the measurement. Although fictitious noise was introduced to the voltage signal in [234] to simulate sensor inaccuracies, those simulations do not accurately represent real-world scenarios [237] where the battery model may not precisely capture actual battery system dynamics. Furthermore, these studies only accounted for cell-level parameter heterogeneity, neglecting the impact of the interconnection resistances, which is one of the most significant sources of heterogeneity in parallel-connected modules as shown in the Chapters 7 and 8.

Chapter contribute

This chapter aims to estimation the unmeasurable states for each cell within parallel-connected configurations under various scenarios using a MHE approach. It is worth noting, that considering CtC variations in BMS algorithm is the key step towards enhancing battery pack optimal charging, cell balancing, and the development of novel fault detection and isolation strategies [238, 239].

The main contributions of this chapter can be mainly divided in three as follows:

1. *According to Section 3.2.1 the parallel-connected module is described as a system of ODEs coupled with AEs. As noted in [110], these laws can be integrated into the module-level state-space formulation, transforming the DAEs into ODEs. Building on this foundation, we extend our approach to accommodate parallel-connected modules that include interconnection resistances (R_{int}) and SOC-dependent parameters. Furthermore, we provide an analytical proof of the invertibility of the matrix Ψ_2, which results Kirchhoff's laws embedding and is crucial for the simulation of the embedded model.*

2. *Based on the formulated embedded model, we analyze the non-linear observability of the module-level dynamics to evaluate the feasibility of reconstructing the state of individual cells from the overall module voltage and current [33]. This study extends the findings presented in the literature [232, 240], which previously focused on only two cells in parallel and did not account for SOC dependency in the parameters and interconnection resistance (R_{int}). Our analysis encompasses modules with varying numbers of cells, different values of R_{int}, and SOC-dependent parameters.*

3. *In conventional estimation schemes [232, 233, 234, 235], embedding Kirchhoff's laws in the module-level state-space formulation is essential for the state observer design. However, while this approach offers a compact representation and simplify the observability analysis, it also results in a highly nonlinear model. In contrast, this work leverages the capabilities of the MHE method to manage equality constraints without directly incorporating Kirchhoff's circuit laws into the module dynamics. This strategy simplifies the module-level model and enhances computational efficiency. Consequently, a primary contribution of this research is the comparative analysis of MHE-based algorithmic schemes with and without the embedding of Kirchhoff's laws in the model formulation. We validate our methodology through simulation and,*

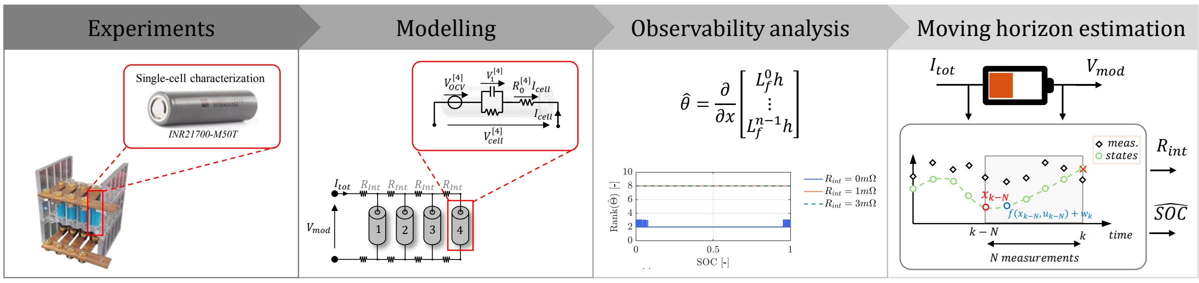
Experiments
Modelling
Observability analysis
Moving horizon estimation
Single-cell characterization
INR21700-M50T
I_{tot}
R_{int}
V_{mod}
1
2
3
4
$V_{cell}^{[4]}$
I_{cell}
$\hat{\theta} = \frac{\partial}{\partial x}\begin{bmatrix} L_f^0 h \\ \vdots \\ L_f^{n-1} h \end{bmatrix}$
Rank($\hat{\Theta}$) [-]
SOC [-]
$R_{int} = 0m\Omega$
$R_{int} = 1m\Omega$
$R_{int} = 3m\Omega$
meas.
states
$k-N$
k
time
N measurements
$\widehat{SOC}$

Figure 9.1: Visual overview of the MHE-based state estimation procedure presented in this chapter.

for the first time, against experimental data obtained from a battery module comprising four cells [8]. This validation is conducted under various interconnection resistance scenarios, demonstrating the robustness and applicability of our approach in real-world settings.

Chapter Structure

- **Section 9.1** provides an overview of the cell-level and module-level ECM-based models. Specifically, the governing equations and identification results of the cell-level ECM for the LG M50T[1] are presented in Section 9.1.1. The module-level model formulation is discussed in Section 9.1.2.

- **Section 9.2** presents both the theoretical basis for observability analysis of nonlinear systems and the analysis results for the module-level model in Section 9.2.1.

- **Section 9.3** provides both the theoretical foundation for MHE and the simulation results for the module-level state estimation problem in Section 9.3.1. Specifically, Sections 9.3.1.1 and 9.3.1.2 validate the MHE-based algorithms against simulated and experimental data, respectively. Finally, the preliminary results on joint state and interconnection resistance estimation are reported in Section 9.3.1.3.

- **Section 9.4** summarizes the conclusions and outlines future research opportunities.

---

[1] Based on the SECL experimental campaign described in Chapter 4

9.1 ECM-based Cell model

In this section the indeintifaction of the cell-level ECM model, described in Section 3.1.1. Specifically, the cell-level characterization experiments described in Section 4.2.2.1 are used to calibrate the single-cell ECM for the LG Chem M50T, in accordance with [23]. Then, the module-level dybanics are introduced in Section 9.1.2.

9.1.1 Single cell first order ECM identification

The mathematical formualtion of the ECM model was reviewed in Sectin 3.1.1. In particular, in this chapter a first-order RC ECMs is considered and the model state-space model (3.1) is written as:

$$\begin{cases} \dot{x}(t) = Ax(t) + Bu(t) \\ y(t) = h(x(t), u(t)) \end{cases} = \begin{cases} \begin{bmatrix} \dot{V_1}(t) \\ \dot{SOC}(t) \end{bmatrix} = \begin{bmatrix} \frac{-1}{R_1C_1} & 0 \\ 0 & 0 \end{bmatrix} \begin{bmatrix} V_1(t) \\ SOC(t) \end{bmatrix} + \begin{bmatrix} \frac{1}{C_1} \\ \frac{1}{C_{\text{bat}}} \end{bmatrix} I_{cell}(t) \\ V_{cell}(t) = V_{OCV}(SOC(t)) + V_1 + R_0 I_{cell}(t) \end{cases} \tag{9.1}$$

It is worth noting that V_{OCV} is determined by fitting the cell voltage data collected during a Pseudo-OCV testing protocol, described in Section 4.2.2.1, which involves a discharge cycle at an extremely low C-rate from 100% to 0% of SOC (i.e. C/20 CC discharge). Specifically, Fig. 9.2(a) shows the comparison between the C/20 Constant Current (CC) discharge cycle at 23°C and the V_{OCV}, which is identified as a polynomial function of SOC, with its expression provided in equation (9.3). Additionally, following the approach in [127], the parameters of the dynamic components of the ECM (i.e. R_1, C_1, and R_0) are determined by minimizing the root mean square error between the model voltage and the cell voltage observed during testing with time-varying HPPC and Multi Sine (MS) current profiles. To enhance model accuracy, R_1 and R_0 are expressed as polynomial functions of SOC. The corresponding expressions and estimated parameters are detailed in equation (9.4). The final ECM identification results, with the corresponding RMSE, are shown in Fig. 9.2(b).

9.1.2 Module-level model formulation

The ECM-based module-level model was introduced in the Example 3.2.1 in Section 3.2.1. Here, we consider a parallel-connected battery module arranged in a ladder configuration, consisting of N_p cells. Fig. 9.3 provides a schematic representation of the battery module, highlighting the interconnection electrical resistance (R_{int}) for each parallel string. In the following, the superscript $[k]$ denotes the quantity associated with the k-th cell in the module, where [1] and $[N_p]$ refer to the cells closest to and farthest from the load terminals, respectively. The final ODAEs governing equations, derived from considering N_p ECMs, are expressed as follows:

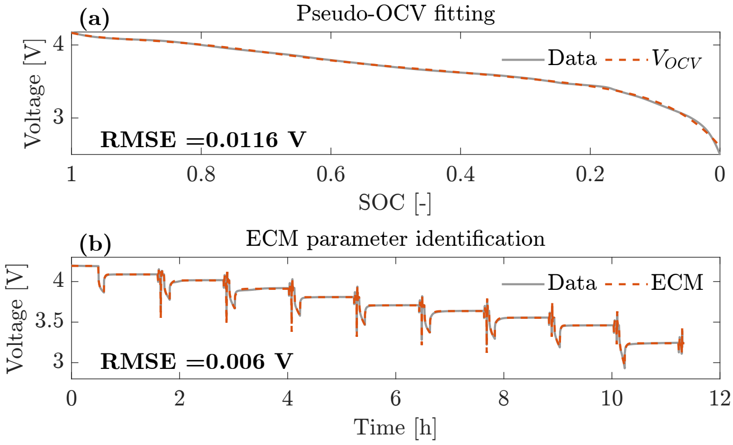

Figure 9.2: ECM identification results for the *LG Chem M50T*: (a) Comparison between the C/20 Pseudo-OCP test and V_{OCP}. (b) Comparison between the HPPC+MS test and the ECM. Both tests refer to cell *P10* in [8].

Table 9.1: Cell-level and module-level models formulation

Cell-level Equivalent Circuit Model (ECM)

$$\Sigma_{\text{Cell}}:\begin{cases}\dot{x}(t)=Ax(t)+Bu(t)\\ y(t)=h(x(t),u(t))\end{cases}\quad\Rightarrow\begin{cases}\begin{bmatrix}\dot{V}_1(t)\\ \dot{SOC}(t)\end{bmatrix}=\begin{bmatrix}\frac{-1}{R_1C_1} & 0\\ 0 & 0\end{bmatrix}\begin{bmatrix}V_1(t)\\ SOC(t)\end{bmatrix}+\begin{bmatrix}\frac{1}{C_1}\\ \frac{1}{C_{bat}}\end{bmatrix}I_{Cell}(t)\\ V_{Cell}(t)=V_{OCV}(SOC(t))+V_1(t)+R_0(SOC(t))I_{Cell}(t)\end{cases}\tag{9.2}$$

$$V_{OCV}(SOC)=105.753SOC^7-386.828SOC^6+577.809SOC^5-460.12SOC^4+214.77SOC^3-60.29SOC^2+10.47SOC+2.609\tag{9.3}$$

$$R_o(SOC)=-0.056SOC^3+0.116SOC^2-0.073SOC+0.0393;\qquad R_1(SOC)=-0.0225SOC^2+0.0123SOC;\qquad C_1=2913.1\tag{9.4}$$

Module-level Parallel-connected Model

$$\Sigma_{\text{mod}}:\begin{cases}\dot{x}_{mod}(t)=(A_{mod}-B_{mod}\Psi_2^{-1}\Psi_1)x_{mod}(t)-B_{mod}\Psi_2^{-1}\Psi_3-B_{mod}\Psi_2^{-1}\Psi_4I_{tot}(t)\\ V_{mod}(t)=V_{OCV}^{[1]}(SOC^{[1]}(t))+V_1^{[1]}(t)+R_0^{[1]}(-\Psi_2^{-1}(\Psi_1x_{mod}(t)+\Psi_3))_1+(R_0^{[1]}(-\Psi_2^{-1}\Psi_4)_1+2R_{int})I_{tot}(t)\end{cases}\tag{9.5}$$

$$A_{mod}=\begin{bmatrix}A^{[1]} & & 0\\ & \ddots & \\ 0 & & A^{[N_p]}\end{bmatrix}\qquad B_{mod}=\begin{bmatrix}B^{[1]} & & 0\\ & \ddots & \\ 0 & & B^{[N_p]}\end{bmatrix}\qquad \Psi_1=\begin{bmatrix}-1 & 0 & 1 & 0 & 0 & \cdots & 0\\ \vdots & \vdots & \vdots & \vdots & \ddots & \vdots & \vdots\\ 0 & 0 & \cdots & -1 & 0 & 1 & 0\\ 0 & 0 & \cdots & 0 & 0 & 0 & 0\end{bmatrix}\qquad \Psi_4=\begin{bmatrix}2R_{int}\\ \vdots\\ 2R_{int}\\ -1\end{bmatrix}$$

$$\Psi_2=\begin{bmatrix}-R_o^{[1]}-2R_{int} & R_o^{[2]} & 0 & \cdots & 0 & 0\\ -2R_{int} & -R_o^{[2]}-2R_{int} & R_o^{[3]} & \cdots & 0 & 0\\ \vdots & \vdots & \ddots & \vdots & \vdots & \vdots\\ -2R_{int} & -2R_{int} & \cdots & -R_o^{[N_p-2]}-2R_{int} & R_o^{[N_p-1]} & 0\\ -2R_{int} & -2R_{int} & \cdots & -2R_{int} & -R_o^{[N_p-1]}-2R_{int} & R_o^{[N_p]}\\ 1 & 1 & \cdots & 1 & 1 & 1\end{bmatrix}\qquad \Psi_3=\begin{bmatrix}V_{OCP}^{[2]}-V_{OCP}^{[1]}\\ \vdots\\ V_{OCP}^{[N_p]}-V_{OCP}^{[N_p-1]}\\ 0\end{bmatrix}$$

$$\begin{bmatrix} \dot{V}_1^{[1]} \\ \dot{SOC}^{[1]} \\ \vdots \\ \dot{V}_1^{[N_p]} \\ \dot{SOC}^{[N_p]} \end{bmatrix} = \underbrace{\begin{bmatrix} A^{[1]} & & 0 \\ & \ddots & \\ 0 & & A^{[N_p]} \end{bmatrix}}_{A_{mod}} \underbrace{\begin{bmatrix} V_1^{[1]} \\ SOC^{[1]} \\ \vdots \\ V_1^{[N_p]} \\ SOC^{[N_p]} \end{bmatrix}}_{x_{mod}} + \underbrace{\begin{bmatrix} B^{[1]} & & 0 \\ & \ddots & \\ 0 & & B^{[N_p]} \end{bmatrix}}_{B_{mod}} \underbrace{\begin{bmatrix} I_{cell}^{[1]} \\ \vdots \\ I_{cell}^{[N_p]} \end{bmatrix}}_{I_{mod}} \tag{9.6}$$

where the module state vector $x_{mod} \in \mathbb{R}^{2N_p \times 1}$ includes the states of each individual ECM, while $I_{mod} \in \mathbb{R}^{N_p \times 1}$ denotes the vector of currents flowing through each parallel branch within the module, and the matrices $A_{mod} \in \mathbb{R}^{2N_p \times 2N_p}$ and $B_{mod} \in \mathbb{R}^{2N_p \times 2N_p}$. Note that $I_{cell}^{[k]}$, where $k \in [1, \cdots, N_p]$, are algebraic variables which depend on the module input I_{tot}, i.e. the total input current of the module, through the Kirchoff's circuit laws. Denoting with $V_{cell}^{[k]}$ the voltage of each cell $[k]$, calculated according to (9.2), the corresponding N_p algebraic constraints are:

$$\begin{cases} V_{cell}^{[j+1]} = V_{cell}^{[j]} - 2R_{int}(I_{tot} - \sum_{z=1}^{j} I_{cell}^{[z]}), \quad j \in \{1, \cdots, N_p - 1\} \\ I_{tot} = \sum_{j=1}^{N_p} I_{cell}^{[j]} \end{cases} \tag{9.7}$$

Finally, the model output $V_{mod} = V_{cell}^{[1]} + 2R_{int}I_{tot}$ is the voltage across the module terminals. The overall dynamics of the module, described by eqs. (9.6) to (9.7), constitute a system of DAEs.

According to [110], it is possible to incorporate algebraic constraints directly into the model dynamics, thereby converting the DAEs into ODEs. Building on this approach, we extend it to parallel-connected modules with interconnection resistances R_{int}. In particular, the system of equations (5.26) can be rewritten as:

$$0 = \Psi_1 x_{mod} + \Psi_2(x_{mod}) I_{mod} + \Psi_3(x_{mod}) + \Psi_4 I_{tot} \tag{9.8}$$

where the matrices $\Psi_1 \in \mathbb{R}^{N_p \times 2N_p}$ and $\Psi_2(x_{mod}) \in \mathbb{R}^{N_p \times N_p}$, and the vectors $\Psi_3(x_{mod}) \in \mathbb{R}^{N_p \times 1}$ and $\Psi_4 \in \mathbb{R}^{N_p \times 1}$, are listed in Table 9.1. The dependencies of Ψ_2 and Ψ_3 on x_{mod} arise from the dependencies of R_0 and the open circuit voltage potential on the State of Charge[2]. From (9.8), given the invertibility of the matrix Ψ_2 (see Section 9.1.2), the vector I_{mod} can be calculated as:

$$I_{mod} = -\Psi_2^{-1}(x_{mod})[\Psi_1 x_{mod} + \Psi_3(x_{mod}) + \Psi_4 I_{tot}] \tag{9.9}$$

Finally, combining (9.6) and (9.9) the module dynamics are written as reported in (9.10), in the control-oriented system of ODEs in the form:

$$\Sigma : \begin{cases} \dot{x}_{mod}(t) = f(x_{mod}(t))(t) + g(x_{mod}(t)) I_{tot}(t) \\ V_{mod} = h(x_{mod}(t)) + l(x_{mod}(t)) I_{tot}(t) \end{cases} \tag{9.10}$$

---

[2] These dependencies may be occasionally omitted for the sake of brevity in the notation.

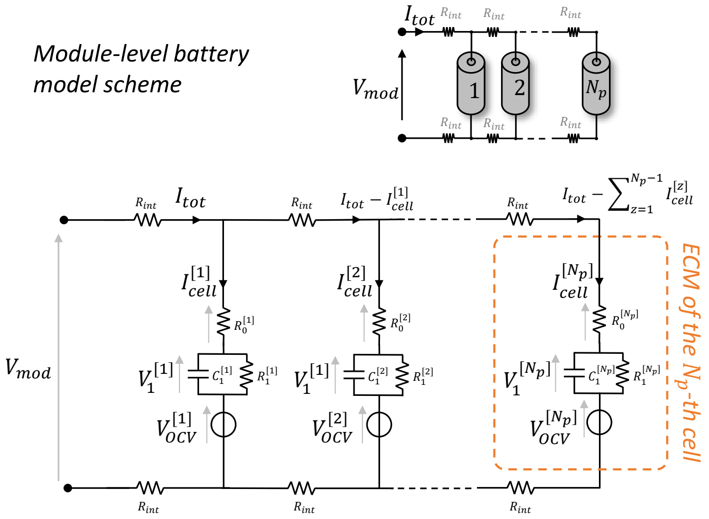
Module-level battery model scheme
I_{tot}
R_{int}
V_{mod}
1
2
N_p
$I_{tot} - I_{cell}^{[1]}$
$I_{tot} - \sum_{z=1}^{N_p-1} I_{cell}^{[z]}$
$I_{cell}^{[1]}$
$I_{cell}^{[2]}$
$I_{cell}^{[N_p]}$
$R_0^{[1]}$
$R_0^{[2]}$
$R_0^{[N_p]}$
$V_1^{[1]}$
$V_1^{[N_p]}$
$C_1^{[1]}$
$C_1^{[2]}$
$C_1^{[N_p]}$
$R_1^{[1]}$
$R_1^{[2]}$
$R_1^{[N_p]}$
$V_{OCV}^{[1]}$
$V_{OCV}^{[2]}$
$V_{OCV}^{[N_p]}$
ECM of the N_p-th cell

Figure 9.3: Schematic representation of the module-level ECM-based model

where

$$\begin{aligned}
f(x_{mod}) &= (A_{mod} - B_{mod}\Psi_2^{-1}(x_{mod})\Psi_1)x_{mod} - B_{mod}\Psi_2^{-1}(x_{mod})\Psi_3(x_{mod}) \qquad (9.11)\\
g(x_{mod}) &= -B_{mod}\Psi_2^{-1}(x_{mod})\Psi_4\\
h(x_{mod}) &= V_{OCV}^{[1]}(SOC^{[1]}) + V_1^{[1]} + R_0^{[1]}(-\Psi_2^{-1}(x_{mod})(\Psi_1 x_{mod} + \Psi_3(x_{mod})))_1\\
l(x_{mod}) &= R_0^{[1]}(-\Psi_2^{-1}(x_{mod})\Psi_4)_1 + 2R_{int}.
\end{aligned}$$

where with the notation $(\cdot)_1$ we indicate the first component of the resulting vector.

On the invertibility of Ψ_2

Preliminaries

- An $n \times n$ matrix $B \in \mathbb{R}^{n\times n}$ is called a P-matrix if all its principal minors are positive. Recall that a principal minor is simply the determinant of a submatrix obtained from B when the same set of rows and columns are removed. The diagonal entries, as well as the determinant of B, are thus among its principal minors.

- According to [241], the sign pattern matrix written as:

$$S_n = \begin{bmatrix} + & - & 0 & 0 \\ + & + & - & 0 \\ + & + & + & - \\ + & + & + & + \end{bmatrix} \qquad (9.12)$$

  is a qualitative P-matrix.

- If $B \in \mathbb{R}^{n\times n}$ is an $n \times n$ matrix, and $k \in \mathbb{R}$ is a constant, then:

$$det(kB) = k^n det(B) \qquad (9.13)$$

Theorem 2. Consider a matrix $A_n \in \mathbb{R}^{n \times n}$ with the structure given by

$$A = \begin{bmatrix} -a_{1,1} & a_{1,2} & 0 & \cdots & 0 & 0 \\ -a_{2,1} & -a_{2,2} & a_{2,3} & \cdots & 0 & 0 \\ \vdots & \vdots & \ddots & \ddots & \vdots & \vdots \\ -a_{n-2,1} & -a_{n-2,2} & \cdots & -a_{n-2,n-2} & a_{n-2,n-1} & 0 \\ -a_{n-1,1} & -a_{n-1,2} & \cdots & -a_{n-1,n-2} & -a_{n-1,n-1} & a_{n-1,n} \\ 1 & 1 & \cdots & 1 & 1 & 1 \end{bmatrix} \tag{9.14}$$

where $a_{i,j} > 0 \; \forall i, j = 1, \cdots, n$. The matrix A_n is invertible for any $n \geq 2$.

Proof: First, consider the cases with $n = 2, 3, 4$. Denoting with $M_{ij}(A_n)$ the minor of matrix A_n formed by eliminating row i and column j, the determinant of the matrix A_n, calculated by expanding along its last column, is given by:

$$|A_2| = \begin{vmatrix} -a_{1,1} & a_{1,2} \\ 1 & 1 \end{vmatrix} = -a_{1,2} - a_{1,1} < 0$$

$$|A_3| = \begin{vmatrix} -a_{1,1} & a_{1,2} & 0 \\ -a_{2,1} & -a_{2,2} & a_{2,3} \\ 1 & 1 & 1 \end{vmatrix} = -a_{2,3} \underbrace{\begin{vmatrix} -a_{1,1} & a_{1,2} \\ 1 & 1 \end{vmatrix}}_{|A_2|<0} +1 \begin{vmatrix} -a_{1,1} & a_{1,2} \\ -a_{2,1} & -a_{2,2} \end{vmatrix} = \underbrace{-a_{2,3}|A_2|}_{>0} + a_{1,1}a_{2,2} + a_{1,2}a_{2,1} > 0$$

$$|A_4| = \begin{vmatrix} -a_{1,1} & a_{1,2} & 0 & 0 \\ -a_{2,1} & -a_{2,2} & a_{2,3} & 0 \\ -a_{3,1} & -a_{3,2} & -a_{3,3} & a_{3,4} \\ 1 & 1 & 1 & 1 \end{vmatrix} = \underbrace{-a_{3,4} \underbrace{\begin{vmatrix} -a_{1,1} & a_{1,2} & 0 \\ -a_{2,1} & -a_{2,2} & a_{2,3} \\ 1 & 1 & 1 \end{vmatrix}}_{|A_3|>0}}_{<0} +1 \underbrace{\begin{vmatrix} -a_{1,1} & a_{1,2} & 0 \\ -a_{2,1} & -a_{2,2} & a_{2,3} \\ -a_{3,1} & -a_{3,2} & -a_{3,3} \end{vmatrix}}_{|M_{44}(A_4)|} < 0 \tag{9.15}$$

where the last inequality follows from the fact that $-M_{44}(A_4)$ adheres to the sign pattern in (9.12). Using property (9.13), one has that $|M_{44}(A_4)| = (-1)^3|-M_{44}(A_4)| < 0$. Building on the previous steps, it is possible to verify that, for $n \geq 4$

$$|A_n| = -a_{n-1,n}|A_{n-1}| + (-1)^{n-1} \underbrace{|-M_{nn}(A_n)|}_{>0}. \tag{9.16}$$

Note that $-M_{nn}(A_n)$ satisfies the sign pattern in (9.12) for any $n \geq 4$, thus implying that $|-M_{nn}(A_n)| > 0$. Moreover, since $a_{i,j} > 0 \; \forall i, j = 1, \cdots, n$, it is easy to verify that the sign of $-a_{n-1,n}|A_{n-1}|$ is $(-1)^{n-1}$. As a consequence, the two terms in the summation (9.16) have consistent sign. This, together with the positivity of $a_{i,j}$ for all $i, j = 1, \cdots, n$ implies that $|A_n| \neq 0$, for any $n \geq 2$ thus proving the theorem.

It is worth noting that the matrix Ψ_2 is always invertible, based on Theorem 2, since all the coefficients in Ψ_2 are always positive.

9.2 Non-linear observability analysis

Preliminaries

Definition 1 (Lie derivative). *Given a smooth scalar function* $\alpha : \mathbb{R}^n \times \mathbb{R}^m \to \mathbb{R}$ *and* *a smooth vector field $\beta : \mathbb{R}^n \times \mathbb{R}^m \to \mathbb{R}^n$. Then the J-th order Lie derivative of β with respect to α is defined as:*

$$L^J_\beta \alpha = \frac{\partial L^{J-1}_\beta \alpha}{\partial x} \cdot \beta \tag{9.17}$$

where the zero-order Lie derivative of β with respect to α is $L^0_\beta \alpha = \alpha$, while the second order Lie derivative can be also expressed as $L^2_\beta \alpha = L_\beta L_\beta \alpha$.

Definition 2 (Diffeomorphism [242]). *Let $U \subset \mathbb{R}^n$ be an open subset in $\mathbb{R}^n$. A function $f : \mathbb{R}^n \to \mathbb{R}^n$ is a diffeomorphism, if f is a bijection and differentiable, and its inverse f^{-1} is differentiable.*

Theorem 3 (Inverse Function Theorem [242]). *Let $U \subset \mathbb{R}^n$ be an open subset in $\mathbb{R}^n$ and let $f : \mathbb{R}^n \to \mathbb{R}^n$ be a function. If for $x_0 \in U$, $df/dx|_{x_0}$ is of full rank, then there exists an open neighborhood V of x_0 and an open neighborhood W around $f(x_0)$ (i.e. image of f) such that $f : V \to W$ is a bijection, and its inverse f^{-1} is also continuously differentiable. In this case the derivative of f^{-1} at $y_0 = f(x_0)$ is $d(f^{-1}(y_0))/dx = (df(x_0)/dx)^{-1}$*

In dynamical systems theory, observability refers to a system's ability to reconstruct its initial state using input-output data. This study focuses on the analysis of nonlinear observability as described in [243], using the observability rank condition for nonlinear systems. Based on Lie Algebra, this condition provides a sufficient criterion for local observability.

Let's consider a non-linear system of the following form:

$$\Sigma : \begin{cases} \dot{x}(t) = f(x(t)) + g(x(t))u(t) \\ y = h(x(t)) + l(x(t))u(t) \end{cases} \tag{9.18}$$

where $x \in \mathbb{R}^n$, $u \in \mathbb{R}$, $y \in \mathbb{R}$, $f : \mathbb{R}^n \times \mathbb{R} \to \mathbb{R}^n$ and $g : \mathbb{R}^n \times \mathbb{R} \to \mathbb{R}^n$ are smooth vector fields, and $h : \mathbb{R}^n \times \mathbb{R} \to \mathbb{R}$ and $l : \mathbb{R}^n \times \mathbb{R} \to \mathbb{R}$ are a smooth scalar function. In the following, $x(t, x_0, u)$ will indicate the solution of (9.18) for a given initial condition x_0 and input sequence $u(\cdot)$ defined over the time interval $[0, t)$. The corresponding output will be denoted as $y(t, x_0, u)$.

Definition 3 ([243]). Consider system (9.18). Two states $x_0, x_1 \in \mathbb{R}^n$ are distinguishable if there exist an input sequence $u(\cdot)$ such that $y(t, x_0, u) \neq y(t, x_1, u)$.

Definition 4 ([243]). System Σ is locally observable at $x_0 \in X \subseteq \mathbb{R}^n$ if there exists an open neighborhood Ω of x_0 such that every $x \in \Omega$ other than x_0 is distinguishable from x_0. Finally, the system is said to be locally observable if it is locally observable at each $x_0 \in X$.

Given the nonlinear system (9.18), the first two time derivatives of the output can be expressed as in equations (9.19) and (9.20), respectively. It is important to note that the time derivatives of y ($y^{(k)}$) are expressed as a linear combination of terms of the form $(L_{z_s} L_{z_{s-1}} \cdots L_{z_1} \alpha)(x)$, where $1 \leq s \leq k$. Each vector field $z_1, \cdots, z_s$ is selected from the set $\{f, g\}$ and α is chosen from the set $\{h, l\}$.

$$
\begin{aligned}
\dot{y} &= \frac{d(h(x)+l(x)u)}{dt} = \frac{dh(x)}{dx}\dot{x} + u\frac{dl(x)}{dx}\dot{x} + \dot{u}l(x) = \\
&= \frac{\partial h(x)}{\partial x}(f(x)+g(x)u) + u\frac{\partial l(x)}{\partial x}(f(x)+g(x)u) + \dot{u}l(x) = \\
&= L_f h(x) + L_g h(x)u + L_f l(x)u + L_g l(x)u^2 + l(x)\dot{u} = \\
&= L_f h(x) + [L_g h(x) + L_f l(x)]u + L_g l(x)u^2 + l(x)\dot{u}
\end{aligned}
\tag{9.19}
$$

$$
\begin{aligned}
&\ddot{y} = \frac{d\dot{y}}{dt} = \frac{\partial L_f h(x)}{\partial x}(f(x)+g(x)u) + \frac{d[L_g h(x) + L_f l(x)]u}{dt} + \frac{dL_g l(x)u^2}{dt} + \frac{dl(x)\dot{u}}{dt} = \\
&= L_f(L_f h(x)) + L_g(L_f h(x))u + [L_g h(x) + L_f l(x)]\dot{u} + \frac{d[L_g h(x) + L_f l(x)])}{dt}u + \\
&+ L_g l(x)2u\dot{u} + \frac{dL_g l(x)}{dt}u^2 + l(x)\ddot{u} + \frac{dl(x)}{dt}\dot{u} \\
&= L_f(L_f h(x)) + L_g(L_f h(x))u + [L_g h(x) + L_f l(x)]\dot{u} + \\
&+ \frac{d[L_g h(x) + L_f l(x)]}{dx}(f(x)+g(x)u)uL_g l(x)2u\dot{u} + \frac{dL_g l(x)}{dx} \\
&(f(x)+g(x)u)u^2 + l(x)\ddot{u} + \frac{dl(x)}{dx}(f(x)+g(x)u)\dot{u} \\
&= L_f^2 h(x) + L_g(L_f h(x))u + [L_g h(x) + L_f l(x)]\dot{u} + L_f(L_g h(x))u + \\
&+ L_f^2 l(x)u + (L_g^2 h(x))u^2 + L_g(L_f l(x))u^2 + L_g l(x)2u\dot{u} + L_f(L_g l(x))u^2 + \\
&+ L_g^2 l(x)u^3 + l(x)\ddot{u} + L_f l(x)\dot{u} + L_g l(x)u\dot{u}
\end{aligned}
\tag{9.20}
$$

Definition 5 (Observation space $\mathcal{O}$). The observation space $\mathcal{O}$ of the system in the form (9.18) is the linear space of functions over the field $\mathbb{R}$ spanned by all functions of the form:

$$L_{z_s}L_{z_{s-1}}\cdots L_{z_1}\alpha(x), \quad s \geq 0, \quad z_j \in \{f, g\}, \quad \alpha \in \{h, l\} \tag{9.21}$$

$\mathcal{O}$ comprises all linear combinations of functions in the form (9.21) with constant and real coefficients (not functions of x). It is important to note that Definition 5 updates the definition originally presented in [243] for nonlinear systems where the output function explicitly depends on the input through a smooth scalar function $l : \mathbb{R}^n \times \mathbb{R} \to \mathbb{R}$. Similarly, Lemma 84 in Section 7.3 in [243] can be extended to the system described by (9.18) as follows:

Lemma 1. For the system described by (9.18), let $\mathcal{J}$ denote the linear space of functions over the field $\mathbb{R}$ spanned by all functions of the form:

$$L_{v_s}L_{v_{s-1}}\cdots L_{v_1}\alpha(x), \quad s \geq 0$$

where $[v_1, \cdots, v_s]$ are vector fields in the form:

$$v = f(x) + g(x)u$$

with u being a real number in $\mathbb{R}$. Then $\mathcal{J}$ is equal to $\mathcal{O}$.

The proof of Lemma 1 in [243] remains applicable in this context when considering the linear space of functions over the field $\mathbb{R}$ spanned by all functions of the form $(L_{z_s}L_{z_{s-1}}\cdots \cdots L_{z_1}\alpha)(x)$. Finally, the Sufficient Condition for Local Observability proposed in [243] can be extended for systems in the form (9.5) as shown in the following:

Theorem 4. Consider the system described by (9.18), and assume $x_0 \in X$ is given. Consider the forms

$$\left.\frac{dL_{z_s}L_{z_{s-1}}\cdots L_{z_1}\alpha(x)}{dx}\right|_{x=x_0}, \quad s \geq 0, \quad z_j \in \{f, g\}, \quad \alpha \in \{h, l\} \tag{9.22}$$

evaluated at x_0. If there are n linearly independent row vectors in this set, then the system is locally observable around x_0.

Without loss of generality, the proof of the theorem in [243] is applicable to the current case, as it relies on Definition 5 and Lemma 1, both of which have been established to hold in this context. It is important to note that, due to Lemma 1, local observability can be assessed without needing to explicitly consider the values of the input. According to [243], the condition (9.22) becomes:

$$rank(\Theta|_{x=x_0}) = n, \qquad \text{with:} \quad \Theta = \frac{\partial}{\partial x} \begin{bmatrix} \alpha(x) \\ L_f\alpha(x) \\ L_g\alpha(x) \\ L_fL_g\alpha(x) \\ L_gL_f\alpha(x) \\ L_f^2\alpha(x) \\ L_g^2\alpha(x) \\ \vdots \end{bmatrix} \quad \text{with: } \alpha \in \{h, l\} \tag{9.23}$$

where n denotes the number of states in the system. Condition (9.23) requires that the matrix $\Theta|_{x=x_0}$ includes at least n linearly independent row vectors. Finally, it is worth noting that the rank test (9.23) assesses whether the system is weakly locally observable but does not provide insights into estimation accuracy or reliability. To evaluate the system's observability more comprehensively, the condition number of the matrix $\Theta|_{x=x_0}$

$$\kappa\left(\Theta|_{x=x_0}\right) = \left\|\Theta|_{x=x_0}{}^{-1}\right\| \left\|\Theta|_{x=x_0}\right\| \tag{9.24}$$

can be used as a metric, as discussed in [244].

9.2.1 Nonlinear observability analysis: results from the module-level model

Previous studies have investigated the observability of parallel-connected battery models using first-order ECMs through both linearized and nonlinear approaches, as demonstrated in, e.g., [240] and [232], respectively. These analyses primarily focused on the observability of two parallel cells without accounting for R_{int} and the SOC dependency of model parameters. They consistently found that the model states are unobservable when the cells have identical parameters. Additionally, observability is lost when the cells have identical OCV values and the $dV_{OCV}/dSOC$ is zero.

In this study, we apply the rank condition from (9.23) to analyze the observability of the parallel-connected model in (9.5) which consists of N_p cells and accounts for both R_{int} and SOC-dependent parameters (see eq. (9.4)). According to Theorem 4, the system is locally observable around the considered state if there are n linearly independent row vectors in the set defined in (9.22). In the parallel-connected model here considered, $n = 2N_p$, the state vector is $x_{mod} = [V_1^{[1]}, SOC^{[1]}, \cdots, V_1^{[N_p]}, SOC^{[N_p]}]$ and functions f, g, h, l are defined as in (9.11). Local observability is ensured if there are $n = 2N_p$ linearly independent row vectors of the form given in (9.22). In the following, for simplicity and computational aspects, instead of considering all possible functions of the form in (9.22), we construct the matrix $\hat{\Theta} \in \mathbb{R}^{2N_p} \times \mathbb{R}^{2N_p}$ using only a specific subset of these functions

$$\hat{\Theta} = \frac{\partial}{\partial x} \begin{bmatrix} h(x_{mod}) \\ L_{f(x_{mod})} h(x_{mod}) \\ L_{g(x_{mod})} h(x_{mod}) \\ L^2_{f(x_{mod})} h(x_{mod}) \\ L^2_{g(x_{mod})} h(x_{mod}) \\ \vdots \\ L^{N_p}_{f(x_{mod})} h(x_{mod}) \end{bmatrix} \tag{9.25}$$

As will be explained further, this choice is sufficient for drawing conclusions about local observability. Note that the same choice was made in [232] (equation (27)), where nonlinear observability was analyzed for two parallel cells without considering R_{int} or the SOC dependency of model parameters. Figure 9.4 illustrates the observability results for the parallel-connected battery module. The analysis is performed under a 0.75C-rate CC discharging cycle, considering R_{int} values of 0, 1, and 3 $m\Omega$, and for N_p values of 2, 3, and 4. Additionally, concerning the initial conditions of the N_p ECMs, the cells are assumed to be fully charged (i.e. $SOC^{[i]} = 100\%$ with i=1, $\cdots, N_p$), and the voltage across each resistance-capacitor block is set to 0 V (i.e. $V_1^{[i]} = 0$ V with i=1, $\cdots, N_p$). It is important to highlight that the analytical calculation of $\hat{\Theta}$ becomes increasingly complex as the number of cells increases. In general, it becomes computationally impractical for models with more than ten states [245]. Additionally, the SOC-dependent parameters add further complexity to the computation. To address these challenges efficiently, $\hat{\Theta}$ was computed using symbolic expressions in Matlab with the CasADi toolbox. The rank and condition number of $\hat{\Theta}$ were then evaluated numerically by substituting the model states, derived from the model solution under the previously described conditions, at each time step. Figure 9.4(d-f), clearly shows that $\hat{\Theta}$ loses its maximum rank, regardless of the N_p value when R_{int} is 0. Theoretically, to rule out local observability, one would need to evaluate all possible functions of the form given in (9.22), not just the subset considered here, and verify that n linearly independent row vectors cannot be found. However, it is crucial to note that in this scenario, cells with identical parameter formulations, listed in eq. (9.4) within Table 9.1, and initial conditions experience the same current, SOC, and terminal voltage during operation. As a result, the parallel-connected module acts as a single lumped cell with a total capacity equal to the sum of the individual cell capacities. This lack of differentiation impedes the ability to observe the distinct states of each cell, corroborating the findings in [240] and [232]. On the other hand, when $R_{int} > 0$, $\hat{\Theta}$ attains maximum rank. This occurs even when the cells in parallel have identical parameters, as they are required to deliver different currents to satisfy (5.26) at each time instant. This leads to varying SOC levels, resulting in distinct values for V_{OCV}, R_0 and R_1 across the cells. Additionally, the voltage drop across R_{int} causes differences in cell voltages, as illustrated in Figure 9.4(a-c). The voltage discrepancy between the cells increases with the distance from the terminals, making the behavior of each cell distinguishable. Finally, the condition number $\kappa(\hat{\Theta})$ is shown in Figure 9.4(g-i). As N_p increases, $\kappa(\hat{\Theta})$ also rises, indi-

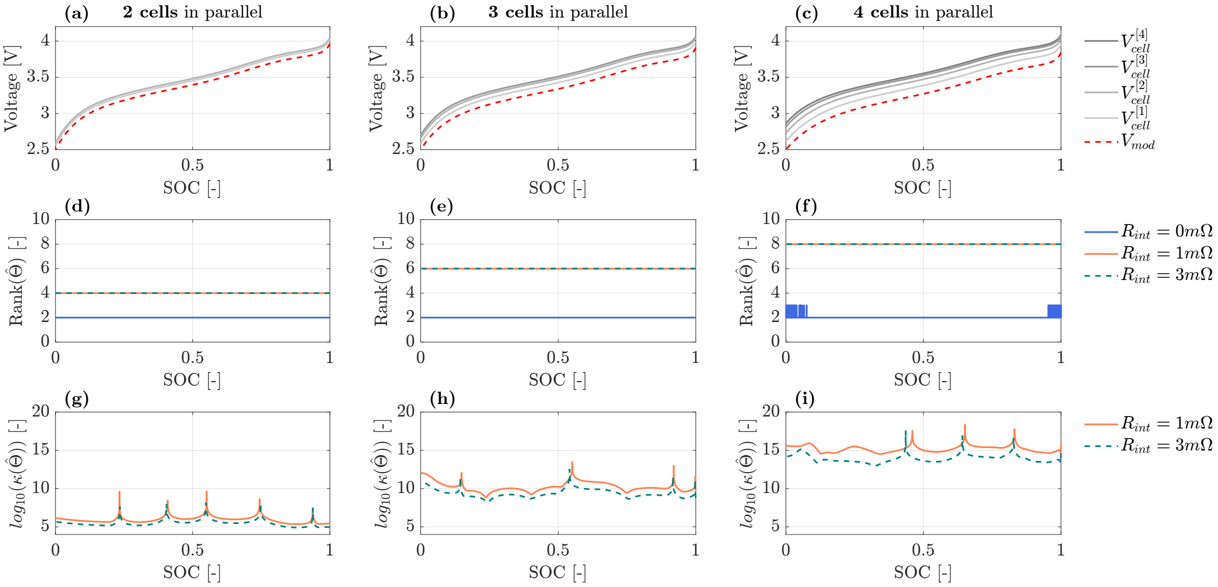

Figure 9.4: Observability analysis results. Panels (a-c) show the voltage across each cell ($V_{cell}^{[i]}$ with $i = 1, \cdots, N_p$) and at the module terminals during a $0.75C$-rate constant current cycle with $R_{int} = 3\ m\Omega$ for $N_p = 2, 3$, and 4, respectively. Panels (d-f) display the rank of $\hat{\Theta}$ (from (9.25)) for $R_{int} = 0, 1$ and $3m\Omega$ and panels (g-i) present the condition number of $\hat{\Theta}$ for the same R_{int} values and $N_p = 2, 3$ and 4.

cating a likely decrease in observer accuracy with larger battery modules. Moreover, for a fixed number of cells, $\kappa(\hat{\Theta})$ increases as R_{int} decreases. This is because lower resistance reduces the heterogeneity between the cells, making the model states less distinguishable.

9.3 Moving horizon estimation

Consider a non-linear discrete-time system given as:

$$\Sigma : \begin{cases} x_{k+1} &= f(x_k, u_k) + w_k \\ y_k &= h(x_k, u_k) + v_k \end{cases} \tag{9.26}$$

where $x_k \in \mathbb{R}^n$, $u_k \in \mathbb{R}^m$, and $y_k \in \mathbb{R}^p$ represent the state, input, and output vectors of the model at the k-th time instant, respectively. The functions $f : \mathbb{R}^n \times \mathbb{R}^m \to \mathbb{R}^n$, and $h : \mathbb{R}^n \times \mathbb{R}^m \to \mathbb{R}^p$ are smooth mappings. The terms $w_k \in \mathbb{R}^n$ and $v_k \in \mathbb{R}^p$ denote the state and measurement noise, respectively. In the following, $x(k, x_0, u, w)$ will indicate the solution of (9.26) for a given initial condition x_0 and input sequences $u(\cdot)$ and $w(\cdot)$ defined over the time instants $0, \cdots, k$. The corresponding output will be denoted as $y(k, x_0, u, w, v)$. According to [246], based on a sequence of N measurements, from the time instants $k - N$ up to k, the system states are estimated by minimizing the following cost function:

$$\begin{aligned}
&\min_{x_{k-N},\{w_z\}_{z=k-N}^{k-1}} \left[(\delta x_{k-N}^T P_{k-N|k-N-1}^{-1} \delta x_{k-N}) + \sum_{z=k-N}^{k} v_z^T V^{-1} v_z + \sum_{z=k-N}^{k-1} w_z^T Q^{-1} w_z\right] \\
&\text{subject to:} \qquad\qquad\qquad\qquad\qquad\qquad\qquad\qquad\qquad\qquad\qquad (9.27) \\
&\qquad x_{j+1} = f(x_j, u_j) + w_j,\ j \in \{k-N, \cdots, k-1\} \\
&\qquad lb_x \le x_j \le ub_x,\ j \in \{k-N, \cdots, k\}
\end{aligned}$$

where the term $\delta x_{k-N} = (x_{k-N} - x_{k-N|k-N-1})$ represents the discrepancy between the initial state (x_{k-N}), which is to be optimized, and the prior state estimate $(x_{k-N|k-N-1})$ while $v_z = y_z^{meas} - h(x_z, u_z)$, with y_z^{meas} being the plant measurement and x_k being computed as the solution of model (9.26) subject to the initial condition x_{k-N} and disturbance sequence $\{w_z\}_{z=k-N}^{k-1}$. The matrices $V \in \mathbb{R}^{p\times p}$, $Q \in \mathbb{R}^{n\times n}$ and $P_{k-N|k-N-1} \in \mathbb{R}^{n\times n}$ are symmetric and positive definite and represent the covariance matrices for measurement noise, model uncertainty and initial condition uncertainty, respectively. Additionally, lb_x and ub_x are the upper and lower bounds of the state variables, respectively. Note that, $P_{k-N|k-N-1}$ is computed using the Riccati equation to approximate past information, as detailed in equation (32) of [228]. The objective in (9.27) is to determine the state (x_{k-N}) and process noise sequence $(\{w_z\}_{z=k-N}^{k-1})$ that minimize the discrepancy between the predicted and measured data $(v_z^T V^{-1} v_z)$, while ensuring that the estimated state aligns with the expected system dynamics $(w_z^T Q^{-1} w_z)$, and that the initial condition is consistent with the uncertainty in the initial state estimate $(\delta x_{k-N}^T P_{k-N|k-N-1}^{-1} \delta x_{k-N})$. It is worth mentioning that when fewer than N measurements are available $(k < N)$, $P_{k-N|k-N-1}$ is set to P_0. For further information on MHE, readers are encouraged to consult [246].

9.3.1 MHE for parallel-connected module

To evaluate the accuracy of the proposed SOC estimation method, we consider a battery module consisting of 4 parallel-connected cells (i.e. $N_p = 4$). Note that the MHE-based algorithm for the module-level model is implemented in discrete time, with the module dynamics discretized using the Forward Euler method, as in [227]. Sections 9.3.1.1 and 9.3.1.2 validate the method using simulated and experimental data, respectively, covering various current profiles and R_{int} values. Finally, Section 9.3.1.3 presents preliminary findings on the joint estimation of model states and R_{int}. In this study, we address the state estimation of a parallel-connected battery module by comparing two distinct MHE-based schemes.

- **Approach 1:** ***ODE model.*** In this approach, we utilize the module-level model with Kirchhoff's circuit laws directly incorporated into the ODEs, as described in

(9.10). According to (9.27), the optimization problem is written as:

$$\min_{x_{mod,k-N},\{w_z\}_{z=k-N}^{k-1}} \left[(\delta x_{mod,k-N}^T P_{k-N|k-N-1}^{-1} \delta x_{mod,k-N}) + \sum_{z=k-N}^{k} v_z^T V^{-1} v_z + \sum_{z=k-N}^{k-1} w_z^T Q^{-1} w_z \right]$$

subject to:

$$\begin{aligned} & x_{mod,j+1} = f(x_{mod,j}) + g(x_{mod,j}) I_{tot,j} + w_j,\ j \in \{k-N, \cdots, k-1\} \\ & lb_x \leq x_{mod,j} \leq ub_x,\ j \in \{k-N, \cdots, k\} \end{aligned} \tag{9.28}$$

Here, $\delta x_{mod,k-N} = x_{mod,k-N} - x_{mod,k-N|k-N-1}$ represents the deviation between the optimized state at time $k-N$ and the prior estimate $x_{mod,k-N|k-N-1}$ at the same time. The state vector $x_{mod} = [V_1^{[1]}, SOC^{[1]}, \cdots, V_1^{[N_p]}, SOC^{[N_p]}]$ encompasses the voltages and state of charge (SOC) of each cell in the module. The measurement noise v_z is defined as the difference between the measured and simulated module voltage, i.e. $v_z = V_{mod}^{meas} - V_{mod}$.

- **Approach 2: *DAE model.*** The second approach leverages the ability of MHE to handle equality constraints by incorporating Kirchhoff's circuit laws directly into the optimization framework. The optimization problem, based on the DAE model (eq. (9.6) and (9.7)), is formulated as:

$$\min_{x_{mod,k-N},\{I_{mod,z},w_z\}_{z=k-N}^{k-1}} \left[(\delta x_{mod,k-N}^T P_{k-N|k-N-1}^{-1} \delta x_{mod,k-N}) + \sum_{z=k-N}^{k} v_z^T V^{-1} v_z + \sum_{z=k-N}^{k-1} w_z^T Q^{-1} w_z \right]$$

subject to:

$$\begin{aligned} & x_{mod,j+1} = A_{mod} x_{mod,j} + B_{mod} I_{mod,j} + w_j,\ j \in \{k-N, \cdots, k-1\} \\ & V_{cell,j}^{[l+1]} = V_{cell,j}^{[l]} + 2R_{int}(I_{tot,j} - \sum_{z=1}^{l} I_{cell,j}^{[z]}),\ l \in \{1, \cdots, N_p - 1\} \\ & I_{tot,j} = \sum_{l=1}^{N_p} I_{cell,j}^{[l]}, \\ & lb_x \leq x_{mod,j} \leq ub_x,\ j \in \{k-N, \cdots, k\} \\ & lb_{I_{cell}} \leq I_{mod,j} \leq ub_{I_{cell}},\ j \in \{k-N, \cdots, k\} \end{aligned} \tag{9.29}$$

where $lb_{I_{cell}}$ and $ub_{I_{cell}}$ denote the lower and upper bounds for the branch currents respectively. Despite introducing $N_p \cdot N$ additional algebraic optimization variables (i.e. $\{I_{mod,z}\}_{z=k-N}^{k-1}$), this approach reduces the nonlinearities within the module-level dynamics compared to the previously described approach.

In Section 9.3.1.1, the two MHE-based schemes are compared in terms of both accuracy and computational load. Accuracy is assessed using two key performance indicator (KPI): ΣSOC^{RMS} and ΣV_1^{RMS}, as defined in eq. (9.30) and (9.31) in Table 9.2. Note that $SOC_i^{[k],\text{ref}}$ and $V_{1,i}^{[k],\text{ref}}$ in equations (9.30) and (9.31) represent the reference SOC and V_1 of the k-th cell at the i-th time instant. These reference values are obtained from an open-loop simulation of the model when the MHE algorithms are validated against simulated data, as detailed in Section 9.3.1.1. For the experimental validation phase, however, $SOC_i^{[k],\text{ref}}$ is computed using Coulomb counting, based on the measured current and capacity of each cell. It is important to note that $V_{1,i}^{[k],\text{ref}}$ cannot be derived from experimental data, as it represents an internal model state that is not directly measurable. As a result, ΣV_1^{RMS} is not included in the analysis presented in Section 9.3.1.2. Finally,

Table 9.2: Summary of the MHE-based algorithm performance indicators

MHE performance indicator		*Unit*
$\Sigma SOC^{RMS} = \sum_{k=1}^{N_p} \sqrt{\frac{1}{t_{sim}} \sum_{i=1}^{t_{sim}} (SOC_i^{[k]} - SOC_i^{[k],ref})^2}$	(9.30)	[%]
$\Sigma V_1^{RMS} = \sum_{k=1}^{N_p} \sqrt{\frac{1}{t_{sim}} \sum_{i=1}^{t_{sim}} (V_{1,i}^{[k]} - V_{1,i}^{[k],ref})^2}$	(9.31)	[V]
$MTPI = \frac{1}{t_{sim}} \sum_{i=1}^{t_{sim}} TPI_i$	(9.32)	[s]

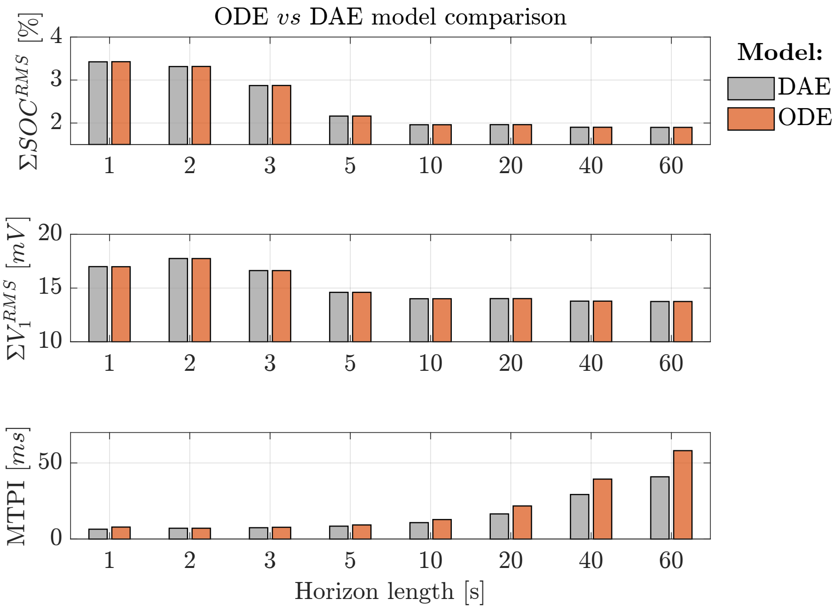

Figure 9.5: Comparison of MHE schemes on simulated data: ODE vs. DAE models. (a) shows ΣSOC^{RMS}, (b) presents ΣV_1^{RMS} and (c) displays $MTPI$ under different horizon lengths.

the computational load is quantified by calculating the Mena time per iteration (MTPI), as described in (9.32) where t_{sim} refers to the total simulation time, measured using Matlab's built-in timer. Moreover, it is important to note that the optimization problem for both approaches is reformulated using the direct multiple shooting method [247].

9.3.1.1 Validation using simulated data

First, the estimation algorithm is validated through simulation. To account for cell-to-cell (CtC) differences, we randomly selected four distinct cells from the dataset [8] (cells labeled as *P19, P4, P10, P16*) and individually identified their ECM parameters for use in the module-level model. While those parameters were used to simulate the plant, the MHE-based algorithm uses the same parameters as specified in (9.4) for all cells. This scenario reflects a practical case where identifying individual cells within the module is unfeasible due to the absence of dedicated sensors. For simulating noisy output voltage measurements, we added white Gaussian noise with a covariance of $V = 5 \times 10^{-4}$ V to the open-loop simulation output of the model (V_{mod}). In the following, the estimation horizon is set to 20 seconds (i.e. $N = 20$) with a sampling time of 1 second, $R_{int} = 3m\Omega$. The matrices $P_0 = diag(P_0^{[1]}, \cdots, P_0^{[N_p]})$, $Q = diag(Q^{[1]}, \cdots, Q^{[N_p]})$ and vector $X_0 = [X_0^{[1]}, \cdots, X_0^{[N_p]}]$ assume the following values $P_0^{[k]} = diag(1 \times 10^{-1}, 5 \times 10^{-2})$, $Q^{[k]} = diag(10^{-6}, 10^{-7})$ and $X_0^{[k]} = [-0.02, 0.95]$, $k \in \{1, \cdots, N_p\}$). Additionally, the cell SOC is constrained for each cell between 0% and 100%. For V_1, the bounds are set to ±50 mV, while the bounds for I_{mod} are established at ±10 A. These values are deemed appropriate for the module model under consideration.

Figure 9.5 provides a comparative analysis of the two MHE-based schemes (ODE vs DAE models), applied to a CC discharging cycle from 80% to 0% in the simulation condition described in the following lines. The performance and computational efficiency of both schemes across various horizon lengths, are evaluated using the metrics ΣSOC^{RMS}, ΣV_1^{RMS} and $MTPI$. Note that the total simulation time t_{sim}, which is necessary for calculating the MTPI as indicated in equation (9.32) , is shown on the x-axis of Fig. 9.6. The results, as expected, show that both approaches achieve similar accuracy, evidenced by the close matching values of ΣSOC^{RMS} and ΣV_1^{RMS}. However, the DAE model offers superior computational efficiency, leading to reduced processing times, as highlighted by the $MTPI$. For this reason, the following sections will focus exclusively on the results obtained using the DAE model. Fig. 9.6 illustrates the estimation performance of the MHE based on the DAE model for two distinct current profiles: constant current (CC) discharge and a regulatory driving cycle (DV), specifically the Worldwide Harmonized Light Vehicles Test Procedure (WLTP). In both simulations, it is assumed that each cell is at 80% of SOC (i.e. $SOC^{[i]} = 100\%$ with i=1, $\cdots$,4), and the voltage across each resistance-capacitor block is set to $0V$ (i.e. $V_1^{[i]} = 0$ V with i=1, $\cdots$,4). In both cases, the MHE algorithm effectively tracks the terminal voltage measurements, as shown in Fig. 9.6(a) and (c), demonstrating notable robustness against voltage noise. Additionally, as shown in Fig. 9.6(b-c) and (e-f), the SOC distribution among parallel-connected cells is accurately estimated, with maximum SOC errors of 1.44% and 0.55% for the CC and DV profiles, respectively. This trend is further highlighted by the metric $\Sigma SOC^{RMS} = \sum_{k=1}^{N_p} \sqrt{\frac{1}{t_{sim}} \sum_{i=1}^{t_{sim}} (SOC_i^{[k]} - SOC_i^{[k],ref})^2}$, which measures 1.8% and 0.89% for CC and DV scenarios, respectively. for the CC and DV scenarios, respectively. This level of accuracy is quite satisfactory for real-world applications, where the typical acceptable SOC accuracy threshold is around [248]. It is worth highlighting the significant impact of the horizon on algorithm accuracy: as the value of N increases, ΣSOC^{RMS} decreases notably, as illustrated in Figure 9.5(a). This improvement in accuracy underscores the advantage of the MHE approach over traditional state estimation techniques [232, 233, 234, 235].

Note that the four interconnected cells exhibit different SOC trends throughout the discharge, due to the non-zero R_{int}. Specifically, the cell closest to the module terminals (Cell 1) delivers the highest current to compensate for the voltage drop across the lowest resistance, as clearly shown in Fig. 9.7(f), resulting in a more significant SOC decline. Toward the end of the discharge, a shift in the current distribution occurs, leading to a

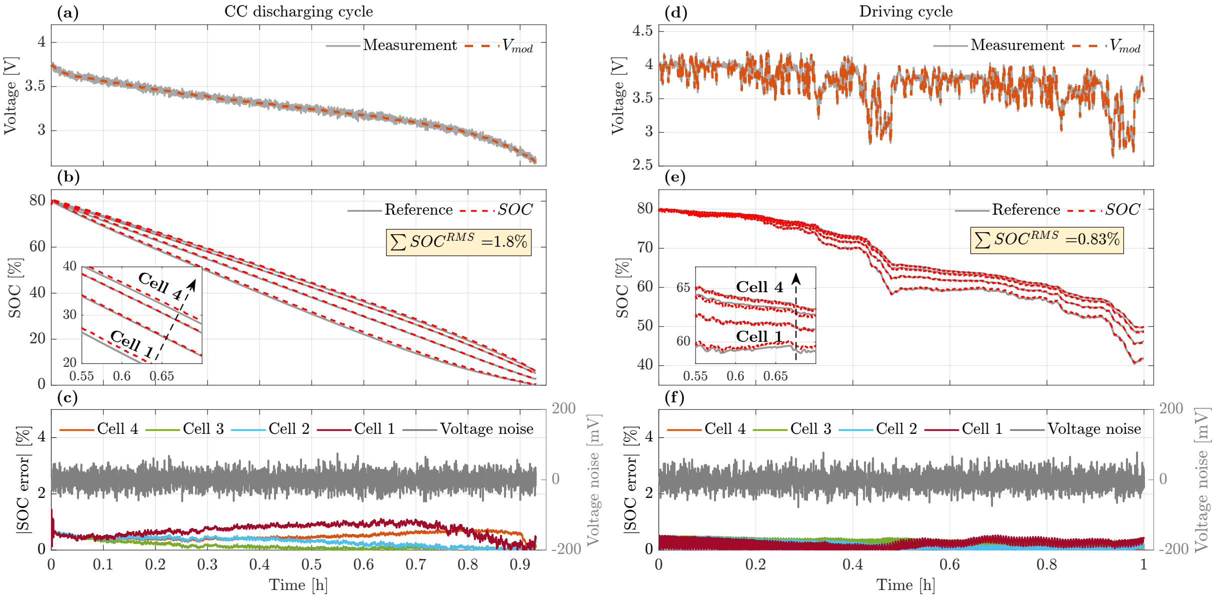

Figure 9.6: Validation of the MHE-based SOC estimation algorithm in constant current (CC) (a-c) and driving cycle (d-f) scenarios. (a)(d) Comparison of measured and estimated module voltage (V_{mod}). (b)(e) SOC distribution across cells. (c)(f) SOC estimation error for each cell, along with voltage measurement noise.

convergence in SOC values, driven by the higher V_{OCP} of the cells that still retain charge.

9.3.1.2 Validation with experimental data

To evaluate the effectiveness of the MHE algorithm in practice, the method is applied to experimental data from two discharge tests characterized by identical $0.75C$ constant current profiles but with different internal resistances, R_{int}, set at $1m\Omega$ and $3m\Omega$ [8]. The reference SOC for each cell is calculated using Coulomb counting, based on the measured current and cell capacity. The estimation horizon is set to 10 seconds, considering a sampling time of 1 second, while t_{sim} refers to the time needed to fully discharge the module. The covariance matrices and initial conditions defined as follows: $V = 10^{-5}$, $P_0^{[k]} = diag(1 \times 10^{-1}, 5 \times 10^{-2})$, $Q^{[k]} = diag(10^{-3}, 10^{-4})$, and $X_0^{[k]} = [-0.02, 0.95]$, where $k \in 1, \cdots, N_p$. Compared to the previous section, the Q matrix has been re-calibrated to account for structural uncertainties present in the physical system. Fig.9.7(a-c) and (d-f) display the results obtained with R_{int}=1mΩ and 3mΩ, respectively. The MHE algorithm once again demonstrates precise SOC estimation, maintaining the SOC error below 1.8% throughout the full discharge. The calculated ΣSOC^{RMS} values are 2.7% for $R_{int} = 1m\Omega$ and 3.2% for $3m\Omega$. The higher estimation error, compared to the results in Section 9.3.1.1, can be attributed to inherent differences between the model and the real system dynamics. Additionally, as shown by Fig.9.7(c) and (f), the estimated cell current in each branch consistently follows the measured current, capturing both the converging and diverging phases. It is important to note that cell currents in the experimental setup were measured using Hall sensors, as detailed in [8].

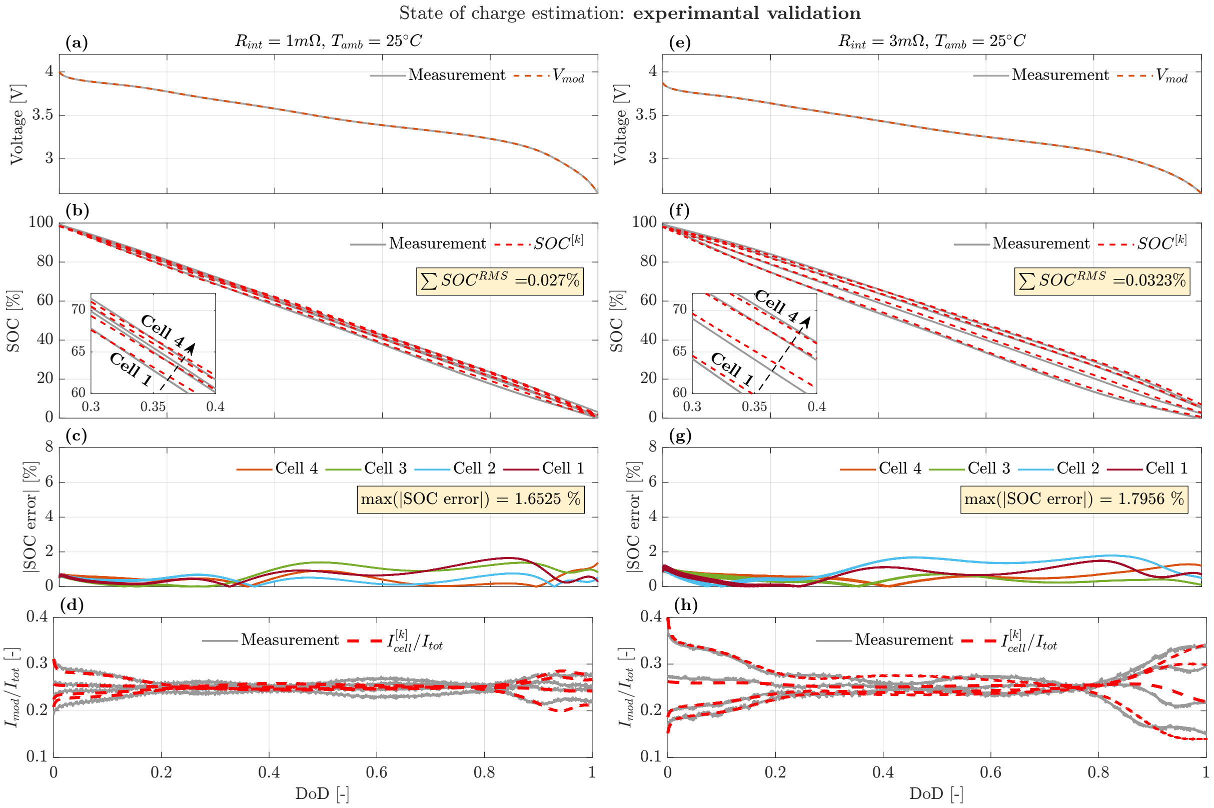

Figure 9.7: Validation of the MHE-based SOC estimation algorithm using experimental data under two different R_{int} values: $1m\Omega$ (a-c) and $3m\Omega$ (d-f) scenarios. (a)(d) Comparison of measured and estimated V_{mod}. (b)(e) SOC error for each cell. (c)(f) Comparison of measured and estimated current distribution over the Depth of Discharge (DOD).

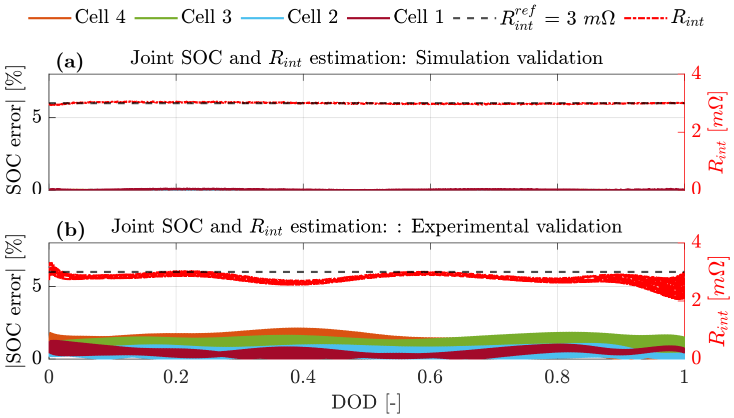

Figure 9.8: Joint SOC and R_{int} estimation results using the same data as Fig. 9.7(d-f). (a) Maximum SOC error (b) Comparison of estimated and reference R_{int} values.

9.3.1.3 Joint SOC and interconncetion resistance estimation

In the simulations presented, the interconnection resistance is assumed to be known and not estimated. In practical applications, measuring R_{int} typically requires extensive and systematic testing at the module or pack level, which can be economically prohibitive. Therefore, online estimation of R_{int} could be a practical solution for characterizing the module-level model. This approach would enable the development of advanced fault detection strategies to prevent connection issues among interconnected cells [238]. This section tackles this challenge by incorporating an additional state, R_{int}, with null dynamics (i.e. $\dot{R}_{\text{int}} = 0$), into the modulel-level model (9.5). This modification transforms the problem into a joint estimation task for both SOC and R_{int}.

Assuming a constant R_{int} across parallel branches, Fig. 9.8 (a) and (b) show preliminary estimation results using both simulated and experimental data previously presented in Fig. 9.6(a-c) and Fig. 9.7(d-f), respectively. For these estimates, R_{int} is initially set to $0m\Omega$ due to the lack of prior knowledge. The values for Q, P_0 and X_0 are maintained as in the previous sections, and the voltage covariance is consistently set at $V = 10^{-5}$ for both scenarios. As illustrated in Fig. 9.8(a), both SOC and R_{int} are accurately estimated using simulated data. The maximum SOC error and ΣSOC^{RMS} stay below 2.2% and 3.3%, respectively, throughout the discharge. Additionally, R_{int} is estimated with high accuracy, closely approximating the actual value of $3m\Omega$, as shown in Fig.9.8(b). While the addition of the R_{int} state results in a slight increase in the maximum SOC estimation error compared to previous results, the error remains within acceptable limits. Future research could focus on addressing the assumption of uniform R_{int} across parallel branches, potentially through the incorporation of temperature or current sensors within the module.

9.4 Conclusion

In summary, this paper introduces an MHE-based approach for estimating the state of charge (SOC) of individual cells within parallel-connected battery modules for battery electric vehicles (BEVs). The MHE method is selected for its capability to handle directly nonlinear dynamics and constraints. Unlike previous studies, our method accounts for cell-to-cell (CtC) variations and their effects on battery pack performance and heterogeneity, while also considering the interconnection resistance between parallel branches.

The estimation algorithm relies on a module-level ECM-based model that integrates N_p parallel cells, each of them identified at the cell-level via standard cell characterization testing procedures. We perform a nonlinear observability analysis of the module-level model under various configurations of R_{int} and N_p. Compared to existing literature, the analysis has been extended to account for the presence of interconnection resistance, SOC-dependent parameters, and varying numbers of cells. The analysis reveals that system states are observable when $R_{int} > 0$. However, estimation accuracy declines as the number of parallel cells N_p increases or R_{int} decreases. The performance of two different MHE algorithms is compared using two distinct model structures: the ODE model, which incorporates Kirchhoff's equations into the state-space model, and the DAE model, which treats Kirchhoff's laws as equality constraints in the MHE optimization problem. Results show that while both approaches offer comparable accuracy, the DAE model is more computationally efficient, making it better suited for real-time applications with limited computational resources. The proposed MHE-based method is validated using both simulated and experimental data across various current profiles and interconnection resistance scenarios. It demonstrates high accuracy, with SOC errors remaining below 1.8% in experimental data and negligible errors in simulations. Preliminary results suggest the feasibility of joint SOC and resistance estimation, providing a promising avenue for scenarios where R_{int} is unknown.

Future research will explore integrating additional measurements, such as current, voltage, or temperature, to improve estimation accuracy and relax the assumption of uniform R_{int} across parallel branches. It is important to highlight that addressing cell-to-cell (CtC) variations and their effects on module performance, heterogeneity, and aging is a crucial first step toward improving the reliability and effectiveness of charging optimization, cell balancing, and fault detection strategies.

Conclusions

This dissertation presents two primary contributions to the advancement of Battery Management Systems (BMS) for Lithium Iron Phosphate (LFP)-based and parallel-connected battery systems.

Building upon the high-fidelity CSa-ESPM developed in [9, 10], two distinct reduced-order models (ROMs) are proposed: Firstly, the POD-Galerkin method is employed to reduce the dimensionality of the original CSa-ESPM. This reduction decreases the number of state variables from 169 to just 9. Validation results, obtained by comparing both experimental data and CSa-ESPM simulations, demonstrate that the POD-based ROM accurately predicts cell voltage and electrode SOC. Additionally, the ROM successfully captures phase transition dynamics, voltage hysteresis, and path dependence effects. Secondly, the FVM is utilized to spatially discretize the CSa-ESPM model for LFP batteries. This technique substantially reduces the number of solid-phase state variables to fewer than 6, while ensuring mass conservation and avoiding the need for ad hoc snapshot matrix generation typical of the POD-Galerkin method. Experimental validation confirms that the FVM-based reduced-order CSa-ESPM provides an accurate match for both cell voltage and electrode SOC. These ROMs represent a crucial first step toward developing control-oriented, model-based strategies aimed at improving BMS algorithms for LFP-based battery systems.

Furthermore, the impact of CtC variations in parallel-connected modules is thoroughly analyzed using statistical methods. A comprehensive 54-condition full-factorial DOE was conducted on four ladder-parallel connected modules. This approach enabled the independent evaluation of how variations in module current, SOC, temperature heterogeneity, and TTSB respond to different interconnection resistances, operating temperatures, combinations of cell chemistries, and levels of aging. The feature importance analysis, based on the formulated MLR and ML models, reveals that interconnection resistance is consistently the most significant source of CtC variation. Additionally, the integration of NMC and NCA cells is feasible for future second-life applications. Simulation results demonstrate that simple MLR models are sufficient to predict module heterogeneity in battery modules. Moreover, it was demonstrated that using a high-fidelity digital twin for the battery system provides deeper insights into the understanding of the CtC effects on module responses under both short-term and long-term scenarios. Additionally, a simple cell arrangement strategy is presented to reduce CtC thermal gradients, thereby decreasing aging heterogeneities over the long term. According to simulation results, this method allows for a thermal gradient reduction of 51.8% and a consequent decrease of 5.2% in module energy loss after 500 aging cycles.

Finally, a state estimation algorithm for individual cells within parallel-connected battery configurations is formulated and validated against experimental data using the MHE technique. The algorithm demonstrates high accuracy, with SOC errors remaining below 1.8% in experimental data and exhibiting negligible errors in simulations. Preliminary results suggest the feasibility of joint SOC and resistance estimation, providing a promising avenue for scenarios where internal resistance (R_{int}) is unknown. Future research will explore integrating additional measurements, such as current, voltage, and temperature, to improve estimation accuracy and relax the assumption of uniform R_{int} across parallel branches. Addressing CtC variations and their effects on module performance, heterogeneity, and aging is a crucial first step toward improving the reliability and effectiveness of charging optimization, cell balancing, and fault detection strategies. Future research will focus on enhancing these models and algorithms to further advance BMS technologies, ultimately contributing to more reliable and efficient battery systems.

Acknowledgments

I would like to express my deepest gratitude to my Ph.D. advisor, Professor Davide Martino Raimondo, for his invaluable support and guidance throughout my doctoral journey. His wisdom, knowledge, and leadership have been instrumental in helping me overcome numerous technical challenges and have profoundly shaped my research.

A special thank you to Professor Simona Onori for the wonderful opportunity to join her research group for a year and for her exceptional guidance on my research endeavors.

I am also profoundly grateful to Anirudh Allam, Le Xu, and Gabriele Pozzato for their unwavering support and expert insights during my time at Stanford University.

My sincere thanks go to Professor Lalo Magni and Professor Giacomo Galuppini for their insightful discussions.

I would also like to extend my gratitude to all my colleagues at Labsisdin, Nikolas, Jorge, Marco, Irene, Edoardo, Paolo, Chiara, Mori, and Ayda for the enjoyable work breaks we shared and for their insightful discussions.

I extend my heartfelt appreciation to all the members of the Stanford Energy Control Lab and the friends I have made during my stay at Stanford. Their collaboration have made my journey both professionally enriching and uniquely memorable.

A big thank you to my American journey companions, Luca, Giulia, Claudia, Matteo, Gabriele, Andrea, and Pietro, for making me feel at home on the other side of the world.

Special thanks to my friends Lorenzo, Davide, Simone, Matteo B., Federico, Andrea N., Matteo O., Alberto, Andrea Z., and the entire Team Barbel. Your support has significantly contributed to my personal growth, and your presence has been fundamental in helping me overcome difficult times.

A heartfelt thank you to my family for their unwavering support throughout these years, especially during moments when problems seemed insurmountable. Your love, encouragement, and belief in me have been my greatest strength and motivation.

List of Publications

- [33] **Fasolato, S.**, and Raimondo, D. M. (2022). *Observability analysis of a li-ion cell equivalent circuit model based on interval arithmetic*, 2022 IEEE Vehicle Power and Propulsion Conference (VPPC), 1-7.
- [29] **Fasolato, S.**, Allam, A., Li, X., Lee, D., Ko, J., and Onori, S. (2022). *Reduced-order model of lithium-iron phosphate battery dynamics: A POD-Galerkin approach.* IEEE Control Systems Letters, 7, 1117-1122.
- [31] Piombo, G., **Fasolato, S.**, Heymer, R., Hidalgo, M., Niri, M. N., Onori, S., Marco, J. (2024). *Unveiling the performance impact of module level features on parallel-connected lithium-ion cells via explainable machine learning techniques on a full factorial design of experiments*, Journal of Energy Storage, 84, 110783.
- [8] Piombo, G., **Fasolato, S.**, Heymer, R., Hidalgo, M. F., Niri, M. F., Raimondo, D. M., Marco, J., and Onori, S. (2024). *Full factorial design of experiments dataset for parallel-connected lithium-ion cells imbalanced performance investigation.* Data in Brief, 53, 110227.
- [207] Moy, K., Khan, M. A., **Fasolato, S.**, and Pozzato, G., Allam, A. and Onori, S. (2024) *Second-life lithium-ion battery aging dataset based on grid storage cycling.* Data in Brief, 57, 111046.
- [121] **Fasolato, S.**, Blasuttigh, N., Galuppini, G., and Raimondo, D. M. (2025). *A Dataset for Large Prismatic Lithium-Ion Battery Cells (CALB L148N58A): Comprehensive Characterization and Real-World Driving Cycles.* Data in Brief, 111301.
- [30] Xu, L., **Fasolato, S.**, and Onori, S. (2024). *Finite-volume method and observability analysis for core-shell enhanced single particle model for lithium iron phosphate batteries.* IEEE 2024 Conference on Decision and Control (CDC), **Accepted**.
- [27] **Fasolato, S.**, Allam, A., Onori, S., and Raimondo, D. M. (2024). *Cell-to-Cell Heterogeneities and Module Configurations analysis in Parallel-Connected Battery Modules via physics-based modeling*, Journal of Energy Storage, **Submitted**.
- [32] **Fasolato, S.**, Acquarone, M. and Raimondo, D. M. (2024). *States estimation for parallel-connected battery module: a moving horizon approach*, IEEE Transaction on Control System Technology, **Submitted**

Bibliography

[1] C. R. Birkl, M. R. Roberts, E. McTurk, P. G. Bruce, and D. A. Howey, “Degradation diagnostics for lithium ion cells,” Journal of Power Sources, vol. 341, pp. 373–386, 2017.

[2] M. T. Lawder, B. Suthar, P. W. Northrop, S. De, C. M. Hoff, O. Leitermann, M. L. Crow, S. Santhanagopalan, and V. R. Subramanian, “Battery energy storage system (bess) and battery management system (bms) for grid-scale applications,” Proceedings of the IEEE, vol. 102, no. 6, pp. 1014–1030, 2014.

[3] V. Ramadesigan, P. W. Northrop, S. De, S. Santhanagopalan, R. D. Braatz, and V. R. Subramanian, “Modeling and simulation of lithium-ion batteries from a systems engineering perspective,” Journal of the electrochemical society, vol. 159, no. 3, p. R31, 2012.

[4] H. Tu, S. Moura, Y. Wang, and H. Fang, “Integrating physics-based modeling with machine learning for lithium-ion batteries,” Applied energy, vol. 329, p. 120289, 2023.

[5] L. Pulvirenti, “Development of innovative methodologies to support the design of connected and electrified vehicles,” 2023.

[6] Y. Li, D. Karunathilake, D. M. Vilathgamuwa, Y. Mishra, T. W. Farrell, C. Zou, et al., “Model order reduction techniques for physics-based lithium-ion battery management: A survey,” IEEE Industrial Electronics Magazine, vol. 16, no. 3, pp. 36–51, 2021.

[7] S. Onori, “Stanford energy control lab,” https://onorilab.stanford.edu/research/facilities-and-equipment.

[8] G. Piombo, S. Fasolato, R. Heymer, M. F. Hidalgo, M. F. Niri, D. M. Raimondo, J. Marco, and S. Onori, “Full factorial design of experiments dataset for parallel-connected lithium-ion cells imbalanced performance investigation,” Data in Brief, vol. 53, p. 110227, 2024.

[9] G. Pozzato, A. Takahashi, X. Li, D. Lee, J. Ko, and S. Onori, “Addressing the surface concentration discontinuity of the core-shell model for lithium iron phosphate batteries,” Journal of the Electrochemical Society, vol. 169, no. 10, p. 100526, 2022.

[10] ——, "Core-shell enhanced single particle model for lithium iron phosphate batteries: model formulation and analysis of numerical solutions," Journal of the Electrochemical Society, vol. 169, no. 6, p. 063510, 2022.

[11] M. Muratori, M. Alexander, D. Arent, M. Bazilian, P. Cazzola, E. M. Dede, J. Farrell, C. Gearhart, D. Greene, A. Jenn, et al., "The rise of electric vehicles—2020 status and future expectations," Progress in Energy, vol. 3, no. 2, p. 022002, 2021.

[12] D. Choi, N. Shamim, A. Crawford, Q. Huang, C. K. Vartanian, V. V. Viswanathan, M. D. Paiss, M. J. E. Alam, D. M. Reed, and V. L. Sprenkle, "Li-ion battery technology for grid application," Journal of Power Sources, vol. 511, p. 230419, 2021.

[13] J. Wen, D. Zhao, and C. Zhang, "An overview of electricity powered vehicles: Lithium-ion battery energy storage density and energy conversion efficiency," Renewable Energy, vol. 162, pp. 1629–1648, 2020.

[14] L. Mauler, F. Duffner, W. G. Zeier, and J. Leker, "Battery cost forecasting: a review of methods and results with an outlook to 2050," Energy & Environmental Science, vol. 14, no. 9, pp. 4712–4739, 2021.

[15] F. Calvão, C. E. A. Mcdonald, and M. Bolay, "Cobalt mining and the corporate outsourcing of responsibility in the democratic republic of congo," The Extractive Industries and Society, vol. 8, no. 4, p. 100884, 2021.

[16] V. Kumar, "Lithium ion battery supply chain technology development and investment opportunities," Benchmark Minerval Intelligence, 2020.

[17] Federal Consortium for Advanced Batteries, "National blueprint for lithium batteries," Vehicle Technologies Office, 2021.

[18] X. Li, M. Xiao, S.-Y. Choe, and W. T. Joe, "Modeling and analysis of lifepo4/carbon battery considering two-phase transition during galvanostatic charging/discharging," Electrochimica Acta, vol. 155, pp. 447–457, 2015.

[19] "Annual battery report," Volta Foundation, 2023.

[20] E. Catenaro, D. M. Rizzo, and S. Onori, "Experimental analysis and analytical modeling of enhanced-ragone plot," Applied Energy, vol. 291, p. 116473, 2021.

[21] A. Yamada, H. Koizumi, N. Sonoyama, and R. Kanno, "Phase change in li x fepo4," Electrochemical and Solid-State Letters, vol. 8, no. 8, p. A409, 2005.

[22] Y. Chen, Y. Kang, Y. Zhao, L. Wang, J. Liu, Y. Li, Z. Liang, X. He, X. Li, N. Tavajohi, et al., "A review of lithium-ion battery safety concerns: The issues, strategies, and testing standards," Journal of Energy Chemistry, vol. 59, pp. 83–99, 2021.

[23] G. L. Plett, Battery management systems, Volume I: Battery modeling. Artech House, 2015.

[24] S. F. Schuster, M. J. Brand, P. Berg, M. Gleissenberger, and A. Jossen, "Lithium-ion cell-to-cell variation during battery electric vehicle operation," Journal of Power Sources, vol. 297, pp. 242–251, 2015.

[25] A. Allam and S. Onori, "Characterization of aging propagation in lithium-ion cells based on an electrochemical model," in 2016 American Control Conference (ACC). IEEE, 2016, pp. 3113–3118.

[26] ——, "Exploring the dependence of cell aging dynamics on thermal gradient in battery modules: A pde-based time scale separation approach," in 2019 18th European Control Conference (ECC). IEEE, 2019, pp. 2380–2385.

[27] S. Fasolato, A. Allam, S. Onori, and D. M. Raimondo, "Cell-to-cell heterogeneities and module configurations analysis in parallel-connected battery modules via physics-based modeling," Journal of The Energy Storage, p. Submitted, 2024.

[28] G. Pozzato, X. Li, D. Lee, J. Ko, and S. Onori, "Accelerating the transition to cobalt-free batteries: a hybrid model for lifepo4/graphite chemistry," npj Computational Materials, vol. 10, no. 1, p. 14, 2024.

[29] S. Fasolato, A. Allam, X. Li, D. Lee, J. Ko, and S. Onori, "Reduced-order model of lithium-iron phosphate battery dynamics: A pod-galerkin approach," IEEE Control Systems Letters, vol. 7, pp. 1117–1122, 2022.

[30] L. Xu, S. Fasolato, and S. Onori, "Finite-volume method and observability analysis for core-shell enhanced single particle model for lithium iron phosphate batteries," in 2024 Conference on Decision and Control (CDC). IEEE, 2024, p. Accepted.

[31] G. Piombo, S. Fasolato, R. Heymer, M. Hidalgo, M. F. Niri, S. Onori, and J. Marco, "Unveiling the performance impact of module level features on parallel-connected lithium-ion cells via explainable machine learning techniques on a full factorial design of experiments," Journal of Energy Storage, vol. 84, p. 110783, 2024.

[32] S. Fasolato, M. Acquarone, and D. M. Raimondo, "States estimation for parallel-connected battery module: a moving horizon approach," IEEE Transaction on Control System Technology, p. Submitted, 2024.

[33] S. Fasolato and D. M. Raimondo, "Observability analysis of a li-ion cell equivalent circuit model based on interval arithmetic," in 2022 IEEE Vehicle Power and Propulsion Conference (VPPC). IEEE, 2022, pp. 1–7.

[34] M. E. V. Team et al., "A guide to understanding battery specifications," Academia.edu, 2008.

[35] J. S. Edge, S. O'Kane, R. Prosser, N. D. Kirkaldy, A. N. Patel, A. Hales, A. Ghosh, W. Ai, J. Chen, J. Yang, et al., "Lithium ion battery degradation: what you need to know," Physical Chemistry Chemical Physics, vol. 23, no. 14, pp. 8200–8221, 2021.

[36] L. Lu, X. Han, J. Li, J. Hua, and M. Ouyang, "A review on the key issues for lithium-ion battery management in electric vehicles," Journal of power sources, vol. 226, pp. 272–288, 2013.

[37] M. Doyle, T. F. Fuller, and J. Newman, "Modeling of galvanostatic charge and discharge of the lithium/polymer/insertion cell," Journal of the Electrochemical society, vol. 140, no. 6, p. 1526, 1993.

[38] S. K. Rahimian, S. Rayman, and R. E. White, "Extension of physics-based single particle model for higher charge–discharge rates," Journal of Power Sources, vol. 224, pp. 180–194, 2013.

[39] V. Srinivasan and J. Newman, "Discharge model for the lithium iron-phosphate electrode," Journal of the Electrochemical Society, vol. 151, no. 10, p. A1517, 2004.

[40] S. Shi, J. Gao, Y. Liu, Y. Zhao, Q. Wu, W. Ju, C. Ouyang, and R. Xiao, "Multi-scale computation methods: Their applications in lithium-ion battery research and development," Chinese Physics B, vol. 25, no. 1, p. 018212, 2015.

[41] K. Leung and J. L. Budzien, "Ab initio molecular dynamics simulations of the initial stages of solid–electrolyte interphase formation on lithium ion battery graphitic anodes," Physical Chemistry Chemical Physics, vol. 12, no. 25, pp. 6583–6586, 2010.

[42] A. Van der Ven and G. Ceder, "Lithium diffusion in layered li x coo2," Electrochemical and Solid-State Letters, vol. 3, no. 7, p. 301, 2000.

[43] R. Malik, D. Burch, M. Bazant, and G. Ceder, "Particle size dependence of the ionic diffusivity," Nano letters, vol. 10, no. 10, pp. 4123–4127, 2010.

[44] F. Naseri, S. Gil, C. Barbu, E. Çetkin, G. Yarimca, A. Jensen, P. G. Larsen, and C. Gomes, "Digital twin of electric vehicle battery systems: Comprehensive review of the use cases, requirements, and platforms," Renewable and Sustainable Energy Reviews, vol. 179, p. 113280, 2023.

[45] W. Li, M. Rentemeister, J. Badeda, D. Jöst, D. Schulte, and D. U. Sauer, "Digital twin for battery systems: Cloud battery management system with online state-of-charge and state-of-health estimation," Journal of energy storage, vol. 30, p. 101557, 2020.

[46] T. Weaver, A. Allam, and S. Onori, "A novel lithium-ion battery pack modeling framework-series-connected case study," in 2020 American control conference (ACC). IEEE, 2020, pp. 365–372.

[47] Y. Zheng, Y. Che, X. Hu, X. Sui, D.-I. Stroe, and R. Teodorescu, "Thermal state monitoring of lithium-ion batteries: Progress, challenges, and opportunities," Progress in Energy and Combustion Science, vol. 100, p. 101120, 2024.

[48] J. M. Reniers, G. Mulder, and D. A. Howey, "Review and performance comparison of mechanical-chemical degradation models for lithium-ion batteries," Journal of The Electrochemical Society, vol. 166, no. 14, pp. A3189–A3200, 2019.

[49] S. E. O'Kane, W. Ai, G. Madabattula, D. Alonso-Alvarez, R. Timms, V. Sulzer, J. S. Edge, B. Wu, G. J. Offer, and M. Marinescu, "Lithium-ion battery degradation: how to model it," Physical Chemistry Chemical Physics, vol. 24, no. 13, pp. 7909–7922, 2022.

[50] Q.-Q. Yu, R. Xiong, L.-Y. Wang, and C. Lin, "A comparative study on open circuit voltage models for lithium-ion batteries," Chinese Journal of Mechanical Engineering, vol. 31, pp. 1–8, 2018.

[51] J. Newman and N. P. Balsara, Electrochemical systems. John Wiley & Sons, 2021.

[52] T. R. Tanim, C. D. Rahn, and C.-Y. Wang, "A temperature dependent, single particle, lithium ion cell model including electrolyte diffusion," Journal of Dynamic Systems, Measurement, and Control, vol. 137, no. 1, p. 011005, 2015.

[53] X. Han, M. Ouyang, L. Lu, and J. Li, "Simplification of physics-based electrochemical model for lithium ion battery on electric vehicle. part i: Diffusion simplification and single particle model," Journal of Power Sources, vol. 278, pp. 802–813, 2015.

[54] ——, "Simplification of physics-based electrochemical model for lithium ion battery on electric vehicle. part ii: Pseudo-two-dimensional model simplification and state of charge estimation," Journal of Power Sources, vol. 278, pp. 814–825, 2015.

[55] E. Prada, D. Di Domenico, Y. Creff, J. Bernard, V. Sauvant-Moynot, and F. Huet, "A simplified electrochemical and thermal aging model of lifepo4-graphite li-ion batteries: Power and capacity fade simulations," Journal of The Electrochemical Society, vol. 160, no. 4, p. A616, 2013.

[56] M. Safari, M. Farkhondeh, M. Pritzker, M. Fowler, T. Han, and S.-k. Chen, "Simulation of lithium iron phosphate lithiation/delithiation: Limitations of the core–shell model," Electrochimica Acta, vol. 115, pp. 352–357, 2014.

[57] W. E. Schiesser, The numerical method of lines: integration of partial differential equations. Elsevier, 2012.

[58] A. N. F. Versypt and R. D. Braatz, "Analysis of finite difference discretization schemes for diffusion in spheres with variable diffusivity," Computers & chemical engineering, vol. 71, pp. 241–252, 2014.

[59] C. Canuto, M. Y. Hussaini, A. Quarteroni, and T. A. Zang, Spectral methods: evolution to complex geometries and applications to fluid dynamics. Springer Science & Business Media, 2007.

[60] R. Drummond, D. A. Howey, and S. R. Duncan, "Low-order mathematical modelling of electric double layer supercapacitors using spectral methods," Journal of Power Sources, vol. 277, pp. 317–328, 2015.

[61] G. Fan, X. Li, and M. Canova, "A reduced-order electrochemical model of li-ion batteries for control and estimation applications," IEEE Transactions on Vehicular Technology, vol. 67, no. 1, pp. 76–91, 2017.

[62] V. R. Subramanian, V. D. Diwakar, and D. Tapriyal, "Efficient macro-micro scale coupled modeling of batteries," Journal of The Electrochemical Society, vol. 152, no. 10, p. A2002, 2005.

[63] J. C. Forman, S. Bashash, J. L. Stein, and H. K. Fathy, "Reduction of an electrochemistry-based li-ion battery model via quasi-linearization and pade approximation," Journal of the Electrochemical Society, vol. 158, no. 2, p. A93, 2010.

[64] L. Li, Y. Ren, K. O'Regan, U. R. Koleti, E. Kendrick, W. D. Widanage, and J. Marco, "Lithium-ion battery cathode and anode potential observer based on reduced-order electrochemical single particle model," Journal of Energy Storage, vol. 44, p. 103324, 2021.

[65] G. Fan, K. Pan, and M. Canova, "A comparison of model order reduction techniques for electrochemical characterization of lithium-ion batteries," in 2015 54th IEEE Conference on Decision and Control (CDC). IEEE, 2015, pp. 3922–3931.

[66] M. Torchio, L. Magni, R. B. Gopaluni, R. D. Braatz, and D. M. Raimondo, "Lionsimba: a matlab framework based on a finite volume model suitable for li-ion battery design, simulation, and control," Journal of The Electrochemical Society, vol. 163, no. 7, p. A1192, 2016.

[67] W. Li, J. Zhang, F. Ringbeck, D. Jöst, L. Zhang, Z. Wei, and D. U. Sauer, "Physics-informed neural networks for electrode-level state estimation in lithium-ion batteries," Journal of Power Sources, vol. 506, p. 230034, 2021.

[68] L. Xu, J. Cooper, A. Allam, and S. Onori, "Comparative analysis of numerical methods for lithium-ion battery electrochemical modeling," Journal of The Electrochemical Society, vol. 170, no. 12, p. 120525, 2023.

[69] Y. Zeng, P. Albertus, R. Klein, N. Chaturvedi, A. Kojic, M. Z. Bazant, and J. Christensen, "Efficient conservative numerical schemes for 1d nonlinear spherical diffusion equations with applications in battery modeling," Journal of The Electrochemical Society, vol. 160, no. 9, p. A1565, 2013.

[70] L. N. Trefethen, Spectral methods in MATLAB. SIAM, 2000.

[71] V. Ramadesigan, V. Boovaragavan, J. C. Pirkle, and V. R. Subramanian, "Efficient reformulation of solid-phase diffusion in physics-based lithium-ion battery models," Journal of The Electrochemical Society, vol. 157, no. 7, p. A854, 2010.

[72] T.-S. Dao, C. P. Vyasarayani, and J. McPhee, "Simplification and order reduction of lithium-ion battery model based on porous-electrode theory," Journal of Power Sources, vol. 198, pp. 329–337, 2012.

[73] M. A. Kehs, M. D. Beeney, and H. K. Fathy, "Computational efficiency of solving the dfn battery model using descriptor form with legendre polynomials and galerkin projections," in 2014 American Control Conference. IEEE, 2014, pp. 260–267.

[74] P. W. Northrop, V. Ramadesigan, S. De, and V. R. Subramanian, "Coordinate transformation, orthogonal collocation, model reformulation and simulation of electrochemical-thermal behavior of lithium-ion battery stacks," Journal of The Electrochemical Society, vol. 158, no. 12, p. A1461, 2011.

[75] A. Bizeray, S. Duncan, and D. Howey, "Advanced battery management systems using fast electrochemical modelling," IET Hybrid and Electric Vehicles Conference, 2013.

[76] A. M. Bizeray, S. Zhao, S. R. Duncan, and D. A. Howey, "Lithium-ion battery thermal-electrochemical model-based state estimation using orthogonal collocation and a modified extended kalman filter," Journal of Power Sources, vol. 296, pp. 400–412, 2015.

[77] D. M. Ajiboye, J. W. Kimball, R. G. Landers, and J. Park, "Computationally efficient battery model for microgrid applications using the chebyshev spectral method," Computers & Chemical Engineering, vol. 153, p. 107420, 2021.

[78] P. Schlatter, "Spectral methods," Lecture Notes KTH, 2009.

[79] J. Marcicki, M. Canova, A. T. Conlisk, and G. Rizzoni, "Design and parametrization analysis of a reduced-order electrochemical model of graphite/lifepo4 cells for soc/soh estimation," Journal of Power Sources, vol. 237, pp. 310–324, 2013.

[80] J. L. Lee, A. Chemistruck, and G. L. Plett, "One-dimensional physics-based reduced-order model of lithium-ion dynamics," Journal of Power Sources, vol. 220, pp. 430–448, 2012.

[81] A. Rodriguez, G. L. Plett, and M. S. Trimboli, "Comparing four model-order reduction techniques, applied to lithium-ion battery-cell internal electrochemical transfer functions," ETransportation, vol. 1, p. 100009, 2019.

[82] L. Cai and R. E. White, "Reduction of model order based on proper orthogonal decomposition for lithium-ion battery simulations," Journal of the Electrochemical Society, vol. 156, no. 3, p. A154, 2008.

[83] A. C. Antoulas, D. C. Sorensen, and S. Gugercin, “A survey of model reduction methods for large-scale systems,” Contemporary mathematics, vol. 280, pp. 193–220, 2001.

[84] B. Moore, “Principal component analysis in linear systems: Controllability, observability, and model reduction,” IEEE transactions on automatic control, vol. 26, no. 1, pp. 17–32, 1981.

[85] W. H. Schilders, H. A. Van der Vorst, and J. Rommes, Model order reduction: theory, research aspects and applications. Springer, 2008, vol. 13.

[86] X. Lin, H. E. Perez, S. Mohan, J. B. Siegel, A. G. Stefanopoulou, Y. Ding, and M. P. Castanier, “A lumped-parameter electro-thermal model for cylindrical batteries,” Journal of Power Sources, vol. 257, pp. 1–11, 2014.

[87] M. Farag, H. Sweity, M. Fleckenstein, and S. Habibi, “Combined electrochemical, heat generation, and thermal model for large prismatic lithium-ion batteries in real-time applications,” Journal of Power Sources, vol. 360, pp. 618–633, 2017.

[88] X. Cui, J. Zeng, H. Zhang, J. Yang, J. Qiao, J. Li, and W. Li, “Optimization of the lumped parameter thermal model for hard-cased li-ion batteries,” Journal of Energy Storage, vol. 32, p. 101758, 2020.

[89] S.-C. Chen, Y.-Y. Wang, and C.-C. Wan, “Thermal analysis of spirally wound lithium batteries,” Journal of the Electrochemical Society, vol. 153, no. 4, p. A637, 2006.

[90] S. Chen, C. Wan, and Y. Wang, “Thermal analysis of lithium-ion batteries,” Journal of power sources, vol. 140, no. 1, pp. 111–124, 2005.

[91] A. Samba, N. Omar, H. Gualous, Y. Firouz, P. Van den Bossche, J. Van Mierlo, and T. I. Boubekeur, “Development of an advanced two-dimensional thermal model for large size lithium-ion pouch cells,” Electrochimica Acta, vol. 117, pp. 246–254, 2014.

[92] D. Bernardi, E. Pawlikowski, and J. Newman, “A general energy balance for battery systems,” Journal of the electrochemical society, vol. 132, no. 1, p. 5, 1985.

[93] A. Swiderska-Mocek, E. Rudnicka, and A. Lewandowski, “Temperature coefficients of li-ion battery single electrode potentials and related entropy changes–revisited,” Physical Chemistry Chemical Physics, vol. 21, no. 4, pp. 2115–2120, 2019.

[94] K. Jalkanen, T. Aho, and K. Vuorilehto, “Entropy change effects on the thermal behavior of a lifepo4/graphite lithium-ion cell at different states of charge,” Journal of Power Sources, vol. 243, pp. 354–360, 2013.

[95] L. O. Valøen and J. N. Reimers, “Transport properties of lipf6-based li-ion battery electrolytes,” Journal of The Electrochemical Society, vol. 152, no. 5, p. A882, 2005.

[96] C.-H. Chen, F. B. Planella, K. O'regan, D. Gastol, W. D. Widanage, and E. Kendrick, "Development of experimental techniques for parameterization of multi-scale lithium-ion battery models," Journal of The Electrochemical Society, vol. 167, no. 8, p. 080534, 2020.

[97] S. Grolleau, A. Delaille, H. Gualous, P. Gyan, R. Revel, J. Bernard, E. Redondo-Iglesias, J. Peter, and S. Network, "Calendar aging of commercial graphite/lifepo4 cell–predicting capacity fade under time dependent storage conditions," Journal of Power Sources, vol. 255, pp. 450–458, 2014.

[98] E. Redondo-Iglesias, P. Venet, and S. Pelissier, "Eyring acceleration model for predicting calendar ageing of lithium-ion batteries," Journal of Energy Storage, vol. 13, pp. 176–183, 2017.

[99] M. Petit, E. Prada, and V. Sauvant-Moynot, "Development of an empirical aging model for li-ion batteries and application to assess the impact of vehicle-to-grid strategies on battery lifetime," Applied energy, vol. 172, pp. 398–407, 2016.

[100] M. Naumann, F. B. Spingler, and A. Jossen, "Analysis and modeling of cycle aging of a commercial lifepo4/graphite cell," Journal of Power Sources, vol. 451, p. 227666, 2020.

[101] J. Wang, P. Liu, J. Hicks-Garner, E. Sherman, S. Soukiazian, M. Verbrugge, H. Tataria, J. Musser, and P. Finamore, "Cycle-life model for graphite-lifepo4 cells," Journal of power sources, vol. 196, no. 8, pp. 3942–3948, 2011.

[102] A. Cordoba-Arenas, S. Onori, Y. Guezennec, and G. Rizzoni, "Capacity and power fade cycle-life model for plug-in hybrid electric vehicle lithium-ion battery cells containing blended spinel and layered-oxide positive electrodes," Journal of Power Sources, vol. 278, pp. 473–483, 2015.

[103] X. Hu, L. Xu, X. Lin, and M. Pecht, "Battery lifetime prognostics," Joule, vol. 4, no. 2, pp. 310–346, 2020.

[104] M. Safari, M. Morcrette, A. Teyssot, and C. Delacourt, "Multimodal physics-based aging model for life prediction of li-ion batteries," Journal of The Electrochemical Society, vol. 156, no. 3, p. A145, 2008.

[105] P. Arora, M. Doyle, and R. E. White, "Mathematical modeling of the lithium deposition overcharge reaction in lithium-ion batteries using carbon-based negative electrodes," Journal of The Electrochemical Society, vol. 146, no. 10, p. 3543, 1999.

[106] X.-G. Yang, S. Ge, T. Liu, Y. Leng, and C.-Y. Wang, "A look into the voltage plateau signal for detection and quantification of lithium plating in lithium-ion cells," Journal of Power Sources, vol. 395, pp. 251–261, 2018.

[107] S. E. O'Kane, I. D. Campbell, M. W. Marzook, G. J. Offer, and M. Marinescu, "Physical origin of the differential voltage minimum associated with lithium plating in li-ion batteries," Journal of The Electrochemical Society, vol. 167, no. 9, p. 090540, 2020.

[108] X. Zhang, W. Shyy, and A. M. Sastry, "Numerical simulation of intercalation-induced stress in li-ion battery electrode particles," Journal of the Electrochemical Society, vol. 154, no. 10, p. A910, 2007.

[109] R. Deshpande, M. Verbrugge, Y.-T. Cheng, J. Wang, and P. Liu, "Battery cycle life prediction with coupled chemical degradation and fatigue mechanics," Journal of the Electrochemical Society, vol. 159, no. 10, p. A1730, 2012.

[110] R. Drummond, L. D. Couto, and D. Zhang, "Resolving kirchhoff's laws for parallel li-ion battery pack state-estimators," IEEE Trans. Control Syst., vol. 30, no. 5, pp. 2220–2227, 2021.

[111] C. F. Lopez, J. A. Jeevarajan, and P. P. Mukherjee, "Experimental analysis of thermal runaway and propagation in lithium-ion battery modules," Journal of the electrochemical society, vol. 162, no. 9, p. A1905, 2015.

[112] X. Lin, H. E. Perez, J. B. Siegel, and A. G. Stefanopoulou, "Robust estimation of battery system temperature distribution under sparse sensing and uncertainty," IEEE Transactions on Control Systems Technology, vol. 28, no. 3, pp. 753–765, 2019.

[113] Z. Guo, J. Xu, X. Wang, and X. Mei, "Fast multilayer temperature distribution estimation for lithium-ion battery pack," ETransportation, vol. 18, p. 100266, 2023.

[114] J. P. Christophersen, "Battery test manual for electric vehicles, revision 3," Idaho National Lab.(INL), Idaho Falls, ID (United States), Tech. Rep., 2015.

[115] A. Barai, K. Uddin, M. Dubarry, L. Somerville, A. McGordon, P. Jennings, and I. Bloom, "A comparison of methodologies for the non-invasive characterisation of commercial li-ion cells," Progress in Energy and Combustion Science, vol. 72, pp. 1–31, 2019.

[116] W. Li, I. Demir, D. Cao, D. Jöst, F. Ringbeck, M. Junker, and D. U. Sauer, "Data-driven systematic parameter identification of an electrochemical model for lithium-ion batteries with artificial intelligence," Energy Storage Materials, vol. 44, pp. 557–570, 2022.

[117] L. Xu, X. Lin, Y. Xie, and X. Hu, "Enabling high-fidelity electrochemical p2d modeling of lithium-ion batteries via fast and non-destructive parameter identification," Energy Storage Materials, vol. 45, pp. 952–968, 2022.

[118] Z. Deng, X. Hu, X. Lin, Y. Che, L. Xu, and W. Guo, “Data-driven state of charge estimation for lithium-ion battery packs based on gaussian process regression,” Energy, vol. 205, p. 118000, 2020.

[119] K. A. Severson, P. M. Attia, N. Jin, N. Perkins, B. Jiang, Z. Yang, M. H. Chen, M. Aykol, P. K. Herring, D. Fraggedakis, et al., “Data-driven prediction of battery cycle life before capacity degradation,” Nature Energy, vol. 4, no. 5, pp. 383–391, 2019.

[120] E. project, https://www.ecomobility-project.eu/.

[121] S. Fasolato, N. Blasuttigh, G. Galuppini, and D. M. Raimondo, “A dataset for large prismatic lithium-ion battery cells (calb l148n58a): Comprehensive characterization and real-world driving cycles,” Data in Brief, p. 111301, 2025.

[122] CALB, “Specification of product: Lithium-ion rechargeable cell. model: L148n58.”

[123] L. Chem, “Product specification: Rechargeable lithium ion battery. model: Inr21700 m50t 18.2wh,” https://www.batteryspace.com/prod-specs/11514.pdf.

[124] Samsung, “Specification of product: Lithium-ion rechargeable cell. model: Inr21700-50e,” https://www.batteryspace.com/prod-specs/7015-INR21700-50E.pdf.

[125] S. Ha, G. Pozzato, and S. Onori, “Electrochemical characterization tools for lithium-ion batteries,” Journal of Solid State Electrochemistry, vol. 28, no. 3, pp. 1131–1157, 2024.

[126] A. Barai, K. Uddin, W. D. Widanage, A. McGordon, and P. Jennings, “A study of the influence of measurement timescale on internal resistance characterisation methodologies for lithium-ion cells,” Scientific reports, vol. 8, no. 1, p. 21, 2018.

[127] W. D. Widanage, A. Barai, G. Chouchelamane, K. Uddin, A. McGordon, J. Marco, and P. Jennings, “Design and use of multisine signals for li-ion battery equivalent circuit modelling. part 1: Signal design,” J. Power Sources, vol. 324, pp. 70–78, 2016.

[128] G. Pozzato, A. Allam, and S. Onori, “Lithium-ion battery aging dataset based on electric vehicle real-driving profiles,” Data in brief, vol. 41, p. 107995, 2022.

[129] M. Ecker, T. K. D. Tran, P. Dechent, S. Käbitz, A. Warnecke, and D. U. Sauer, “Parameterization of a physico-chemical model of a lithium-ion battery: I. determination of parameters,” Journal of The Electrochemical Society, vol. 162, no. 9, p. A1836, 2015.

[130] E. Miguel, G. L. Plett, M. S. Trimboli, L. Oca, U. Iraola, and E. Bekaert, “Review of computational parameter estimation methods for electrochemical models,” Journal of Energy Storage, vol. 44, p. 103388, 2021.

[131] A. M. Bizeray, J.-H. Kim, S. R. Duncan, and D. A. Howey, "Identifiability and parameter estimation of the single particle lithium-ion battery model," IEEE Transactions on Control Systems Technology, vol. 27, no. 5, pp. 1862–1877, 2018.

[132] Z. Chu, G. L. Plett, M. S. Trimboli, and M. Ouyang, "A control-oriented electrochemical model for lithium-ion battery, part i: Lumped-parameter reduced-order model with constant phase element," Journal of Energy Storage, vol. 25, p. 100828, 2019.

[133] C. Edouard, M. Petit, C. Forgez, J. Bernard, and R. Revel, "Parameter sensitivity analysis of a simplified electrochemical and thermal model for li-ion batteries aging," Journal of Power Sources, vol. 325, pp. 482–494, 2016.

[134] X. Zeng, L. Xu, Z. Deng, F. Feng, and X. Hu, "Global sensitivity analysis of battery single particle model parameters," in 2019 IEEE Vehicle Power and Propulsion Conference (VPPC). IEEE, 2019, pp. 1–6.

[135] W. Li, D. Cao, D. Jöst, F. Ringbeck, M. Kuipers, F. Frie, and D. U. Sauer, "Parameter sensitivity analysis of electrochemical model-based battery management systems for lithium-ion batteries," Applied Energy, vol. 269, p. 115104, 2020.

[136] A. U. Schmid, M. Kurka, and K. P. Birke, "Reproducibility of li-ion cell reassembling processes and their influence on coin cell aging," Journal of Energy Storage, vol. 24, p. 100732, 2019.

[137] K. Tang, X. Yu, J. Sun, H. Li, and X. Huang, "Kinetic analysis on lifepo4 thin films by cv, gitt, and eis," Electrochimica Acta, vol. 56, no. 13, pp. 4869–4875, 2011.

[138] C. Julien, A. Mauger, A. Vijh, K. Zaghib, C. Julien, A. Mauger, A. Vijh, and K. Zaghib, Lithium batteries. Springer, 2016.

[139] N. Lin, X. Xie, R. Schenkendorf, and U. Krewer, "Efficient global sensitivity analysis of 3d multiphysics model for li-ion batteries," Journal of The Electrochemical Society, vol. 165, no. 7, p. A1169, 2018.

[140] A. Saltelli, M. Ratto, T. Andres, F. Campolongo, J. Cariboni, D. Gatelli, M. Saisana, and S. Tarantola, Global sensitivity analysis: the primer. John Wiley & Sons, 2008.

[141] M. A. Khan, V. Azimi, and S. Onori, "Global sensitivity analysis of aging parameters for a lithium-ion battery cell using optimal charging profiles," in 2021 IEEE Conference on Control Technology and Applications (CCTA). IEEE, 2021, pp. 234–239.

[142] A. v. van Griensven, T. Meixner, S. Grunwald, T. Bishop, M. Diluzio, and R. Srinivasan, "A global sensitivity analysis tool for the parameters of multi-variable catchment models," Journal of hydrology, vol. 324, no. 1-4, pp. 10–23, 2006.

[143] F. Campolongo, J. Cariboni, and A. Saltelli, "An effective screening design for sensitivity analysis of large models," Environmental modelling & software, vol. 22, no. 10, pp. 1509–1518, 2007.

[144] A. Allam and S. Onori, "Online capacity estimation for lithium-ion battery cells via an electrochemical model-based adaptive interconnected observer," IEEE Transactions on Control Systems Technology, vol. 29, no. 4, pp. 1636–1651, 2020.

[145] M. Andersson, M. Streb, J. Y. Ko, V. L. Klass, M. Klett, H. Ekström, M. Johansson, and G. Lindbergh, "Parametrization of physics-based battery models from input–output data: a review of methodology and current research," Journal of Power Sources, vol. 521, p. 230859, 2022.

[146] S. Lee, P. Mohtat, J. B. Siegel, A. G. Stefanopoulou, J.-W. Lee, and T.-K. Lee, "Estimation error bound of battery electrode parameters with limited data window," IEEE Transactions on Industrial Informatics, vol. 16, no. 5, pp. 3376–3386, 2019.

[147] S. Lee, J. B. Siegel, A. G. Stefanopoulou, J.-W. Lee, and T.-K. Lee, "Electrode state of health estimation for lithium ion batteries considering half-cell potential change due to aging," Journal of The Electrochemical Society, vol. 167, no. 9, p. 090531, 2020.

[148] G. Pozzato and S. Onori, "Combining physics-based and machine learning methods to accelerate innovation in sustainable transportation and beyond: a control perspective," in 2023 American Control Conference (ACC). IEEE, 2023, pp. 640–653.

[149] A. Allam and S. Onori, "An interconnected observer for concurrent estimation of bulk and surface concentration in the cathode and anode of a lithium-ion battery," IEEE Transactions on Industrial Electronics, vol. 65, no. 9, pp. 7311–7321, 2018.

[150] V. Srinivasan and J. Newman, "Existence of path-dependence in the lifepo4 electrode," Electrochemical and solid-state letters, vol. 9, no. 3, p. A110, 2006.

[151] J. Stefan, "Über die theorie der eisbildung, insbesondere über die eisbildung im polarmeere," Annalen der Physik, vol. 278, no. 2, pp. 269–286, 1891.

[152] S. C. Gupta, The classical Stefan problem: basic concepts, modelling and analysis with quasi-analytical solutions and methods. Elsevier, 2017, vol. 45.

[153] J. Crank, "Free and moving boundary problems," (No Title), 1984.

[154] S. Kutluay, A. Bahadir, and A. Özdeş, "The numerical solution of one-phase classical stefan problem," Journal of computational and applied mathematics, vol. 81, no. 1, pp. 135–144, 1997.

[155] H. G. Landau, "Heat conduction in a melting solid," Quarterly of Applied Mathematics, vol. 8, no. 1, pp. 81–94, 1950.

[156] A. Khandelwal, K. S. Hariharan, V. S. Kumar, P. Gambhire, S. M. Kolake, D. Oh, and S. Doo, “Generalized moving boundary model for charge–discharge of lifepo4/c cells,” Journal of Power Sources, vol. 248, pp. 101–114, 2014.

[157] K. Jagannathan and K. Raghunathan, “Charge-discharge asymmetry of phase change electrodes from isotropic solid state diffusion models,” Journal of the Electrochemical Society, vol. 159, no. 1, p. A26, 2011.

[158] S. Koga, L. Camacho-Solorio, and M. Krstic, “State estimation for lithium-ion batteries with phase transition materials via boundary observers,” Journal of Dynamic Systems, Measurement, and Control, vol. 143, no. 4, p. 041004, 2021.

[159] A. Alla and J. N. Kutz, “Nonlinear model order reduction via dynamic mode decomposition,” SIAM Journal on Scientific Computing, vol. 39, no. 5, pp. B778–B796, 2017.

[160] X. Hu, C. Zou, C. Zhang, and Y. Li, “Technological developments in batteries: a survey of principal roles, types, and management needs,” IEEE Power and Energy Magazine, vol. 15, no. 5, pp. 20–31, 2017.

[161] W. Chen, J. Liang, Z. Yang, and G. Li, “A review of lithium-ion battery for electric vehicle applications and beyond,” Energy Procedia, vol. 158, pp. 4363–4368, 2019.

[162] M. Baumann, L. Wildfeuer, S. Rohr, and M. Lienkamp, “Parameter variations within li-ion battery packs–theoretical investigations and experimental quantification,” Journal of Energy Storage, vol. 18, pp. 295–307, 2018.

[163] K. Rumpf, M. Naumann, and A. Jossen, “Experimental investigation of parametric cell-to-cell variation and correlation based on 1100 commercial lithium-ion cells,” Journal of Energy Storage, vol. 14, pp. 224–243, 2017.

[164] R. Gogoana, M. B. Pinson, M. Z. Bazant, and S. E. Sarma, “Internal resistance matching for parallel-connected lithium-ion cells and impacts on battery pack cycle life,” Journal of Power Sources, vol. 252, pp. 8–13, 2014.

[165] C. Reiter, L. Wildfeuer, N. Wassiliadis, T. Krahl, J. Dirnecker, and M. Lienkamp, “A holistic approach for simulation and evaluation of electrical and thermal loads in lithium-ion battery systems,” in 2019 Fourteenth International Conference on Ecological Vehicles and Renewable Energies (EVER). IEEE, 2019, pp. 1–17.

[166] W. Shi, X. Hu, C. Jin, J. Jiang, Y. Zhang, and T. Yip, “Effects of imbalanced currents on large-format lifepo4/graphite batteries systems connected in parallel,” Journal of power sources, vol. 313, pp. 198–204, 2016.

[167] S. Miyatake, Y. Susuki, T. Hikihara, S. Itoh, and K. Tanaka, “Discharge characteristics of multicell lithium-ion battery with nonuniform cells,” Journal of Power Sources, vol. 241, pp. 736–743, 2013.

[168] H. Zhang, T. Wang, R. Lu, C. Zhu, and Y. Zhao, "Study on the impedance increase fault of parallel connected batteries based on simscape model simulation," in 2015 IEEE Vehicle Power and Propulsion Conference (VPPC). IEEE, 2015, pp. 1–6.

[169] T. Bruen and J. Marco, "Modelling and experimental evaluation of parallel connected lithium ion cells for an electric vehicle battery system," Journal of Power Sources, vol. 310, pp. 91–101, 2016.

[170] C. Pastor-Fernandez, T. Bruen, W. D. Widanage, M.-A. Gama-Valdez, and J. Marco, "A study of cell-to-cell interactions and degradation in parallel strings: implications for the battery management system," Journal of Power Sources, vol. 329, pp. 574–585, 2016.

[171] A. Cordoba-Arenas, S. Onori, and G. Rizzoni, "A control-oriented lithium-ion battery pack model for plug-in hybrid electric vehicle cycle-life studies and system design with consideration of health management," Journal of Power Sources, vol. 279, pp. 791–808, 2015.

[172] C. Campestrini, P. Keil, S. F. Schuster, and A. Jossen, "Ageing of lithium-ion battery modules with dissipative balancing compared with single-cell ageing," Journal of Energy Storage, vol. 6, pp. 142–152, 2016.

[173] L. Xie, D. Ren, L. Wang, Z. Chen, G. Tian, K. Amine, and X. He, "A facile approach to high precision detection of cell-to-cell variation for li-ion batteries," Scientific reports, vol. 10, no. 1, p. 7182, 2020.

[174] P. Jocher, M. Steinhardt, S. Ludwig, M. Schindler, J. Martin, and A. Jossen, "A novel measurement technique for parallel-connected lithium-ion cells with controllable interconnection resistance," Journal of Power Sources, vol. 503, p. 230030, 2021.

[175] A. Fill, T. Mader, T. Schmidt, R. Llorente, and K. P. Birke, "Measuring test bench with adjustable thermal connection of cells to their neighbors and a new model approach for parallel-connected cells," batteries, vol. 6, no. 1, p. 2, 2019.

[176] C. Li, N. Cui, L. Chang, Z. Cui, H. Yuan, and C. Zhang, "Effect of parallel connection topology on air-cooled lithium-ion battery module: Inconsistency analysis and comprehensive evaluation," Applied Energy, vol. 313, p. 118758, 2022.

[177] M. J. Brand, P. A. Schmidt, M. F. Zaeh, and A. Jossen, "Welding techniques for battery cells and resulting electrical contact resistances," Journal of Energy Storage, vol. 1, pp. 7–14, 2015.

[178] M. J. Brand, E. I. Kolp, P. Berg, T. Bach, P. Schmidt, and A. Jossen, "Electrical resistances of soldered battery cell connections," Journal of Energy Storage, vol. 12, pp. 45–54, 2017.

[179] P. Taheri, S. Hsieh, and M. Bahrami, “Investigating electrical contact resistance losses in lithium-ion battery assemblies for hybrid and electric vehicles,” Journal of Power Sources, vol. 196, no. 15, pp. 6525–6533, 2011.

[180] A. Fill, S. Koch, and K. P. Birke, “Algorithm for the detection of a single cell contact loss within parallel-connected cells based on continuous resistance ratio estimation,” Journal of Energy Storage, vol. 27, p. 101049, 2020.

[181] ——, “Analytical model of the current distribution of parallel-connected battery cells and strings,” Journal of Energy Storage, vol. 23, pp. 37–43, 2019.

[182] W. Diao, M. Pecht, and T. Liu, “Management of imbalances in parallel-connected lithium-ion battery packs,” Journal of Energy Storage, vol. 24, p. 100781, 2019.

[183] C. Luan, C. Ma, C. Wang, L. Chang, L. Xiao, Z. Yu, and H. Li, “Influence of the connection topology on the performance of lithium-ion battery pack under cell-to-cell parameters variations,” Journal of Energy Storage, vol. 41, p. 102896, 2021.

[184] T. Grün, K. Stella, and O. Wollersheim, “Influence of circuit design on load distribution and performance of parallel-connected lithium ion cells for photovoltaic home storage systems,” Journal of Energy Storage, vol. 17, pp. 367–382, 2018.

[185] L. Chang, C. Ma, Y. Zhang, H. Li, and L. Xiao, “Experimental assessment of the discharge characteristics of multi-type retired lithium-ion batteries in parallel for echelon utilization,” Journal of Energy Storage, vol. 55, p. 105539, 2022.

[186] Y. Tian, Z. Huang, X. Li, and J. Tian, “Parallel-connected battery module modeling based on physical characteristics in multiple domains and heterogeneous characteristic analysis,” Energy, vol. 239, p. 122181, 2022.

[187] N. Yang, X. Zhang, B. Shang, and G. Li, “Unbalanced discharging and aging due to temperature differences among the cells in a lithium-ion battery pack with parallel combination,” Journal of Power Sources, vol. 306, pp. 733–741, 2016.

[188] M. Fleckenstein, O. Bohlen, M. A. Roscher, and B. Bäker, “Current density and state of charge inhomogeneities in li-ion battery cells with lifepo4 as cathode material due to temperature gradients,” Journal of Power Sources, vol. 196, no. 10, pp. 4769–4778, 2011.

[189] B. Wu, V. Yufit, M. Marinescu, G. J. Offer, R. F. Martinez-Botas, and N. P. Brandon, “Coupled thermal–electrochemical modelling of uneven heat generation in lithium-ion battery packs,” Journal of Power Sources, vol. 243, pp. 544–554, 2013.

[190] M. Naylor-Marlow, J. Chen, and B. Wu, “Battery pack degradation-understanding aging in parallel-connected lithium-ion batteries under thermal gradients,” Preprint, 2023.

[191] M. Klein and J. Park, "Current distribution measurements in parallel-connected lithium-ion cylindrical cells under non-uniform temperature conditions," Journal of The Electrochemical Society, vol. 164, no. 9, p. A1893, 2017.

[192] B. Kenney, K. Darcovich, D. D. MacNeil, and I. J. Davidson, "Modelling the impact of variations in electrode manufacturing on lithium-ion battery modules," Journal of Power Sources, vol. 213, pp. 391–401, 2012.

[193] A. Weng, S. Pannala, J. B. Siegel, and A. G. Stefanopoulou, "Parallel-connected battery current imbalance dynamics," IFAC-PapersOnLine, vol. 55, no. 37, pp. 37–43, 2022.

[194] M. J. Brand, M. H. Hofmann, M. Steinhardt, S. F. Schuster, and A. Jossen, "Current distribution within parallel-connected battery cells," Journal of Power Sources, vol. 334, pp. 202–212, 2016.

[195] M. Schindler, P. Jocher, A. Durdel, and A. Jossen, "Analyzing the aging behavior of lithium-ion cells connected in parallel considering varying charging profiles and initial cell-to-cell variations," Journal of The Electrochemical Society, vol. 168, no. 9, p. 090524, 2021.

[196] X. Wang, Z. Wang, L. Wang, Z. Wang, and H. Guo, "Dependency analysis and degradation process-dependent modeling of lithium-ion battery packs," Journal of Power Sources, vol. 414, pp. 318–326, 2019.

[197] F. An, J. Huang, C. Wang, Z. Li, J. Zhang, S. Wang, and P. Li, "Cell sorting for parallel lithium-ion battery systems: Evaluation based on an electric circuit model," Journal of Energy Storage, vol. 6, pp. 195–203, 2016.

[198] R. Spurrett, C. Thwaite, A. Holland, D. Lizius, and G. Dudley, "Modeling of highly-parallel lithium-ion batteries," in Space Power, vol. 502, 2002, p. 685.

[199] M. J. Brand, D. Quinger, G. Walder, A. Jossen, and M. Lienkamp, "Ageing inhomogeneity of long-term used bev-batteries and their reusability for 2nd-life applications," in Electric Vehicle Symposium and Exhibition (EVS 26), 2012.

[200] X. Gong, R. Xiong, and C. C. Mi, "Study of the characteristics of battery packs in electric vehicles with parallel-connected lithium-ion battery cells," IEEE Transactions on Industry Applications, vol. 51, no. 2, pp. 1872–1879, 2014.

[201] N. Kakimoto and K. Goto, "Capacity-fading model of lithium-ion battery applicable to multicell storage systems," IEEE Transactions on Sustainable Energy, vol. 7, no. 1, pp. 108–117, 2015.

[202] L. A. Roman-Ramirez and J. Marco, "Design of experiments applied to lithium-ion batteries: A literature review," Applied Energy, vol. 320, p. 119305, 2022.

[203] J. Antony, Design of experiments for engineers and scientists. Elsevier, 2023.

[204] R. Rangappa and S. Rajoo, “Effect of thermo-physical properties of cooling mass on hybrid cooling for lithium-ion battery pack using design of experiments,” International Journal of Energy and Environmental Engineering, vol. 10, no. 1, pp. 67–83, 2019.

[205] E. Jiaqiang, D. Han, A. Qiu, H. Zhu, Y. Deng, J. Chen, X. Zhao, W. Zuo, H. Wang, J. Chen, et al., “Orthogonal experimental design of liquid-cooling structure on the cooling effect of a liquid-cooled battery thermal management system,” Applied Thermal Engineering, vol. 132, pp. 508–520, 2018.

[206] M. J. Brand, E. I. Kolp, P. Berg, T. Bach, P. Schmidt, and A. Jossen, “Electrical resistances of soldered battery cell connections,” Journal of Energy Storage, vol. 12, pp. 45–54, 2017.

[207] K. Moy, M. A. Khan, S. Fasolato, G. Pozzato, A. Allam, and S. Onori, “Second-life lithium-ion battery aging dataset based on grid storage cycling,” Data in Brief, vol. 57, p. 111046, 2024.

[208] T. Hastie, R. Tibshirani, J. H. Friedman, and J. H. Friedman, The elements of statistical learning: data mining, inference, and prediction. Springer, 2009, vol. 2.

[209] M. S. Thiese, B. Ronna, and U. Ott, “P value interpretations and considerations,” Journal of thoracic disease, vol. 8, no. 9, p. E928, 2016.

[210] H. Akaike, “Information theory and an extension of the maximum likelihood principle,” in Selected papers of hirotugu akaike. Springer, 1998, pp. 199–213.

[211] C. Molnar, Interpretable machine learning. Lulu. com, 2020.

[212] A. Geslin, L. Xu, D. Ganapathi, K. Moy, W. C. Chueh, and S. Onori, “Dynamic cycling enhances battery lifetime,” Nature Energy, pp. 1–9, 2024.

[213] E. Hosseinzadeh, S. Arias, M. Krishna, D. Worwood, A. Barai, D. Widanalage, and J. Marco, “Quantifying cell-to-cell variations of a parallel battery module for different pack configurations,” Applied Energy, vol. 282, p. 115859, 2021.

[214] G. Piombo, J. Marco, and R. Boyd, “Analysis of parallel connected lithium-ion cells imbalanced performance based on electrothermal modelling environment,” in 2021 IEEE Vehicle Power and Propulsion Conference (VPPC). IEEE, 2021, pp. 1–7.

[215] X. Fan, W. Zhang, Z. Wang, F. An, H. Li, and J. Jiang, “Simplified battery pack modeling considering inconsistency and evolution of current distribution,” IEEE Transactions on Intelligent Transportation Systems, vol. 22, no. 1, pp. 630–639, 2020.

[216] K. Rumpf, A. Rheinfeld, M. Schindler, J. Keil, T. Schua, and A. Jossen, “Influence of cell-to-cell variations on the inhomogeneity of lithium-ion battery modules,” Journal of The Electrochemical Society, vol. 165, no. 11, p. A2587, 2018.

[217] S. B. Lee and S. Onori, "A robust and sleek electrochemical battery model implementation: a matlab® framework," Journal of The Electrochemical Society, vol. 168, no. 9, p. 090527, 2021.

[218] M. F. Niri, C. Reynolds, L. A. R. Ramirez, E. Kendrick, and J. Marco, "Systematic analysis of the impact of slurry coating on manufacture of li-ion battery electrodes via explainable machine learning," Energy Storage Materials, vol. 51, pp. 223–238, 2022.

[219] X. Liu, W. Ai, M. N. Marlow, Y. Patel, and B. Wu, "The effect of cell-to-cell variations and thermal gradients on the performance and degradation of lithium-ion battery packs," Applied Energy, vol. 248, pp. 489–499, 2019.

[220] K. Chen, Y. Chen, Z. Li, F. Yuan, and S. Wang, "Design of the cell spacings of battery pack in parallel air-cooled battery thermal management system," International Journal of Heat and Mass Transfer, vol. 127, pp. 393–401, 2018.

[221] P. Saechan and I. Dhuchakallaya, "Numerical investigation of air cooling system for a densely packed battery to enhance the cooling performance through cell arrangement strategy," International Journal of Energy Research, vol. 46, no. 14, pp. 20 670–20 684, 2022.

[222] F. An, L. Chen, J. Huang, J. Zhang, and P. Li, "Rate dependence of cell-to-cell variations of lithium-ion cells," Scientific reports, vol. 6, no. 1, p. 35051, 2016.

[223] R. Xiong, J. Cao, Q. Yu, H. He, and F. Sun, "Critical review on the battery state of charge estimation methods for electric vehicles," Ieee Access, vol. 6, pp. 1832–1843, 2017.

[224] C. Huang, Z. Wang, Z. Zhao, L. Wang, C. S. Lai, and D. Wang, "Robustness evaluation of extended and unscented kalman filter for battery state of charge estimation," Ieee Access, vol. 6, pp. 27 617–27 628, 2018.

[225] A. Tulsyan, Y. Tsai, R. B. Gopaluni, and R. D. Braatz, "State-of-charge estimation in lithium-ion batteries: A particle filter approach," J. Power Sources, vol. 331, pp. 208–223, 2016.

[226] S. Dey, B. Ayalew, and P. Pisu, "Nonlinear robust observers for state-of-charge estimation of lithium-ion cells based on a reduced electrochemical model," IEEE Transactions on Control Systems Technology, vol. 23, no. 5, pp. 1935–1942, 2015.

[227] D. Locatelli, G. Saccani, B. S. Rego, G. V. Raffo, and D. M. Raimondo, "Set-based joint state and parameter estimation of a li-ion cell using constrained zonotopes," in 2022 IEEE Vehicle Power and Propulsion Conference (VPPC). IEEE, 2022, pp. 1–6.

[228] X. Hu, D. Cao, and B. Egardt, "Condition monitoring in advanced battery management systems: Moving horizon estimation using a reduced electrochemical model," IEEE/ASME Transactions on Mechatronics, vol. 23, no. 1, pp. 167–178, 2017.

[229] J.-N. Shen, Y.-J. He, Z.-F. Ma, H.-B. Luo, and Z.-F. Zhang, "Online state of charge estimation of lithium-ion batteries: A moving horizon estimation approach," Chemical Engineering Science, vol. 154, pp. 42–53, Nov. 2016.

[230] J. Yan, S. Li, and Y. Wan, "Lithium-ion battery state-of-charge estimation using a real-time moving horizon estimation algorithm," in 2021 CAA Symposium on Fault Detection, Supervision, and Safety for Technical Processes (SAFEPROCESS). IEEE, Dec. 2021.

[231] Y. Wan, S. Du, J. Yan, and Z. Wang, "Towards fast embedded moving horizon state-of-charge estimation for lithium-ion batteries," J. Energy Storage, vol. 78, p. 110024, 2024.

[232] D. Zhang, L. D. Couto, S. Benjamin, W. Zeng, D. F. Coutinho, and S. J. Moura, "State of charge estimation of parallel connected battery cells via descriptor system theory," in 2020 American Control Conference (ACC). IEEE, 2020, pp. 2207–2212.

[233] D. Zhang, L. D. Couto, P. Gill, S. Benjamin, W. Zeng, and S. J. Moura, "Interval observer for soc estimation in parallel-connected lithium-ion batteries," in 2020 American Control Conference (ACC). IEEE, 2020, pp. 1149–1154.

[234] J. A. Lone, A. Goel, N. K. Tomar, and S. Bhaumik, "Kalman filtering for descriptor systems: An alternative approach and application to cell level estimation of a lithium-ion battery," in 2023 62nd IEEE Conference on Decision and Control (CDC). IEEE, 2023, pp. 2570–2575.

[235] J. A. Lone, N. K. Tomar, and S. Bhaumik, "Functional observer design for parallel connected li-ion battery: A descriptor systems theory approach," IEEE Control Systems Letters, vol. 7, pp. 961–966, 2022.

[236] D. Zhang, L. D. Couto, P. S. Gill, S. Benjamin, W. Zeng, and S. J. Moura, "Thermal-enhanced adaptive interval estimation in battery packs with heterogeneous cells," IEEE Trans. Control Syst., vol. 30, no. 3, pp. 1102–1115, 2021.

[237] G. Pozzato, A. Allam, L. Pulvirenti, G. A. Negoita, W. A. Paxton, and S. Onori, "Analysis and key findings from real-world electric vehicle field data," Joule, vol. 7, no. 9, pp. 2035–2053, 2023.

[238] X. Ding, Z. Cui, H. Yuan, and N. Cui, "Diagnosis of connection fault for parallel-connected lithium-ion batteries based on long short-term memory networks," J. Energy Storage, vol. 55, p. 105552, 2022.

[239] P. Lambert, E. Tredenick, S. Duncan, and R. Drummond, "Detecting faulty lithium-ion cells in large-scale parallel battery packs using current distributions," 2023.

[240] M. Rausch, S. Streif, C. Pankiewitz, and R. Findeisen, "Nonlinear observability and identifiability of single cells in battery packs," in 2013 IEEE International Conference on Control Applications (CCA). IEEE, 2013, pp. 401–406.

[241] C. R. Johnson, D. D. Olesky, and P. Van den Driessche, "Sign determinancy in lu factorization of p-matrices," Linear algebra and its applications, vol. 217, pp. 155–166, 1995.

[242] R. E. Kass and P. W. Vos, Geometrical foundations of asymptotic inference. John Wiley & Sons, 2011.

[243] M. Vidyasagar, Nonlinear systems analysis. SIAM, 2002.

[244] A. Allam and S. Onori, "Linearized versus nonlinear observability analysis for lithium-ion battery dynamics: Why respecting the nonlinearities is key for proper observer design," IEEE Access, vol. 9, pp. 163 431–163 440, 2021.

[245] S. Díaz-Seoane, X. Rey Barreiro, and A. F. Villaverde, "Strike-goldd 4.0: user-friendly, efficient analysis of structural identifiability and observability," Bioinformatics, vol. 39, no. 1, p. btac748, 2023.

[246] C. V. Rao, J. B. Rawlings, and J. H. Lee, "Constrained linear state estimation—a moving horizon approach," Automatica, vol. 37, no. 10, pp. 1619–1628, 2001.

[247] M. W. Mehrez, G. K. I. Mann, and R. G. Gosine, "An optimization based approach for relative localization and relative tracking control in multi-robot systems," Journal of Intelligent & Robotic Systems, vol. 85, pp. 385–408, 2017.

[248] C. Taborelli, S. Onori, S. Maes, P. Sveum, S. Al-Hallaj, and N. Al-Khayat, "Advanced battery management system design for soc/soh estimation for e-bikes applications," International Journal of Powertrains, vol. 5, no. 4, pp. 325–357, 2016.